PHYSICAL MODELING OF TSUNAMIS GENERATED BY THREE-DIMENSIONAL DEFORMABLE GRANULAR LANDSLIDES

A Dissertation
Presented to
The Academic Faculty

by

Fahad Mohammed

In Partial Fulfillment
of the Requirements for the Degree
Doctor of Philosophy in the
School of Civil and Environmental Engineering

Georgia Institute of Technology
December 2010

PHYSICAL MODELING OF TSUNAMIS GENERATED BY THREE-DIMENSIONAL DEFORMABLE GRANULAR LANDSLIDES

Approved by:

Dr. Hermann M. Fritz, Advisor
School of Civil and Environmental Engineering
Georgia Institute of Technology

Dr. Kevin Haas
School of Civil and Environmental Engineering
Georgia Institute of Technology

Dr. Paul Work
School of Civil and Environmental Engineering
Georgia Institute of Technology

Dr. Donald Webster
School of Civil and Environmental Engineering
Georgia Institute of Technology

Dr. Andrew Newman
School of Earth and Atmospheric Sciences
Georgia Institute of Technology

Dr. Joseph Dufek
School of Earth and Atmospheric Sciences
Georgia Institute of Technology

Date Approved: August 06, 2010

ACKNOWLEDGEMENTS

I would like to take this opportunity to thank several people whose constant support, guidance and encouragement were invaluable during my doctoral work.

At the onset, I would like to express my deepest gratitude for my advisor and mentor, Dr. Hermann Fritz for his guidance throughout the study. I am extremely grateful for his unending support during the course of my graduate studies. I am grateful to Dr. Paul Work, Dr. Kevin Haas, Dr. Donald Webster, Dr. Andrew Newman and Dr. Josef Dufek for serving as the committee members. Their time, effort, comments and suggestions are invaluable to give this dissertation its final shape.

I want to show my greatest appreciation and thanks to my parents, my sister Farah and brother Faiz for their constant love and support. Though miles apart, we are always close. Last but not the least, I would like to thank the good friends I have made over the years, especially, Vivek, Aditya, Mesut, Sri, Zafer, Chad, Donsik, among others for their support and help throughout my stay in Savannah.

This work was supported by National Science Foundation, Division of Civil, Mechanical and Manufacturing Innovation through the grant nos. CMMI-0421090, CMMI-0936603, CMMI-0402490 and CMMI-0927178.

In the end, I would like to thank the excellent faculty of the School of Civil and Environmental Engineering at Georgia Institute of Technology for the excellent education they provided.

TABLE OF CONTENTS

LIST OF TABLES

LIST OF FIGURES

SUMMARY

Tsunamis are gravity water waves that are generated by impulsive disturbances such as submarine earthquakes, landslides, volcanic eruptions, underwater explosions or asteroid impacts. Submarine earthquakes are the primary tsunami source, but landslides may generate tsunamis exceeding tectonic tsunamis locally, in both wave and runup heights. The field data on landslide tsunami events are limited, in particular regarding submarine landslide dynamics and wave generation in the impact region. The objective of the present study is to physically model tsunamis generated by three-dimensional deformable granular landslides. Predictive equations for tsunami wave and runup characteristics are obtained which may be used for initial rapid hazard assessment and mitigation.

The physical model was setup in the NEES 3D tsunami wave basin at Oregon State University in Corvallis, Oregon. A pneumatic landslide tsunami generator was deployed to simulate natural landslide motion on a hill slope. The instrumentation consists of four underwater and above water cameras, a particle image velocimetry (PIV) camera, twenty five wave and runup gauges and a multi-transducer acoustic array (MTA). The subaerial landslide shape and kinematics on the hill slope and the surface elevation of the offshore propagating tsunami wave and runup on the hill slope are measured.

The evolution of the landslide front velocity, maximum landslide thickness and width are obtained along the hill slope. The landslide surface velocity distribution is obtained from the PIV analysis of the subaerial landslide motion. The shape and the size of the submarine landslide deposit are measured from the MTA data.

The subaerial landslide impact on the water surface displaces water away from the impact region. The leading tsunami wave crest and trough are generated by the water displacement and the subsequent drawdown. The trailing waves are generated by the subsequent oscillating shoreline runup and drawdown on the hill slope until the still water surface is restored. The 3D tsunami waves propagate away from the landslide source as radial wave fronts.

The amplitudes of the first 3 waves decay in the radial and the angular direction. The rate of radial decay is primarily dependent on the landslide width and Froude number at impact. The angular decay follows $\cos\theta$ and $\cos^2\theta$ for the first and the second wave, respectively . The first wave amplitudes depend primarily on the landslide Froude number and relative thickness at impact. The landslide volume mainly influences the amplitudes of the second waves. The wave celerity of the leading tsunami wave may be approximated by the solitary wave speed while the trailing waves are slower due to the dispersion effects caused by decay in wave period and wavelength from the front to the back of the wave. The wave periods and wavelengths are dependent on the landslide Froude number, landslide thickness, width at impact and the landslide volume. The wave periods and wavelengths increase with the propagation distance due to dispersion effects but vary minimally in the angular direction.

Between 1-15% of the landslide kinetic energy is converted into the wave train energy in the experimental study. The efficiency of wave generation is relatively low in 3D as compared to 2D due to energy dissipation by frictional losses and internal deformations during the landslide motion and the distribution of the unidirectional landslide energy by the radial wave. The landslide generated waves are weakly nonlinear in nature and span from shallow to deep water depth regimes with the bulk of the waves in the intermediate water depth regime. Analytical wave theories describing the 3D tsunamis in the present study are limited to segments of the wave train or specific cases, but certain wave profiles may be approximated by Stokes theory or

cnoidal wave theory depending on the water depth regime. The experimental data serves as benchmark for numerical simulations and model advancement.

CHAPTER I

INTRODUCTION

Tsunami is a Japanese word with "tsu" meaning harbor and "nami" meaning wave. The term "harbor wave" for a tsunami is deficient of the description of the source mechanism for the wave generation. Tsunamis belong to the class of gravity water waves with long wave periods and long wavelengths relative to the ocean depth. Tsunamis are barely perceptible in the deep ocean due to their large wavelengths and small wave heights. However, as they approach shallow waters, they undergo wave shoaling, diffraction, refraction and wave breaking depending on the bathymetry and the topography of the coastal region. In general, tsunamis are caused by the displacement of a large volume of water due to impulsive disturbances such as submarine earthquakes, landslides, volcanic eruptions, underwater explosions or asteroid impacts. Tsunamis are primarily generated by earthquakes but landslides can often generate tsunamis with extremely high waves and runup compared with earthquake tsunamis but the generated waves usually decay faster. Landslides account for roughly 10% of tsunamis observed in the oceans (Kajiura (1990)).

The term *landslide* is used to describe the movement of a mass of rock, debris or earth down a slope (Cruden (1991)). The mass flow may be grouped into high density rock and soil movements and low density glacier falls and snow avalanches (Cruden and Varnes (1996), Hutter *et al.* (2005)). Landslides are primarily triggered by seismic activity but other possible causes can be precipitation, changes in water levels close to slopes, failure of natural dams, volcanic eruptions or erosion (Cruden and Varnes (1996)). A comprehensive study on the landslide initiation process and dynamics is beyond the scope of this work. Herein, focus in on the hazardous effects of landslides

in relation with tsunami generation. Tsunamis generated by landslides may be classified based on the initial position of the landslide as subaerial, partially submerged or submarine landslide generated tsunamis depending on the initial position of the landslide relative to the water depth. There is a gradual transition from subaerial to submarine case with increasing depth of landslide submergence. This classification is commonly used for observations and in describing the landslide generated tsunami models.

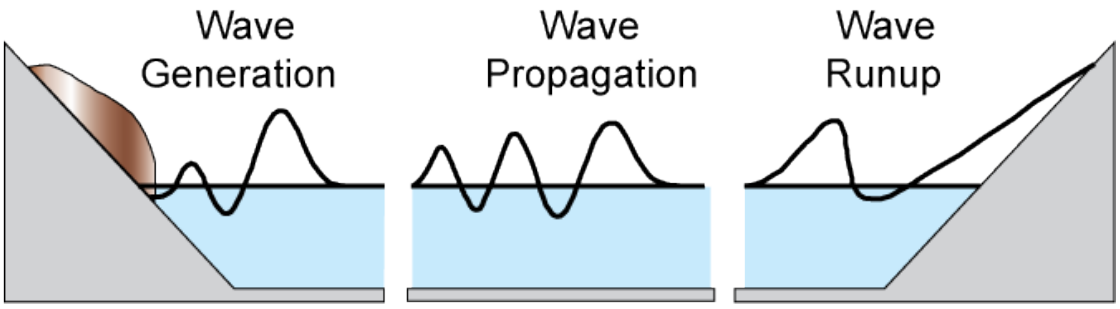

Figure 1: Phases of landslide generated tsunamis: wave generation, propagation and runup

Landslide generated tsunamis can occur either in coastal areas or in closed water basins such as bays and lakes. Submarine landslide generated tsunamis can also occur offshore where the continental shelf breaks. The initial position of the landslide determines the characteristics of the generated tsunami and the importance of air as the third phase. The landslide tsunami process involves the landslide motion, tsunami wave generation, landslide runout, tsunami propagation and runup. These processes are studied independently but in the context of landslide tsunamis, these need to be coupled. The landslide tsunami schematics are shown in Fig. 1.

Landslide generated tsunamis may pose a hazard in populated coastal areas and are of particular concern in confined water bodies such as bays, fjords, lakes and reservoirs. The largest recorded tsunami waves in history were generated by a landslide at Lituya bay in Alaska in 1958. The event generated a tsunami wave which reached a wave runup of 524 m as shown in Fig. 2 (Miller (1960), Fritz *et al.* (2001), Fritz *et al.*

(2009)). The landslide was a result of an earthquake which had a Moment magnitude M_w of 8.3 on the Richter scale (Tocher and Miller (1959)).

(a)

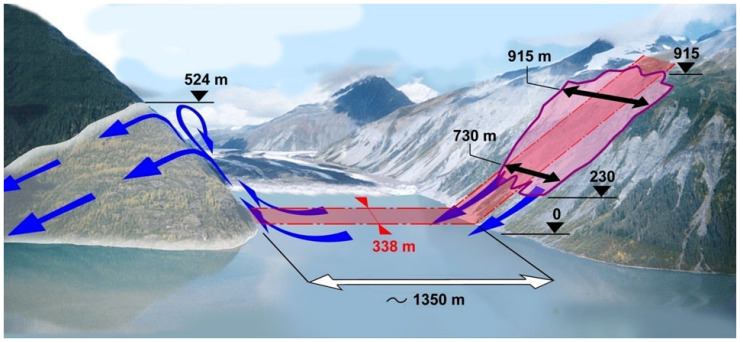

(b)

Figure 2: The 1958 Lituya bay landslide tsunami event: (a) trimline of the tsunami runup measured from the destroyed vegetation and (b) maximum recorded tsunami runup of 524 m in the direction of landslide prolongation (Miller (1960), Fritz *et al.* (2001)).

One of the most destructive tsunamis generated by landslide occurred in the Vajont reservoir, Italy in 1963 (Müller (1964)). The reservoir was formed when a dam measuring 265.5 m high was constructed across a narrow portion of the Vajont river

with a width of 160 m. The drawdown of water in the reservoir led to the collapse of the southern flank of Vajont reservoir on October 9, 1963. The partially submerged landslide with a volume of 0.24 km^3 penetrated like a piston almost horizontally into the reservoir with speeds up to 30 m/s. The wave runup in the direct prolongation of the slide axis reached 270 m above the reservoir level before impact corresponding to 245 m above the dam crest (Müller (1964)). The generated dam break like flood wave overtopped the dam by more than 100 m destroying the village of Longarone resulting in 2000 casualties (Müller (1964)).

A few of the important landslide generated events in the last two centuries are summarized in Table 1. The summary includes the date, location of the event, governing parameters such as the slide volume V_s, hill slope angle α and the water depth h. Also included are the wave runup heights R and the number of fatalities.

The hazards associated with landslide generated tsunamis are usually due to tsunami runup along the shoreline and overtopping of dams. Landslide tsunamis are often triggered unexpectedly after a strong earthquake and they usually have extremely short propagation times to target coastlines (for e.g. Skagway, Alaska 1994; Kulikov *et al.* (1996), Synolakis *et al.* (2000)). Hence robust warning systems are necessary to predict the landslide motion as well as the tsunami generation and runup impact. It is often difficult to prevent a landslide from occurring, but in some cases it was possible to arrest active landslide creeping with massive remedial methods. The most costly example is of the Clyde dam in New Zealand. The creeping of most active slides were stopped by a combination of drainage works to lower the ground water level and large scale mass displacements by unloading the head of active frontal lobes and buttressing the toe of the lobes (Jennings *et al.* (1991), MacFarlane and Gillon (1996), MacFarlane and Jenks (1996), Gillon and Saul (1996)). Landslide monitoring can help predict the landslide failure and impact, and aids in hazard mitigation of the generated tsunami wave.

Table 1: Historical landslide generated tsunamis

Date	Location	Parameters			Effects		Reference
		$V_s(10^6\mathrm{m}^3)$	α (^{o})	h(m)	R(m)	Fatalities	
1756	Tjelle (NO)	15	>25	>200	46	38	Jϕrstad (1968)
1792	Unzen Volcano (JP)	500	10	64	10	>15000	Ogawa (1924)
1883	Krakatau (ID)	-	-	-	35	36,000	Simkin and Fiske (1983), Fritz (2002)
1888	Ritter Island (PNG)	5000	10-15	1000	20	<100	Ward and Day (2003)
1934	Tafjord (NO)	2-3	60	>200	62	41	Jϕrstad (1968), Slingerland and Voight (1979)
1936	Lake Loen (NO)	1	25	<60	74	73	Slingerland and Voight (1979), Grimstad and Nesdal (1991)
1958	Lituya Bay (USA)	31	40	122	524	2	Miller (1960), Fritz *et al.* (2001)
1959	Pontesei Reservoir (IT)	5	≈5	47	-	1	Panizzo *et al.* (2005)
1963	Vaiont Reservoir (IT)	240	0-40	-	270	≈2000	Müller (1964)
1971	Yanahuin Lake (P)	0.1	45	38	30	400-600	Plafker and Eyzaguirre (1979), Slingerland and Voight (1979)
1980	Spirit Lake (USA)	430	-	-	200	0	Voight *et al.* (1981), Voight *et al.* (1983), Fritz (2002)
1998	Papua New Guinea	4-6	-	-	-	>2000	Synolakis *et al.* (2002)
2006	Java	-	-	-	21	600	Fritz *et al.* (2007)

The field data from landslide tsunami events are quite sparse and limited to very few cases. The landslide field data is limited to landslide scarps and subaqueous deposits where mapped. The tsunami field data are limited to far-field wave measurements and trimline from the vegetation destroyed by the tsunami runup. The near-field information in the wave generation region is not available. Hence an effort is needed to physically and numerically model landslide tsunamis in order to improve the understanding of such events and aid in hazard prediction and mitigation. The observations and conclusions from physical models and field data can provide for the validation, verification and advancement of numerical models and supplement the development of robust warning systems for tsunamis generated by landslides.

A concise understanding of landslide tsunamis requires multidisciplinary studies that build upon experiences in engineering seismology, geotechnical engineering, marine geology, modeling of sediment deposition and runout and hydrodynamics. However a comprehensive study is beyond the scope of a single Ph.D thesis. The aim of the present work is to physically model fully three-dimensional tsunamis generated by deformable granular landslides. The focus is on the landslide kinematics during impact, near field wave characteristics during the landslide impact, tsunami generation, far field wave propagation and lateral tsunami runup characteristics.

CHAPTER II

LITERATURE REVIEW

2.1 Introduction

The hazardous nature of landslide generated tsunamis is compounded by the limited availability of field data on the slide motion, near-field wave characteristics in the wave generation region and the wave train. Physical and numerical modeling of landslide generated tsunamis are needed to explore the inherent link between the landslide and the generated wave characteristics. The process of landslide generated tsunamis can be divided into the following categories.

- The mechanism of tsunamigenic landslides.
- The tsunami wave generation in the near field region.
- The tsunami wave propagation.
- The hazards associated with tsunami wave runup and impact.

These categories have been studied independently, but in the context of landslide generated tsunamis, these processes are coupled and need to be studied simultaneously.

This chapter begins with the classification of events and inferences derived from observations of landslide generated tsunami events. This is followed by a brief introduction on landslides and a review of the physical and numerical modeling efforts of deformable granular landslides. This is followed by a section on landslide generated tsunamis. In this context, physical and numerical modeling of landslide generated tsunamis are presented. The chapter concludes with a summary of the identified research gaps that need to be addressed.

2.2 *Landslide generated tsunamis*

The landslide generated tsunamis belong to the gravity water waves family. These impulsive waves are a response generated by an impulsive disturbance on the water body. Landslide driven tsunamis are described by the parameters shown in Fig. 3.

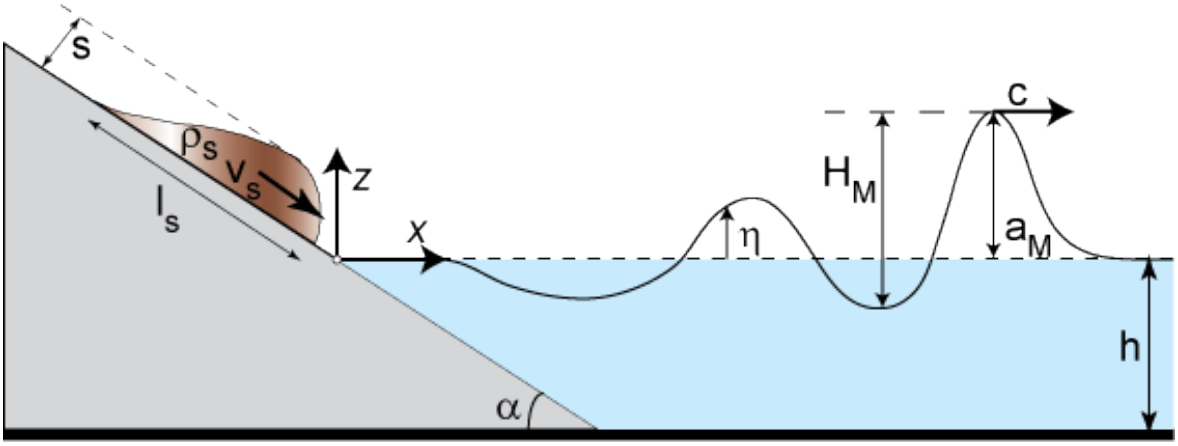

(a)

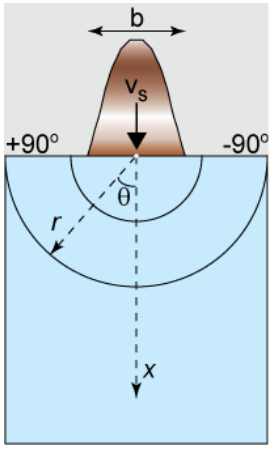

(b)

Figure 3: Landslide generated tsunamis: (a) definition of parameters in the direction of slide motion; (b) coordinate system to quantify the generated tsunami wave.

The landslide may be characterized by the slide thickness s, slide width b, slide length l_s, slide velocity at impact v_s and slide density ρ_s. The slide velocity can be characterized by either the slide centroid or the slide front velocity. In the case of a broadly spreading deformable landslide, the estimation of the slide centroid velocity may become tedious and thus slide front velocity can be used to describe the slide

dynamics. The alongshore topography may be approximated by either a linear (Enet and Grilli (2005), Enet and Grilli (2007), Liu *et al.* (2005), Panizzo *et al.* (2005)) or a curved coastline (Briggs *et al.* (1995), Risio *et al.* (2009b)). The bathymetry of the basin can be approximated by the still water depth h and the hill slope angle α. Two different coordinate systems are used in the study. For studying the landslide dynamics the origin is fixed at the initial rest position of the landslide and the coordinate system follows the topography of the terrain. The generated impulse waves are studied in a cylindrical coordinate system where the origin may be fixed at the impact location or the intersection of the waterline with the hill slope. The waves η are defined as a function, $f(r, \theta, t)$, where r is the distance from the origin relative to the landslide direction. The landslide direction corresponds to $\theta = 0^\circ$ while the runup direction on the hill slope corresponds to $\theta = +90^\circ$ and -90°. The wave characteristics are described by the wavelength L, wave period T and wave height H. The crest and trough amplitudes are denoted as a_c and a_t. Linear wave approximation yields equipartition of the wave height. But the nonlinearity of landslide generated tsunamis may yield wave crests and troughs which deviate from equipartition of wave height. The individual waves from the landslide generated tsunami wave train can be identified using the upcrossing technique, wavelets, or Fourier analysis. The wavelength can be described from upcrossing to upcrossing points, downcrossing to downcrossing points, crest-to-crest or trough-to-trough. These wavelengths are the same in the case of a linear wave. However, these quantities are different for a landslide generated tsunami due to the difference in the wave generation mechanism between the first and second wave crest and trough. The individual wave celerity c can be determined from the above wave quantities.

The landslide generated tsunami events are commonly classified into three categories based on the initial position of the slide relative to the water body as shown in Fig. 4. These are

- **Subaerial** landslide generated tsunamis involves all the three phases of air, water and slide material. This involves the subaerial landslide motion, impact of landslide on the water surface and the submarine runout and deposition. In general, the wave train starts as an elevation. In some high velocity impact cases, the formation of an impact crater separates the water surface from the slide surface.

- **Partially submerged** events also involve all the three phases.

- **Submarine** or subaqueous landslide generated tsunamis can be treated as two phase flow involving only the slide and water. In this case, the initial landslide position is fully submerged underwater and generally the wave train begins with a depression or a trough

The tsunami wave heights tend to decrease with increasing submergence of the initial position of the landslide. The results from the subaerial, partially submerged or the submarine landslide generated tsunami cases are not transferable among them.

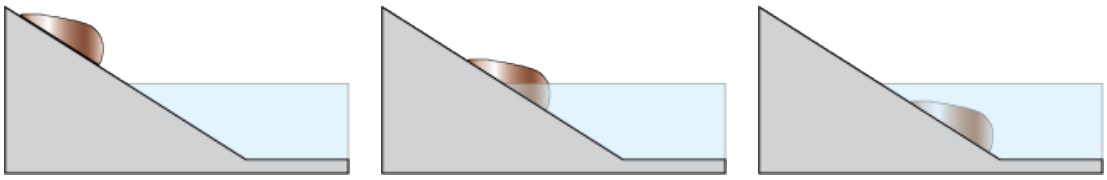

Figure 4: Classification of landslide generated tsunami based on the initial position of the landslide: (a) subaerial; (b) partially submerged and (c) subaqueous.

2.3 Inferences from Landslide Generated Tsunami Events

The main conclusions from Table 1, the available documentation and review of historical cases are summarized below:

- The combined documented human death toll from mass flow generated tsunamis

probably exceeds 60,000 (Table 1). This number is inclusive of tsunamis generated during the volcanic events of Krakatau, Indonesia (Fritz (2002)) and Shimabara, Japan (Ogawa (1924)).

- The landslide dynamics and generated tsunami wave characteristics from field cases are sparse and quite limited (Kamphuis and Bowering (1970)).

- The slide data from field cases is mostly limited to the landslide scarp and deposits. The mapped submarine deposits are usually devoid of information on thickness, volume and matrix composition of the slide material (Hampton *et al.* (1996)).

- Information on wave data for field cases are limited to far field tide gauges, eyewitnesses and trimlines due to wave runup. The wave runup and far field wave data may be used to back calculate and estimate the near field wave characteristics.

- Tsunamigenic landslides are primarily triggered by seismic activity (e.g Lituya Bay case, Miller (1960)). The other possible triggers are, precipitation, changes in water levels close to slopes (e.g Vaiont case, Müller (1964)), failure of natural dams (Schuster and Wieczorek (2002)), volcanic eruptions (e.g Shimabara, Japan, Ogawa (1924), Mount St. Helens, USA, Voight *et al.* (1983)) or erosion.

- The landslide volumes may exceed the volume of confined water bodies such as lakes and reservoirs (e.g Vaiont case (Italy), Müller (1964); Spirit Lake (USA), Voight *et al.* (1981)).

- Hill slope angle, α, between $0° - 90°$ are possible (Slingerland and Voight (1979)).

- The slide volume in general increases with decreasing slope angle α or increasing submergence of the initial position.

- The slide grain density varies from $\rho_g \approx 850$ kg/m^3 for ice to $\rho_g \approx 2700$ kg/m^3 for granite gneiss. The bulk slide density depends on the porosity of the slide material and the slide matrix composition.

- The mean bulk porosity n of the slides varies typically between 0.3 and 0.4 (Fritz (2002)).

- Landslides may propagate with slow speeds (e.g Pontesei case; Caratto *et al.* (2002)) or very fast speeds (e.g $v_s = 92$ m/s in the Lituya Bay case, Fritz (2002)). Landslides with velocities up to 150 m/s resulting in slide Froude number $F = v/\sqrt{gh}$ up to 5 are possible (Fritz (2002)).

- Landslides volumes V_s up to 5000 km^3 were estimated for slides with submarine runouts (Normark *et al.* (1993)). In case of events where the landslide volume is below 10,000 m^3, the generated tsunami rarely poses a threat. Tsunami waves generated by slides with volumes up to 100,000 m^3 pose a threat mostly in limited areas and small water bodies.

- The largest wave runup of 524 m in recorded history was observed to have been caused by a landslide with velocities up to 100 m/s and slide Froude number F up to 3 (Fritz *et al.* (2001)).

- The available field data and back calculations from wave runup provides evidence for the strong non-linearity of the generated tsunami waves.

- The largest wave and runup heights usually occur in the direction of the slide motion if there is an opposing coastline (e.g Lituya Bay case; Miller (1960), Fritz *et al.* (2001)). However, depending on the topography, the largest wave runup may occur laterally to the landslide direction (e.g Tafjord, Norway; Jϕrstad (1968)). In case of continental coastlines with offshore landslide motion, the lateral tsunami runup on the coastline becomes important.

Table 2: Landslide classification after Varnes (1978)

MOVEMENT TYPE		TYPE OF MATERIAL		
		BEDROCK	ENGINEERING SOILS	
			COARSE	FINE
Falls		Rock fall	Debris fall	Earth fall
Topples		Rock topple	Debris topple	Earth topple
Slides	rotational	Rock slump	Debris slump	Earth slump
	translational	Rock block slide	Debris block slide	Earth block slide
		Rock slide	Debris slide	Earth slide
Lateral spreads		Rock spread	Debris spread	Earth spread
Flows		Rock flow	Debris flow	Earth flow
Complex		Combination of two or more types of movement		

- The first wave may not necessarily be the highest wave.
- Improved prediction of the landslides and the landslide generated tsunamis are needed for hazard mitigation.

2.4 Landslides

The term landslide is generally used to describe the movement of a mass of rock, debris or earth down a slope (Cruden (1991)). In the English literature, the most widely used classification of landslides is given by Varnes (1978). The landslide can be classified and described by two nouns, the first noun describes the landslide material and the second noun describes the type of movement. The landslide material is divided into two classes: rock and engineering soils; soils are further divided into debris and earth. The types of movement are divided into five groups: falls, topples, slides, spreads and flows. The classification of slope movement by Varnes (1978) is shown in Table 2. Further graphic illustrations and discussion on the combinations of the slide material and types of movements can be found in Varnes (1978) and Cruden and Varnes (1996).

There is a complete gradation from debris slides to debris flows depending on the

water content, mobility and the character of the movement. Radbruch-Hall (1978) proposed the terms to describe the water content of landslide materials made by simple observations of the displaced material. Varnes (1978) presented the modified terms of Radbruch-Hall (1978) as follows:

- **Dry**: no visible moisture.
- **Moist**: contains some water but no free water; the material may behave as a plastic solid but does not flow.
- **Wet**: contains enough water to behave in parts as a liquid, has water flowing from it or supports significant bodies of standing water.
- **Very wet**: contains enough water to flow as a liquid under low gradients.

As the slide movement becomes more rapid, the transition from debris slide to debris avalanche becomes important regarding the generation of tsunamis. The term debris avalanche is used in general to describe very rapid and extremely rapid debris flows of dry or largely unsaturated granulates (Cruden and Varnes (1996)).

Two limiting cases of landslide avalanche are termed flow avalanche and powder avalanche (Hutter (1996)) depending on the role of the interstitial fluid. Flow-avalanche is a dense gravity driven laminar flow where the solid particles dominate the flow dynamics and the behavior of the interstitial fluid is negligible. The typical flow of this nature are sturzstorms, debris flows, rockfalls and snow avalanches. Powder avalanche is the turbulent flow of air borne particles in which the fluid phase dominates the flow dynamics and the particle flow dynamics are of less significance. Density and turbidity currents such as dust clouds in deserts, in pyroclastic volcanic eruptions, in submarine slides and in snow and ice avalanches are the typical flows belonging to powder avalanche. In this section, the development of the granular landslide physics, their governing dynamical equations and the numerical solutions to the

dynamic problem are reviewed. In the end, comparative studies between experimental data and numerical solutions are summarized. The focus is on the dynamics of granular landslides without delving into the source or cause of the landslides.

2.4.1 Landslide Dynamics

Heim (1932) as quoted by Hsü (1975), found that the slope of the energy line for landslides is approximately the same as the coefficient of friction for sliding masses. This friction coefficient was referred as the equivalent coefficient of friction by Shreve (1968). The equivalent coefficient of friction was found to depend on the size of a landslide unlike the coefficient of friction which is a material constant. A log-log plot of the equivalent coefficient of friction as a function of the landslide volume is shown in Fig. 5 (Fritz (2002)). The plot includes subaerial dry-rock avalanches of non volcanic origin (Scheidegger (1973)), submarine landslides (Hampton *et al.* (1996)) and Martian landslides (McEven (1989)). All of the above cases indicate a decay in the equivalent friction of coefficient with increasing landslide volume. The correlation for subaerial landslides between the coefficient of friction f and the landslide volume V_s in m^3 is given as (Fritz (2002))

$$\log f = 0.15666 \log V_s + 0.62419 \tag{1}$$

with a correlation coefficient of 0.82. The relation in Eq. 1 also depends on the type of landslide material. For example, quick clays have friction coefficients at the lower end of friction coefficients observed for submarine landslides (Edgers and Karlsrud (1982)). The impact velocity of a landslide may be predicted using the equivalent coefficient of friction computed from Eq. 1 if the landslide volume is known a priori. The slide velocity v_s from the Newtonian laws of motion is

$$v_s = \sqrt{2g\Delta z\,(1 - f\cot\alpha)} \tag{2}$$

where g is the acceleration due to gravity, α is the hill slope and Δz is the drop height of the landslide. Landslide velocities up to 150 m/s have been observed in

recorded history (Körner (1976)). The submarine landslides reached volumes more than two orders of magnitude larger than the largest known subaerial landslides. Hence, submarine landslides can originate on surfaces with small slopes and can travel long distances due to lower equivalent of friction compared to subaerial landslides. The scatter of submarine landslide cases in Fig. 5 demonstrates the limitation of the simple linear slide dynamic model. The presence of drag force from the surrounding fluids on the front and on the top of the moving slide makes it an important feature for submarine landslides.

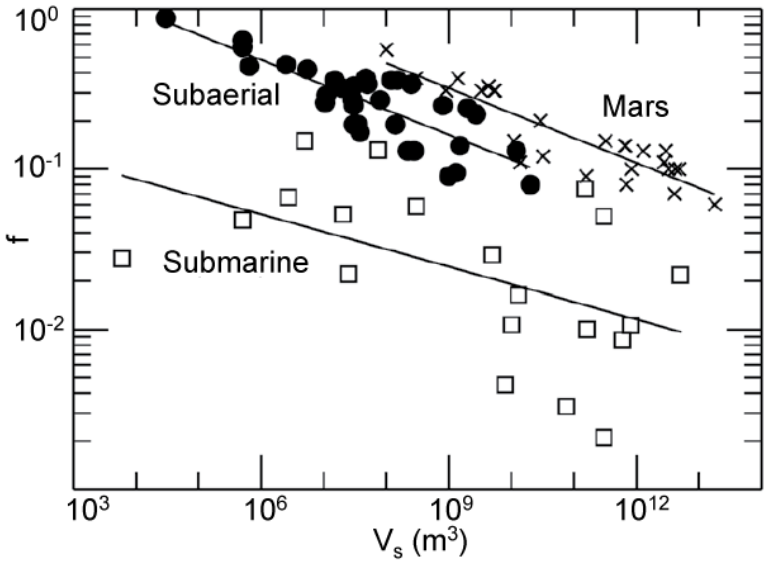

Figure 5: Equivalent coefficient of friction f vs landslide volume V_s for subaerial landslides (Scheidegger (1973)), submarine landslides (Hampton *et al.* (1996)) and Martian landslides (McEven (1989)), compiled by Fritz (2002).

In nature, landslides have been observed to behave in a near fluid-like manner and are found to deposit in a very long and thin layer. The front of the slide moves a surprisingly longer distance when compared with the tail of the slide and the runout distance usually depends on the slide volume (Scheidegger (1975) and Davies (1982)). Several hypotheses have been proposed to explain the fluidization process that causes such high mobility of granular landslides. Some of the hypotheses includes an upward flow of air (Kent (1966)), a hovercraft action (Shreve (1966), Shreve (1968), Hsü

(1975)),generation of high pressure steam (Habib (1975), Goguel (1978)), lubrication by molten rock (Erismann (1986)), mechanical fluidization (Davies (1982)), development of a thin rapidly shearing layer of vigorously fluctuating particles beneath a densely packed overburden or acoustic fluidization. (Kent (1966) and Melosh (1986)).

2.4.2 Granular landslide experiments

Experimental studies on granular avalanches range from the initial one-dimensional study of mass flow down rough, inclined surfaces to the unconfined three-dimensional mass flow over complex topographies. Selected 1D experimental setups are shown in Fig. 6.

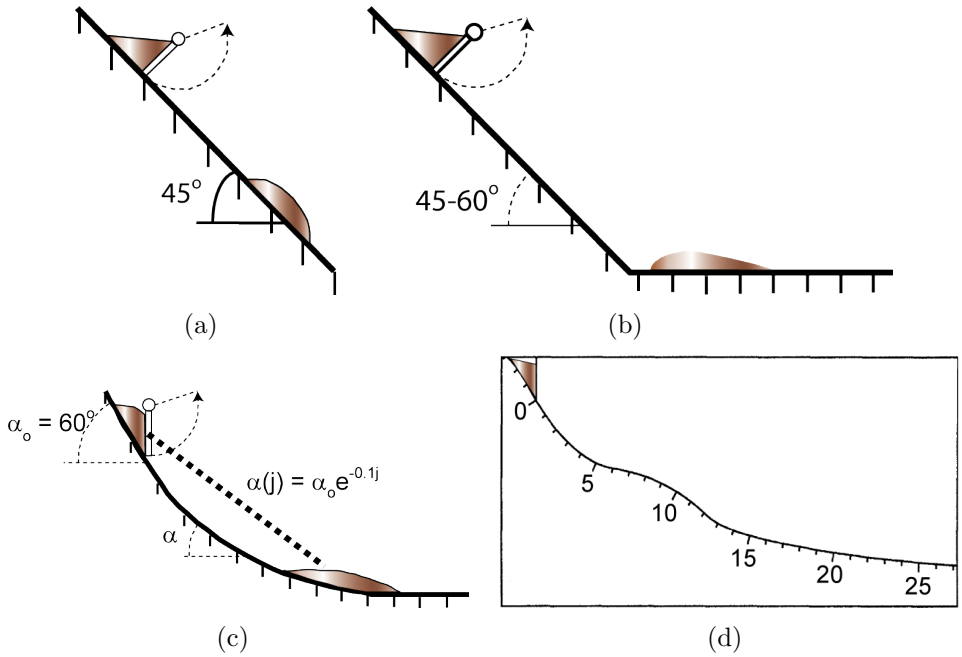

Figure 6: Experimental setup for one-dimensional granular mass flow: (a) Experimental setup by Huber (1980) (Hutter (1991)); (b) Experimental setup by Pluss (1987); (c) Experimental setup by Koch (1989) and (d) Experimental setup by Greve and Hutter (1993). (from Hutter (1991)

These studies were later extended to include lateral granular spreading and fully three-dimensional granular landslides as shown in Figs. 7(a) and 7(b). The experimental studies were also conducted to study confined flows in inclined rectangular channels with flat and complex topographies as shown in Fig. 7(c). Recently, more

complex scenarios involving granular mass flows in channels with twisting thalwegs have been physically modeled as shown in Fig. 7(d).

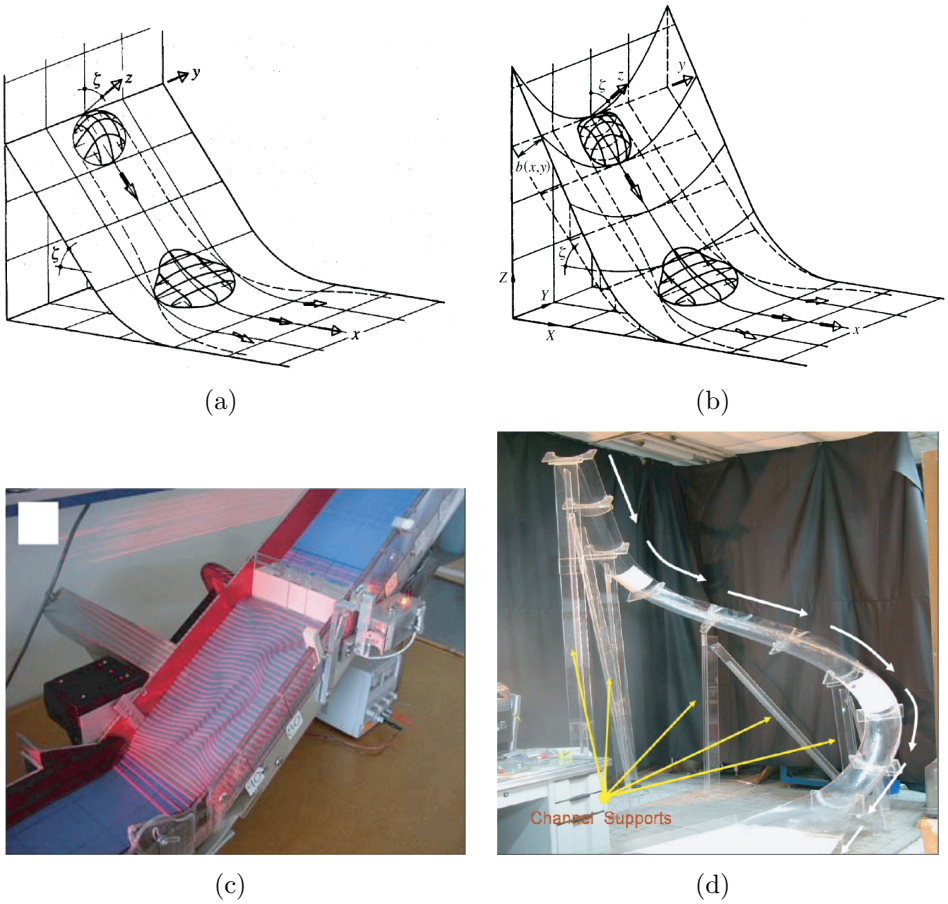

Figure 7: Granular flows on inclined surfaces: (a) Experimental setup by Koch *et al.* (1994), (b) by Gray *et al.* (1999), (c) Iverson *et al.* (2004) and Pudasani *et al.* (2008)

2.4.3 Granular landslide models

The flow of granular materials can be applied to study geophysical flows such as landslides, rock, ice and snow avalanches and pyroclastic flows (Hutter and Rajagopal (1994)). Kinetic theory and molecular dynamics models were developed to describe the rheology of granular materials (Jenkins and Savage (1983), Haff (1983), Lun *et al.* (1986), Jenkins and Richman (1985), Campbell and Brennen (1985), Campbell and Gong (1986),Walton and Braun (1986)). For example, in the Jenkins-Savage model (Jenkins and Savage (1983)) the granular material is assumed to be composed of

identical spheres of constant diameter which under collisions may transmit linear momentum but not angular momentum. The collision of the particles is assumed to be inelastic. Ahmadi and Shahinpoor (1983) extended the dilute gas model where the assumption is that as particles collide, a fraction of the particles after the collisions behave according to the Maxwell-Boltzmann distribution. This fraction is adjustable in the model. The model implicitly assumes that the interstitial space between the granular material is filled with gas and thus a drag due to flow of a fluid past a solid is introduced as a mechanism for the interaction of the interstitial gas with the granular particles. The model of Massoudi and Boyle (1991) adapts the Enskog dense gas theory, which allows for gradients in the volume fraction and predicts normal stress differences in simple shear flows of the granular materials. Oppenheim and McBride (1990) and Oppenheim (1991) used methods of statistical mechanics to model the granular dynamics. The model assumes that spherical particles are inelastic and have many degrees of freedom which are essentially at equilibrium close to zero Kelvin except for very short times. The model employs techniques of statistical mechanics to formulate the Hamiltonian for the system from which the equations of motion are obtained by using a projection operator technique (VanKampen and Oppenheim (1986)). However, the requirement that the particles are essentially in equilibrium close to zero degrees Kelvin is a very stringent assumption which might make the theory inapplicable to granular materials (Hutter and Rajagopal (1994)).

Other models describing granular landslides assume them as single mass points sliding along a prescribed geometry of a mountain side (Perl *et al.* (1980)) or hydraulic-type models (Voellmy (1955), Salm (1966)). In these models, the point masses are exposed to resistive forces that can be represented by the sum of two contributions, a dry Coulomb type and a turbulent friction type. These contributions involve a phenomenological parameter that can be adjusted according to the terrain and landslide considered. However, these assumptions limit the calculation of the temporal

evolution of the geometry of the moving landslide. Continuum models describe landslides as linear Newtonian fluids (Brugnot (1979), Dent and Lang (1980)) leading to Navier-Stokes equations and thus describe the slide motion.

The models based on kinetic theories and molecular dynamics were found to be difficult to solve in temporally developing gravity driven flows. A simpler hydraulic model for granular avalanche and landslide dynamics was developed by Savage and Hutter (1989) and Savage and Hutter (1991) analogous to fluid flow models. Field observations and experimental studies have shown that the granular landslides behave in a near fluid-like manner and are found to deposit in a very long and thin layer. This general behavior of granular avalanches coupled with certain simplified assumptions makes it possible to model granular mass flows similarly to fluid flows. The assumptions that make this model possible and true to the granular physics are incompressibility or density preserving, shallow avalanche piles and topography curvature, uniform velocity profile across the avalanche depth, Coulomb-type sliding on the bed and Mohr-Coulomb frictional behavior in the interior of the granular mass.

Field observations and experimental study have shown minimal density changes in granular avalanches and were observed to move as a thin, long and wide mass with small aspect ratios. It was also suggested by Melosh (1986) that the sliding occurs on a thin basal layer with high shear rates and where nearly all shearing takes place. Hence, the depth changes due to dilation are small and the mass flow behaves like a Boussinesq medium without any buoyancy forces. The thin basal layer also shows that the depth-averaged streamwise velocity is close to the actual velocity everywhere across the depth except in the basal layer. The rheology of the granular material is described by treating it as an incompressible Coulomb continuum. A basal friction law is imposed to allow for sliding on the incline bed. This is a dry Coulomb-like friction law that relates the shear traction to the normal pressure at the base and involves the friction angle between the gravel and the rough bed.

These assumptions lead to a dynamical fluid flow-like model which is derived from the conservation laws of mass and momentum. In general, the model consists of nonlinear partial differential equations for the landslide thickness and two depth averaged velocity components. The last two equations for the depth averaged velocities can either be expressed in terms of the streamwise and the transverse velocity components or in terms of the two topography parallel velocity components. In any case, these depth-averaged velocity components define the landslide propagation and deformation along the slide slope topography.

The model has been developed for flows in straight and curved chutes by Hutter and Nohguchi (1990), Hutter and Koch (1991), Greve and Hutter (1993), Hutter and Greve (1993), Hutter *et al.* (1993) and Hutter *et al.* (1995) and in rectangular channels by Iverson *et al.* (2004). In case of granular slide flows on plane and parabolic cross-sections and simply curved thalwegs by Voellmy (1955), Greve *et al.* (1994), Koch *et al.* (1994), Hutter (1996), Gray *et al.* (1999), Tai (2000), Tai *et al.* (2001), Tai *et al.* (2002), Koschdon and Schäfer (2003). The model has also been extended to flows in corries having arbitrarily curved and twisted thalwegs and arbitrary topographies by Pudasani and Hutter (2003), Pudasani *et al.* (2003a) and Pudasani *et al.* (2003b). The avalanche model of Savage and Hutter was extended by Iverson (1997) and Denlinger and Iverson (2001) to include the effects of pore fluid and model debris flow problems.

The early numerical solutions of the granular avalanche model were solved using a Lagrangian finite-difference schemes with central difference approximation and leap frog method in time by Savage and Hutter (1989), Savage and Hutter (1991), Hutter and Koch (1991), Greve and Hutter (1993), Hutter and Greve (1993), Greve *et al.* (1994), Koch *et al.* (1994), Hutter *et al.* (1995), Gray *et al.* (1999) and Wieland *et al.* (1999). The Lagrangian scheme required the addition of an explicit numerical diffusion when the gradients of the avalanche thickness and the velocities were large. These methods were also unable to capture the shocks and may have smoothed out

the shocks due to the nature of the finite difference based schemes. A two-dimensional Eulerian shock capturing scheme and a one-dimensional front tracking method was developed and employed by Tai (2000) and Tai *et al.* (2002). Wang *et al.* (2004) used a high resolution non-oscillatory (NOC) scheme and made a comparison for various cell reconstruction techniques. These techniques were four different second order total variation diminishing (TVD) limiters and a third order essentially non-oscillatory (ENO) cell reconstruction scheme. Of the numerical methods above, the NOC scheme with the minmod TVD limiter showed best performance for granular flows down curved chutes merging into a horizontal plane (Wang *et al.* (2004) and Hutter *et al.* (2005)). Apart from these numerical models, Denlinger and Iverson (2004), Iverson *et al.* (2004) and Pudasani *et al.* (2008) used shock capturing techniques to solve the extended model equations on a regular Cartesian grid. Pitman *et al.* (2003) computed flow along a two-dimensional surface using a parallel, adaptive grid, shock capturing method to solve the avalanche model. The model was solved on a cartesian grid which was developed from digital elevation topographic data using a parallel finite volume Godunov solver. A Lagrangian-Eulerian, finite-volume method with unstructured boundary fitted, moving, adaptive grid following the free boundary was developed by Koschdon and Schäfer (2003). While the flow solver in this case consists of a Godunov-type solver, Vollmöller (2004) used a wave propagation method on an unstructured finite volume grid.

The initial comparisons between numerical solutions of the Savage-Hutter granular avalanche model and experimental data were made by Savage and Hutter (1989). The experimental data were taken from the laboratory experiments of Huber (1980) on impulse wave generation by granular landslides. The measurements made relating to the granular mass motion released from rest were compared with the motion of the slide front, tail and maximum thickness from the numerical solution. The slide motion in both the cases is shown in Fig. 8. The gravel mass was found to spread quickly

and approaches a long and thin layer with depth of one or two particles within one second. Figure 8 inset shows the comparison of the dimensionless velocity of the slide front, middle and tail between the experiments of Huber (1980) and the numerical solution of Savage and Hutter (1989).

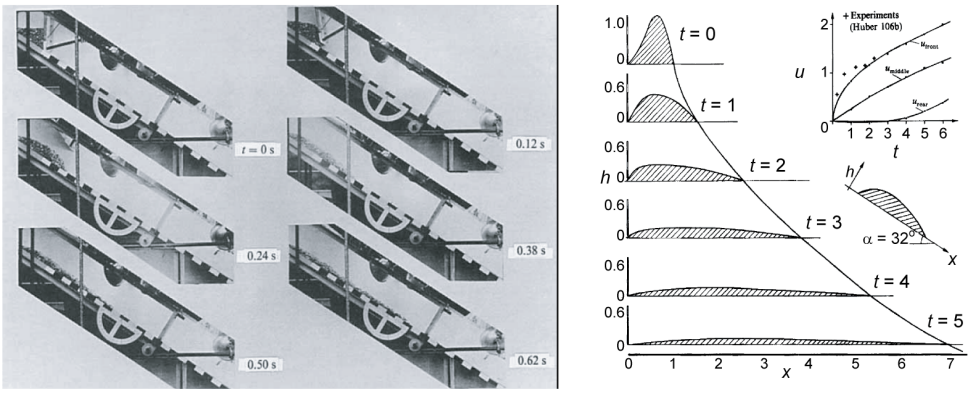

(a) (b)

Figure 8: Granular slide motion comparison between experiment and numerical model: (a) slide motion from rest on an inclined surface(Huber (1980)) and (b) numerical slide motion by Savage and Hutter (1989)

Comparative studies between physical models and numerical simulations of the Savage-Hutter avalanche model can be found in Hutter and Koch (1991), Savage and Hutter (1991), Greve and Hutter (1993), Koch *et al.* (1994), Hutter *et al.* (1995), Hutter (1996), Gray *et al.* (1999), Tai *et al.* (1999), Tai (2000), Tai *et al.* (2002), Wieland *et al.* (1999), Tai (2000), Denlinger and Iverson (2001), Iverson *et al.* (2004), McDougall and Hungr (2004) and Pudasani *et al.* (2008). The scenarios include one-dimensional flow on rough straight and curved inclines, fully three-dimensional unconfined lateral spreading flow along straight and curved inclines, confined flows in rectangular channels with straight surface and complex topographies, confined flows in twisted and curved channels and straight and deflected runout flows. The observations made from the experimental and numerical studies can be summarized as follows.

- The numerical models confirm well with the experimental model when the friction angle, δ is smaller than the internal friction angle ϕ.
- The model does not resolve small granular piles because of the extensively bouncing particles in the pile.
- The comparison fails in some cases due to numerical instability or coarse division of the granular mass into cells.
- The comparison fails in terms of the slide tail motion probably due to the simplicity of the Coulomb friction law, which in reality can be quite complex.
- Since the friction angle can change from a static to a dynamic state in real flows, a constant friction factor angle can under predict dilation. This can be resolved by having different friction angles for the slide tail and the rest of the slide body.
- Complex topographies can confine and channelize granular flows.
- In three-dimensional slide flows, strong Coulomb shear stresses develop normal to the basal surface. These stresses result in strong energy dissipation in case of obstructions. Thus the numerical models should include multi-dimensional momentum transport and Coulomb friction to account for these stresses and energy dissipation.

In the experiment, the rounded gravel constituting the landslide mass was released from rest which results in an instant collapse of the slide mass. This leads to a large spread of the granular mass and while the first grain is at the bottom of the incline, the last grain is still at the initial rest position. However, in nature most landslides usually originate as a sliding block which then transitions from block slide to a debris avalanche (Varnes (1978)).

2.5 Physical Modeling of landslide generated tsunamis

Landslide generated tsunamis are physically modeled to study the tsunami wave characteristics and identify the dependence of the generated wave on the landslide parameters. The experiments involve assumptions from scaling laws and dimensional analysis. Physical models with perfect similitude requires geometric, kinematic and dynamic similarity (Hughes (1993)). Geometric similarity requires the ratios of the length scales between model and prototype to be equal to one. Similarly, the kinematic similarity implies similar motion between the model and the prototype and the ratios for all the dynamical forces must be identical to satisfy dynamic similarity. In the case of tsunamis generated by landslides, the relevant forces are the inertial, gravitational, viscous, surface tension and elastic compression forces. Unless the model has the same scale as the prototype, no fluid may satisfy all of the force ratio requirements. Hence an important task before model experiments is to identify the important force ratio and to provide justification for neglecting the rest (Hudson *et al.* (1979)). In the case of free surface flows, the most relevant force ratio is the Froude number, which is the ratio of the inertial and gravity forces. If the flow is governed by Froude similitude, then the Reynolds criterion including viscous forces, the Weber criterion including surface tension forces and the Cauchy criterion as the ratio of inertial to elastic forces can be neglected. Most of the experiments are performed at constant water depths thereby neglecting bathymetry effects. The physical modeling of landslide generated tsunamis or impulse waves are broadly classified based on the method used to describe or simulate the landslides and the dimensionality of the model (2D or 3D). They are solid block type landslide models, piston type landslide models and granular slide type landslide models. While block and granular models are gravity driven, piston models are forced motion.

2.5.1 Block Slide Models

2.5.1.1 2D block models

Landslides may be modeled as a solid block impacting the water surface vertically when dropped or moving on an incline. The simplest and the earliest experiments to study impulse waves were performed by holding a solid block above the surface of water and letting it free fall into a water channel at one end. This classic plunger configuration was used by Russell (1837) and Russell (1844) to study the solitary wave as shown in Fig. 9(a). Since then focus has been on the far field rather than the wave generation. Russell found that the volume of displaced water is equal to the volume of water in the wave when the box is released above the water surface and that the wave moved with celerity

$$c = \sqrt{g(h+a)} \tag{3}$$

where h is the water depth and a is the thickness of the box. Monaghan and Kos (2000) extensively studied Russell's configuration to understand the wave generation process. The 2D experiments were performed in a 0.4 m wide wave tank. The visualization from the experiments showed that the jet from below the falling box forced the water in the tank to form a reverse plunging wave and the forward solitary wave. The vortex formation as observed by Monaghan is shown in Fig. 9(b). The vortex generation, shape and downstream propagation are similar to the PIV velocity vector fields from an infinitesimal segment of a vortex ring formed by an impulsively started jet. (Gharib *et al.* (1998) and Shusser and Gharib (2000)). The 2D experiment was extended to study impulse wave runup and return by Monaghan and Kos (1999) by including a mildly sloping beach on the other end of the wave tank. Using simple scaling arguments, Monaghan and Kos (2000) determined the leading wave crest amplitude a_{c1} to be

$$a_{c1} = 3h \left(\frac{m_s}{40\rho_w shb} \right)^{2/3} \left(\frac{s}{h} \right) \tag{4}$$

with the mass of the box m_s, water depth h, the drop height being equal to the water depth, water density ρ_w, box thickness s and box width b.

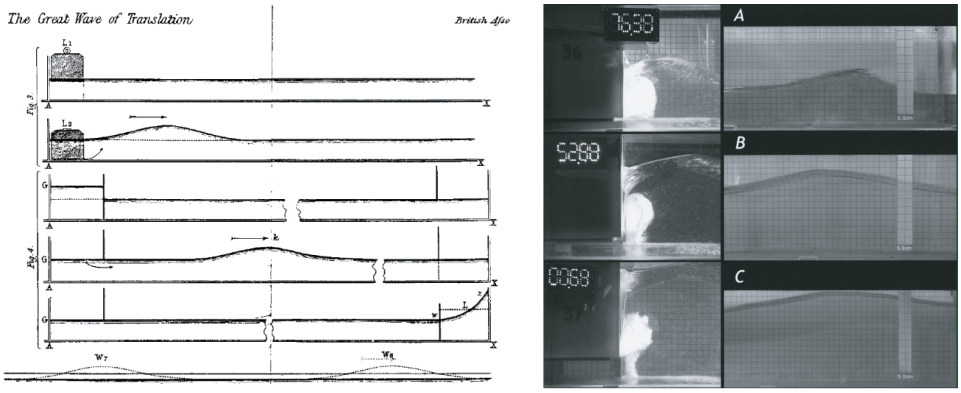

(a) (b)

Figure 9: (a) Russell's solitary wave generator (Russell (1844)) and (b) near field recordings by Monaghan and Kos (2000)

The studies undertaken by Noda (1970) and Wiegel (1955) established the wave profiles for initially, fully submerged rigid bodies falling vertically and sliding down ramps in tanks. The wave profiles are shown in Fig. 10(b). Wiegel (1955) found from the experiments that the generated wave amplitudes increased with increased density of the falling blocks. The generated waves were found to be dispersive in nature and the energy conversion rates between the underwater landslides and the waves were estimated to be $1\% - 2\%$. The rest of the underwater landslide energy was dissipated by friction and turbulence. Noda (1970) performed theoretical and experimental studies where the landslides are modeled as a vertical box-drop. Based on the experimental results the generated waves were classified based on the slide Froude number, $F = v_s/\sqrt{gh}$ and the relative slide box thickness. Four main wave types were noticed: oscillatory wave, nonlinear transition wave, solitary wave and bore. These wave classifications are also given in Wiegel *et al.* (1970). The wave type classification is shown in Fig. 10(a).

The experimental results were compared with the mathematical models of Kranzer and Keller (1959) and Kajiura (1963). The wave height decay for the oscillatory

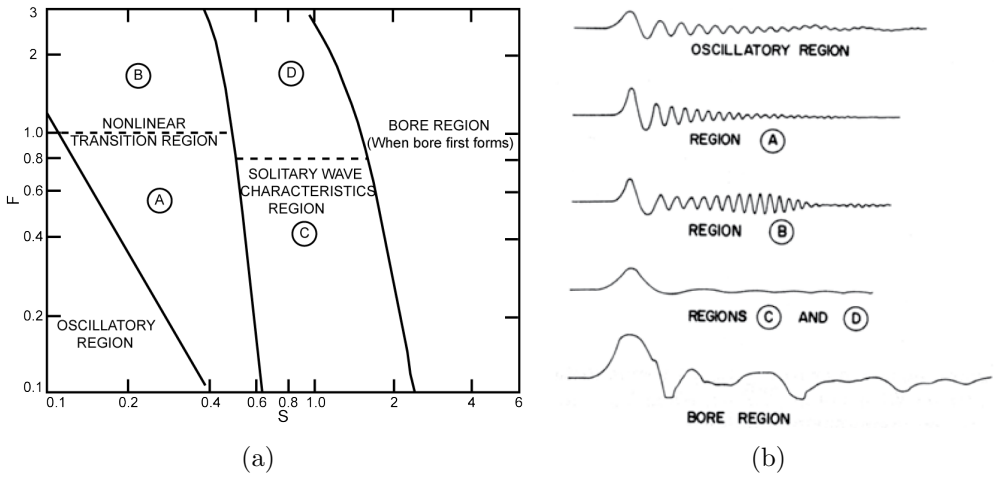

Figure 10: (a) Wave classification type based on slide Froude number F and relative slide thickness S; (b) observed wave types by Noda (1970).

waves followed $H(x)/h \propto x^{-1/5}$ as shown in Fig. 11 for different falling heights of the block, while the theoretical solution of Kranzer and Keller (1959) resulted in $H(x)/h \propto x^{-1/3}$. The Russell wave generator was also applied by Bukreev and Guseev (1996) in still water depths of 0.04 m to 0.08 m and by Panizzo *et al.* (2002) as a pre-study for 3D model tests. However, the small water depths may result in laboratory scale effects due to viscous wave damping.

Fritz (2002) conducted preliminary experiments with vertically falling solid blocks and a weighted wedge on an incline. The wedge was placed on rollers to reduce friction and allow motion on a hill slope with angle $\alpha = 10^o$. The wave generation process for a vertically falling solid block and the sliding wedge on an incline differ due to the difference in the slide motion and dynamics. When compared to a falling block, no water jet is driven from beneath the sliding wedge, which leads to an absence of the backward plunging vortex in front of the block.

Law and Brebner (1968) conducted experiments in a 0.61 m wide channel, where boxes of different lengths, heights and weights were slid down a 6.1 m roller with ball-bearings on a slope at an angle of 18^o - 25^o. The wave height attenuation with distance follows the relationship $H \propto x^{-0.5}$. A more useful parametric correlation study was

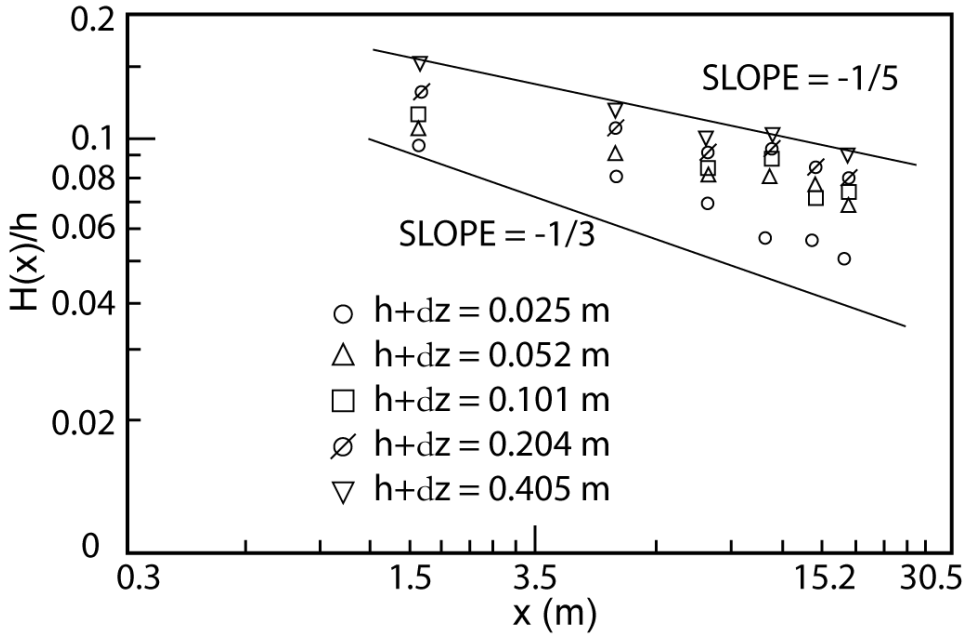

Figure 11: Comparison of wave height decay from experiments and theory of Kranzer and Keller (1959) (Wiegel *et al.* (1970))

undertaken by Kamphuis and Bowering (1970) according to Brebner in Slingerland and Voight (1979). Kamphuis and Bowering (1970) provided more details of the impulse wave generation by subaerial landslides by conducting experiments similar to Law and Brebner (1968). A weighted tray on a roller ramp was slid down a hill slope with inclination angle $\alpha = 20^o - 60^o$ into a flume 45 m long and 1 m wide in the study of Kamphuis and Bowering (1970). The two-dimensional wave generation was studied at still water depths of 0.23 m and 0.46 m. The hill slope angle α was varied from $20^o - 90^o$. The resulting wave heights decayed with increasing slope angles but the effect was minor between 20^o and 60^o. It was found that the far-field, stable wave height depended on the slide volume q per unit width and the slide Froude number F, where

$$\begin{aligned} q &= \frac{l_s}{h} \times \frac{s}{h} \\ F &= \frac{v_s}{\sqrt{gh}} \end{aligned} \tag{5}$$

and the far field wave height at $x = 37h$ was found to be

$$\frac{H(x = 37h)}{h} = F^{0.7}\,(0.31 + 0.20 \log q) \tag{6}$$

where s is the slide thickness and l_s is the slide length. This relation was found to be constant for thick slides with $s/h > 0.5$. For thin slides with $s/h < 0.5$, a decrease in the relative slide thickness resulted in smaller wave heights. The dependency of the relative wave height on the slide Froude number F and the relative slide thickness S is shown in Fig. 12. The wave height decreased exponentially with distance from the source according to

$$\frac{H}{h} = \frac{H(x = 37h)}{h} + 0.35e^{-0.08\frac{x}{h}} \tag{7}$$

The wave period was found to increase linearly with x/h and seemed independent of other variables. Though wave height and velocity appeared to reach a stable value, wave period and length did not. Kamphuis and Bowering (1970) related the speed of the highest wave in a wave train with the solitary wave celerity given by Eqn. 3. Energy conversion from landslide kinetic energy to water wave varied between $10\% - 50\%$.

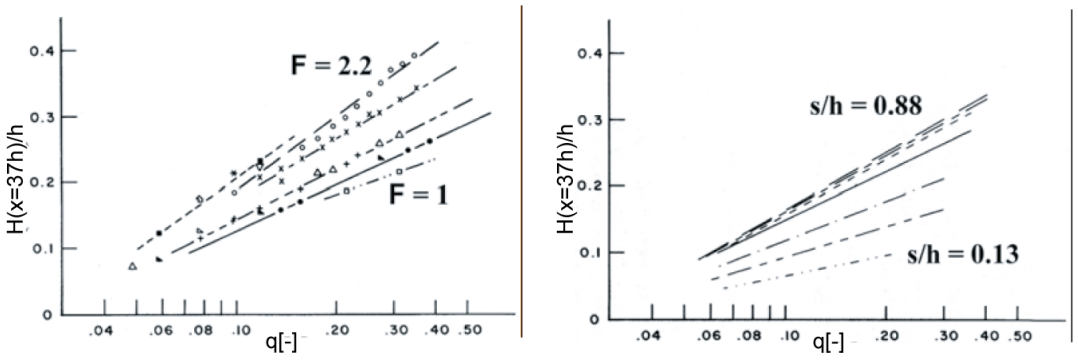

(a) (b)

Figure 12: Dependency of the relative wave height on the slide Froude number F and the relative slide thickness S, from Kamphuis and Bowering (1970)

Watts (1997), Watts (1998) and Watts (2000) conducted experiments where underwater landslides are modeled as a right triangle initially at rest on an incline with

slope 45^o with the horizontal in a wave tank 0.1 m wide, 9.14 m long and 0.66 m high. The characteristics of the generated wave directly correlated to the block geometry and motion. The vertical motion of the block draws down the water surface which then rebounds, while the horizontal motion of the front face of the block generates a leading crest that is followed by a large trough. This gives the wave maker physics for the triangular cross-section. The Hammack number, given by

$$Ha = t_{sd}\sqrt{gh}/(l_s \cos\alpha) \tag{8}$$

was identified as the non-dimensional wave maker time. The time scale of the wave generation process depends on the time of the slide water interaction t_{sd} and the horizontal projection of the slide length l_s. The Hammack number relates the time scale of wave generation to the duration of the linear long wave propagation out of the generation region (Hammack (1973)). Hammack (1973) used a bottom wave generator with vertical piston motion in a wave flume 31.6 m long, 0.61 m deep and 0.4 m wide to generate tsunamis by bed deformation and define the Hammack number. Watts (2000) used the Ursell number to classify water waves propagating in constant depth. Most underwater solid block experiments converted between $3\% - 7\%$ of the maximum block kinetic energy into a characteristic wave energy. The energy conversion increased with decreasing initial submergence.

Walder *et al.* (2003) studied impulsive waves generated in a smoothly curving flume by solid blocks. The focus was on the near field and the wave properties were recorded with a camera. The block density was $\rho_s = 2900$ kg/m^3 in water depths of $h = 0.051, 0.09, 0.13$ m and the slide impact angles varied from $11.2^o - 19.5^o$. A scaling analysis of the Euler equations resulted in the following governing dimensionless quantities: (1) vertical slide Froude number $F \sin\alpha$, (2) relative slide volume $V = V_s/bh^2$ and (3) relative time of underwater landslide motion $T_s = t_s(g/h)^{1/2}$, analogous to underwater landslide generated impulse waves (Watts (2000)). The

maximum amplitude was determined with a correlation coefficient $r^2 = 0.66$ as

$$\frac{a_{max}}{h} = 1.32\left(\frac{T_s}{V}\right)^{-0.68}, a_{max}/h < 0.85 \tag{9}$$

The influence of the vertical slide Froude number was found to be negligibly small and the time t_s was found to depend only on the relative slide length l_s/h and was shown to be $T_s = 4.8\,(l_s/h)^{0.4}$.

Ataie-Ashtiani and Najafi-Jilani (2008), Ataie-Ashtiani and Nik-Khah (2008) and Najafi-Jilani and ATaie-Ashtiani (2008) conducted two-dimensional experiments in a 2.5 m wide, 1.8 m deep and 25 m long wave tank where the width of the flume is larger than the width of the slide and the width of the sliding slope. The slide slope was inclined at angles ranging from $15^o - 60^o$. Solid steel blocks with different dimensions and shapes and granular materials were used to model the landslide. Energy conversion rates ranged from $5\% - 50\%$ depending on the landslide that was used to generate the waves with the rigid landslides having the maximum rate and the unconfined deformable slide having the least conversion rate. The wave generation depends on slide shape and kinematics given as

$$\frac{a_{cmax}}{h} = \left(0.405 + 0.078(VF^2)^{1.28}\right)\left(\frac{T_s}{V}\right)^{-0.278}\left(\frac{l_s}{t_s}^{-0.12}\right)\left(\frac{r}{h}\right)^{-0.48} \tag{10}$$

where V is the dimensionless slide volume (V_s/wh^2), F is slide Froude number $(v_s/\sqrt{gh})$, T_s is the dimensionless underwater travel time $(t_s\sqrt{g/h})$, l_s is the slide length, w is the slide width, r is the distance away from the source and h is the water depth. Hence the main parameters that were used to define the wave generation are the slide volume, the slide Froude number and the underwater slide travel time.

2.5.1.2 3D block models

In the 3D block models, the generated tsunami waves are functions of the relative radial distance r/h and the angular direction away from the landslide direction θ as shown in Fig. 3(b). In contrast, the 2D experiments result in the wave dependence

only on the relative stream wise distance. Johnson and Bermel (1949) conducted experiments where metal discs impacted the water surface of a reservoir in an axially symmetric water basin to study waves generated by nuclear explosions. The wave amplitude decay was found to be $a(r)/h = 2.5\,(h/r)$ and $a(r)/h = 3.63\,(h/r)$ for the two tests presented by Slingerland and Voight (1979). The amplitude decay was found to be proportional to r^{-1}.

Experimental studies on 3D impulse wave generation by solid blocks were carried out by Panizzo *et al.* (2005). The experiments were conducted in a 12 m long, 6 m wide and 0.8 m deep wave basin. Assuming symmetry, the solid blocks were released from one end of the wave basin. The landslides were modeled as symmetric solid blocks with zero porosity and a slide density $\rho_s = 2200$ kg/m^3 sliding on rectangular trolleys on a ramp. The still water depths were 0.4 m and 0.8 m and the hill slope angles were $\alpha = 16^o, 26^o, 36^o$. The setup is shown in Fig. 13(a). The generated waves were classified based on a wavelet analysis of the generated analysis shown in Panizzo *et al.* (2002). The wavelet analysis reported that the great part of the generated water waves demonstrated energy propagation according to the linear wave theory. Similar to Walder *et al.* (2003), the relative time of underwater landslide motion was found to be a key parameter for describing the generated impulsive waves.

$$T_s = 0.43 \left(\frac{b_s}{h}\right)^{-0.27} \mathrm{F}^{-0.66} \left(\sin\alpha\right)^{-1.32} \tag{11}$$

The maximum near field wave height as predicted by Panizzo *et al.* (2005) is given as

$$\frac{H_{max}}{h} = 0.07 \left(\frac{t_s^*}{A_w^*}\right)^{-0.45} \left(\sin\alpha\right)^{-0.88} e^{0.6\cos\theta} \left(\frac{r}{h}\right)^{-0.44} \tag{12}$$

with H_{max} the maximum wave height, water depth h, the non-dimensional slide duration time $T_s = t_s\sqrt{\frac{g}{h}}$, the non-dimensional slide front surface $A_w^* = wh/d^2$, slope inclination angle α, angular direction away from the slide propagation direction θ and the r is the distance away from the slide impact position at the water surface. The

non-dimensional maximum wave height was found to increase with increasing landslide front surface and impact velocity and decreases with increasing non-dimensional distance away from the source. Further predictive equations for the maximum time period and the surface elevation of the generated wave are given in Panizzo *et al.* (2005).

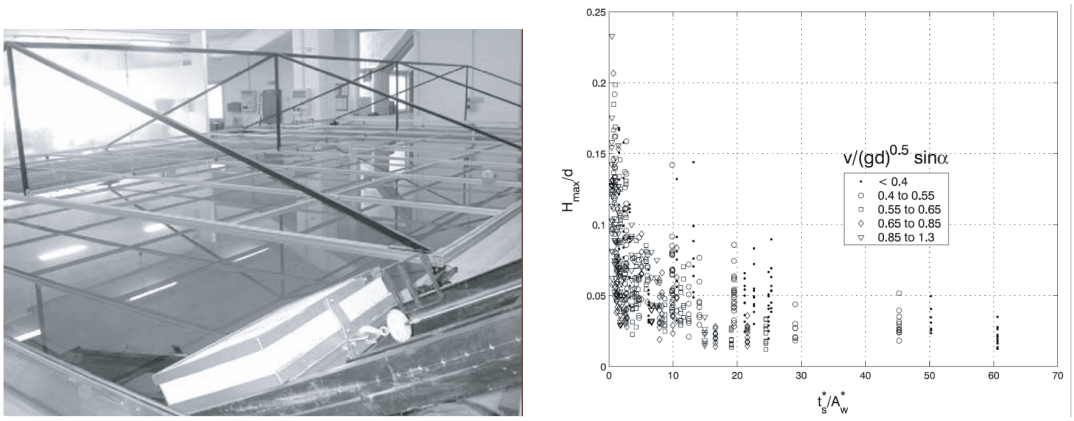

(a) (b)

Figure 13: (a) 3D Experimental setup by Panizzo *et al.* (2005); (b) measured wave height as a function of relative time of slide motion and slide front surface area (Panizzo *et al.* (2005).

Panizzo *et al.* (2005) compared the data from his 3D experiments with the 2D data from Fritz *et al.* (2004) and the 3D data from Huber and Hager (1997) as shown in Fig. 14. Since the time of the underwater landslide motion was not measured in the studies of Huber and Hager (1997), Panizzo *et al.* (2005) estimated t_s based on the empirical relationship obtained in his experiments. The 2D experiments overestimated the relative amplitude by a factor of 5 to 10 as compared with their own data. This may be due to the difference in parameter definitions describing the wave generation mechanism between solid block slide and deformable granular slides. In case of granular slides, the bulk of the wave generation occurs during the initial stages of the impact and the primary wave is usually fully developed before the granular slide comes to rest (Fritz (2002), Heller (2008)). Hence the time of granular slide motion does not correspond directly to the time when the solid block comes to rest. Also,

the time of slide motion t_{sd} for a granular slide is not an independent parameter and inherently depends on the slide velocity, slide shape and the slope of the incline. In the experiments by Panizzo *et al.* (2005), the solid block is suddenly decelerated at the bottom of the incline by a system of a spring which results in the removal of the block kinetic energy from the system. Hence this results in a difference in the energy conversion rates between the slide and water body. This can be remedied by means of sliding the block on guide rails or on an incline which gently transforms into the horizontal basin bottom and reaching the rest position under the effect of gravity and surrounding fluid. While the 3D formula of Huber and Hager (1997) overestimated the relative maximum wave height by a factor of 2 to 3 as compared with the data of Panizzo *et al.* (2005). The discrepancies in the wave height can also be due to the fact that t_{sd} for the granular experiments of Fritz (2002) and Huber and Hager (1997) were computed with the results obtained from the solid block experiments of Panizzo *et al.* (2005).

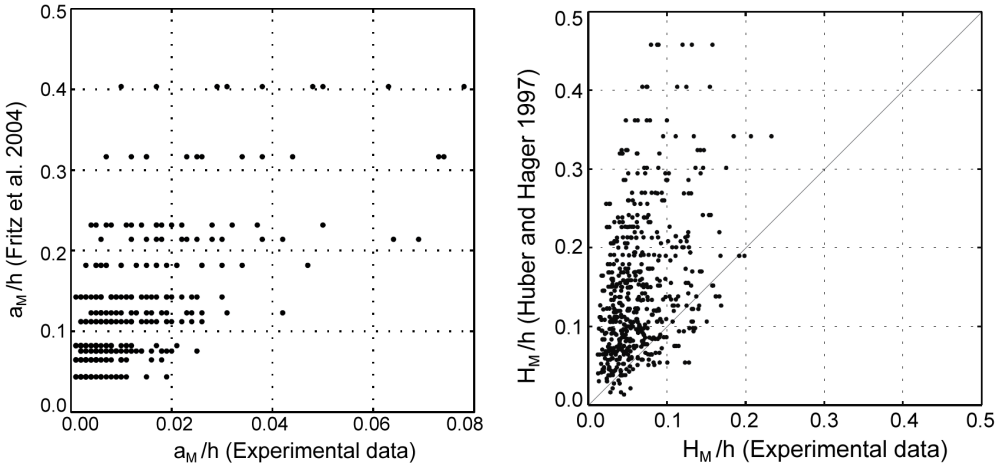

Figure 14: (a) Comparison of relative maximum wave amplitude a_M/h of the experimental data versus Eq. 18 from Fritz *et al.* (2004) and (b) comparison of relative maximum wave height H_M/h of experimental data of Panizzo *et al.* (2005) with Eq. 16 (Panizzo *et al.* (2005)).

The solid block was replaced by a smooth streamlined rigid body with an approximated Gaussian cross section (Enet and Grilli (2005), Enet and Grilli (2007) and Grilli and Watts (2005)) and semi-elliptic rigid bodies (Risio *et al.* (2009a)) that was released on a slope to impact the water body and generate the tsunami waves. Enet and Grilli (2007) and Grilli and Watts (2005) choose the particular geometry for the slope and the landslide model to perform comparisons with the numerical simulations from the fully non-linear potential flow model of Grilli *et al.* (2002). Enet and Grilli (2007) performed experiments in a 3.7 m wide 1.8 m deep and 30 m long wave tank on a slope of 15^o to study 3D impulse waves generated by submarine landslides. The analysis of the video recordings of the shoreline during the impact showed that the subaerial landslide generated waves with higher lateral runups when compared with submarine landslide cases. Risio *et al.* (2009a) conducted experiments in a wave tank 10.80m $\times$ 5.50m $\times$ 0.80m with hill slope angle of 18.43^o. The near field analysis in this case demonstrated that partially submerged landslides resulted in a V-shaped shoreline while subaerial landslides resulted in a deep U-shaped shoreline as a result of a stronger water body displacement.

2.5.2 Piston Slide Models

In some cases, the landslide motion may be approximated by a vertical wall moving horizontally in the water body. This applies in particular to cases where the landslide thickness is comparable to or exceeds the water depth and the distance of landslide motion remains short relative to the thickness. Example of such an event is the Vajont dam case (Müller (1964)). The landslide was modeled as a piston type wave maker by Miller (1970) in an experimental study on coastal landslides and as a vertical piston type wave maker by Hammack (1973) to study tsunami generation. The main disadvantage here is the assumption of the forced piston motion and the fixed boundary condition at the piston surface. The piston type of wave maker has

been used to study plane wave maker theory and relation between relative depth and wave height to stroke ratio by Synolakis (1991), Madsen (1971), Hughes (1993) and Dean and Dalrymple (1991). While Galvin (1964) reasoned that the water displaced by the piston should be equal to the volume of the crest of the propagating wave, the study of Ursell *et al.* (1960) is only applicable when the plate motions remain small.

Noda (1970) obtained a theoretical solution for the problem of a wall moving horizontally into a body of water. The problem was linearized by assuming that the wall displacement was much smaller than the water depth. It was found that the maximum water surface elevation occurred at $x/h \approx 2$ and not at $x = 0$ and was predicted by

$$\frac{a}{h} = 1.32\frac{v_s}{\sqrt{gh}} \tag{13}$$

for a displacement at constant horizontal velocity v_s. The linear solutions compared to the nonlinear experimental data of Miller and White (1966) in Fig. 15. The linear solution gives conservative assumptions. Experiments by Das and Wiegel (1972) showed that the regions of wave characteristics described by Noda (1970) for the box drop problem approximately describe the general characteristics of the waves generated by a horizontally translating wall in a water flume.

Noda (1971) used Fourier analysis of the transient wave systems for approximations of the wave systems downstream of the probe. But the transient wave systems did not behave as if it were a series of steady sinusoidal waves and the discrepancies became larger with distance from the probe and increasing wave frequency. The method of characteristics was used to compute numerical solutions for water waves generated by close landslides modeled with a vertical wall moving horizontally into a reservoir by Gozali and Hunt (1989). The nonlinear, non dispersive long waves approximation was applied.

Sander (1990) investigated unidirectional shallow water waves generated by a moving boundary. This can be produced by a partially submerged landslide penetrating

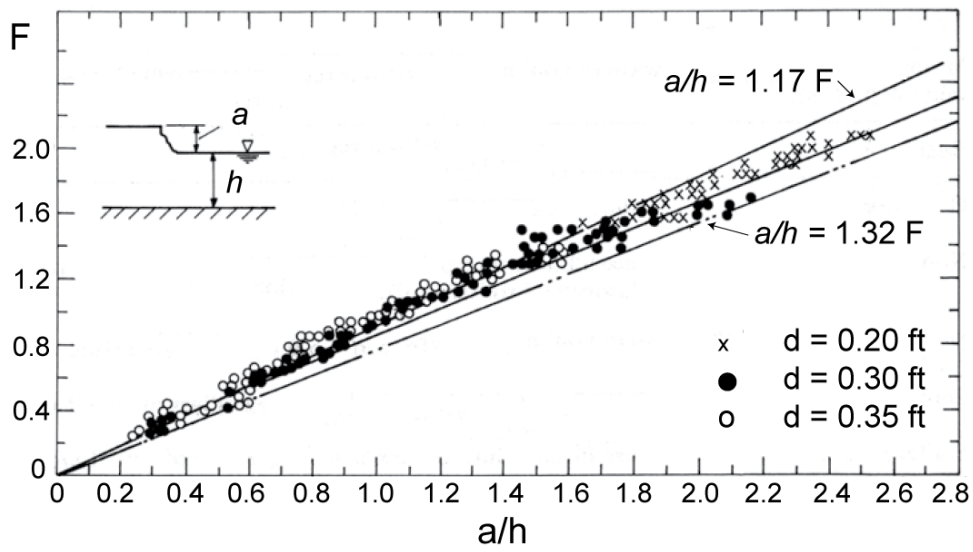

Figure 15: Comparison of the theoretical solution of Noda (1970) with the experimental data of Miller and White (1966) for a vertical wall penetrated by a forced piston motion horizontally into a water body.

slowly, relative to wave propagation velocity, into a water body.

A classical piston type of wave maker with forced motion as shown in Fig. 16(a) was used to produce waves within the range: Froude number $F = v_s/\sqrt{gh}$ from 0.01 to 0.4, amplitude to water depth ratios from $a/h = 0.01$ to 0.4 and water depth from $h = 0.05$ to 0.15m. Most of the generated waves were weakly nonlinear. The type of the boundary motion might be similar to the Vajont landslide (Müller (1964)) but relatively slower. At Vajont, rough Froude number estimates ranged from $F = 0.6$ to 1. The experiments showed that for a wedge type piston wave generator both wave height and length are related to piston or slide Froude number. Small Froude numbers produced smaller wave crests but deeper troughs whereas higher Froude numbers resulted in larger wave crests and smaller troughs. A numerical solution of Boussinesq type equations presented by Wu (1981) and Villeneuve and Savage (1993) sufficiently reproduced the weakly nonlinear shallow water waves recorded in the VAW-laboratory.

Saelevik *et al.* (2009) modeled the landslide as a series of boxes fixed from the

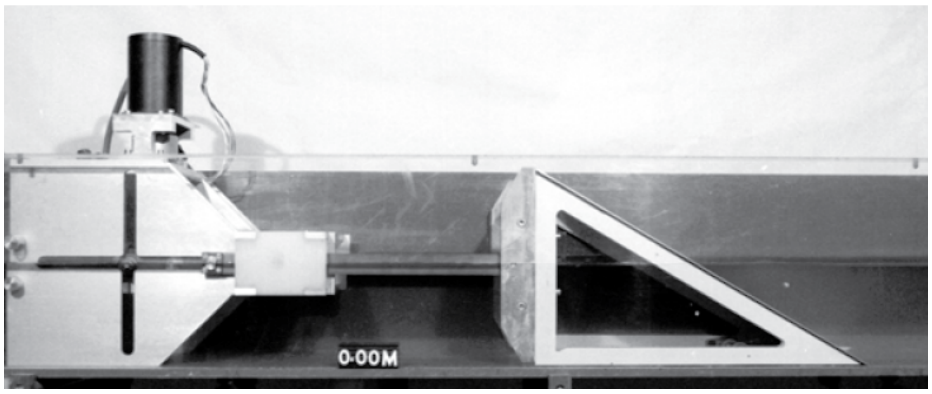

(a)

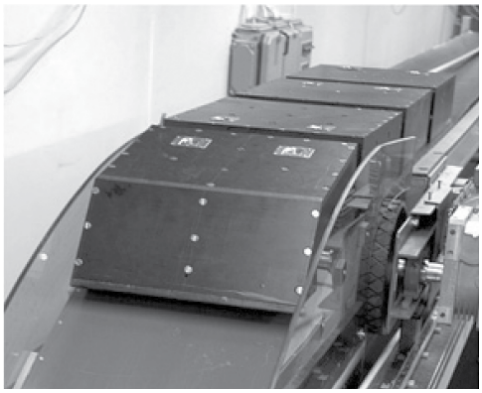

(b)

Figure 16: (a) Piston type wave generator with a wedge cross-section by Sander (1990) and (b) Saelevik *et al.* (2009).

back to a driving conveyor belt in a wave flume 25 m long, 0.51 m wide and 1 m deep. The slide model is showed in Fig. 16(b). The connection at the back of the train of landslide boxes allowed o control the landslide from initiation to deposit without the conveyor belt remaining outside of the water. The effect of slide length and volume on the wave generation process were studied. Saelevik *et al.* (2009) inferred from the experimental results that the leading wave generation was strongly influenced by the slide volume, while the slide length played an important role in the generation of trailing waves. The PIV measurements of the velocity in the water column demonstrated the applicability of higher order Boussinesq equations to describe the generated waves in the far field.

2.5.3 Granular Slide Models

2.5.3.1 2D models

Slingerland and Voight (1982) presented an empirical regression for the prediction of the relative wave amplitude of the first wave from the dimensionless kinetic energy. The experimental data was obtained from two 3-dimensional, site-specific physical model studies conducted at scales of 1:120 and 1:300 by Davidson and Whalin (1974), Davidson and McCartney (1975) and Ball (1970).The slides were either tabular or triangular in shape. The slide material consisted of gravel, iron or lead bags. The bags were moderately porous in nature with minimal deformation and perform closely like solid blocks with some porosity. The maximum first wave crest amplitude measured in the direction of the slide axis at a distance of $x/h = 4$ was given as

$$\log \frac{a}{h} = -1.25 + 0.71 \log E_{sk} \tag{14}$$

with the dimensionless slide kinetic energy E_{sk} and still water depth h. The dimensionless slide kinetic energy was defined as

$$E_{sk} = \frac{1}{2} \frac{\rho_s}{\rho_w} \frac{V_s}{h^3} \frac{v_s^2}{gh} \tag{15}$$

with slide and water density ρ_s and ρ_w, slide impact velocity v_s and gravity g. The characteristic radial wave pattern is shown in Fig. 20(a). The data was obtained for 20 experiments from 3 different slides at three different water levels. The slide thickness s to water depth h ratio ranged from $0.37 < s/h < 0.8$, the slide volume V_s ranged from $0.7 - 39 \times 10^6$ m^3 in prototype scale and the slide Froude number $\mathrm{F} = v_s/\sqrt{gh}$ roughly from 0.5 to 5.

Huber (1980) conducted comprehensive experimental studies on impulse waves generated by granular landslides. The study consisted of over 1000 2D and 3D experiments. In the 2D experiments, the granular slide mass consisted of rounded river gravel with a continuous grain diameter distribution from 8 mm to 30 mm with mean

diameter of 20 mm and grain density of $\rho_g = 2,700$ kg/m^3. The slide material was placed in a triangular shape behind a vertical flap gate on an inclined ramp. The granulate was released from rest by lifting the flap. By varying the initial position of the slide, different impact velocities for the slide were obtained. The following parameters were varied to study the relation between the generated wave characteristics and the slide parameters. The slide mass was varied from 5 to 50 kg, impact slide front velocity 1 m/s to 4 m/s, water depth 0.12 m to 0.36 m and slope angle α from 28^o to 60^o. The slide Froude number was in the range $0.5 < F < 3.7$ and the relative slide volume was $0.03 <= V_s/(bh^2) <= 2.57$. A summary of the experimental results of Huber (1980) can be found in Huber and Hager (1997) and Vischer and Hager (1998). Huber (1980) observed sinusoidal, cnoidal and solitary waves including intermediate type of waves. In the experiments, energy conversion of $1\% - 40\%$ was observed. The wave height for the two dimensional impulse wave prediction was given by

$$H = 0.88 \sin\alpha \left(\frac{\rho_s}{\rho_w}\right)^{1/4} \left(\frac{V_s}{b}\right)^{1/2} \left(\frac{x}{h}\right)^{-1/4} \tag{16}$$

with slope angle α, slide density ρ_s, water density ρ_w, slide volume V_s, slide width b, still water depth h and location x. The assumption that the velocity does not play a role in determining the characteristics of the generated wave is non-physical due to the nature of the landslide motion and impact with the water surface in the experiments of Huber (1980). Since the granular mass was released from rest, the landslide collapses immediately and begins to slide down the incline. This results in the development of an extremely long and thin slide shape with the slide front moving extremely large distance when compared with the tail of the slide as shown in Fig. 8(a). To vary the slide velocity, it needs to be released at higher initial positions thus resulting in thick slow slides and thin fast slides. Hence the slide velocity and thickness are dependent parameters and not independent as obtained from dimensional analysis. In this context, a pile of gravel released from rest is not a realistic model of landslides as the landslide initially slides as a solid block along

a low friction bed layer, then disintegrates into a debris slide and later into a debris avalanche. To model this phenomenon, Fritz and Moser (2003) designed a pneumatic machine which launches the granular mass as a solid block first and then the debris avalanche follows.

Fritz (2002) conducted a wide range of 2D experiments on impulse waves generated by granular landslides. The results of these experiments are summarized in Fritz *et al.* (2001),Fritz (2002), Fritz *et al.* (2003a), Fritz *et al.* (2003b), Fritz *et al.* (2004) and Fritz *et al.* (2009). The 2D experiments were conducted in a rectangular prismatic water channel which was 11 m long, 0.5 m wide and 1 m deep. The landslide dynamics was controlled by means of a novel pneumatic landslide generator (Fritz and Moser (2003)). The landslide generator allowed to independently vary the slide parameters that govern the wave generation. A scaling analysis led to the identification of 7 parameters that are relevant to the impulse wave generation: (i) still water depth h, (ii) slide thickness s, (iii) grain diameter d_g, (iv) slide impact velocity v_s, (v) bulk slide volume V_s, (vi) bulk slide density ρ_s and (vii) hill slope angle α. A total of 137 experimental runs were conducted while varying the experimental trial conditions. The still water depth h ranged from 0.3 m to 0.675 m, the hill slope angle α varied from $30^o - 90^o$, the slide mass m_s ranged from 27 kg - 108 kg, the relative slide thickness and relative slide volume ranged from 0.07-0.6 and 0.07-1.6 respectively. The slide impact velocity varied from 2.7 m/s to 8.2 m/s and the slide Froude number F varied from 1-4.8. The landslide material consisted of artificial granular materials (PP-Ba$S0_4$) with the grain density of $\rho_g = 2.64$ t/m^3 and bulk density $\rho_s = 1.62$ t/m^3. The generated waves belonged to either of the four classes of gravity waves: weakly nonlinear oscillatory waves, nonlinear transition waves, solitary-like waves and dissipative transient bores.

The near field measurements of the wave generation process using a PIV setup (Fritz *et al.* (2003b)) yielded valuable information on the wave kinematics in the

impact zone. These were the first near field measurements of the water column in the wave generation region by a granular landslide. The PIV measurements yielded velocity vector field in the channel which will aid the calibration and validation of numerical models (Madsen and Gittings (2002), Quecedo *et al.* (2004), Weiss and Wuennemann (2007)). Based on the slide Froude number, four flow regimes in the impact zone were identified namely no flow separation, local flow separation, backward collapsing impact craters and outward collapsing impact craters. The schematics for these flows are shown in Fig. 17.

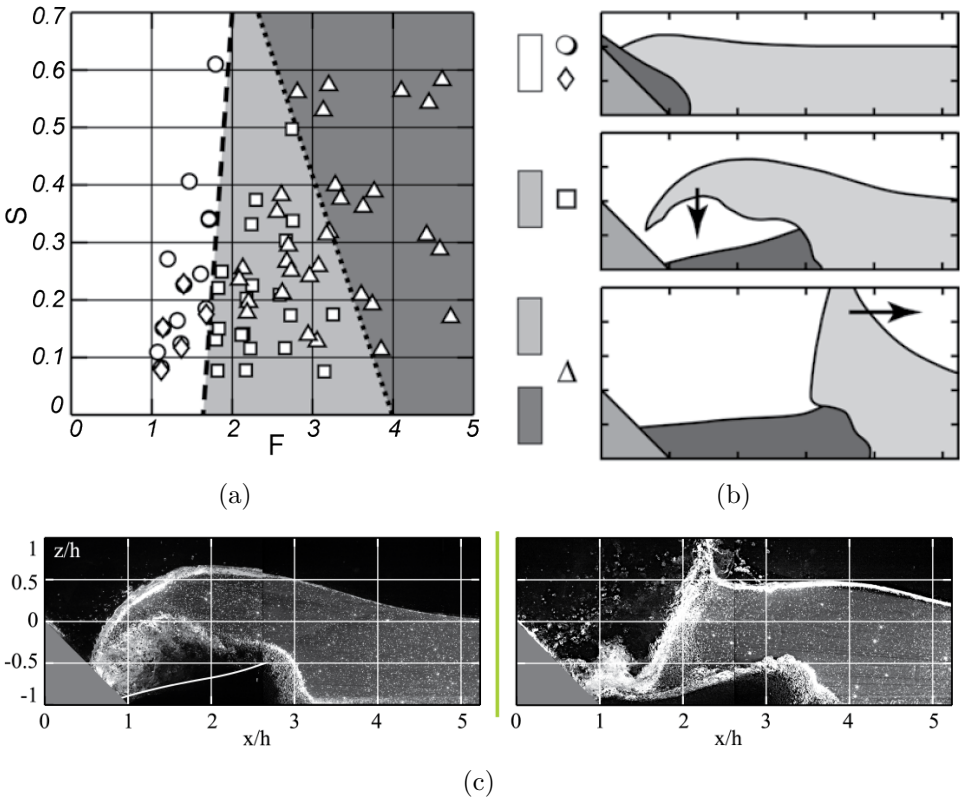

Figure 17: Flow separation and crater type formation from Fritz *et al.* (2003b): (a) in terms of slide Froude number F and relative slide thickness S, (b) crater type formation, (c) example of cavity formation.

It was observed that at high impacts, flow separation occurs leading to formation of impact craters, which can lead to large water displacement volumes when compared to the slide volumes. Flow separation was found for the cases when the slide Froude

number satisfies the relationship

$$F > \left(\frac{5}{3} + \frac{1}{2}S\right) \tag{17}$$

with S being the dimensionless slide thickness. The maximum wave crest amplitude of the generated impulse waves is given by

$$\frac{a_c}{h} = 0.25 \left(\frac{v_s}{\sqrt{gh}}\right)^{1.4} \left(\frac{s}{h}\right)^{0.8} \tag{18}$$

with v_s slide impact velocity, s slide thickness and still water depth h. It was found that between $2\% - 30\%$ of the slide kinetic energy was converted into the first wave energy and the efficiency of wave generation was found to decrease with increasing dimensionless slide volume. The parametric relation for the maximum amplitude given by Eq. 18 was applied to the Lituya Bay case (Fritz *et al.* (2004), Fritz *et al.* (2009)) and the maximum amplitude was compared with the model results of Fritz *et al.* (2001) and Eqn. 16 from Huber and Hager (1997), Eqn. 7 from Kamphuis and Bowering (1970), block and piston type models of Noda (1970), Eqn. 14 of Slingerland and Voight (1982) and numerical models of Madsen and Gittings (2002), Quecedo *et al.* (2004) and Weiss and Wuennemann (2007). The results of these models in comparison with their own results varied in the range of $-50\% - +100\%$ while the piston model of Noda (1970) overestimated the maximum amplitude of Eqn. 18 by 230%.

The physical model of Fritz (2002) was extended by Zweifel (2004) to investigate the effects of the bulk slide density ρ_s with granular slide densities ranging from $\rho_g = 955$ kg/m^3 to 2,640 kg/m^3. The correlation for the maximum wave amplitude was given in Zweifel and Hager (2006).

$$\frac{a_M}{h} = \frac{1}{3} F S^{1/2} M^{1/4} \tag{19}$$

where F is the slide Froude number, S is the relative slide thickness and $M = m_s/(\rho_w b h^2)$ is the dimensionless slide mass. The wave amplitude was found to decay

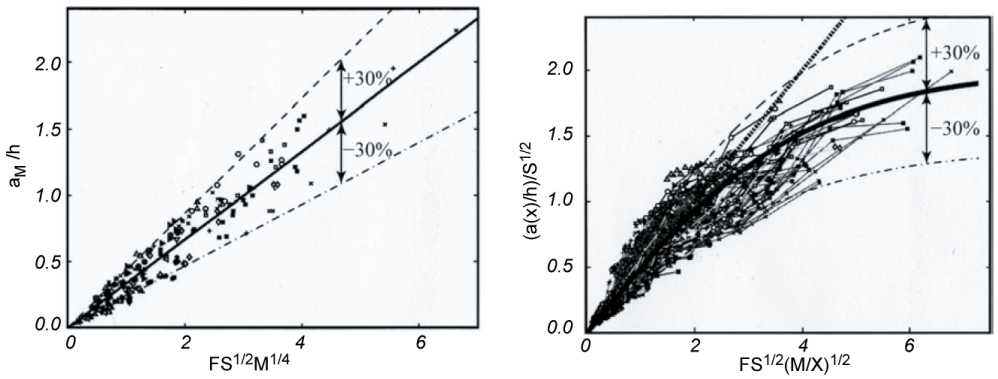

Figure 18: (a) Maximum relative amplitude versus $FS^{1/2}M^{1/4}$ with (-) Eq. 18 and (b) amplitude decay versus $F^{3/2}(M/X)^{1/2}$ with Eq. 20 (Zweifel (2004)).

with distance as

$$\frac{a(x)}{h} = 2S^{1/2} \tanh 0.25F^{3/2} \left(M/X\right)^{1/2} \tag{20}$$

Analogous to Fritz (2002), Zweifel and Hager (2006) observed oscillatory, cnoidal, solitary and bore waves as a function of the slide Froude number, relative slide thickness and the relative slide volume. The box experiments of Zweifel (2004) in the same channel resulted in over prediction of maximum wave amplitudes when compared with the slide tests for the same conditions at small Froude numbers. However, the results became similar for $F > 3.0$. The comparison between the maximum amplitude for the box and the slide follows

$$\frac{a_{Mbox}/h - a_M/h}{a_{Mbox}/h} = 1 - 0.26F, \quad \text{for} 0.5 <= F <= 2.8 \tag{21}$$

with a correlation coefficient of $r^2 = 0.97$.

Heller (2008) extended the experimental work of Fritz (2002) and Zweifel (2004) to analyze scale effects and the effect of slide mass and granulate characteristics on the generated tsunami waves. The maximum wave amplitude was obtained as

$$\frac{a_m}{h} = \frac{4}{9}P^{4/5} \tag{22}$$

$$P = FS^{1/2}M^{1/4} \left(\cos\beta\right)^{1/2} \tag{23}$$

The angle $\beta = (6/7)\alpha$ accounts for the effect of the hill slope angle on the wave amplitude up to $\alpha = 90^o$. The wave height decay was obtained as

$$A(X) = \frac{3}{5}\left(PX^{-1/3}\right)^{4/5} \tag{24}$$

Rzadkiewicz and an P. Heinrich (1997) conducted experimental studies on granular submarine landslides by allowing a mass of sand to slide freely down a frictionless inclined plane with a slope of 30^o or 45^o in a channel 4 m long, 0.3 m wide and 2 m high. Three different sand types with grain diameters between 50-250 μm, 0.8-2 mm and 2-7 mm were used to model the submarine landslide. The experimental result for the case of coarse sand sliding down the slope is shown in Fig. 19.

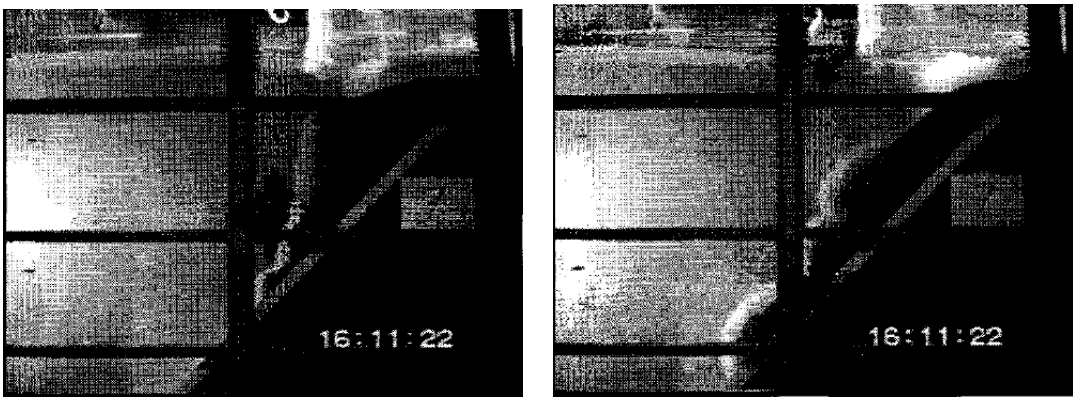

(a) t = 0.4 s (b) t = 0.8 s

Figure 19: Experimental results for coarse sand sliding down 45^o incline at $t = 0.4$ s and $t = 0.8$ s (Rzadkiewicz and an P. Heinrich (1997)).

2.5.3.2 3D deformable landslide models

The early 3D studies with granular slide material were site specific cases studies such as the study of Davidson and Whalin (1974) or WCHL (1970). The wave height or amplitude estimation were given by Huber and Hager (1997) based on the experimental data of Huber (1980) and by Slingerland and Voight (1979) based on the experimental data of Davidson and Whalin (1974) and WCHL (1970). Davidson and Whalin (1974) conducted model studies of Lake Koocanusa in Montana at 1:120 scale

where the slide was modeled with bags of iron and lead at different locations around the lake. The bags were moderately porous in nature and behave close to solid blocks with some porosity. The generated waves were measured by a set of 16 wave gages. WCHL (1970) modeled the Mica Reservoir in British Columbia at a scale of 1:300. The slide was modeled with bags of gravel. The model study is shown in Fig. 20(a).

Huber (1980) conducted roughly 150 3D experiments in a wave basin. It was observed that the landslide induced impulse waves in a water body propagate radially over the water surface. The radial spread was characterized by a strong dependency of wave height on the propagation direction θ and the radial travel distance r. The wave height was maximum in the direction of the slide and the wave was found to decay rapidly in the lateral direction. The strong radial component is shown in Fig. 20(b). The relative wave height in a 3D water body was predicted as

$$\frac{H}{h} = 2 \times 0.88 \sin\alpha \cos^2 \frac{2\gamma}{3} \left(\frac{\rho_s}{\rho_w}\right)^{1/4} \left(\frac{V_s}{bh^2}\right)^{1/2} \left(\frac{r}{h}\right)^{-2/3} \tag{25}$$

The decay in the wave height with the relative propagation direction increased for 3D wave propagation as compared with 2D wave propagation as shown in Fig. 20(b). In the radial direction as well, the 3D wave height damping ($a(r) \propto r^{-1/4}$) was found to be faster than in 2D case ($a(x) \propto x^{-1/4}$).

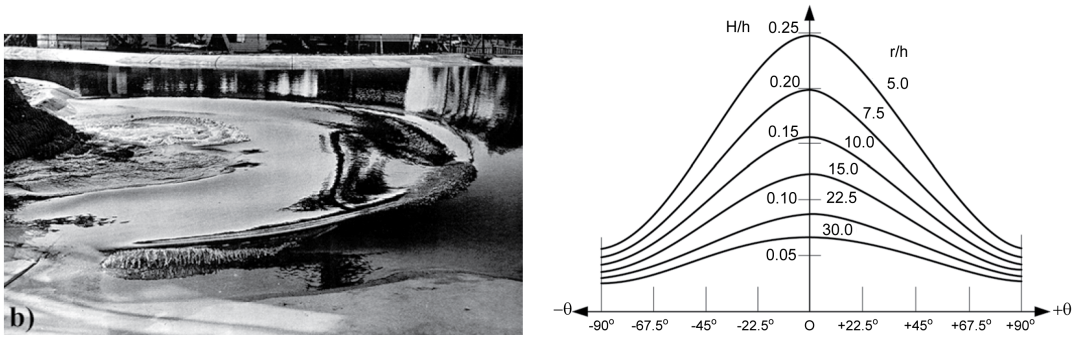

(a) (b)

Figure 20: 3D granular slide model experiments: (a) case study of the Mica Reservoir (WCHL (1970)) and (b) relative wave height damping in the radial and angular direction manually fitted to experimental data (Huber and Hager (1997)).

2.6 Related modeling of impulse waves

Prins (1958) modeled impulse waves with an initial dam-up or lowering of the water surface over a finite length in a 2D water channel. Four different wave types were generated depending on the amount and length of the initial rise or lowering of the water level relative to the water depth. The four wave types are: oscillatory waves, leading solitary waves followed by dispersive trailing waves, solitary waves separated from the trailing waves and multiple solitary waves. The experimental data were compared with the theoretical work of Unoki and Nakano (1953) and Kranzer and Keller (1959), but the wave heights could not be predicted satisfactorily. Hunt (1988) produced an analytical solution for water waves generated by distant landslides by injecting a volume of fluid at a point source through the bottom of a reservoir. This approximation is justified by the assumption that the times are large relative to the duration of the time of the landslide and when the distances are large compared to a characteristic horizontal dimension of the volume flux of water displaced by the slide material.

Storr and Behnia (1999) conducted experimental studies on impulse waves generated by large diameter gravity driven liquid jets impacting into a pool with variable water depth. The liquid jets comprised of a finite volume of liquid released well above the still water surface from a cylinder with variable diameter. The fluid properties of the jet were varied within the following ranges: density from 1.0 to 1.58 t/m^3, surface tension σ from 0.014-0.076 N/m, and dynamic viscosity μ from 0.0006-2 N/m^3. The viscosity of the liquid jet had a significant effect on the deformation of the jet during the impact and the size and shape of the air cavity formation.

LeMéhauté and Wang (1995) extensively summarized the earlier work and literature on impulse wave generation by underwater explosions. The efficiency of the wave generation increased from shallow waters to deeper waters. In shallow water depths, when the cavity generated by explosions reached the bottom, only 5% of the

explosion energy was transmitted in the form of water waves. Similarities between explosion generated waves and the landslide generated impulse waves were proposed based on wave characteristics and air cavity collapse. In a similar study, Johnson and Bermel (1949) and Jordaan (1969) conducted laboratory experiments on underwater explosions by replacing the explosion with falling weights.

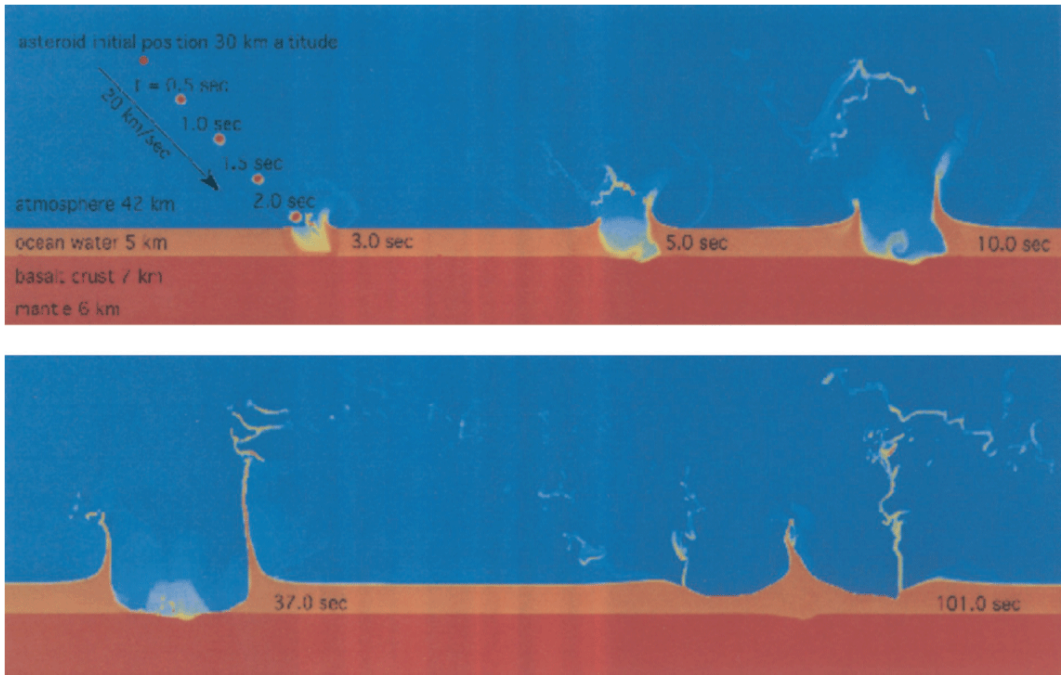

Figure 21: A sequence of 10 images from the 3D simulation of an impact of 1 km bolide at an angle of 45^o with an ocean of 5 km depth. Shown are the density rasters from Gisler *et al.* (2003).

Crawford and Mader (1998) numerically modeled the interaction of a typical stony asteroid with the atmosphere and a 5 km deep ocean with a basalt bottom with a CTH code for a multi-dimensional, multi-material, large deformation and strong shock wave physics (McGlaun *et al.* (1990)). The CTH code was also successfully applied to simulate the impact of Shoemaker-Levy 9 comet on Jupiter (Crawford *et al.* (1994)). The asteroids had variable diameters, density of 3.32 t/m^3 and an impact velocity of 20 km/s. The collapse of the impulse cavity, the resulting tsunami wave and the

circular propagation was modeled with the ZUNI code which solves the incompressible Navier-Stokes equation (Mader (1988)). Gisler *et al.* (2003) simulated impacts of asteroids into the 5 km deep ocean using the SAGE model from Los Alamos National Laboratory shown in Fig. 21. The model is a compressible Eulerian hydrodynamics code with continuous adaptive mesh refinement with realistic equations of state for atmosphere, water, the oceanic crust and the mantle. Weiss *et al.* (2006) used a combination of an extended iSALE model (Wünnemann *et al.* (2006)) and the MOST model (Titov and Synolakis (1995), Titov and Synolakis (1998)) to simulate the oceanic impacts of asteroids and the generated tsunami propagation and runup respectively. The wave pattern from the impact calculated using the iSALE model is used as a boundary condition in MOST model for evaluating wave propagation and runup. A similar technique was used by Glimsdal *et al.* (2007) where a multimaterial hydrocode model SOVA (Shuvalov *et al.* (1999)) is used initially to model the impact and then a wave propagation model is used to simulate wave propagation and runup. The tsunami propagation models was based on the solution of the Boussinesq equations. The wave generation and propagation from asteroid impacts are strongly influenced by nonlinearities, the material, size and direction of the asteroid and the oceanic environment. In most simulations, the deep ocean asteroid impact generated waves were not in shallow water waves but in the intermediate water depth range similar to landslide generated tsunamis. The simulations of asteroid impact generated tsunami wave runup and breaking can be found in Korycansky and Lynett (2005) and Korycansky and Lynett (2007).

2.7 Numerical modeling of landslide generated tsunamis

Noda (1970) used linear theory to predict the wave form of the wave motion produced by a body falling vertically into a tank. The model assumes that the time history of the falling block is known. The assumptions of linear theory breaks down near the

falling block. The solution only produced reasonable agreement with experimental data for thin blocks with initial submergence. Even for initially submerged blocks, the theoretical solutions depart from the experimental data with increasing relative block thickness s/h and increasing wave amplitude.

Monaghan and Kos (2000) conducted 2D numerical simulations to clarify the details of the wave formation and the box dynamics from their experimental study. The setup for the numerical simulations were similar to the experimental setup. They successfully simulated the box dynamics and the wave formation including the wave breaking and air entrainment during cavity collapse with the Lagrangian particle method - smoothed particle hydrodynamics (SPH) described in Monaghan (1992). The numerical results overshot the experiment by $3 - 18\%$. Monaghan and Kos (1999) successfully simulated gravity currents descending a ramp in a stratified tank with the SPH method. Further SPH simulations by Monaghan *et al.* (1999) accurately reproduced experiments on the run-up of a solitary wave on a beach of varying slope and in particular the wave breaking during the run-down including the bore formation.

Heinrich (1992) conducted numerical studies on tsunamis generated by landslides using the NASA-VOF2D model. In this study, the landslides were modeled as a rigid body with a triangular cross section sliding down a ramp. The model is a nonlinear Eulerian model which solves the complete Navier-Stokes equations by a finite difference method. This model was extended to allow for the movement of the fluid domain boundaries to simulate landslides. Subaerial as well as submarine landslides and bottom movement were modeled using this code. The velocity vector fields and the free surface comparison between the numerical simulations and the experimental results are shown in FIGURE. While the first wave crest and trough showed good comparison the latter dispersive trains showed a phase shift and variations in the wave amplitude. A three dimensional version of the model was also developed by Heinrich (1992). The NASA-VOF2D model was also used to simulate tsunamis generated by submarine

landslides by Rzadkiewicz and an P. Heinrich (1997). The submarine landslide was modeled as a fluid with an ideal Bingham plastic law, in which no deformation takes place until a specified shear is applied to the fluid. The comparison of the model simulations with experimental results is shown in Fig. 22.

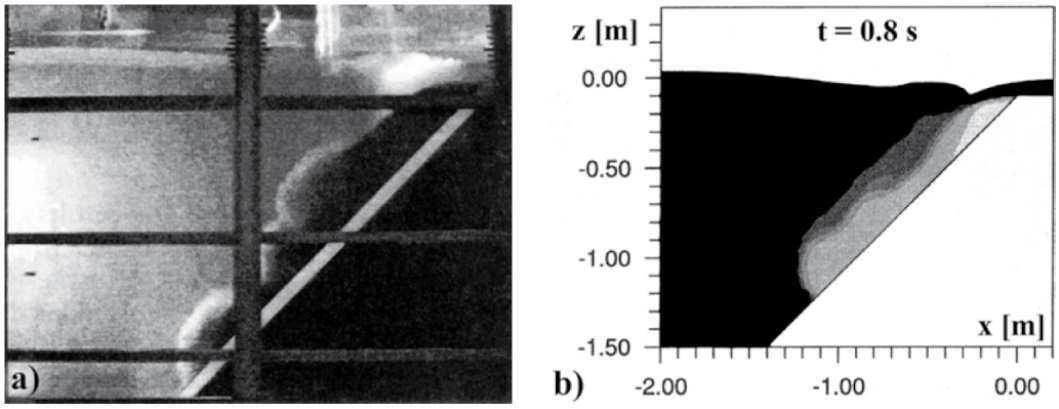

Figure 22: Submarine landslide: (a) experiment of coarse sand sliding down a ramp with slope angle $\alpha = 45^o$; (b) computed density map at t = 0.8 s (Rzadkiewicz and an P. Heinrich (1997)).

Ward (2001a) computed tsunamis generated from complex landslides by using a pseudo Green's function method that computes the tsunami from sums of many small simple slides of varying thickness, length, width, velocity, orientation and initiation time. This method was employed to simulate the potential collapse of the Cubmre Vieja volcano and model the tsunami at La Palma, Canary Islands (Ward and Day (2001)). Ward and Day (2008) developed a new granular approach of tsunami balls to model the tsunami runup and inundation. The tsunami generation, propagation and runup phases are modeled as balls of tsunami energy which behave similar to a debris avalanche but without the underlying basal friction which results in the return of the water phase to the ocean body. The formulation of the ball accelerations enable both wave-like and flood-like behavior so that the tsunami waves can transition smoothly from deep water, through wave breaking to final runup. The tsunami balls track according to long wave theory in deep water and behave like a water landslide on

land.

Depth-averaged nonlinear shallow water wave equations were used to simulate tsunamis generated by different landslide scenarios by Raney and Butler (1975), Chiang *et al.* (1981), Chaudhry *et al.* (1983), Townson and Kaya (1988), Mader (1988), Mader (1999), Harbitz *et al.* (1992), Jiang and LeBlond (1992), Jiang and LeBlond (1993), Jiang and LeBlond (1994), Johnson and Mader (1994), Imamura and Gica (1996) and Tinti and Bortolucci (2000). However, neglecting vertical accelerations in the water body during the wave generation and on the shore during wave runup is inaccurate as showed by Fritz (2002). The landslide generated tsunamis are mainly in the intermediate water depth regime and hence subjected to dispersion, which is not included in the nonlinear shallow water wave equations, as seen in real cases.

Lynett and Liu (2002) derived a mathematical model to describe the tsunami wave generation and propagation by submarine landslides. The depth integrated continuity and momentum equations were solved using a high-order finite difference model and the results were compared with experimental data and other numerical models. The model simulations were compared with experimental results of Hammack (1973) and Watts (1997). The model has capabilities to simulate either weakly nonlinear effects or a non-dispersive wave system.

Watts (2000) performed numerical simulations of water waves generated by an underwater landslides and compared them with the experimental results. The landslide was modeled as a block of semi elliptical cross-section. The model based on the depth averaged nonlinear shallow water wave equations appear to underestimate the wave amplitudes. Watts *et al.* (2003) used a Bingham rheology as a superposition on a center-of-mass treatment for submarine landslides. They also showed that nonlinear and dispersive tsunami propagation models may be necessary for modeling landslide tsunami cases. This was done using GEOWAVE by combining the TOPICS (Tsunami Open and Progressive Initial Condition Systems) model with the fully

nonlinear Boussinesq water wave model FUNWAVE.

Grilli and Watts (1999) developed 2D-FNPF, a two dimensional fully non linear potential flow solver to model tsunamis generated by submarine landslides in a numerical wave tank developed by Grilli *et al.* (1989). The submarine landslide is modeled by a fully submerged semi-ellipse on a plane slope. The model was also used to simulate tsunamis generated by submarine slides and slumps by Grilli and Watts (2005). The 2D-FNPF model was then extended by Grilli *et al.* (2002) in a three dimensional numerical wave tank to model three dimensional tsunamis generated by submarine landslides. This model was based on the fully nonlinear potential flow theory solved using a higher order boundary element method. The numerical results were compared with the experimental results for a quasi two dimensional landslide. The deformation in the underwater slide shape was achieved by specifying a positive uniform normal velocity along the slide boundary. However, the deformation of an underwater slide is also subjected to the shear forces acting on the front and the top of the slide which cannot be simulated in the present model. This can be overcome by the use of multi-phase models which describe the landslide theology as well as the fluid properties of the water body.

The multi-phase models usually involve solving the Navier-Stokes equations in an Eulerian grid based framework for the three phases of the landslide material, water and air. Accurately modeling the material interfaces is the key in these models since these interfaces are subjected to numerical diffusion and are subject to shocks during material interactions. Madsen and Gittings (2002) obtained the near-field wave characteristics of impulse waves generated by subaerial landslides using the solution of the compressible Navier-Stokes equations in the SAGE model. The model uses a continuous Adaptive Mesh Refining (AMR) scheme to simulate the different phases in the solution. In the SAGE model, the compressible Navier-Stokes equations are solved by a high resolution Godunov differencing scheme. The model was used to

simulate the Krakatoa hydrovolcanic explosion and tsunami by Mader and Gittings (2006). Quecedo *et al.* (2004) implemented the level set formulation of the Navier-Stokes equations (Sethian (1996), Fedkiw *et al.* (1999)) to differentiate and define the different phases in the landslide tsunami problem. The landslide material is modeled as a generalized viscoplastic fluid proposed by Chen and Ling (1996). Abadie *et al.* (2008) used a Volume of Fluid (VOF) method to model the coupling between the slide material and the water body. The model was validated for the case of solitary wave generation by Russell's wave generator. Horrillo (2006) also used the VOF technique to develop a two dimensional numerical model to study tsunami wave generation, propagation and runup. In contrast, Schwaiger and Higman (2007) used a mesh free Lagrangian hydrocode based on the Smoothed Particle Hydrodynamics (SPH) to reduce the effects of numerical dissipation and improve tracking of the material interfaces.

Weiss *et al.* (2009) adapted the multi-material iSALE (Wünnemann *et al.* (2006)) to simulate the Lituya Bay landslide tsunami event. The model is a multi-material, finite-difference hydrocode for simulating fluid flows and solid body deformations at subsonic and supersonic speeds (Amsden *et al.* (1980)). The computed wave runup agrees with both the experimental results of Fritz *et al.* (2001) and the measured field runup. Beget and Kowalik (2006) compared numerical models of tsunami height and inundation with field data from tsunami deposits and historic accounts of the 1883 Augustine tsunami. Sensitivity testing and calibration of numerical models based on real world data can provide a high degree of confidence in the validity and accuracy of numerical models.

2.8 Conclusions

The conclusions from the review of literature are summarized below:

- Most model studies were based on the Froude similarity.

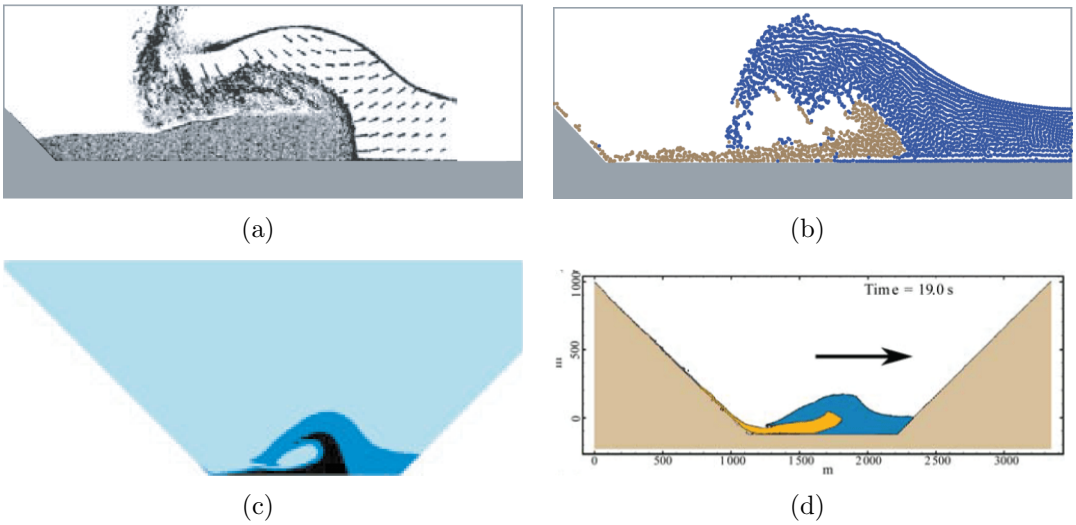

Figure 23: Modeling of Lituya bay, Alaska event of 1958: (a) Physical modeling by Fritz *et al.* (2001); (b) SPH model by Schwaiger and Higman (2007); (c) Navier-Stokes solution by Quecedo *et al.* (2004) and (d) iSALE modeling by Weiss *et al.* (2009).

- Analytical models cannot accurately model the wave generation process in real world cases and are not suitable for hazard mitigation purposes.
- The analytical solutions might not accurately describe the generated tsunamis in the nonlinear range.
- Landslide generated tsunami are typically shorter in wave period and wave length than tectonic tsunamis, which places them mostly in the intermediate water depth range.
- The observed wave types were: oscillatory, cnoidal, solitary, bore and intermediate characteristics.
- The leading wave is not necessarily the largest wave in the generated wave train.
- The identified parameters governing tsunami generation by landslides are: still water depth h, slide thickness s, slide length l, slide width b or the bulk slide volume V_s, slide impact velocity V_s, slide mass m_s, bulk slide density ρ_s, grain

slide density ρ_g, slide porosity n, hill slope angle α, time of underwater slide motion t_s and in some cases the slide front angle.

- The wave propagation depends on the stream wise or radial distance x or r depending on 2D or 3D case respectively, the time t and the propagation direction θ.

- In most physical models, bathymetry effects were neglected by conducting the experiments with a horizontal bottom.

- In most physical models, the tsunami generation showed a dependence on the slide Froude number F, relative slide thickness s/h, hill slope angle α, relative distance x/h or r/h and the wave propagation direction θ.

- Some conclusions from subaerial, partially submerged and submarine landslides are not interchangeable among themselves.

- In physical models involving solid blocks, a large amount of kinetic energy of the block is abruptly removed from the system by either hitting the basin bottom or by means of a form of stopper, which results in biased energy conversion rates between the slide and the wave. This complicates direct comparisons between studies with deformable and block landslides as tsunami source.

- Solid block models do not reproduce the long submarine runout of the landslides observed in nature. In most cases, they do not accurately simulate the slide deformation, porosity and time history of emplacement.

- The block models overestimate the maximum wave amplitude when compared with granular slide models.

- The wave attenuation is underestimated in 2D models when compared with 3D wave propagation.

- The maximum wave heights in 3D models are in the direction of the slide propagation.
- Lateral runups from the generated tsunami could pose a hazard close to the generation region.
- Data from physical models may provide height precision data sets for validating numerical models.
- The two dimensional depth averaged wave models incorrectly disregard the vertical fluid accelerations in the generation region.
- A fully three dimensional model can accurately simulate the landslide-fluid dynamics in the wave generation region.
- The accuracy of the full three dimensional Navier-Stokes model depend on the description of the landslide rheology and the interface tracking between the different phases in the flow.
- The boundary element methods may fail in case of shock formation or development of sharp fronts.
- The boundary element method is deficient to model subaerial or partially submerged landslide impact cases.
- The SPH methods are promising with regard to the wave generation.
- Empirical predictive equations from 2D or 3D tests are often difficult to employ in real scenarios due to bathymetry and topographic effects on wave transformation, propagation and runup.

2.9 Identified research gaps

The identified research gaps are summarized as follows:

- The currently available data sets are deficient in terms of the three dimensional landslide deformation, 3D landslide water body interaction, kinematics of the 3D wave generation process and submarine landslide dynamics.
- The information needed for 3D numerical model validations are limited.
- No study exists in which all the governing parameters for the slide models were independently varied.
- The tsunami wave generation by 3D deformable landslides is not investigated with modern instrumentation.
- The effect of 3D landslide deformation on the main wave characteristics is not quantified
- The dependency of the generated wave train on the angular propagation direction is poorly established.
- Effects of complicated bathymetry and topography at the tsunami source are not determined, which are typical for volcanic islands or fjord like bays.
- The knowledge of the impulse wave generation in unsatisfactory for engineering applications for hazard mitigation. Landslide generated tsunamis are not included in FEMA hazard maps and mitigation plans.

CHAPTER III

EXPERIMENTAL SETUP

3.1 Introduction

Experiments on tsunamis generated by unconfined deformable granular landslides were conducted in the O. H. Hinsdale wave research laboratory at Oregon State University in Corvallis, Oregon. The experiments were conducted in the large three-dimensional NEES Tsunami Wave Basin (TWB). The granular landslides were deployed using a novel pneumatic Landslide Tsunami Generator (LTG). The landslide tsunami generator was designed at Georgia Institute of Technology and manufactured by TIC in Savannah. The landslide tsunami generator was then shipped to Oregon and deployed in the tsunami wave basin at Oregon State University. This chapter describes the physical model setup and the instrumentation deployed in the experiment.

3.2 Dimensional Analysis

The theory of dimensional analysis is given by Buckingham (1914), Yalin (1971) and Novak and Cabelka (1981). Detailed discussion on dimensional analysis of fluid flow may be found in Hughes (1993), Dalrymple (1985), Sedov (1959) and others. Dimensional analysis cannot produce a complete solution nor can it reveal the inner fundamental physics of a phenomenon. According to the Π theory of Buckingham (1914), the governing independent parameters $r_1, r_2, ..., r_n$ can be reduced to $m = n - o$ governing dimensionless parameters $\Pi_1, \Pi_2, ..., \Pi_m$ without loosing physical information, where n is the number of independent parameters, o is the number of fundamental dimensions such as mass, length and time and m is the number of non-dimensional

Table 3: Governing parameters for tsunamis generated by granular landslides.

symbol	description	dimension	fundamental dimension
h	still water depth	[m]	[L]
s	slide thickness	[m]	[L]
b	slide width	[m]	[L]
l_s	slide length	[m]	[L]
V_s	slide volume	[m^3]	[L^3]
v_s	slide velocity	[m/s]	[LT^{-1}]
α	hill slope angle	[^{o}]	[-]
ρ_s	slide density	[kg/m^3]	[ML^{-3}]
ρ_w	water density	[kg/m^3]	[ML^{-3}]
g	acceleration due to gravity	[m/s^2]	[LT^{-2}]
r	radial propagation distance	[m]	[L]
θ	propagation direction	[^{o}]	[-]
t	time	[s]	[T]

parameter. A hydraulic model is similar to the prototype if all of the dimensionless parameters are identical. The establishment of the dimensionless parameters is arbitrary if the number of parameters exceed six, which leads to an arbitrariness in the determination of the condition of similitude (Birkhoff (1950)). With reference to Fig. 3, the governing parameters for the tsunami wave generation by landslide are shown in Table. 3.

A total of 14 independent parameters which govern the tsunami wave generation are identified. The gravitational acceleration g, the water density ρ_w and the slide density ρ_s are constant in this study. The initial slide length was not varied, thus making it redundant for the study as the initial slide volume V_s includes the initial slide length, width and thickness. However the slide length at impact is defined as $l_s = V_s/(sb)$ in terms of the landslide thickness and width at impact. The mass of the slide may be expressed using the bulk slide density and the slide volume as $m_s = \rho_s V_s$ and hence is not considered as an independent parameter. The slide geometries in the present study are described by the slide volume V_s, slide thickness s, width b and

Table 4: Non-dimensional parameters that govern tsunami generation by 3D deformable granular landslides.

dimensionless parameter	description
$\Pi_1 = \mathrm{F} = v_s/\sqrt{gh}$	relative slide impact velocity or slide Froude number
$\Pi_2 = \mathrm{S} = s/h$	relative slide thickness
$\Pi_3 = \mathrm{B} = b/h$	relative slide width
$\Pi_4 = \mathrm{V} = V_s/h^3$	relative slide volume
$\Pi_5 = \mathrm{D} = \rho_s/\rho_w$	relative slide density
$\Pi_6 = \alpha$	hill slope angle
$\Pi_7 = \mathrm{R} = r/h$	relative propagation distance
$\Pi_8 = \theta$	propagation direction
$\Pi_9 = \mathrm{T}_r = t\,(g/h)^{1/2}$	relative time

length l_s. The slide bulk density ρ_s is defined as

$$\rho_s = (1-n)\rho_g \tag{26}$$

in terms of the granulate density ρ_g and the slide porosity n. The slide porosity includes effects of slide shape and the grain diameter d_g. The time of the underwater slide motion t_s is not considered due to the poorly defined end of motion for deformable granular landslides (Fritz (2002)) in contrast with solid block slides which abruptly come to a stop. The time of underwater motion is a dependent parameter and depends on the landslide velocity and shape (Heller (2008), Heller *et al.* (2008)). With the above, a total of nine dimensionless parameters were identified that govern the wave generation. These non-dimensional parameters are summarized below.

All the variables that characterize the tsunami waves depend upon the above non-dimensional parameters. The relative slide density and the hill slope angle are constant in this study. In the present study, all the predictive equations are determine by a multi-variable regression analysis of the measured values. Thus the relative amplitude $A = a/h$ may be expressed as

$$A(R) = f(F, S, B, V, R, \alpha, \theta, T_r) \tag{27}$$

3.3 Physical Model

The experiment setup was deployed in the George E. Brown Network for Earthquake Engineering Simulation (NEES) tsunami wave basin (TWB). The wave basin is 48.8 m long, 26.5 m wide and 2.1 m deep. The tsunami wave basin is equipped with a large stroke, directional wavemaker with active wave absorption to study tsunami wave propagation and runup properties. However, a novel landslide tsunami generator was deployed from the opposite shore in the tsunami wave basin to study tsunami wave generation by landslides and their propagation away from the landslide source. The schematics of the experimental setup are shown in Fig. 24.

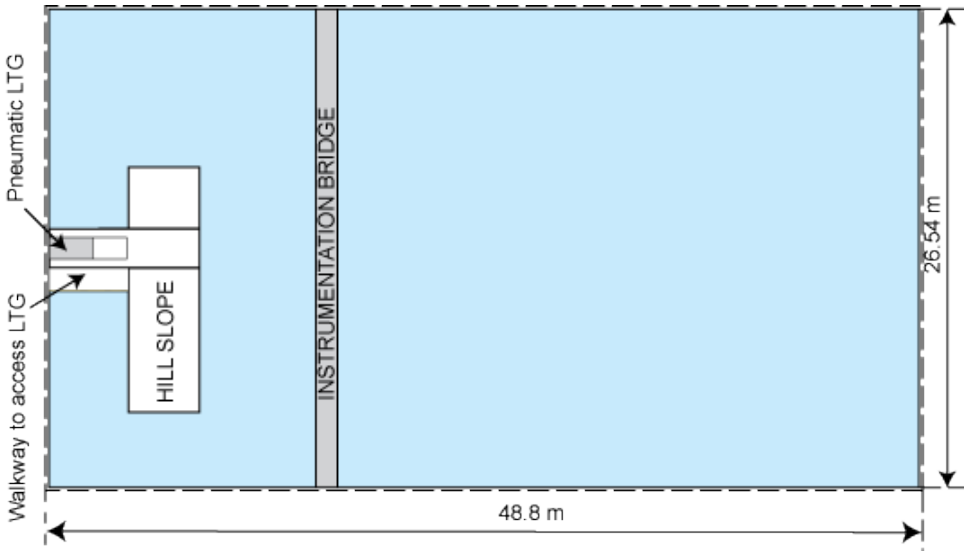

Figure 24: The pneumatic landslide tsunami generator setup in the tsunami wave basin.

A hill slope was built on one end of the wave basin with a slope of one vertical

to two horizontal ($\alpha = 27.1°$). The major portion of the hill slope was built with wood on a wooden mount, while the central portion where the landslide tsunami generator was mounted was made of steel. The hill slope configuration is shown in Fig. 24(b). A wooden walkway provides access to the landslide tsunami generator on the hill slope. A translational bridge measuring 1.2 m wide spans across the width of the TWB. This bridge was used for mounting various measurement instrumentation. The bridge is capable of moving on a set of rails on either ends of the TWB. Thus the position of the bridge and the instrumentation can be moved accordingly with changes in water depth or subaqueous landslide runout.

The other end of the wave basin has a multi-paddle tsunami wave generator which is static during the experiment. This location is sufficiently far from the landslide tsunami generator to avoid wave reflections in the landslide impact region. The reflections from the paddles do not interfere with the measurements of the first three waves in the generated wave train by the landslide from the other end of the wave basin.

3.4 Pneumatic Landslide Tsunami Generator

The design of the pneumatic landslide tsunami generator (LTG) is an extension of the generator designed by Fritz and Moser (2003). The design is capable of mimicking natural landslide motion where the landslide initially begins to move as a solid block post failure and then disintegrates under the influence of gravity and bottom friction to form a debris avalanche. The landslide tsunami generator is designed as a pneumatically driven box filled with gravel. The landslide tsunami generator consists of a slide box which measures 2.1 m long, 1.2 m wide and 0.3 m deep. The slide box is driven by means of four pneumatic pistons. The pistons have a full stroke length of 2 m. The pneumatic setup allows for controlled box movement by means of the pneumatic circuit, which allows for a controlled acceleration of the slide box. The

pneumatic control chart is shown in Fig. 25(b). The slide box is designed such that by fixing plates in the box, the slide volume can be varied to study its effect on the wave generation process.

The pneumatic acceleration of the landslide box at a certain pre-determined pressure creates pressurized air in a chamber ahead of the piston. The release of the pressurized air in the cylinder drives the pistons forward to accelerate the slide box. The slide box is accelerated for roughly half of the stroke length. A pressurized air cushion in the lower half of the cylinder damps the piston motion thus causing the slide box to decelerate and come to rest at the end of the piston stroke. The front of the box was enclosed with a tarp material by means of string on either ends which were designed to fail during the launch. The entire pneumatic setup is placed on the hill slope.

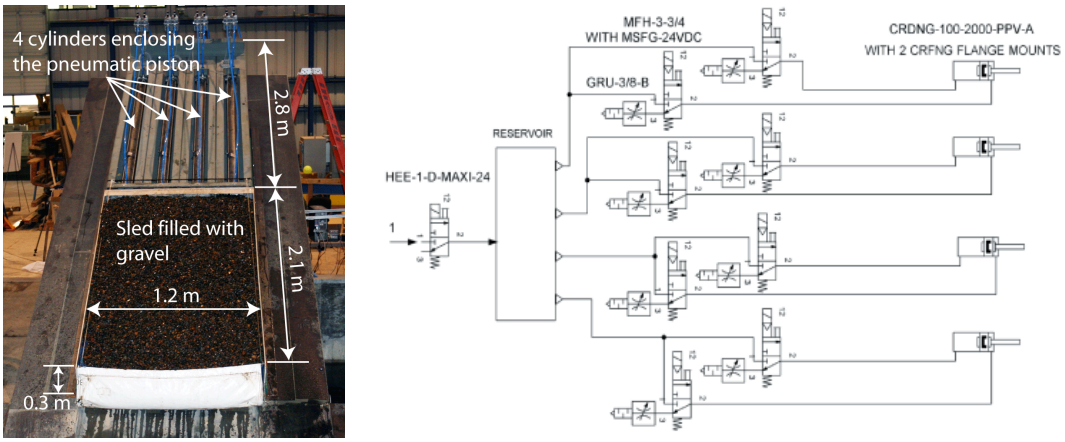

(a) (b)

Figure 25: (a) Pneumatic landslide tsunami generator; (b) flowchart for the pneumatic control.

3.5 Landslide tsunami generator performance

The position of the box was measured with a cable-extension transducer. The pneumatic landslide tsunami generator was pneumatically accelerated with four different initial pressures of 10 bar, 8 bar, 6 bar and 4 bar. The measured box positions for

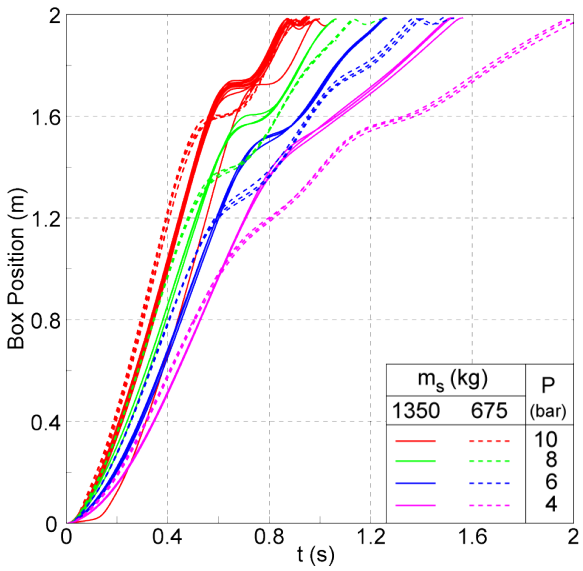

Figure 26: The measured landslide tsunami generator box positions for all the experimental trials.

all the experimental trials are shown in Fig. 26. The box velocities were obtained using the first derivative of the measured box distance. The high frequency noise was removed from the data prior to taking the first and second derivative to obtain the velocity and acceleration. The original signal was filtered using a wavelet filter. The measured slide box velocity for the four different firing pressures are shown in Figs. 27(a) and 27(b).

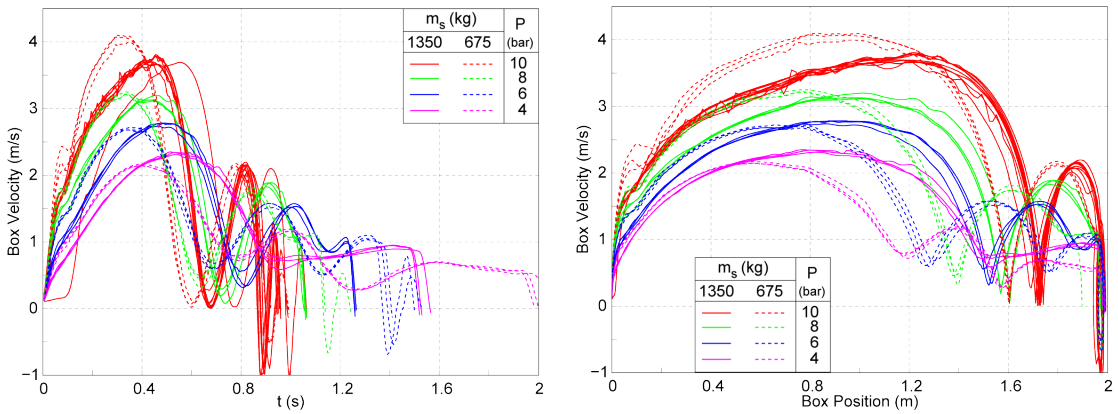

(a) (b)

Figure 27: Performance of the pneumatic landslide tsunami generator: (a) The measured slide box velocity for the duration of slide motion t and (b) measured slide box velocity with respect to the slide box position.

The peak box velocity varies with slide volume in the box. The performance of the pneumatic system strongly depended on the accelerated mass and the propulsion pressure. The maximum box velocity for a slide volume of $V_s = 0.378$ m^3 was found to be 4.0 m/s while for a slide volume of V_s =0.756 m^3, it was found to be 3.7 m/s. The slide box accelerations were computed as the second derivative of the slide box distance displacement. The maximum slide box acceleration in the experiments reached $4g$ for a slide mass of roughly 1350 kg. During deceleration, the slide box reached accelerations up to $-12g$.

3.6 Granular Landslide Material

The granular material (Green and White Rock Products Inc, Corvallis, Oregon from Willamette River) for the landslide consists of naturally rounded river gravel spanning sieve sizes 19 mm to 12.7 mm. The bed friction angle of the granulate material is lower than the experimental hill slope which allows for the landslide motion on the slope. The rounded shape of the granulate material allows the gravel to behave as natural landslides post the pneumatic acceleration and spread naturally on the hill slope. The physical characteristics of the gravel are summarized below.

- slide grain density, ρ_g : 2.556 t/m^3.
- bulk slide density, $\rho_s = 1.76$ t/m^3
- porosity, n : 0.31
- Internal friction angle, ϕ : 41^o
- friction angle, δ : 23^o

Figure 28: Granular material used for modeling the 3D deformable landslides

3.7 Instrumentation deployed in the tsunami wave basin

3.7.1 Camera Setup

The dynamic and granular nature of the landslides launched by the landslide tsunami generator requires non-intrusive measurement techniques to quantify the slide motion. A total of seven cameras recorded the landslide motion from its inception to the final deposition on the bottom of the tsunami wave basin. The camera locations in the tsunami wave basin are shown in Fig. 29. Two cameras were placed on the hill slope, one above the water surface and the other underwater. The images recorded by these cameras are used to determine the slide front velocity and the slide profile shape on the hill slope.

A high resolution particle image velocimetry camera is placed with the viewing area on the hill slope above the water surface and the impact region on the water surface. The images from these cameras are used to measure the slide front velocity, slide width and the slide surface velocity. More information on the PIV setup can be found in the subsequent section. A camera is placed on the bridge with the viewing focus on the lateral wave runup on the hill slope while another camera is placed

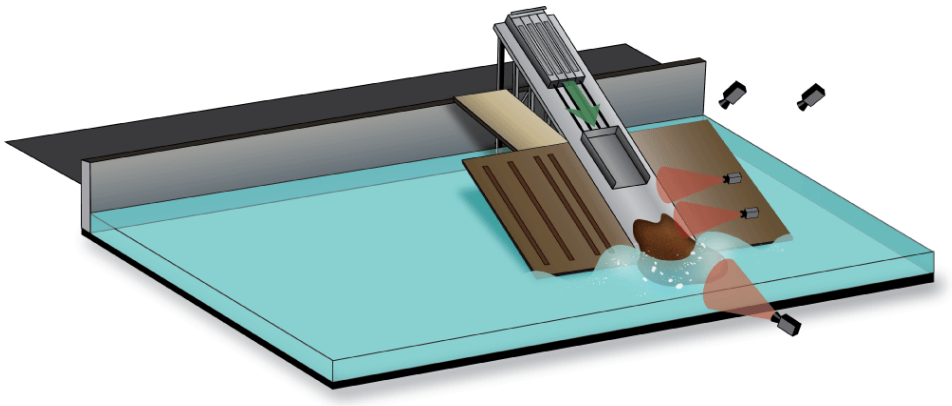

Figure 29: Schematics representation of the camera array setup in the tsunami wave basin to measure the landslide motions.

underwater focusing on the slide front. The last camera is located overhead of the tsunami wave basin to provide an overall view of the experimental process. Except for the particle image velocimetry camera, all the other cameras have standard video resolution. The viewing area of these cameras are shown in Fig. 30. All the cameras are calibrated in situ by placing calibration plates with a regular pattern of dots in the various measurement planes both above and underwater. Some of the calibration images are shown in Fig. 31.

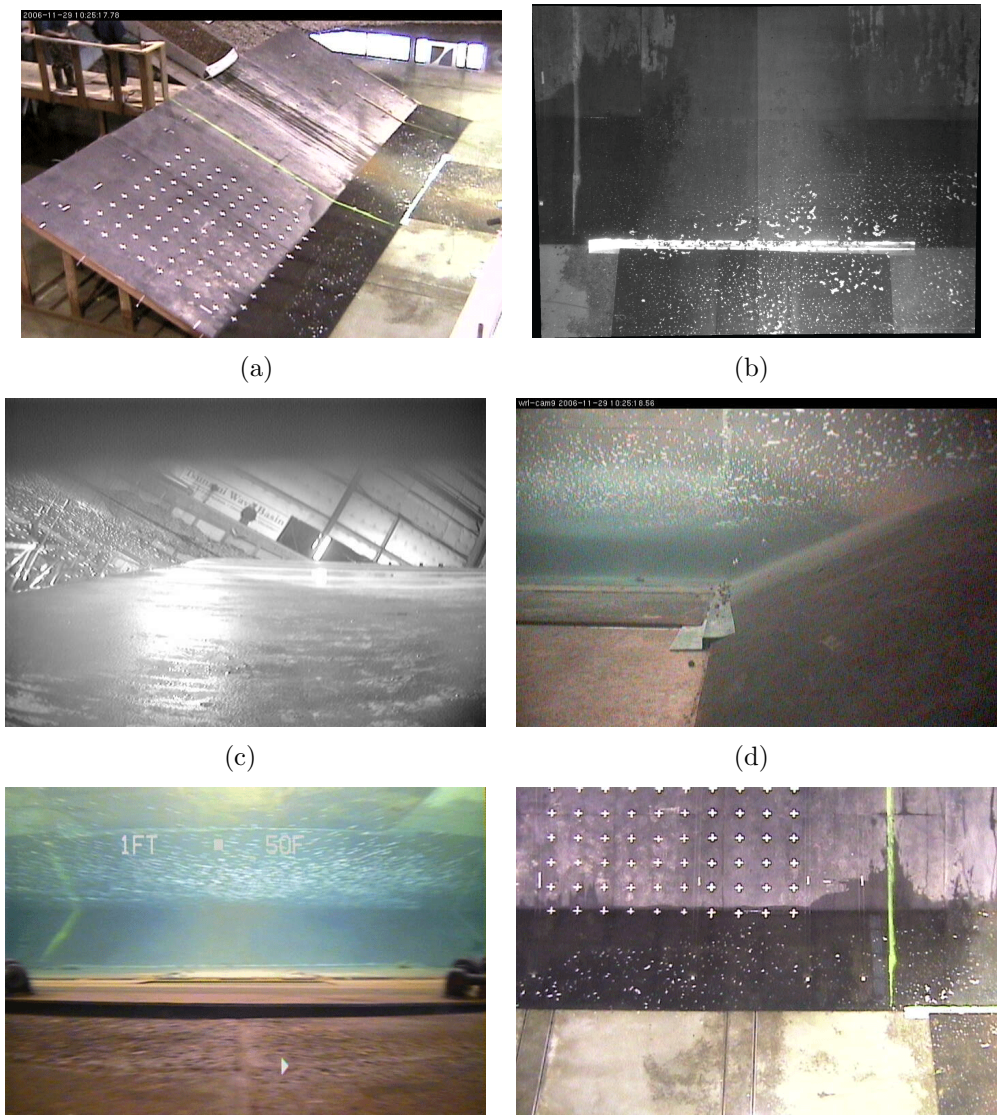

Figure 30: Image frames displaying the viewing area of the cameras: (a) Overview of the experimental setup; (b) PIV camera view; (c) above water side view; (d) under water side view; (e) under water front view and (f) view of the wave runup area on the hill slope

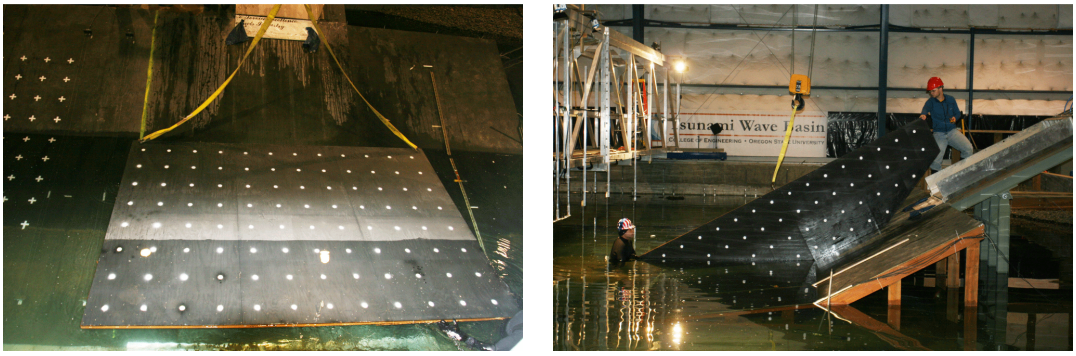

(a) (b)

Figure 31: In situ calibration of the cameras.

3.7.2 Multi-Transducer Acoustic Array

A multi-transducer acoustic (MTA) array surveyed the landslide deposit at the bottom of the wave basin after each experimental trial prior to landslide recovery. The acoustic array measures the underwater distance to the landslide surface. The acoustic array consists of four transducer arrays connected in series for a total of 32 transducers. Each array consists of eight transducers that are housed in a stainless steel housing with a 0.08 m transducer spacing. Each transducer array measures 0.64 m in length with the composition totaling 2.56 m. The transducers have a diameter of 0.02 m and operate at 2 MHz with a half-beam angle of 1.1^o. The acoustic array has a measurement range of 0.05-4.20 m. The eight transducer individual array and the composite 32 transducer array are shown in Fig. 32.

The acoustic array is mounted on the front end on the bridge, facing the landslide tsunami generator. The horizontal reference distance for the acoustic array is measured by means of a laser range finder (LRF), which is mounted on the back end of the bridge. The target for the laser range finder is mounted on the rear wall of the wave basin. The acoustic array setup is shown in Fig. 33. The data from the acoustic array and the laser range finder are interpolated using the time of measurement to obtain the horizontal coordinate for the measured survey depths. At the end of an

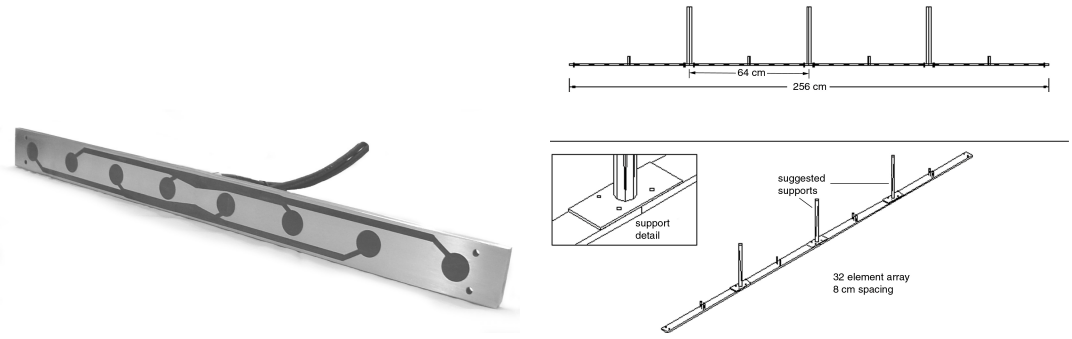

(a) (b)

Figure 32: Multi-transducer acoustic array

experimental trial, the acoustic array is lowered such that the transducer housing is below the water surface. Then the bridge is moved slowly towards the hill slope and the acoustic array scans the basin bottom to survey the slide deposit.

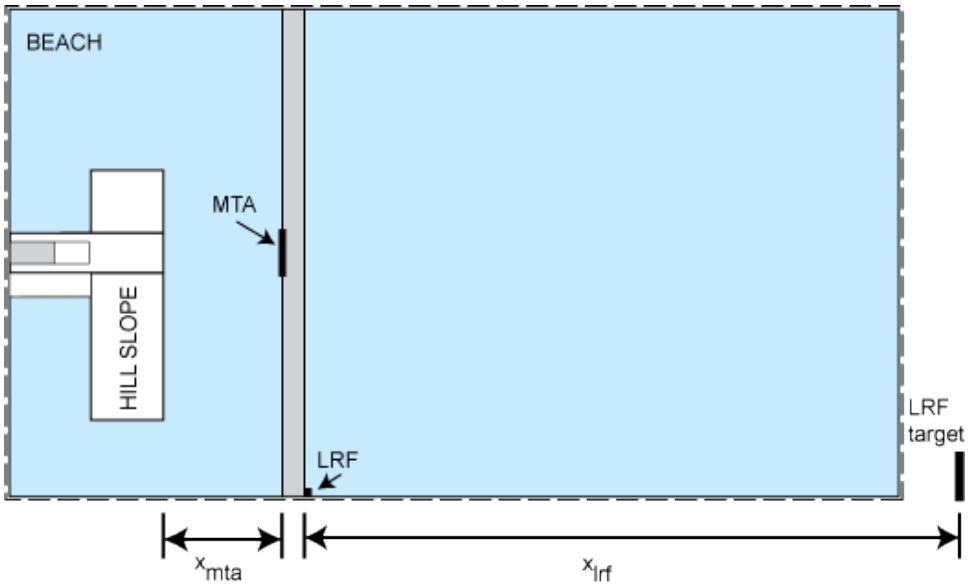

Figure 33: The multi-transducer acoustic array setup in the wave basin.

The acoustic array and the laser range finder data was acquired by a dedicated computer. The scanned 32 longitudinal landslide profiles describe subaqueous landslide deposit including shape, volume and the runout length.

3.7.3 Wave Gauges

An array of wave gauges records the water surface elevations to characterize the generated tsunami waves and runup. The wave gauges are of resistance type, where the conductivity of the water medium is used to determine the wave height. The resistance wave gauge consists of two equally spaced conductors immersed in water. By holding a constant voltage across the two conductors, varying water levels vary the resistance between the conductors and hence the current drawn between the two conductors is varied.

The resistance wave gauge consists of an oscillator that produces a constant amplitude sine wave and the circuit is based on the Wein bridge oscillator. This circuit produces a 20 volt peak-to-peak 10 kHz sine wave with a stable amplitude. The output of the oscillator is AC coupled to a differential probe drive. A high speed 100 milliamp current booster is used to produce the current required to drive the probe. Current sensing is done by measuring the voltage drop across a 1 Ohm resistor placed in series with the probe. The sensed 10 kHz voltage is AC coupled to an instrumentation amplifier and the output of this is a single ended 10 kHz signal that is amplitude modulated by the change in current in the probe and thus the wave amplitude. The signal is demodulated with a full wave precision rectifier which also doubles as a low-pass filter. The output of this rectifier filter combination is an analog voltage signal proportional to the wave height. The block diagram for the circuit setup is shown in Fig. 34(a)

The wave gauge consists of two probes which are 3.2 mm diameter stainless steel rods 0.72 m long. These rods are supported at the top by a lucite block that has two parallel bores on 2.54 cm centers to accept the rods. The spacing at the bottom is maintained by means of a 3.2 mm thick lucite plate. The probe is connected to the drive circuit with a 20 gauge twisted shielded pair cable. The power supply for the gauge is a regulated plus and minus 15 volt, 200 milliamp supply. This wave probe,

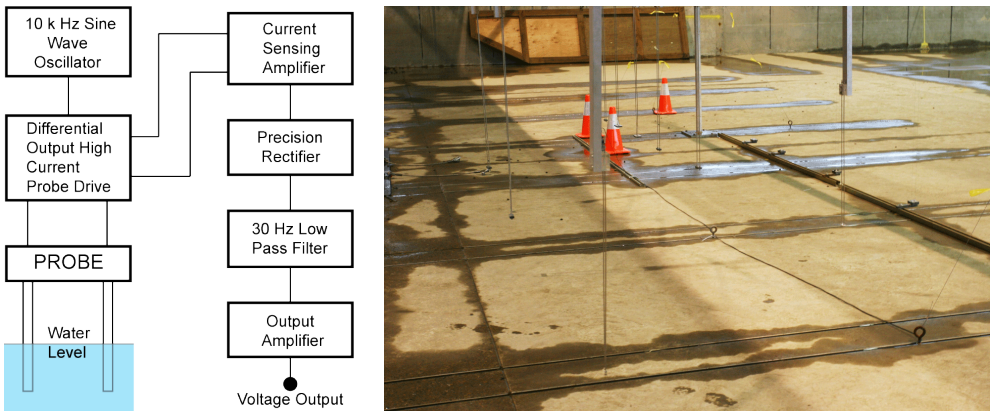

Figure 34: (a) Resistance wave gauge block diagram; (b) installed wave gauges in the tsunami wave basin.

when immersed completely in tap water, has a minimum resistance of about 160 ohms, corresponding to a 50 cm wave peak. By setting the output of the differential drive signals to 2.5 volts peak to peak each, the peak current draw from the current buffers would be about 15.6 milliamps at the maximum wave crest. Thus the gauge exhibits a nominal sensitivity of 0.2 volts per cm. The calibration of the wave gauges has shown them to be extremely linear over the 0.5 m range with a 0.7% error over the length of the probe. The largest source of error in this wave gauge has been due to the change in resistivity over time on the order of 2%. The wave gauges are calibrated during the filling of the tsunami wave basin by measuring the water depth with an acoustic sensor and determining the calibration factor for the wave gauges from the measured analog voltage signal during the filling.

A total of 25 wave gauges were used to measure the tsunami wave in the wave basin. Out of the 25 wave gauges, 21 were used in the wave basin to measure the wave propagation in both the radial and the angular direction away from the landslide source. Four wave gauges were placed on the hill slope to measure the runup wave characteristics. The wave gauges in the tsunami wave basin were placed along 5 sections parallel to the hill slope direction. The rear 3 sections are fixed relative to the wave basin coordinates and the front 2 sections are mounted on a movable bridge.

The wave gauge locations at a water depth of 0.6 m are shown in Fig. 35.

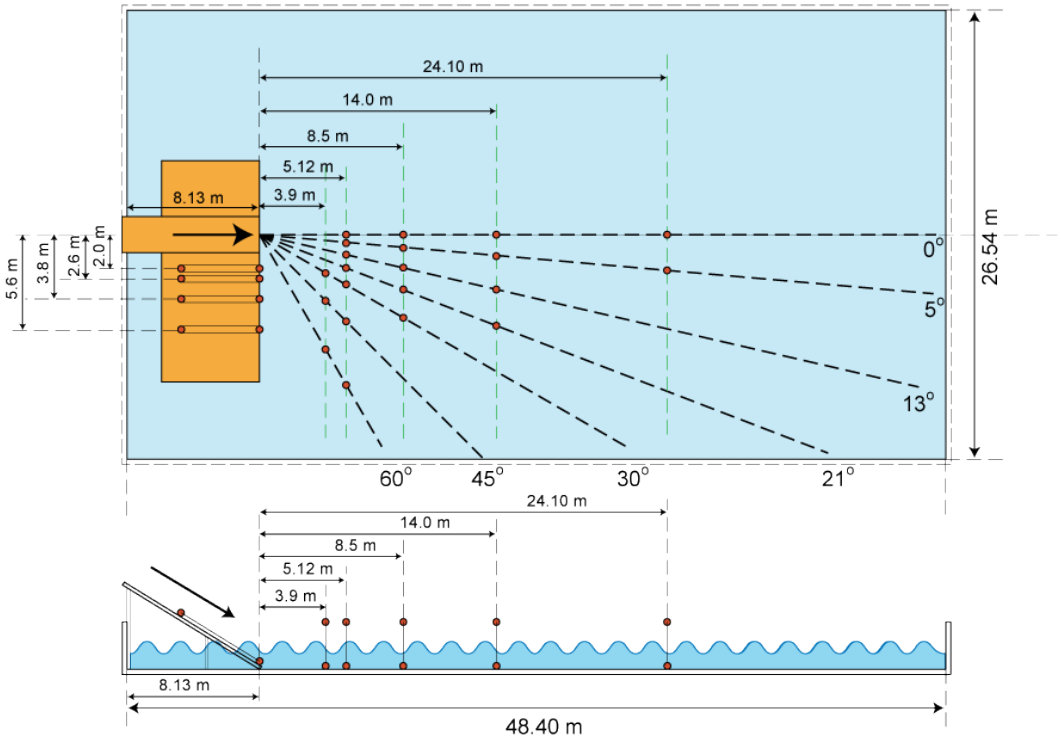

Figure 35: Wave gauge location at a water depth of 0.6 m

3.7.4 Particle Image Velocimetry Camera Setup

A high resolution CCD camera records images for the purpose of particle image velocimetry analysis. The camera is a Image Pro Plus 2M CCD progressive-scan-camera with dual frame capabilities for correlation purposes. The CCD has a resolution of 1600×1200 pixel and is capable of capturing images at 30 frames per second. The camera was setup to record the landslide on the hill slope above the water surface and the water surface in the impact zone. The camera is setup at a distance of 6.8 m perpendicular to the hill slope providing an approximate viewing area of 15 m^2 (4.5 m by 3.38 m) of the impact zone as shown in Fig. 30(b). The image acquisition and PIV analysis is performed by a PIV software program named DaVis, developed by La Vision Inc. The image acquisition is initiated in the experiment by means of a programmable timing unit (PTU) which is controlled by the trigger mechanism on

the slide box. The images are recorded as single exposure image at a frame rate of 15 fps in the experimental program. Using statistical correlation based analysis, the surface velocity on the water surface and the slide surface is determined. The speckled pattern of the granular slide surface is used to measure the slide surface velocity by the PIV correlation analysis (Raffel *et al.* (1998)). The water surface is seeded with buoyant reflective particles to measure the water surface kinematics during the wave generation process by cross-correlation based PIV analysis.

3.7.5 Data Acquisition System

The various instruments are acquiring data over different time spans during an experimental trial. Hence four separate acquisition systems record the measured data. The images recorded by the camera array are stored on a central networked server where the images from all the cameras are time stamped with the current local time, which are later converted into the experimental time. The PIV camera is operated through a stand alone computer, where the images are stored. Likewise, the acoustic array is also operated through a dedicated computer where the recorded information is stored. The data from the trigger, the wave gauge array and the cable extender transducers are stored through a 64 channel 16 bit analog acquisition system. The trigger provides a reference time stamp for the stringpot and the wave gauge measurements.

3.8 Uncertainty in Measurements

3.8.1 Error Analysis

The uncertainty in experimental measurements Δ, arise due to *systematic* and *random* errors. The actual value x_{actual} is obtained from the experimental measurements as

$$x_{actual} = x_{measured} \pm \Delta \tag{28}$$

where x is any measured variable in the experiment and Δ is the total error in the measurement. Systematic errors may arise due to temporal drifts in the instrumentation

over long periods of time, errors in calibration of the instrumentation or changes in the experimental environment. The systematic errors are often unknown and cannot be removed by averaging a number of experimental trials with the same conditions. The systematic errors in the present study were assumed to be negligibly small over the duration of the experimental study. Random errors are inherently unpredictable and may cause a scatter about the true value of a measured variable. They may arise due to fluctuations in the instrument measurements, interpretation of the instrumental reading or environmental interference in the measurement process. These errors may be estimated based on the measurement methodology. In the present study, the potential errors remain to be discussed for the following measurements

- wave profile measurements by the wave gauges
- shoreline extraction based on recorded videos.
- landslide shape and velocity measurements from video sequences
- PIV analysis of image sequences

The errors from the camera measurements can be summarized as

$$\epsilon_{tot} = \epsilon_{\nu} + \epsilon_{optics} \tag{29}$$

where ϵ_{tot} is the total error in the measurement, ϵ_{ν} is the random error and ϵ_{optics} is the optical imaging error. The random errors arise due to the interrogation technique in the recorded images, which can be through an algorithm or manual collection of data points from the image sequences. The optical imaging error arises due to the recording, image rectification and calibration process. In case of particle tracking by PIV analysis, additional errors are introduced, ϵ_{bias} and ϵ_{track} which is due to the error in tracking the particle flow. The image distortion errors arise due to the assumptions of collinearity made in the direct linear transformation method during

the image rectification process. The images recorded by the camera array in the experiment have a constant frame rate except for the above water side cam. Hence the errors in temporal coordinate can be neglected. The images recorded by the above water side cam are captured and stored on a server over a network which places a time stamp on each image with a resolution of $1/100^{th}$ of a second. Based on the image calibration, the errors in image rectification and spatial measurements made in the image are summarized in Table 5.

Table 5: Summary of absolute value of errors in the image measurements

Errors	AW Cam	Runup Cam	PIV Cam
Image rectification	1.5 pixel	0.6 pixel	2.2 pixel
ϵ_x, ϵ_y	1.35 mm	3.3 mm	1.8 mm
ϵ_t	5 ms	-	-

The maximum error for the PIV analysis was estimated based on a combination of numerical simulations with synthetic images and benchmark cases conducted by Huang *et al.* (1997), Raffel *et al.* (1998) and Westerweel (2000). The absolute maximum error of the displacement vector in the experiment is found as $\epsilon_{tot} \leq 0.02$ m/s. Since the PIV analysis involves an adaptive multi-pass algorithm with window deformation, the bias error in vector displacements can be neglected $\epsilon_{bias} \approx 0$ (Scarano and Riethmuller (2000)). The landslide granulate matter itself provides the particles for the landslide velocity flow estimation. Hence the error in particle tracking can be neglected, $\epsilon_{track} \approx 0$. The random displacement error can be conservatively assumed as $\epsilon_{\Delta x} = 0.1$ pixels, allowing the minimum resolvable displacement fluctuation (Raffel *et al.* (1998); Scarano and Riethmuller (2000)). The random error in velocity measurement can be estimated as $\epsilon_v \leq 0.004$ m/s for the constant frame rate of the recorded image sequence. The random error in velocity measurement changes with the frame rate on the image sequence and the minimum resolvable pixel in the image. Additional errors in the PIV measurements may arise due to the out of plane motion of the landslide mass. As the landslide spreads down the hill slope, the thickness

of the landslide decreases. The motion of the granular particles is downwards and outwards with reference to the plane of the hill slope. Over the measured range on the hill slope, the maximum change in the landslide thickness is approximately 0.15 m. The change in the vertical of the measured landslide surface with reference to the camera position is approximately 2%. Thus, errors due to out of plane motion of the granular landslide are neglected and the granular landslide surface is considered as a planar surface for the PIV analysis.

3.8.2 Uncertainty in landslide measurements

The maximum uncertainty in the experimental measurements of the landslide shape and velocity can be estimated with the errors estimates of the camera setup shown in Table 5. The error estimates are based on the camera image calibrations and scaling. Herein, the uncertainty in the measurements is quantified through the percentage of the maximum error observed in all the experimental trials. For the purpose of analysis, the measured quantities and the camera recordings that were used to measure those quantities are summarized in Table 6. The maximum relative error in the quantities

Table 6: Camera recordings that are used to measure the landslide parameters.

Parameter	Camera	Absolute Error	Units
Thickness, s	AW Cam	$\epsilon_x = 1.35$	[mm]
		$\epsilon_y = 1.35$	[mm]
Width, b	PIV Cam	$\epsilon_x = 1.8$	[mm]
		$\epsilon_y = 1.8$	[mm]
Front	PIV Cam	$\epsilon_x = 1.8$	[mm]
Displacement x_s		$\epsilon_y = 1.8$	[mm]
Δt	PIV Cam	$\epsilon_t = 0$	[s]

dependent on the above parameters does not exceed the sum of the relative individual errors (Demidovich and Maron (1987)). The error for a product of parameters is expressed as the sum of individual relative parameters. Hence, the maximum relative

error in the landslide front velocity cannot exceed

$$\left|\frac{\Delta v_s}{v_s}\right| \leq \left|\frac{\Delta x_s}{x_s}\right| + \left|\frac{\Delta t}{t}\right| \tag{30}$$

Similarly , the maximum error in the non dimensional landslide parameters can be obtained as

$$\begin{aligned} \left|\frac{\Delta F}{F}\right| &\leq \left|\frac{\Delta v_s}{v_s}\right| + \frac{1}{2}\left|\frac{\Delta h}{h}\right| \\ \left|\frac{\Delta S}{S}\right| &\leq \left|\frac{\Delta s}{s}\right| + \left|\frac{\Delta h}{h}\right| \\ \left|\frac{\Delta B}{B}\right| &\leq \left|\frac{\Delta b}{b}\right| + \left|\frac{\Delta h}{h}\right| \end{aligned} \tag{31}$$

Based on the absolute error estimates in Tables 5 and 6, the maximum uncertainty in the non-dimensional landslide parameters is estimated . The maximum uncertainty

Table 7: Maximum uncertainty in the experimental measurements of the nondimensional landslide parameters.

Nondimensional landslide parameter	Uncertainty [%]
F	3.8
S	4.1
B	1.8
V	5.0

in the individual dimensional parameters is estimated among all the measurements and the maximum is determined. The maximum uncertainty for the landslide front velocity, thickness and width is estimated as 3%, 2.4% and 0.15% respectively. The uncertainty in the measurement of the water depth in the tsunami wave basin is estimated as 1.7%, which is used in the uncertainty estimation of the non-dimensional parameters in Table 7. Since the landslide parameters are measured as functions of the propagation distance of the landslide, additional errors may arise in the estimation of the position of the landslide front from the recorded image sequences. The maximum uncertainty in the position of the front is estimated to be approximately 1.6% based on the maximum error in the incremental distance traveled by the landslide.

3.8.3 Experiment Repeatability

An estimation of accuracy of the test repetition within the experimental parameters was performed by repeating selected tests. In some experimental trials, the initial position of the landslide was changed by moving the landslide tsunami generator up or down the hill slope to change the landslide parameters at the impact. Since the slide box motion and the resulting landslide dynamics above the water surface before the impact are independent of the water depth in the wave basin, the experimental trials for different water depths but with the same pneumatic conditions can be used to estimate the repeatability in the measurements of the landslide shape and velocity from the recorded image sequences. The repeatability of the experimental trials for two different cases with 5 runs and 2 runs is shown in Table 8.

Table 8: Repeatability of the experiments. Measurements shown for two experimental runs with initial pneumatic pressure P =10, 8 bar. Δ is the maximum difference in the experimental trials.

parameter	dimension	run 1	run 2	run 3	run 4	run 5	Δ	run 1	run 2	Δ
h	[m]	0.6	0.58	0.6	0.6	0.59	0.02	0.6	0.6	0
v_s	[m/s]	5.33	5.33	5.29	5.32	5.28	0.05	4.77	4.8	0.03
s	[m]	-	-	0.215	0.217	0.224	0.009	0.19	0.19	3×10^{-4}
b	[m]	1.886	1.91	1.944	1.961	1.892	0.075	1.59	1.56	0.03
V_s	[m^3]	0.756	0.756	0.756	0.756	0.756	0	0.72	0.72	0

3.9 Experimental Methodology

3.9.1 Experimental Procedure

The procedure for an experimental run is summarized below:

- The wave basin is filled with water to the required water depth. The wave gauges are calibrated during the filling of the wave tank.
- The control parameters of the pneumatic LTG are set with the slide box in the retracted position.
- The slide box is filled with gravel from a storage bucket using an overhead crane.

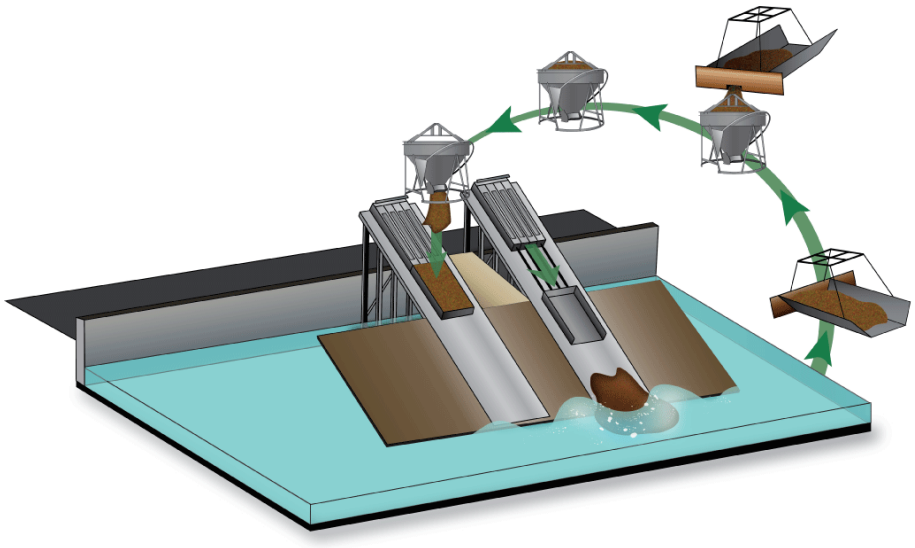

Figure 36: An experimental cycle of physical modeling of tsunamis generated by granular deformable landslides.

- The data acquisition system and the camera recordings are initiated.
- Then the pneumatic pistons of the landslide tsunami generator are fired.
- The initiation of the slide box motion activates a trigger mechanism that activates the data acquisition system to record the measurements from the cable extender transducers and the wave gauges and activates the PIV camera through the programmable timing unit.
- The slide material is accelerated in the box by means of the pneumatic pistons. The slide material is launched from the box while the slide box is pneumatically decelerated. Then the landslide forms a debris avalanche driven only by gravity and impacts with the water surface generating the tsunami waves.
- After the termination of the landslide and the wave measurements, the multi-transducer acoustic array surveys the underwater landslide deposit.
- The acoustic array is lowered such that the transducers are below the water surface and the bridge is steadily moved towards the hill slope to scan the

landslide deposit. Then the acoustic array is retracted back above the water surface.

- The granular slide settles mostly on a steel plate with three hinged flaps and is lifted by means of an overhead crane forming a recovery bucket. The material is then poured back in the storage bucket.

- Then the experimental parameters are varied and the slide box is filled with gravel for the next experimental trial.

The experimental cycle is shown in Fig. 36.

3.9.2 Range of non-dimensional parameters

A total of 65 experimental runs were conducted with varying landslide characteristics at varying water depths. The following parameters were varied over the various experimental runs.

- Initial landslide volume

- The initial pneumatic pressure of the landslide tsunami generator, varying the peak slide box velocity and the slide impact velocity

- Varying water depths to study generated wave characteristics in different water depth regimes.

The experimental parameters varied during the experimental program are shown in Table. 9.

Table 9: Experimental parameters varied during the program

Parameter	Parameter value			
Water Depth	0.3 m	0.6 m	0.9 m	1.2 m
Maximum Slide Box Velocity	4.0 m/s	3.23 m/s	2.76 m/s	2.33 m/s
Slide Volume	0.756 m^3	0.328 m^3		

The dimensional analysis resulted in nine independent and non-dimensional quantities that govern the tsunami wave generation by 3D deformable granular landslides. During the experimental runs, the landslide density and the hill slope angle are constant and are not included in the analysis. The non-dimensional wave propagation distance and the directional angle describe the wave propagation characteristics.

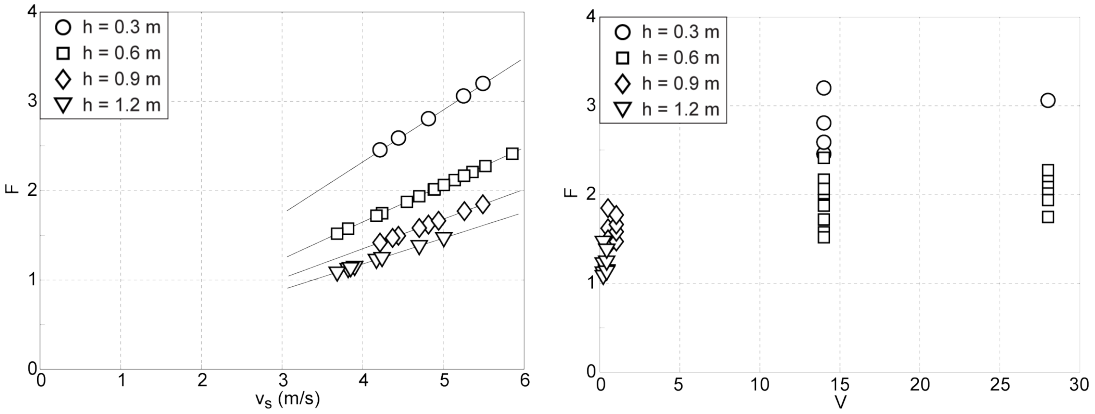

Figure 37: Range of non-dimensional parameters in experiment: (a) landslide Froude number $F = v_s/\sqrt{gh}$ dependency on the landslide impact velocity v_s and the water depth h; (b) landslide Froude number F versus the relative landslide volume $V = V_s/h^3$

The investigated quantities that govern tsunami wave generation are the landslide Froude number, the relative landslide thickness, relative landslide width at impact and the relative landslide volume. The landslide density and hill slope angle are constant during the experiment. The relative propagation distance, angular direction and relative time define a coordinate system for the landslide motion and wave propagation. The landslide Froude number is defined as $F = v_s/\sqrt{gh}$ and measures the landslide velocity v_s relative to the speed of shallow water wave propagation $\sqrt{gh}$. The bandwidth of the landslide Froude number, landslide impact velocities v_s and the water depth h that are investigated during the experimental study are shown in Fig. 37(a). Since $F \propto h^{-0.5}$, the effect of change in water depth is relatively weaker when compared with the effect of the landslide impact velocity. The range of F during the

experiments roughly spans between 1 and 4. The landslide impact velocity was in the range 3.8 m/s< v_s <6.5 m/s.

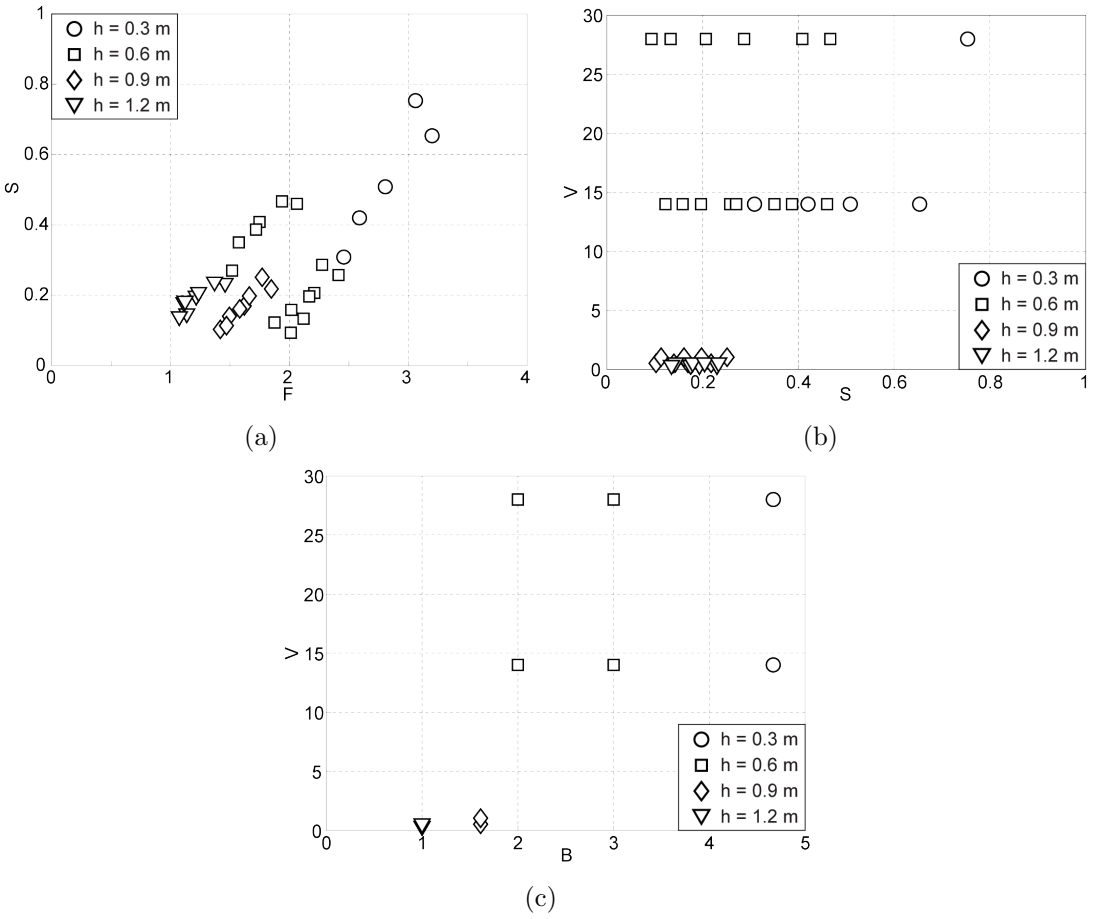

(a) (b) (c)

Figure 38: Range of non-dimensional parameters in experiment: (a) landslide Froude number F with respect to relative landslide thickness S, (b) relative landslide volume $V = V_s/h^3$ dependency on the relative slide thickness $S = s/h$ and (c) relative landslide width $B = b/h$ at impact.

To compare with the real world cases, the Lituya Bay case, for example had one of the highest recorded landslide Froude number of F = 3.2 determined with a water depth of h = 122 m and a landslide impact velocity of v_s = 110 m/s (Fritz *et al.* (2001)). While most landslide Froude numbers are in the range 1-3, higher Froude numbers can be modeled typically in very shallow water, where the generated wave heights are subject to scale effects. Typical submarine cases have Froude numbers $F < 1$. The relative landslide thickness versus the landslide Froude number is shown

in Fig. 38(a). The relative landslide thickness depends on the water depth, landslide motion and the drop height of the landslide on the incline which governs the landslide thickness s. The relative landslide thickness S in the experimental program varies roughly between $0.08 < S < 0.85$. The effect of relative landslide thickness weakens for $S > 0.6$ according to the block studies made by Kamphuis and Bowering (1970). The relative landslide volume versus the relative landslide thickness and the relative landslide width are shown in Figs. 38(b) and 38(c) respectively. The relative landslide volumes are in the range $0.25 < V < 28$. The relative landslide thickness varied from $0.08 < S < 0.85$ and the relative landslide width at the impact are in the range $1 < B < 4.6$.

CHAPTER IV

GRANULAR LANDSLIDE

4.1 Introduction

Tsunami wave generation by landslides is a complex phenomenon with the granulate material, water and air interacting with each other during the impact and wave generation process. Landslide studies are a challenging problem due to their complex dynamics and varying material composition from the initial landslide position on a mountain slope to the eventual submarine deposit. The study of historic landslide events provides a general understanding of the landslide behavior. The field case studies complemented with experimental studies provide a deeper understanding of the landslide characteristics and the general landslide dynamics. In this chapter, the granular landslide motion is studied as source characteristics for tsunami generation. The granular landslide motion is analyzed with reference to shape and kinematics to understand the wave generation process and the energy exchange between the landslide mass and the water body. The granular landslides are deployed using a novel pneumatic landslide tsunami generator in the three-dimensional tsunami wave basin. The landslides are modeled with naturally rounded river gravel with landslide volumes of 0.756 and 0.378 m^3. The landslide motion by the pneumatic landslide generator consists of 4 distinct phases.

1. Initial solid block motion when the granular material is in the LTG box.

2. The granular landslide collapse from the box and the subsequent gravity driven subaerial landslide motion on the ramp.

3. Landslide impact with the water surface and,

4. The subaqueous runout of the landslide mass.

The granular landslide is continuously monitored during these three phases to measure the landslide shape and kinematics. The landslide measurements are performed using an array of above water and underwater cameras, a high resolution PIV camera and a Multi-Transducer Acoustic Array (MTA). The description of the instrumentation and their deployment can be found in Chapter 3. The image sequences recorded during the experimental trials are used to measure the shape and motion of the landslide as the granular material launches from the slide box, accelerates down the hill slope, impacts the water surface and travels underwater. The acoustic array measurements provide the shape and runout distance of the landslide deposit. This chapter gives an overview of the granular landslide measurements in the experimental study.

4.2 Granular Landslide Description

4.2.1 Landslide Shape

The landslide shape is measured from the image sequences recorded by the above water side camera on the hill slope. The recorded images are calibrated by means of calibration boards. The model for calibrating and dewarping the images is based on a pin hole mapping model. The pin hole model was chosen since the calibration plate does not need to fill the entire field of view of the camera lens and the calibration can be extrapolated over the entire field of view. This model is based on the theorem of intersecting lines. The calibration parameters in the pin hole model accounts for translation lengths from the camera to the calibration plates and the rotational angle at which the cameras see the calibration plate (Hartley and Zissermann (2000)). During the calibration process, the images are corrected for barrel distortions and the scale factor relating the image pixels to the wave basin coordinates are obtained. The original raw image from the camera and the calibrated image are shown in Fig.

39.

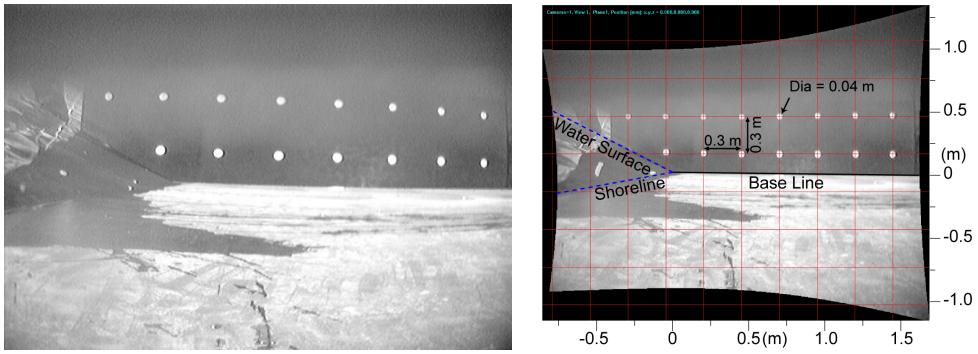

(a) (b)

Figure 39: (a) Raw image of the calibration board, (b) calibrated and scaled image.

The plane of the calibration board coincides with the plane of symmetry passing through the centerline of the landslide mass and the slide box. The base of the calibration board shown in Fig. 39(b) is used as the datum for measuring the landslide thickness on the hill slope. The intersection of the axis of symmetry with the shoreline is taken as reference for transforming the image coordinate system on to the hill slope coordinate system.

The image sequence recorded by the above-water side camera on the hill slope is shown in Fig. 40. The landslide motion is shown for two experimental trials with landslide mass $m_s = 1350,\ 675$ kg and volume $V_s = 0.756,\ 0.378$ m^3. The peak slide box velocity is $v_b = 3.8$ and 4.0 m/s due to the effect of the varying landslide mass during the initial acceleration phase. The landslide mass in both cases maintains the shape of the landslide box during the initial phase of the landslide tsunami generator box acceleration. At approximately the location of the peak box velocity, the landslide collapses out of the box and accelerates under the influence of inertia and gravity down the hill slope.

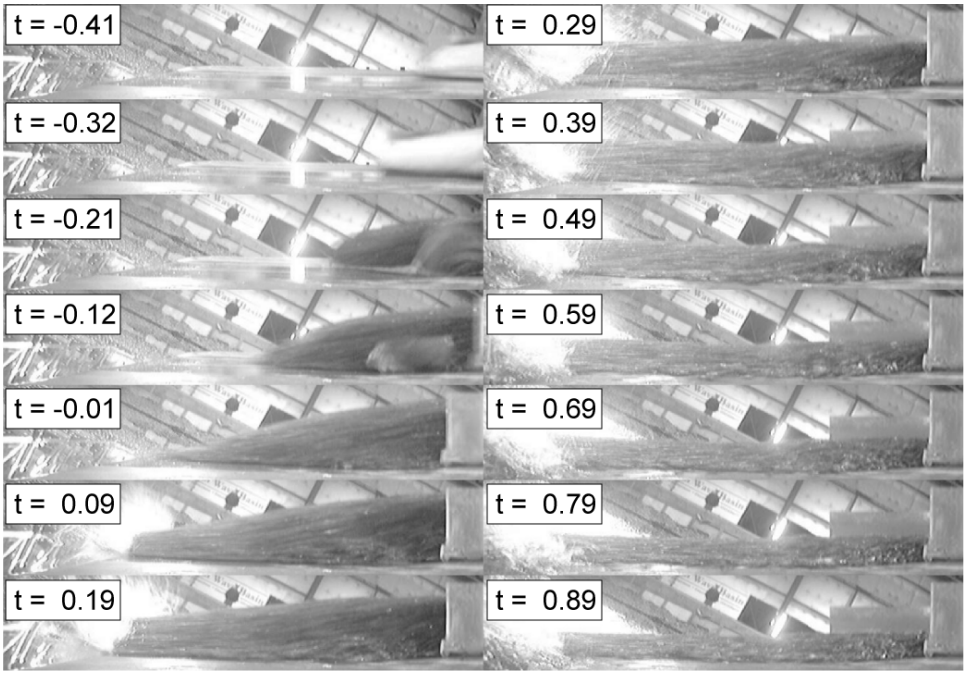

(a)

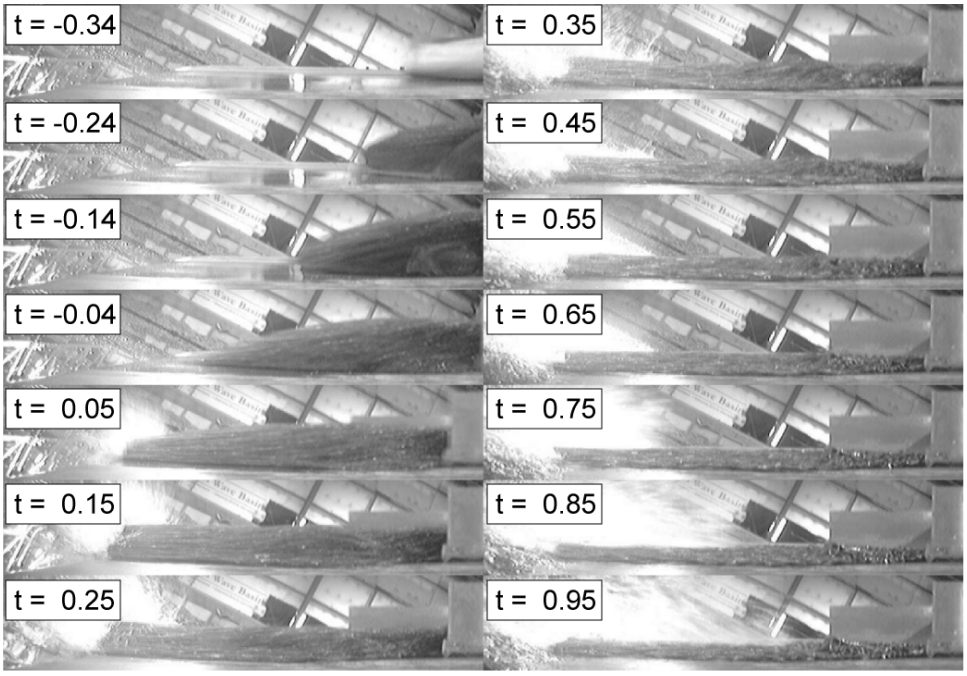

(b)

Figure 40: Image sequence on the hill slope for slide mass m_s of (a) 1350 kg and (b) 675 kg. $t = 0$ corresponds to the time of impact.

The landslide shape is measured at uniform cross-sections across the hill slope, shown in Fig. 41, above the water surface from the sequence of the recorded images. The number of sections where the shape is measured varies through the experimental trials and depends on the depth of the water in the TWB and the extent of the above-water hill slope area available in the image frame. A sample measurement is shown in Fig. 41 for $h = 0.6$ m, $m_s = 1350$ kg and $v_b = 3.9$ m/s.

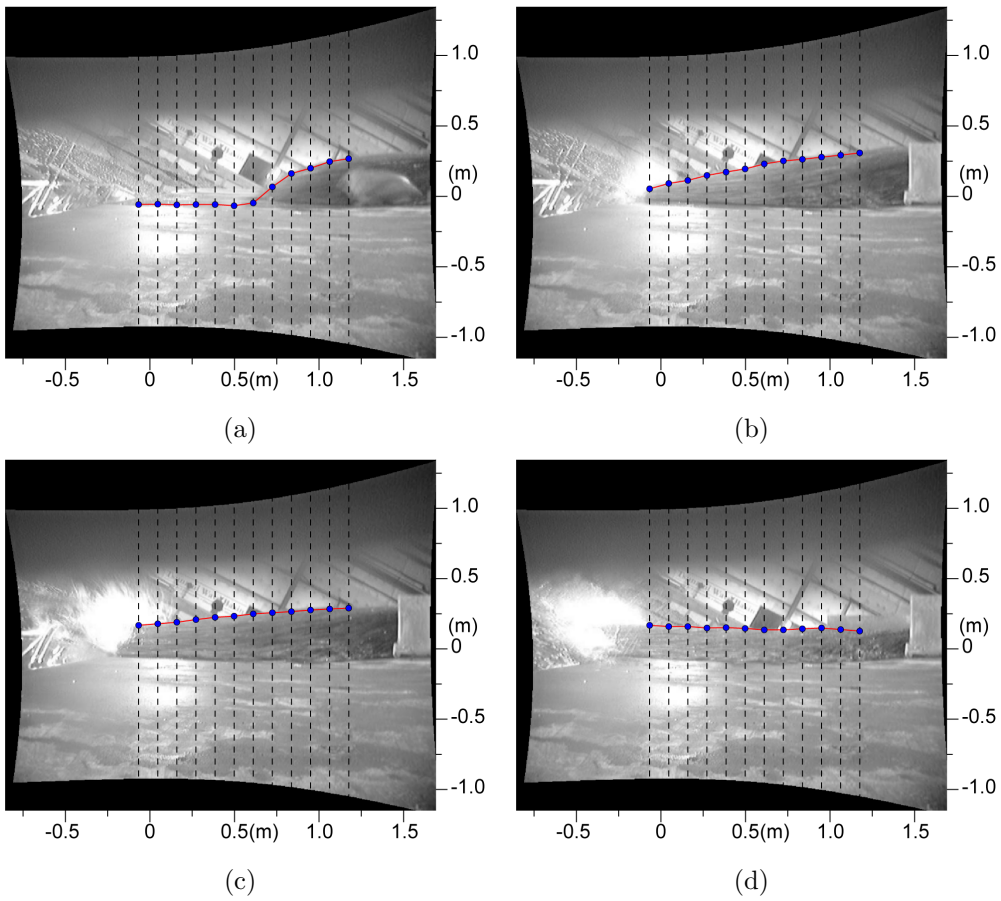

Figure 41: Above-water camera images shown with collected data points at $t =$ (a) -0.15 s, (b) 0.05 s, (c) 0.19 s and (d) 0.52 s. $t = 0$ corresponds to time of landslide impact at water surface.

The thickness measurements are made for all the experimental trials with varying water depths, landslide mass and pneumatic slide acceleration. The measured data from different experimental trials with the same landslide mass and pneumatic

landslide tsunami generator pressure characteristics are combined together by transforming the coordinate system to the static slide box coordinate system. This is possible since the slide box motion is independent of the water depth.

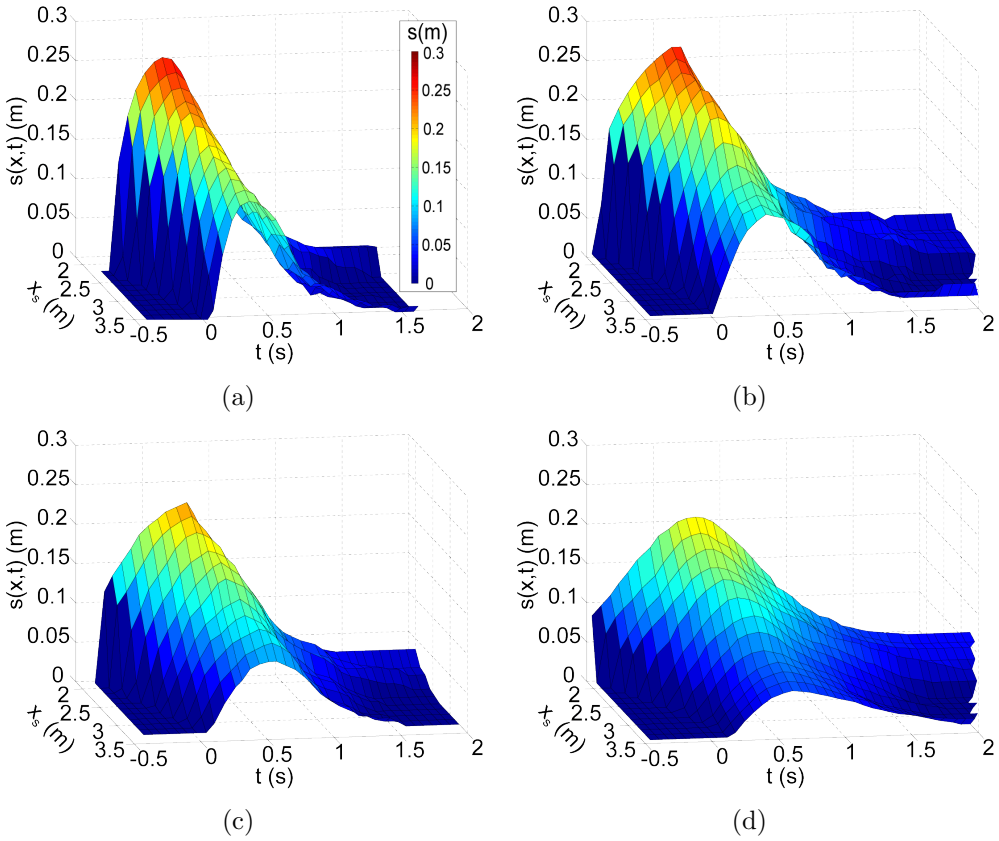

Figure 42: Landslide shape evolution along the hill slope, $s(x_s, t)$ for landslide mass $m_s = 1350$ kg, volume $V_s = 0.756$ m^3 shown for the pneumatic acceleration cases corresponding to landslide box velocity v_b of (a) 3.7 m/s, (b) 3.2 m/s, (c) 2.8 m/s, and (d) 2.3 m/s.

The landslide profile is obtained as a function of time and space above the water surface. The evolution of the measured landslide shape in space and time is shown in Fig. 42 for landslide mass $m_s = 1350$ kg and landslide release velocity $v_b = 3.7$, 3.2, 2.8 and 2.3 m/s. The direction of the landslide motion is along the x_s-axis on the ramp. These measurements are obtained for the cases where the water depth is at $h = 0.6$ m. Along the x_s-axis, $x_s = 0$ correspond to the initial static position of the landslide tsunami generator box. At the specified water depth, the shoreline position on the ramp is at $x_s = 3.356$ m. The time of the landslide motion is shown on the y-axis in the figure. The time axis is referenced to the time of landslide impact with the water surface ($t = 0$). The landslide shape $s(x_s, t)$ is shown on the z-axis of the figure. The initial landslide thickness at rest position is equal to the landslide tsunami generator box thickness, 0.3 m. The landslide profile has a characteristic shape of a relatively steep face leading to a peak thickness and a gradual decay in the thickness towards the tail of the landslide. As the landslide propagates down the hill slope, the unconfined spreading of the landslide in the longitudinal and lateral direction results in a decay in the peak of the landslide profile in the down slope direction along with a decrease in the steepness of the landslide front. Simultaneously, the peak of the profile shifts forward in time and the extent to which the bulk mass spreads increases down the hill slope, as seen in Figs. 42 and 43.

The evolution of the landslide shape along the hill slope in space and time for landslide mass, $m_s = 675$ kg is shown in Fig. 43. The landslide profile shape in the case of half the original volume, shown in Fig. 42 is similar to the characteristic shape seen in Fig. 43. The effect of the landslide mass can be seen in the variations in the decay rate of the profile peak and the rate of spreading of the granular landslide mass. For the same distances and time traveled, the lower landslide volume has a decreased profile peak and extent of the bulk landslide material. The extent of landslide spreading also depends on the mass flux of the granular material. Comparing

the landslide profiles in Figs. 42(a) and 43(a), the reduction in the granular source material for the landslide collapse results in a compact landslide profile. This behavior can be seen across all the pneumatic acceleration cases. For the cases with the same amount of the granular landslide material, a decrease in pneumatic acceleration results in lower rates of mass and momentum flux of the landslide along the hill slope. Thus as the initial acceleration of the landslide mass decreases, the profile peak decreases at the same location and time.

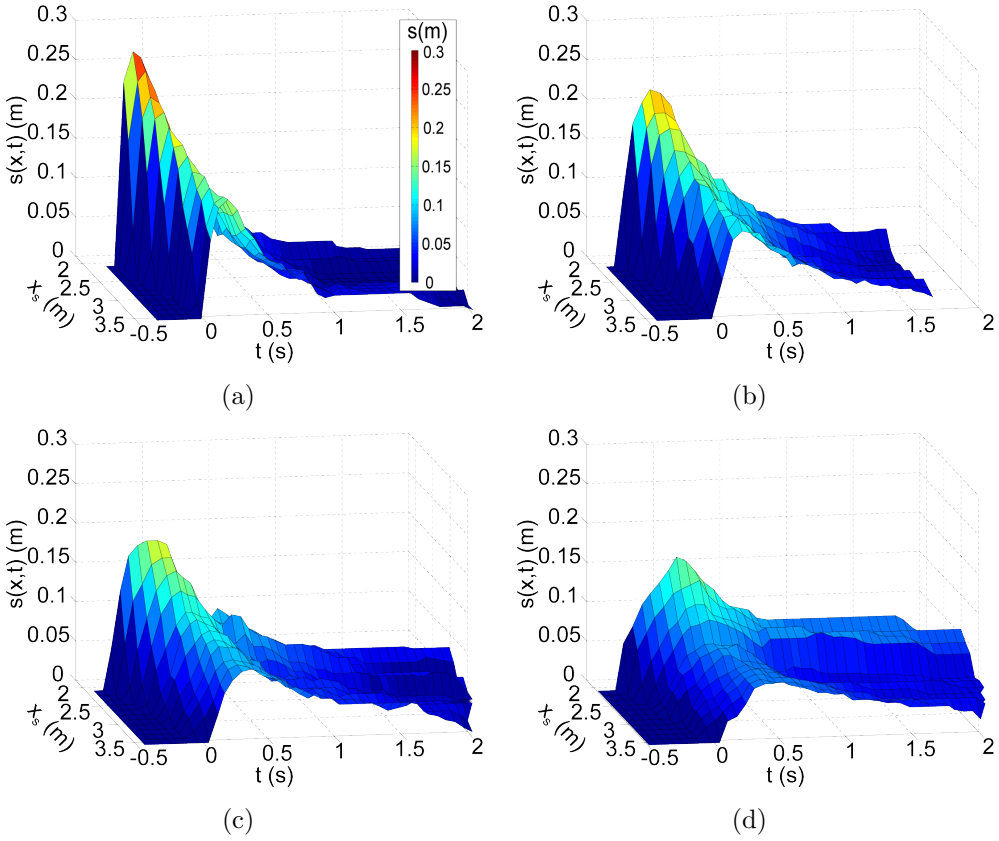

Figure 43: Landslide shape evolution along the hill slope, $s(x_s, t)$ for landslide mass $m_s = 675$ kg, volume $V_s = 0.378$ m^3 shown for the pneumatic acceleration cases corresponding to landslide box velocity v_b of (a) 4.0 m/s, (b) 3.2 m/s, (c) 2.7 m/s, and (d) 2.2 m/s.

The maximum landslide thickness is obtained from the measured landslide shape, $s(x_s, t)$, across the sections on the hill slope. The combination of the data from various experimental trials gives the evolution of the maximum landslide thickness across the hill slope above the water surface and gives the maximum slide thickness at impact for the various experimental trials. The maximum landslide thickness at impact is instrumental in predicting the characteristics of the generated tsunami waves as shown in Chapter 3. The evolution of the maximum landslide thickness for the total eight combinations of landslide launch velocity and mass is shown in Fig. 44. The coordinate system is independent of the water depth and is referenced to the static initial position of the landslide tsunami generator box, $x_s = 0$. Depending on the water depth of a particular experimental trial, the maximum slide thickness at any location on the hill slope in the measured range can be obtained and used in parameterizing the tsunami wave characteristics in terms of the landslide thickness as source characteristics.

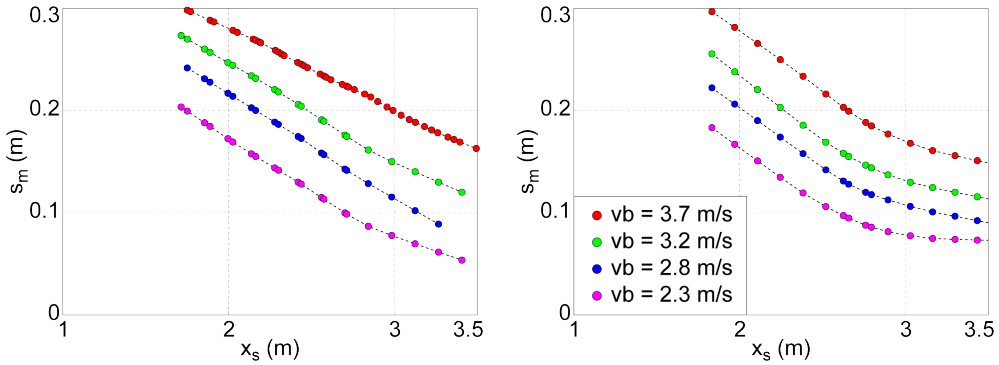

(a) (b)

Figure 44: Maximum landslide thickness, s_m, shown as a function of x_s on the hill slope for landslide mass m_s = (a) 1350 kg and (b) 675 kg.

The initial maximum landslide thickness is 0.3 m. The collapse of the granular material from this initial box shape varies with the mass of the landslide and the initial pneumatic acceleration. The location of the collapse is further down the slope with increasing pneumatic accelerations and landslide mass. At high speeds, the

granular material transformation is less per distance traveled. After the collapse, the rate of decay of the landslide profile depends on the extent of the landslide spreading, which is controlled by the rates of mass and momentum flux of the granular material in the direction of motion. Hence, lower volumes of the granular material tends to a rapid spreading and a higher decay rate of the landslide profile.

4.2.2 Landslide Width

The collapse of the granular landslide from the box is followed by the unconfined landslide motion under the influence of inertia and gravity. On plane hill slopes, such as in the present experiment, the downward motion of the landslide is accompanied by an unconfined lateral spreading of the landslide. The lateral width of the landslide has an influence on the width of the water displacement area or crater at the impact of the granular landslide on the water surface. The width also determines the rate of mass, momentum and energy flux of the landslide, while the rate of lateral spreading effects the speed and shape of the landslide, which is a direct consequence of the mass conservation principles. The width of the landslide affects the radial spreading of the generated tsunami wave and influences the radial decay function of the tsunami wave amplitudes, as shown in the non-dimensional analysis of the experimental parameters in Chapter 3. Hence it is important to quantify the lateral landslide spreading in terms of the evolution of the landslide width in space and time.

The landslide width is measured from the image sequence recorded by the PIV camera. A combination of time stacking and image filtering is applied to segment the image and extract the granular landslide intensities from the hill slope background. The segmentation methodology is shown in Fig. 45. The intensity of the image sequence is initially subtracted from the original background image. This results in images where the areas of the granular landslides are emphasized by high density of intensity values.

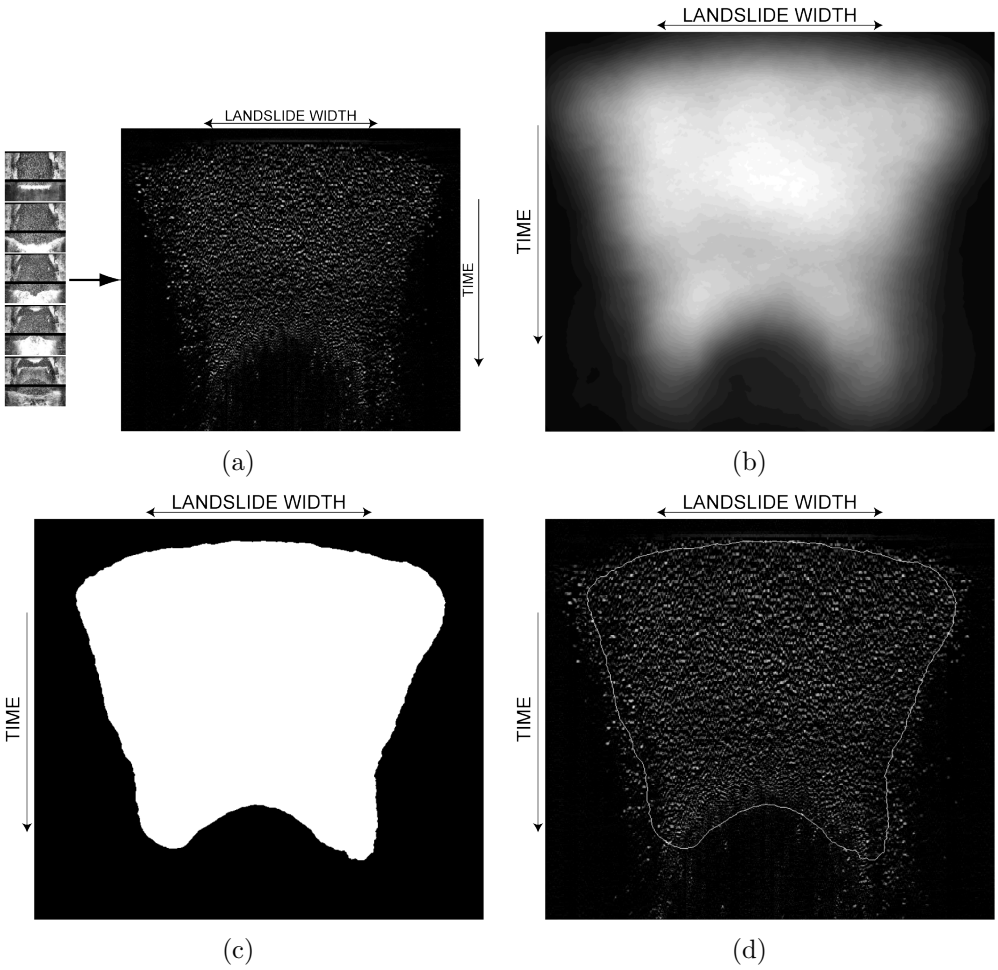

Figure 45: Image segmentation algorithm: (a) image time stacking, (b) filtering the time stacked image, (c) grayscale to binary conversion and (d) time stacked image with extracted edge.

A series of rows at a fixed location from the image sequence are time stacked to create an image where the rows represent the time coordinate (Fig. 45(a)). The time stacked image is filtered using a disc filter with radius 30 pixels to equalize the image intensities in the granular region and sharpen the areas of high intensity gradients (Fig. 45(b)). This is followed by converting the image from grayscale intensities to a binary image by applying a threshold to the grayscale intensities of the time stacked image (Fig. 45(c)). From the binary image, the edge of the landslide area is extracted (white line shown in Fig. 45(d)). The difference between the edges in the longitudinal direction leads to the width of the landslide. This gives the width of the landslide as

a function of time at the specified locations along the hill slope.

The automated time stacking technique works for cases where the recorded images have low noise levels in the background or in cases where the landslide moves relatively fast. In a few cases, due to the effects of ambient lights, the static background was inseparable from the landslide mass. Hence, in those cases, a stronger filter was required to suppress the background noise and highlight the landslide material. This technique is limited to the cases where the extracted landslide width is calibrated with the images, and the maximum landslide width compared with the maximum width measured manually from the maximum extent cases.

The maximum extent of the landslide spreading is measured by using the same series of images. The maximum width of the landslide with x_s on the ramp is measured from the mean of the image sequence. The mean image is such that the areas of the ramp with no granular mass remains unchanged. Then the mean intensity of the granular mass is identified in the mean image and is separated from the background intensities of the hill slope. This leads to the maximum extent of the landslide spread. The image showing the mean of the image sequence intensities is shown in Fig. 46. By averaging the intensities of the image sequence, any effects relating to ambient light, noise in the image background, detached spread of the granular material and high intensities of the splash near the water line are eliminated.

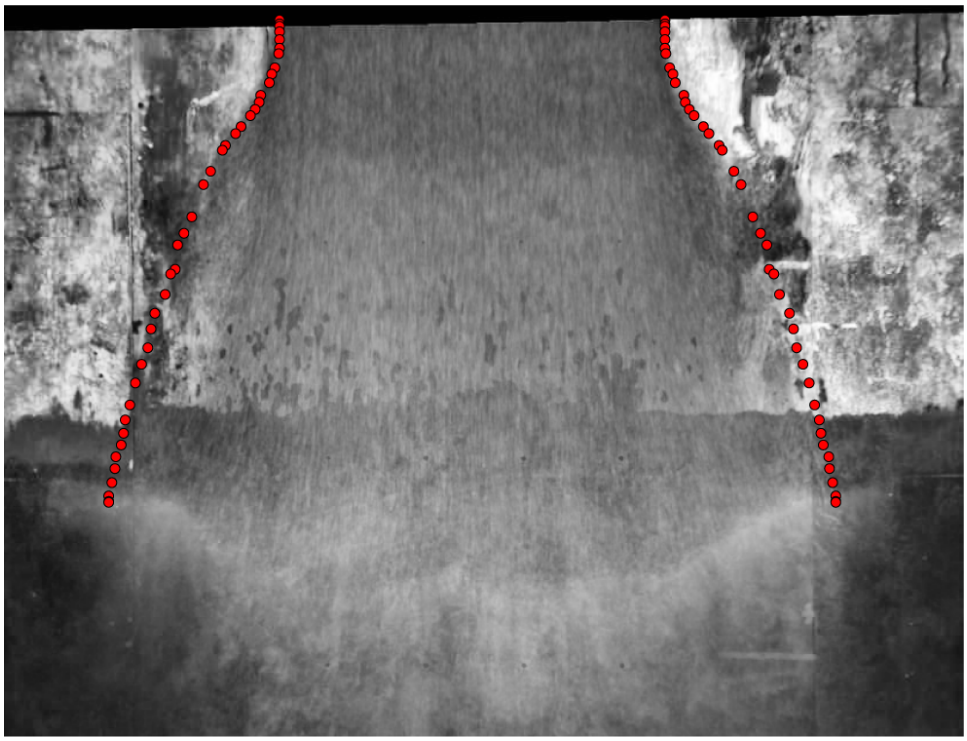

Figure 46: Image showing the mean intensities of the image sequence for m_s=1350 kg and $v_b = 3.7$ m/s.

The measured landslide width behavior is found to be very similar across the range of the conducted experimental trials. Within the experimental range, relatively minor variations are observed in the evolution of the maximum landslide width on the ramp. The landslide width measured from the automated image segmentation technique for the experimental trial with landslide mass $m_s = 1350$ kg, water depth $h = 0.6$ m and landslide release velocity $v_b = 3.7$ m/s is shown in Fig. 47.

After the granular landslide exits the box, it spreads rapidly to reach the maximum width. At this point the main tsunamigenic bulk of the landslide mass travels down the hill slope and impacts the water surface. After the landslide width reaches its maximum, the width gradually decreases until all of the granular material exits the box and travels down the ramp. Figure 47(a) shows the measured landslide width as a function of time at five different locations across the hill slope. For reference, the water line in this case is at $x_s = 3.365$ m. Across the different sections, the behavior

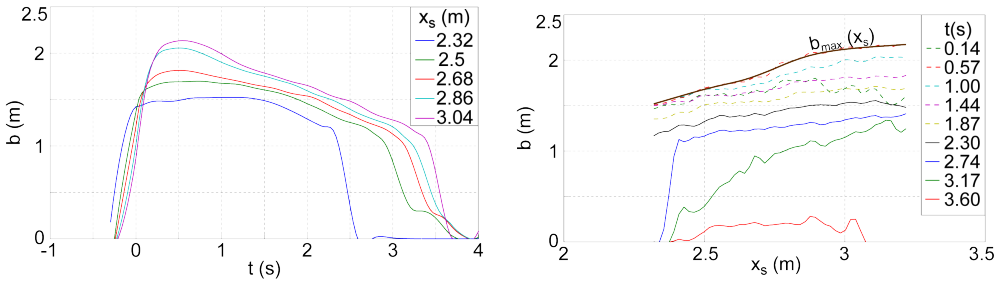

(a) (b)

Figure 47: Measured landslide width $b(x_s, t)$ at $m_s = 1350$ kg, $h = 0.6$ m, $v_b = 3.7$ m/s, (a) along hill slope x_s as function of time and (b) at different times as function of x_s, distance traveled on the hill slope.

of $b(x, t)$ is similar. The rate at which the landslide collapses to reach the maximum width is approximately the same at the shown locations. However, the maximum width that the landslide spreads to, differs, depending on the distance traveled by the landslide on the hill slope. The rate of decay of the width, post peak, is also similar across the sections. The maximum landslide width gradually increases along the hill slope, as shown in Fig. 47(b). The landslide width is shown at different times as a function of the hill slope coordinate, x_s. The maximum width is shown as a smoothed thick line in the figure (The width of the box is 1.2 m).

By using the averaging technique to obtain the maximum extent of the landslide spreading, the maximum landslide width along the hill slope for all the experimental trials were obtained. By combining experimental data collected from the experimental trials with identical pneumatic landslide tsunami generator conditions, the entire spread of the evolution of the maximum width was obtained. The maximum measured landslide extent is shown in Fig. 48.

4.3 Granular Landslide Motion

The studies of historic landslide events in field cases have led to the observation that landslides behave in a near fluid like manner with high mobility and long runouts (Heim (1932), Hsü (1975), Shreve (1966) and Shreve (1968)). The high fluidity has

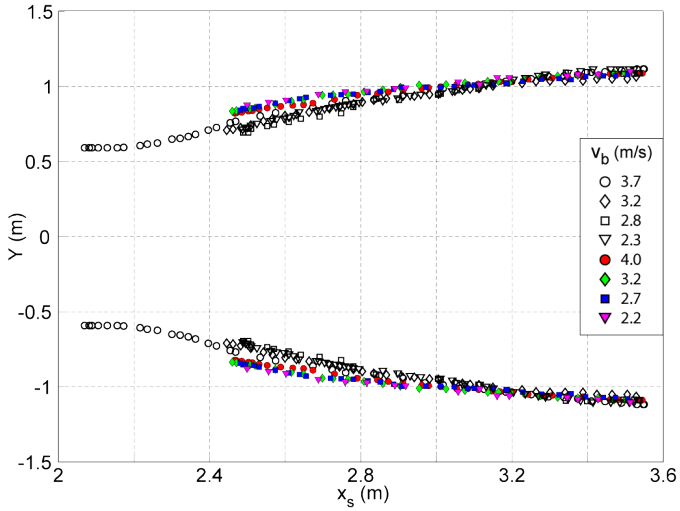

Figure 48: Edge of granular landslide spreading along the hill slope. $x_s = 3.365$ m correspond to the water line. The hollow symbols indicate experimental trials with slide mass $m_s = 1350$ kg and filled symbols, $m_s = 675$ kg.

been explained by several hypotheses such as upward flow of air, hovercraft action, generation of high pressure steam, lubrication by molten rock and formation of a thin rapidly shearing layer of fluctuating particles (Erismann (1986), Goguel (1978), Hsü (1975), Kent (1966), Shreve (1968)). The essence of all these hypotheses is the presence of a thin layer close to the basal surface upon which the landslide material slides under the influence of gravity and inertia. Melosh (1986) suggested the presence of a thin basal layer close to the sliding surface where all the shearing takes place. Hence the depth-averaged streamwise velocity is close to the actual velocity measured everywhere across the depth of the landslide except in the basal layer.

The kinematics of the granular landslide motion are quantified by measuring the velocity distribution on the visible surface of the granular landslide and the velocity of the front of the landslide. The knowledge of the surface velocity distribution will enable computation of mass and momentum flux of the granular landslide on the hill slope, when the landslide shape distributions are known. The surface velocity measured by the PIV analysis may be considered as the depth averaged streamwise velocity of the granular landslide mass. Ideally, the landslide centroid velocity is used

to describe the nature of the bulk motion of the landslide mass. However, due to the large volume and the unconfined three dimensional spreading of the granular material in the experimental trials, it was not possible to measure the landslide centroid velocities exactly. As an alternative, the landslide front velocity was measured and it was shown in Chapter 3 to be one of the parameters that effect the tsunami wave generation and wave height.

The Particle Image Velocimetry (PIV) setup is used to measure the granular landslide surface velocity distribution during the experimental process above the water surface on the hill slope. The unsteady landslide-water body coupled flow complicated the image analysis and the vector field calculation. The landslide flow field is isolated from the hill slope background image and the fluid phase with digital masks (Roth *et al.* (1999), Lindken and Merzkirch (2000)). The masking is done to avoid biased correlation signals caused by total reflections and light scattering of floating seeding particles and air bubbles during the impact. The cross-correlation analysis is conducted using a commercial analysis software (LaVision, DaVis PIV package). The advanced digital interrogation method successfully combines several techniques: digital PIV (Willert and Gharib (1991)), cross-correlation analysis (Keane and Adrian (1992)), discrete window offset (Westerweel *et al.* (1997)), fractional window offset (Scarano and Riethmuller (2000)), iterative multi-grid processing with window refinement (Hart (1998); Scarano and Riethmuller (1999)) and window distortion (Huang *et al.* (1993a), Huang *et al.* (1993b); Fincham and Delerce (2000)). The adaptive multi-pass algorithm initially calculates a reference vector field from the double image input. A standard cross-correlation interrogation is then performed with a relatively large interrogation window size (128X128 pixels) and a mean initial window shift.

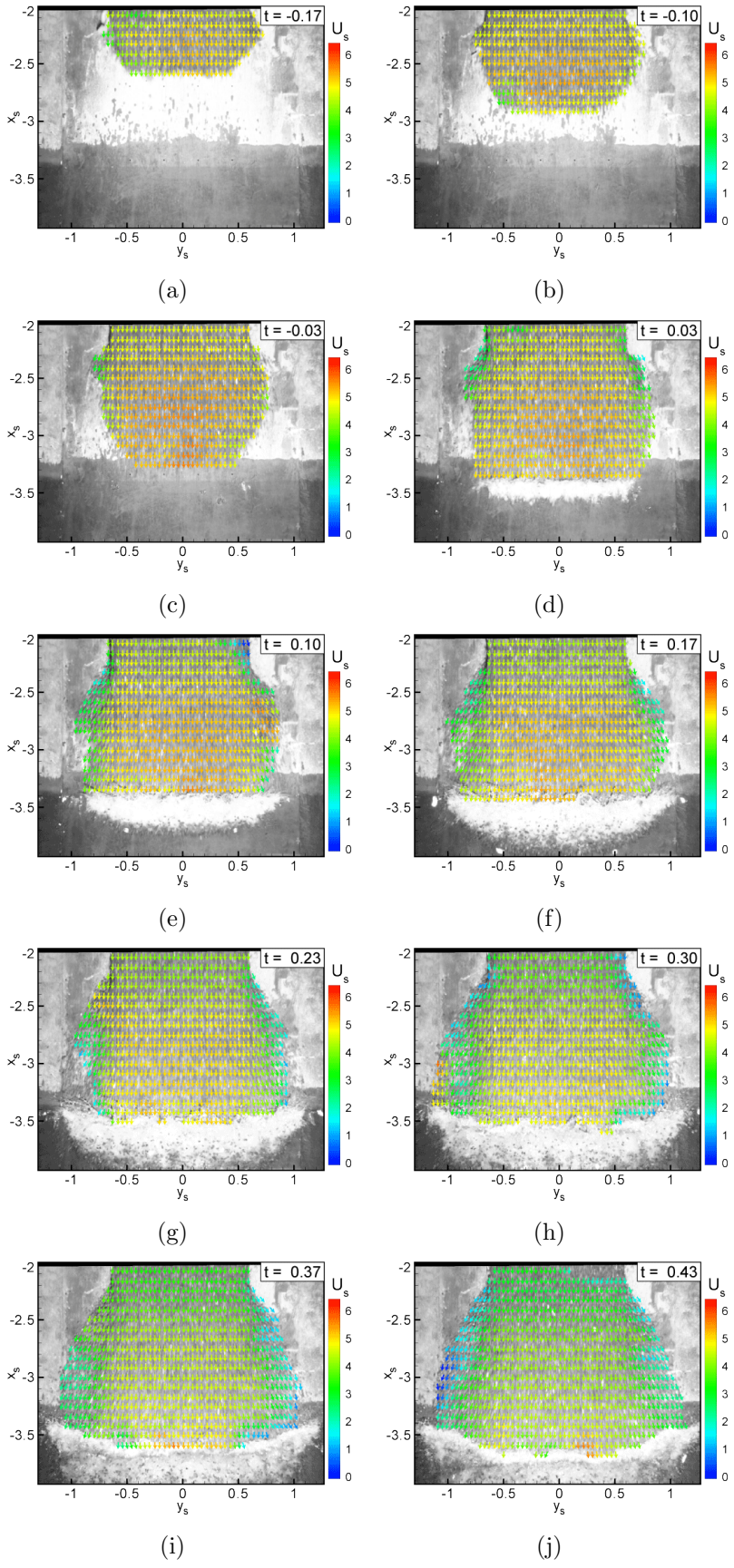

Figure 49: PIV velocity vectors sequence for $m_s = 1350$ kg, $h = 0.6$ m and landslide release velocity $v_b = 3.7$ m/s.

The calculated velocity vector field serves as initial displacement for the multi-pass cross-correlation algorithm to predict the velocity for the next iteration. This velocity prediction determines the window shift for the next higher resolution level with a refined interrogation window size. The iteration is repeated until the final window size (32X32 pixels) is reached. The PIV based correlation analysis is performed on image sequences recorded for the four different pneumatic acceleration cases for the landslide mass of $m_s = 1350$ kg. The analysis is limited to the cases where the image recordings yielded adequate speckled patterns on the surface of the granular landslide. This was essential to perform an accurate spatial correlation analysis and identify the peaks in the correlation plane. In some cases, external lights and unavoidable light reflections caused interference with the granular surface. This resulted in noise contamination over the speckled pattern and poor correlation during the PIV analysis. The measured PIV velocity sequence for the experimental trial with slide mass $m_s = 1350$ kg, water depth $h = 0.6$ m and landslide release velocity $v_b = 3.7$ m/s. is shown in Fig. 49.

The velocity magnitude distribution across the landslide width is extracted across hill slope sections from the PIV velocity distribution shown in Fig. 49. The velocity distributions across sections at $x_s = 2.5$ and 3.0 m are shown in Fig. 50 at different times as the landslide propagates down the hill slope and impacts the water surface. The time of motion has been adjusted such that $t = 0$ corresponds to the time of landslide impact with the water surface.

The velocity magnitude is non-zero over the landslide surface and zero everywhere as seen in the figure. This is a result of using digital masks to isolate the granular material from the background. The velocity magnitude profile may be related to the landslide shape profile with the assumption of Melosh (1986). Since the bulk of the granular mass is present in the central region of the landslide, the velocity tends to be higher there and decreases steadily towards the edge of the landslide. Then the velocity instantly drops to zero in the masked region where any granular mass is

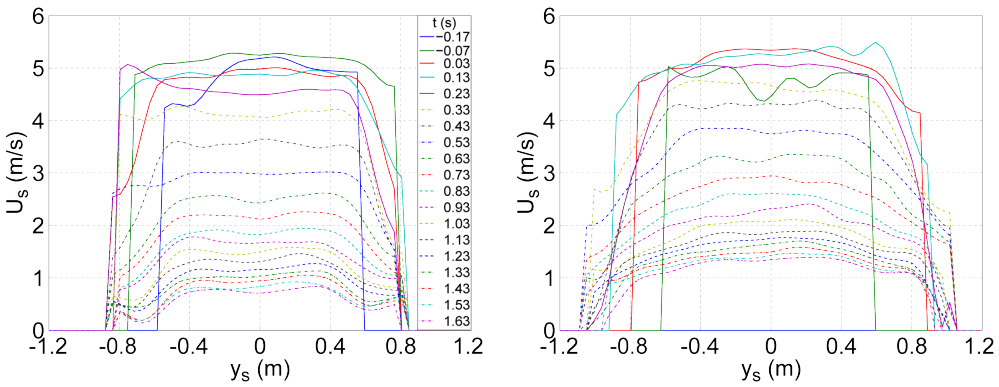

Figure 50: Streamwise velcoity distribution across the landslide width at x_s = (a) 2.5 m and (b) 3.0 m.

absent. The velocity tends to be uniform across the landslide width except close to the edge where a decrease in the thickness of the granular material towards the end leads to reduced velocity of the landslide motion. From the inception of the landslide motion, the velocity magnitude tends to increase towards a peak velocity until the time where the bulk tsunamigenic mass travels down the hill at a particular section, and then the velocity gradually decreases until the landslide motion comes to rest. The landslide velocity increases down the hill slope due to the build up of momentum as the landslide travels down the hill slope.

The initial acceleration of the landslide block and the location of the block collapse and transformation into a granular landslide affects the landslide shape distribution, mass, momentum and energy flux rates as the landslide propagates over the hill slope. This consequently affects the characteristics of the generated tsunami waves. The velocity distribution on the landslide surface is shown in Fig. 51 for $m_s = 1350$ kg, for landslide release velocities $v_b = 3.7$, 3.2, 2.8 and 2.3 m/s. For these four cases, the times of impact from the inception of slide box motion are at 0.9, 0.93, 1.07 and 1.12 s.

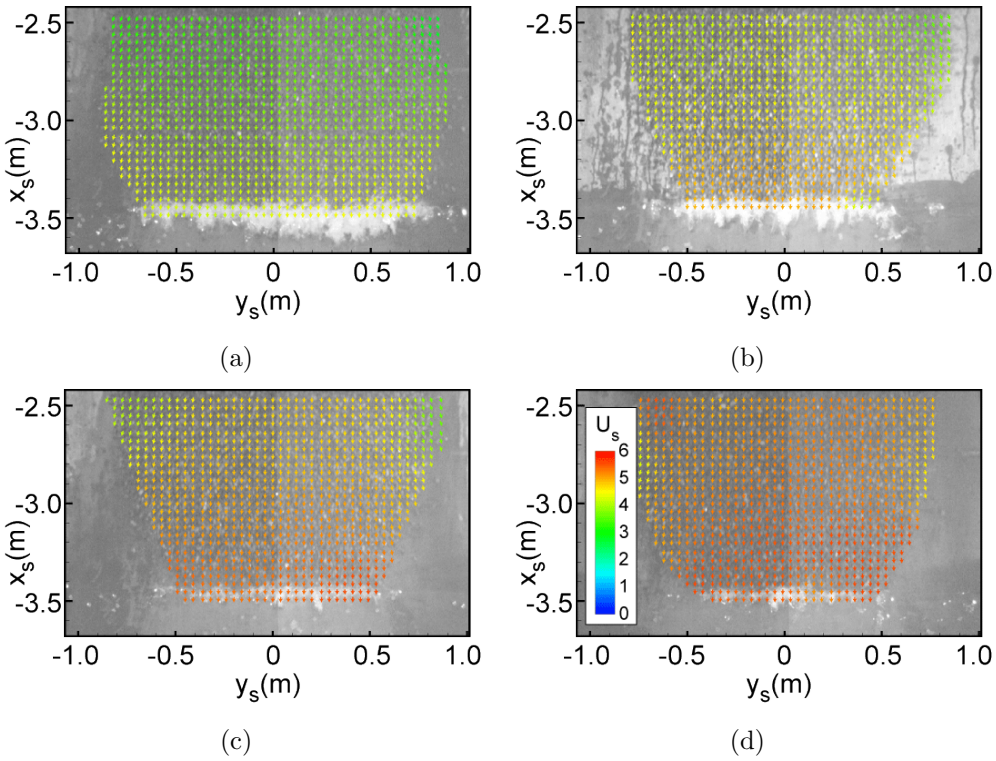

Figure 51: Landslide surface velocity distribution at impact, $m_s = 1350\ kg$, landslide release velocity, v_b = (a) 3.7 m/s, (b) 3.2 m/s, (c) 2.8 m/s and (d) 2.3 m/s.

The granular material experiences positive streamwise velocity gradients as the landslide gradually accelerates down the hill slope. These velocity gradients influence the rate of material spreading down the hill slope. The low acceleration of the case seen in Fig. 51(a) leads to a larger spread down the hill slope with low impact velocity at the water surface. The large spread and low velocity of the front results in small slide thickness from continuity principles, which can also be seen in Fig. 44(a). As the landslide front velocity increases, depending on the initial accelerations, at the same location, the lateral front spread decreases and the front velocity increases which leads to an increase in the slide thickness at impact. The changes in velocity and lateral spread from the initial acceleration can also be seen in Fig. 52 at $x_s = 2.5$ and 3.2 m.

The above observations are also seen in the Savage-Hutter avalanche model for granular flows (Savage and Hutter (1989), Savage and Hutter (1991)). The positive streamwise gradients cause the landslide mass to experience passive earth pressure

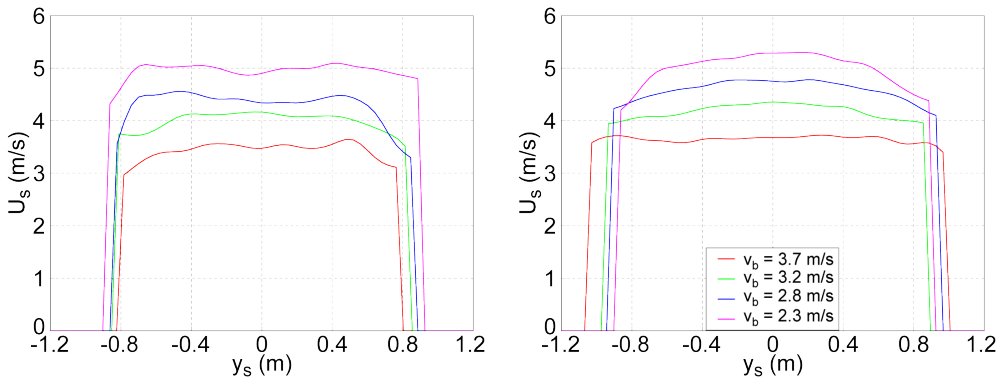

(a) (b)

Figure 52: PIV velocity distribution across the landslide width shown for 4 pneumatic LTG cases at x_s = (a) 2.5 m and (b) 3.2 m, where impact is at x_s=3.356 m.

coefficients. In this state, the landslide material undergoes elongation parallel to the slope bed which leads to unconfined lateral and longitudinal spreading of the granular material. However, the rate at which the material spreads depends on the velocity gradients that develop in the landslide mass as it accelerates down the hill slope.

The landslide front velocity is measured from the combined images of the above water side camera and the PIV camera. The measured data from different experimental trials with the same landslide release velocities, produced by the same initial pneumatic accelerations and landslide mass, are combined to obtain a complete evolution of the slide velocity from rest to impact The granular material exits from the box during the beginning of the pneumatic deceleration phase. The slide transformation from solid block motion to granular motion approximately occurs at the peak velocity position of the slide box. Until this location, the granular slide front velocity is the slide box velocity which is measured from the stringpot data. The landslide release velocity is taken as the maximum landslide box velocity. After this, the measurements from the images provide the landslide front velocity until the impact at the shoreline. The measured landslide velocity from rest to impact for all the control conditions of the pneumatic landslide tsunami generator is shown in Fig. 53.

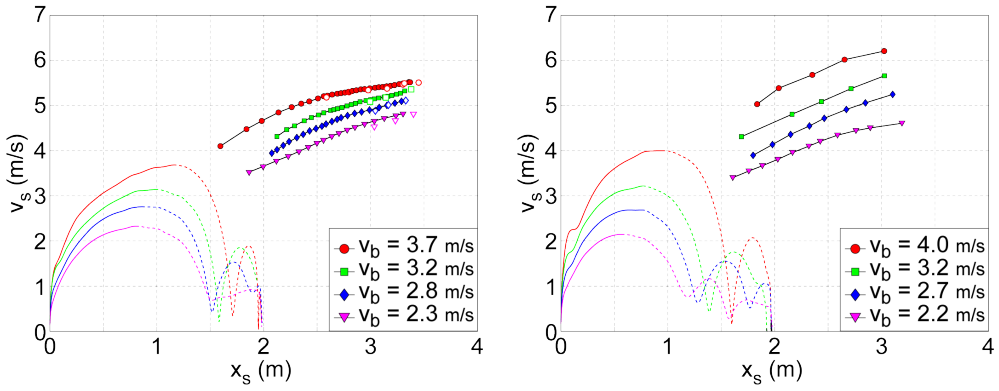

(a) (b)

Figure 53: Landslide front velocity as function of propagation distance on the hill slope shown for landslide mass m_s = (a) 1350 kg and (b) 675 kg.

The landslide front velocity obtained from the PIV measurements for the experimental cases of $m_s = 1350$ kg are shown as hollow symbols in Fig. 53(a). The front velocity extracted from the PIV velocity vectors match with the measured front velocity from the image sequences with a 3% deviation between the two methods. The measured landslide front velocity was found to depend on the landslide mass and volume, the landslide release velocity and the location of the release of the granular material into a gravity driven landslide, for the same granular material and hill slope. The release velocity for landslide volume of 0.756 m^3 ranged from 2.3 m/s to 3.7 m/s and for volume of 0.378 m^3, it ranged from 2.2 m/s to 4.0 m/s. This variation results in a range of landslide front velocity depending on the distance traveled by the landslide. For example, in an experimental trial at a water depth of 0.6 m, the water surface in terms of the hill slope coordinates rests at $x_s = 3.357$ m. At this location the landslide front velocity varies from 4.6 m/s to 6.1 m/s across all the pneumatic cases and for a drop height of 1.6 m. The corresponding landslide front Froude number, $F = v_s/(gh)^{1/2}$ varies from $1 - 4$. Depending on the depth of water and the location of the water surface, the landslide front velocity can be extracted from Fig. 53 for all the pneumatic cases in the study. The measured landslide front velocity serves as one of the parameters that influence the tsunami wave generation

and the tsunami wave amplitudes.

4.4 Landslide Deposits

The landslide deposits are measured at the end of each experimental trial to provide an understanding of the landslide dynamics after the impact under water. The underwater measurements aim at developing an understanding on the shape of the landslide deposits and how the runout of the granular landslide is affected by the intial landslide acceleration, velocity of impact at water surface, depth of water and the water medium. The landslide deposits were measured with a multi-transducer acoustic array (MTA) mounted on the bridge in the tsunami wave basin. After the wave gauge measurements were made, the acoustic array mounted on the bridge is lowered under the water surface so as to wet the transducers. Then the bridge was gently moved towards the hill slope so that the acoustic array sweeps over the landslide deposit. The further working principle of the acoustic array is provided in Chapter 3.

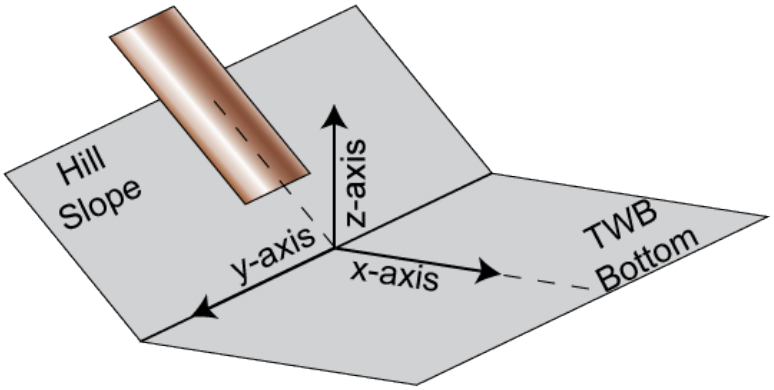

Figure 54: Coordinate axis description for the MTA measurements.

The coordinate system for the acoustic array measurements is shown in Fig. 54. The origin of the coordinate system is the intersection of the mid-longitudinal line of the tsunami wave basin with the bottom of the hill slope on the wave basin. The x_d-axis is positive away from the hill slope, the z_d-axis is zero on the wave basin bottom

and positive in the upwards direction from the wave basin bottom. The y_d-axis is centered on the mid point of the acoustic array.

While the acoustic array measures 2.56 m, the maximum width of the landslide deposits exceeds the width of the multi-transducer acoustic array mount. The acoustic transducers have to be constantly under water for the measurements to be possible. Hence this limits the longitudinal extent of the acoustic array operation. This results in the discontinuous data on the lateral edges and tail of the landslide deposit. The pneumatic landslide tsunami generator aids the landslide granular material in reaching high accelerations over short distances on the hill slope. After the landslide material exits the box and accelerates down the hill slope, it spreads rapidly in the longitudinal and the transverse direction. The landslide impacts with the water surface and deforms. As the landslide reaches the runout zone under water, it decelerates rapidly due to a combination of energy conversion into tsunami waves, frictional resistance by the water body, basal friction and the reduction of the gravitational acceleration component in the runout zone. The granular landslide spreads laterally in the runout zone into a characteristic shape, where the tail of the landslide reduces in width towards the rear of the landslide and the head is expanding in the width in the runout zone.

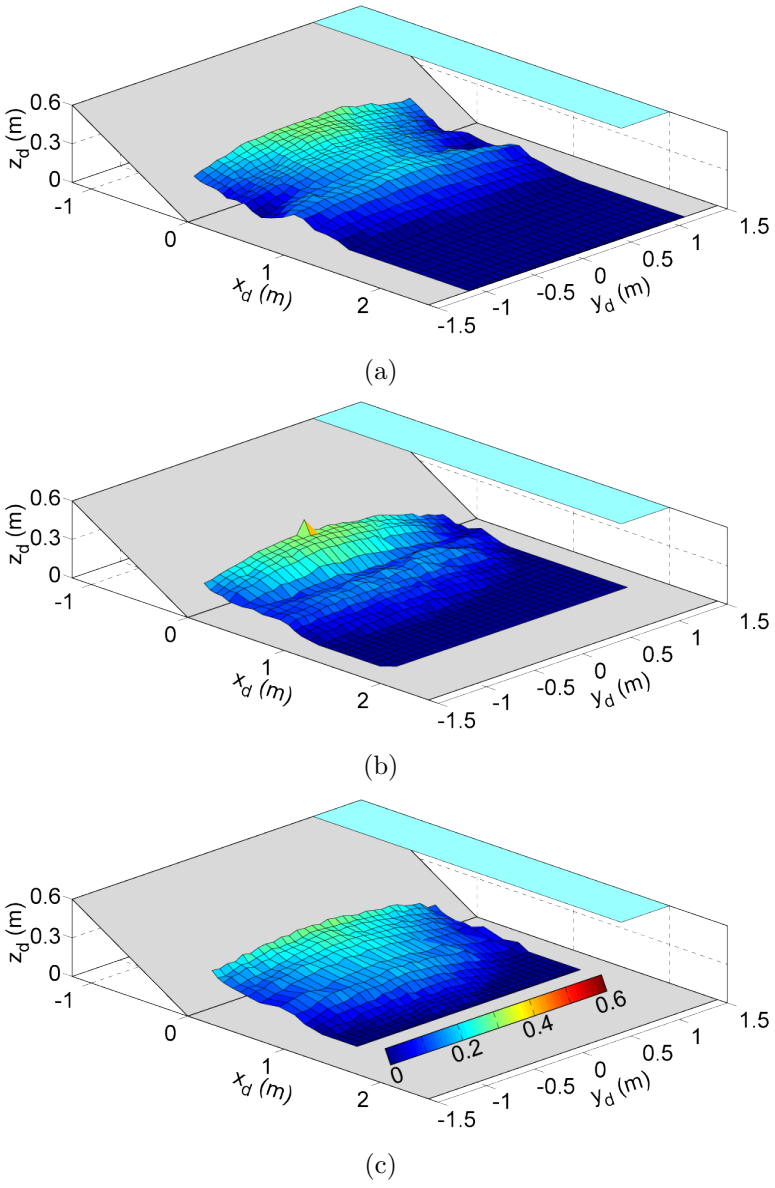

Figure 55: Measured landslide deposit at $h = 0.6$ m for slide box velocity v_b = (a) 3.7 m/s, (b) 3.2 m/s and (c) 2.8 m/s.

The measured underwater landslide deposits are shown in Fig. 55. The cases shown are at a water depth of $h = 0.6$ m, $m_s = 1350$ and 675 kg and different pneumatic landslide tsunami generator acceleration cases. The runout distance of the landslide in the shown figures are 1.54 m, 1.35 m and 1.26 m from the origin at the base of the hill slope. The thickness of landslide deposit gradually increases from the tail of the landslide on the hill slope until it reaches the flat bottom of the wave basin. The sharp transition between the hill slope and the flat bottom acts to rapidly decelerate the landslide. This leads to a pileup of the granular material following the transition point. The thickness of the landslide deposit increases momentarily at this pileup and then rapidly decreases to meet wave basin bottom at the runout point. The initial acceleration of the landslide mass, the volume of the landslide, velocity at impact and the water depth influence the location of the granular mass pileup and the runout distance of the landslide.

The increasing depths of the water body and decreasing impact velocities lead to the location of the pileup to move closer to the transition of the hill slope to the wave basin bottom. Across all the experimental trials, the landslide deposit measured by the acoustic array have similar shape distribution but with varying runout distances and location of the granular pileup. The profile of the landslide deposit is shown in Fig. 56 at water depths of $h = 0.6$, 0.9 and 1.2 m. The experimental cases of $m_s = 1350$ and 675 kg are shown in the figure. The profile is similar across the measured experimental trials and the general variations of the thickness of the landslide deposit, runout distance and the location of the granular mass pileup with respect to the depth of the water column, mass of the landslide and landslide velocity at impact can be seen in Fig. 56.

The effect of water depth on the landslide deposit is shown in Fig. 57 for a landslide mass of $m_s = 1350$ kg and landslide release velocity $v_b = 3.7$ m/s. In these cases, the drop height of the landslide is the same. Hence, in higher water depth, the

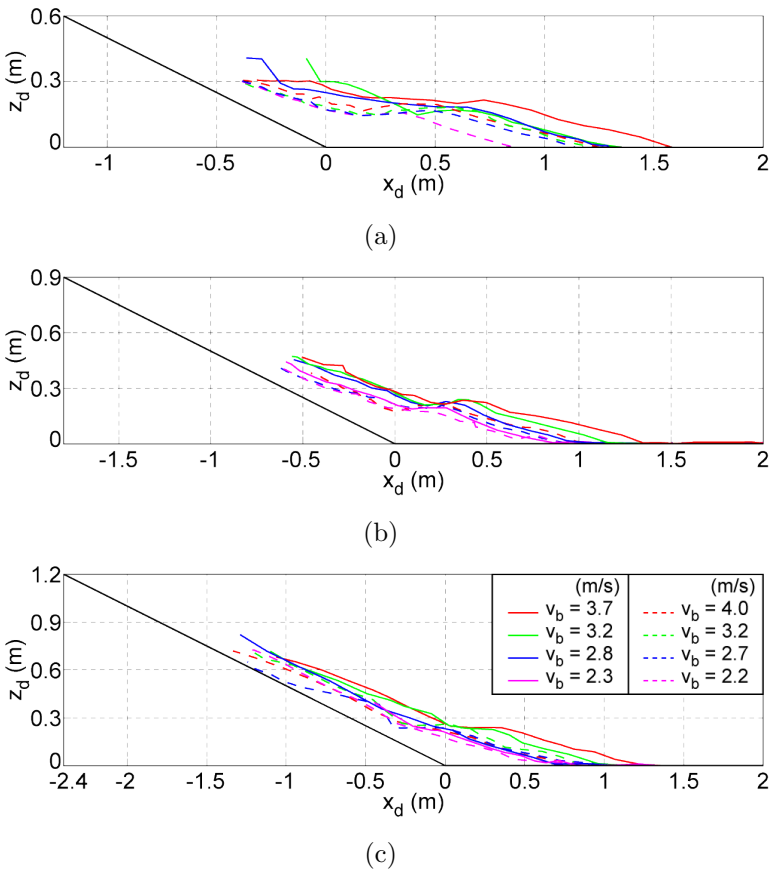

Figure 56: Profile shapes of underwater granular landslide deposits shown at water depths, h = (a) 0.6 m, (b) 0.9 m and (c) 1.2 m.

landslide is in the submarine regime for a longer duration of time compared with the low water depth cases. This leads to a decrease in the runout distance and location of the granular mass pileup as the water depth increases with reference to the wave basin bottom coordinate system shown in Fig. 54. The underwater runout distances are measured from the shoreline along the basal sliding surface of the hill slope. The underwater runout distances for the same landslide mass and release velocity above the water surface increases with increasing depth of submergence. The profile shape shown in Fig. 57(d) shows the shape similarity of the landslide deposits for the same landslide mass and initial acceleration cases.

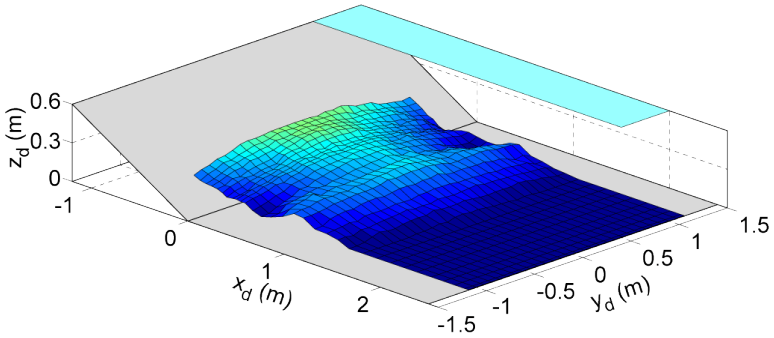

(a)

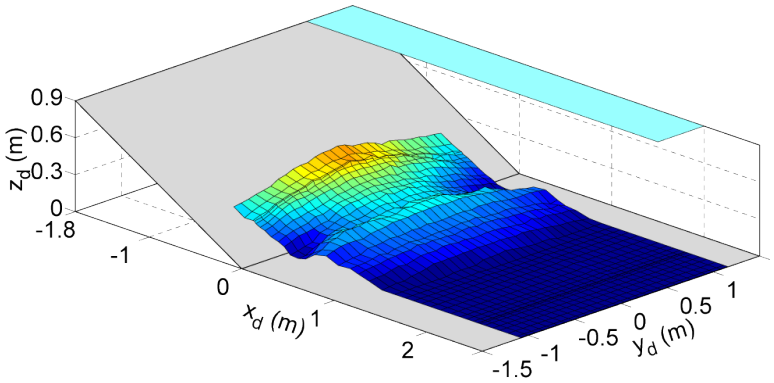

(b)

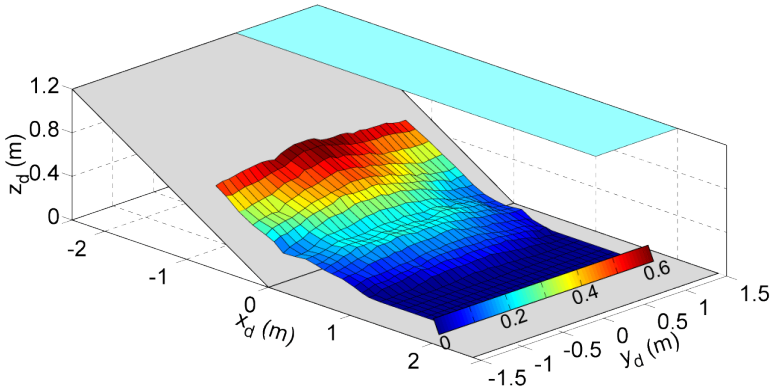

(c)

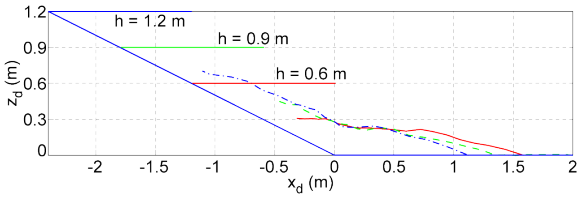

(d)

Figure 57: Underwater granular landslide deposits shown at water depths, h = (a) 0.6 m, (b) 0.9 m and (c) 1.2 m. (d) Underwater landslide profiles along the symmetry axis (centerline) with varying water depths.

On the hill slope, the shape of the deposit and the thickness distribution is similar across the three water depth cases. However, after the transition between the hill slope and the wave basin bottom occurs, the shape is different as can be seen.

4.5 Summary

The measurements of the granular landslide shape and motion are performed in such a way so as to facilitate their use as the source characteristics in tsunami generation by landslides. The specific measurements were made relating to landslide thickness, width, velocity at impact, velocity distribution on the landslide surface and the shape of the underwater landslide deposits. Some of the described variables are shown to be important parameters which influence the tsunami wave generation. The measurements further provide an understanding on the landslide dynamics above the water surface and the transition from the subaqueous to submarine regime.

CHAPTER V

LANDSLIDE GENERATED TSUNAMI WAVES

5.1 Introduction

Tsunami wave generation by subaerial landslides may be characterized by some or all of the following phenomenon:

- landslide motion on the hill slope, pre-impact,
- impact of landslide with the water body,
- formation of an impact crater,
- generation of leading tsunami wave,
- collapse of the impact crater,
- lateral wave runup and rundown on the hill slope
- formation of the trailing waves of the tsunami wave train, and
- wave propagation away from the landslide source.

The unsteady, complex phase mixing of the granular material, air and water complicates the understanding of the landslide tsunami generation process. An analysis of the kinematics and deformation of granular landslides during the impact with the water body can be found in Chapter 4. Henceforth, this section summarizes the tsunami wave generation in the impact region, wave propagation away from the landslide source and the empirical equations that are helpful in predicting the landslide generated tsunami wave properties for hazard assessment.

The tsunami wave measurements are characterized by the parameters shown in Chapter 2. The tsunami waves are measured as the variation of the water surface from the mean undisturbed position, using an array of resistance wave gauges. A total of 25 wave gauges are used in the tsunami wave basin to measure the water surface elevation. Of these, 21 wave gauges are placed in radial and angular directions, while 4 wave gauges are placed on the surface of the hill slope to measure the runup wave profiles. The arrangement of the wave gauges in the tsunami wave basin is shown in Fig. 35. The wave gauges, $WG1 - WG11$ and $WG22 - WG25$ are at fixed locations relative to the wave basin coordinate system. $WG12 - WG21$ are mounted on a bridge parallel to the hill slope which can be moved towards or away from the hill slope, depending on the depth of the water body. The bridge is placed sufficiently close to the impact region in order to measure the near field wave surface elevation during the wave generation without causing any intrusive effects in the impact region. The relative positions of the wave gauges, r/h, vary with varying water depths in the wave basin. In the present study, the ranges that have been considered are $4 - 80$ for the relative propagation distance r/h and $0° - 90°$ for the propagation direction θ relative to the landslide motion. The relatively large spread of the wave gauge locations makes it possible to study the near field characteristics of the generated wave and the wave propagation away from the landslide source.

5.2 Tsunami Wave Generation by Granular Landslides

Tsunamis are generated by landslide by a rapid or an impulsive transfer of momentum from the landslide mass to the water body during the impact and subaqueous runout. The landslide impact acts as a wave generation mechanism while the tsunami is the impulsive response to the landslide or wave generator. The net forces acting on the landslide and water phases during this process are different from each other. While the landslide experiences inertial and gravitational forces, the water body experiences

inertial forces due to water displacement, the pressure drag or form drag and the viscous drag. The amount of energy that is transferred to the water body from the landslide determines the net potential and kinetic energy of the generated waves. Only a part of the landslide energy is transferred to the water body during the wave generation process. Landslide energy losses occur during the motion through internal deformation and bed friction losses between the landslide mass and the hill slope surface and at the bottom of the wave basin. Further energy is lost when the landslide is deflected at the bottom of the wave basin as the landslide mass moves across the abrupt slope sliding surface transition from the hill slope to the wave basin bottom. The landslide runout across the slope change causes the landslide mass to deform resulting in a bulge in the landslide deposit. The displacement of the water body during the impact can lead to a depression or an elevation of the free surface. The water surface displacement corresponds to the potential energy of the water body while the net kinetic energy of the water body is composed of the generated water particles velocity distribution.

The water surface displacement during the landslide impact with the water body may be characterized by an unseparated flow field or a separated flow field (Fritz *et al.* (2003a)). In 2D, the occurrence of a separated or unseparated flow field was found to primarily depend on the landslide Froude number F and the relative landslide thickness S at impact. A separated flow field may result in the formation of hydrodynamic impact craters. In the scenario of landslide generated tsunamis, impact craters are formed when flow separation occurs during the landslide impact at the interface between the penetrating landslide and the water surface. The flow separation for landslide impacts on water surfaces can be defined as the occurrence of the detachment of the water body on the back of the landslide (Fritz *et al.* (2003a), Fritz *et al.* (2003b)).

In the present 3D study, flow fields during the landslide impact with the water

surface are relatively more complex. In the present range of the experimental study, the landslide impact at the water surface is observed to be free of impact crater formations. The sequence of the landslide impact and the wave generation is shown in Figs. 58 and 59. The moment of the impact of the landslide front with the water surface is shown in Fig. 58(a). The initial impact of the landslide on the water surface transfers a portion of the landslide kinetic energy into the water body. The impact results in the displacement of water around the impact region which moves primarily in the direction of the landslide motion and laterally around the landslide front as seen in Fig. 58(b). The dark arrows in the figure portray the direction of the water displacement and subsequent motion. The displaced water moves upward and outward away from the landslide source. The initial water displacement which is strongly directional, develops into a radial wave front owing to the propagation away from the source as seen in Figs. 58(d) and 59(a).

The drawdown of water during the impact results in the corresponding wave trough of the leading wave front. The water surface drawdown occurs until it reaches its maximum extent in Fig. 58(c). At this point, the restoring gravitational forces tend to drive the fluid back to its undisturbed state. Owing to the direction of the landslide motion and momentum transfer into the water body, the restoring forces are dominated in the transverse direction compared with the longitudinal direction. The water surface restores to the undisturbed state in the transverse direction (Fig. 58(d)) which is followed by the longitudinal direction (Fig. 59(a)). The water surface restoration and the subsequent uprush of water leads to the formation of the wave crest of the second radial wave front as seen in Fig. 59(a). The direction of the water particle motion during the surface restoration the water to runup the hill slope as seen in Figs. 59(b) and 59(c). By mass conservation principle, this results in the formation of a depression on the water surface which develops into the trough of the 1^{st} trailing wave front as seen in Fig. 59(d). Post water surface restoration,

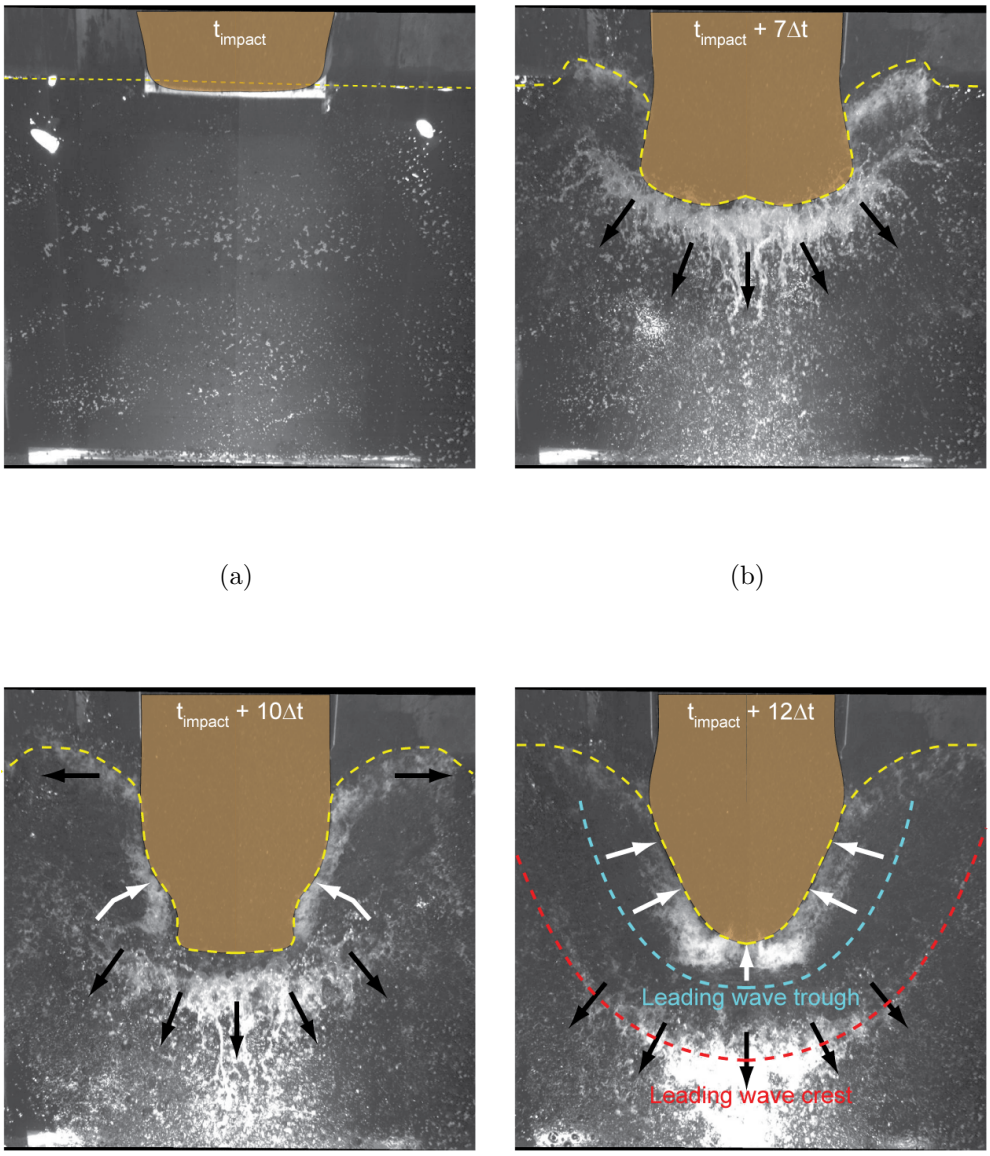

Figure 58: Water displacement by landslide impact on the water surface for landslide Froude number $F = 1.4$, relative landslide thickness $S = 0.23$, relative landslide volume $V = 0.44$ at water depth $h = 1.2$ m: (a) time of initial impact of landslide front with water surface, (b), (c) impact crater formation by water displacement and (d) initiation of crater collapse. The image sequence is recorded at a frame rate $\Delta t = 1/15$ s.

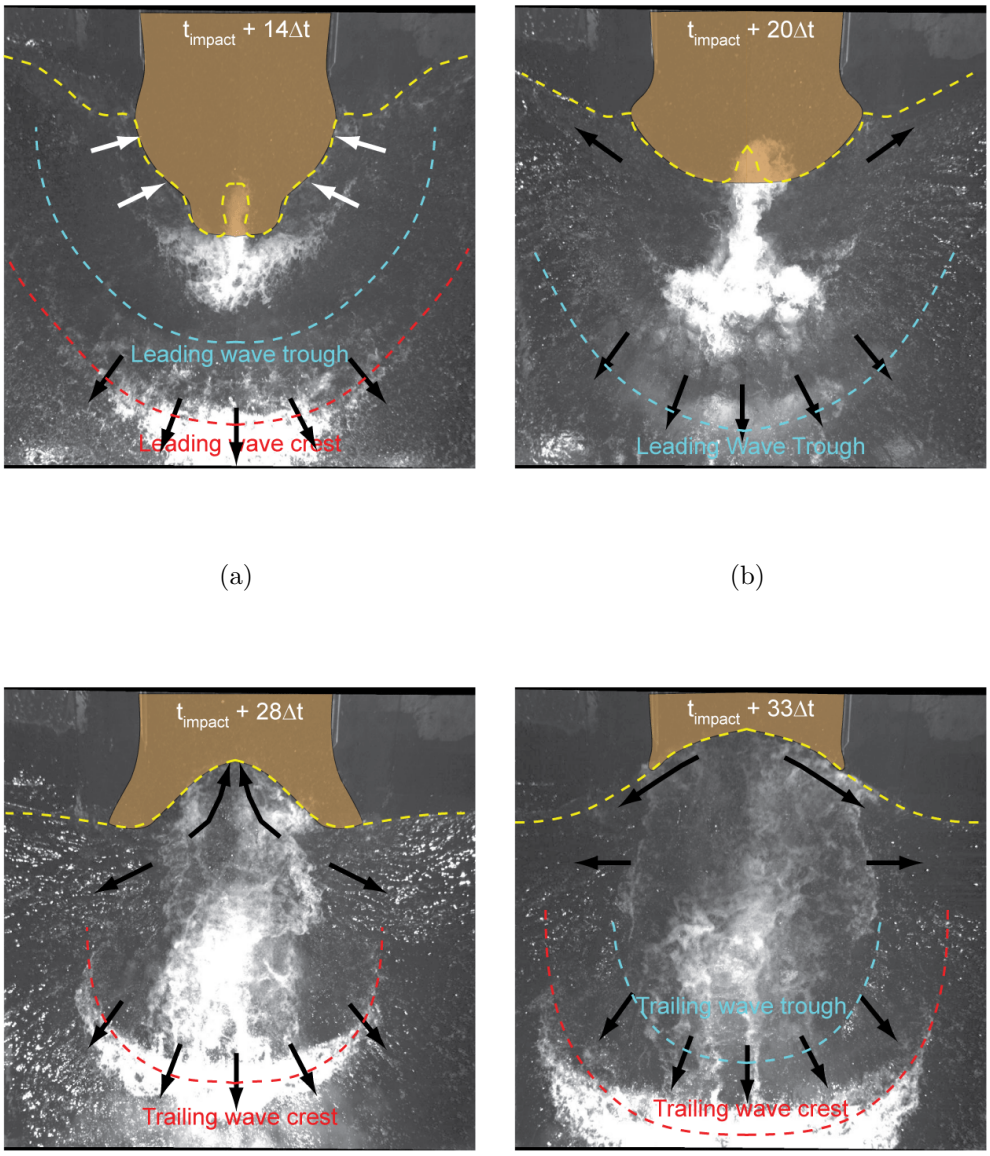

Figure 59: Water displacement by landslide impact on the water surface for landslide Froude number $F = 1.4$, relative landslide thickness $S = 0.23$, relative landslide volume $V = 0.44$ at water depth $h = 1.2$ m: (a) impact crater collapse and radial wave propagation, (b), impact crater collapse and generation of 1^{st} trailing wave (c) backward wave runup on the hill slope post collapse and (d) end of crater collapse. The image sequence is recorded at a frame rate $\Delta t = 1/15$ s.

the flow field consists of multiple oscillating water surface elevations and depressions corresponding with shoreline drawdown and runup on the hill slope which results in the trailing waves formation of the wave train after the first two primary waves. The lateral wave generation on the hill slope is analogous to the outward wave formation.

The formation of the leading lateral wave as an edge wave on the hill slope coincides with the formation and propagation of the leading wave front. The displacement of water in the transverse direction results in the leading runup wave formation as seen in Figs. 58(b) and 58(c). The runup wave oscillations are forced by the crater dynamics in the impact region. The size of the crater was observed to vary with the landslide velocity and shape at impact. The maximum extent of the water surface drawdown at the impact almost never exceeded the maximum width of the landslide at impact. The longitudinal length and the depression of the water surface at impact was observed to vary with the impact velocity and thickness at the impact. This variation occurs since the impact velocity along with the slide thickness and width determines the rate of mass and momentum flux at impact.

5.2.1 Tsunami Wave Profiles

Tsunami waves generated by landslides have been observed to fall into four main types of gravity waves: weakly non-linear oscillatory waves, non-linear transition waves, solitary-like waves and dissipative transient bores. Based on 2D block model experiments, Noda (1970) gave the initial classification depending on the Froude number at impact and the relative thickness of the box. The classification was extended for tsunamis generated by 2D granular landslides by Fritz *et al.* (2004) based on the landslide Froude number F and relative landslide thickness S. Tsunamis generated by 3D granular landslides are observed to fall into the two main categories:

- Non-linear oscillatory type of waves,
- Non-linear transition waves

Solitary and bore-type tsunami waves are not generated in the present range of the experimental study, although cylindrical solitary waves may be generated (Chwang and Wu (1977), Weidman and Zakhem (1988)). The wave profiles of characteristic examples of non-linear oscillatory and non-linear transition waves are shown in Fig. 60

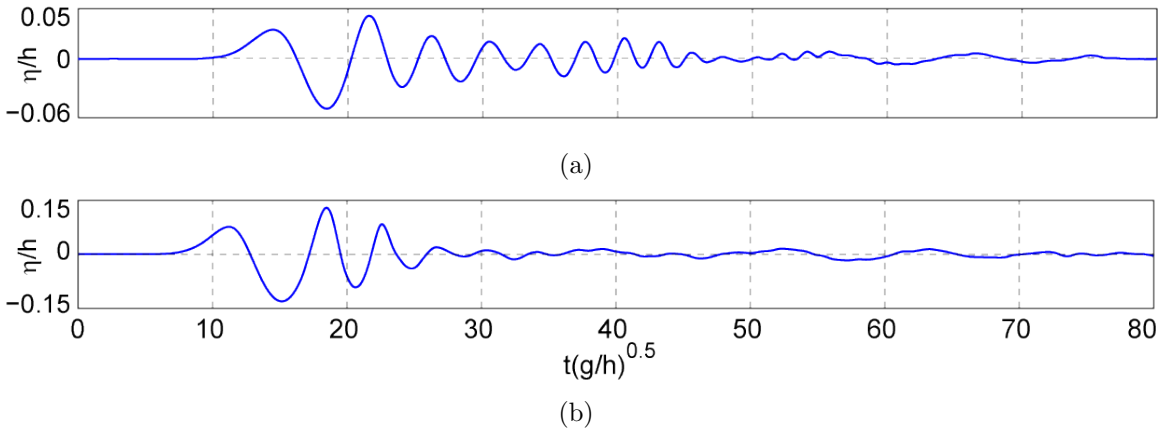

Figure 60: Observed wave types: (a) non-linear oscillatory waves at $F = 1.87$, $S = 0.12$, $V = 1.75$, $h = 0.6$ mand (b) non-linear transition waves at $F = 2.04$, $S = 0.46$, $V = 0.52$, $h = 0.6$ m

The propagation of non-linear oscillatory waves and non-linear transition waves in radial and angular direction away from the landslide source is shown in Figs. 61 and 62. The wave classification is performed for the near field generated tsunami waves. The non-linear oscillatory waves have nearly closed orbital water particle paths and are periodic in the direction of the propagation. Mass transport becomes less significant in these waves and is close to zero on an average. The generated waves demonstrated strong frequency dispersion. The wave train is observed to stretch with the propagation distance due to dispersion effects. The leading wave was found to decay with propagation distance while dispersion effects significantly enhanced the trailing waves in some cases. The maximum crest amplitude was not necessarily of the leading wave front and can be found from the front to the back of the wave train with propagation distance.

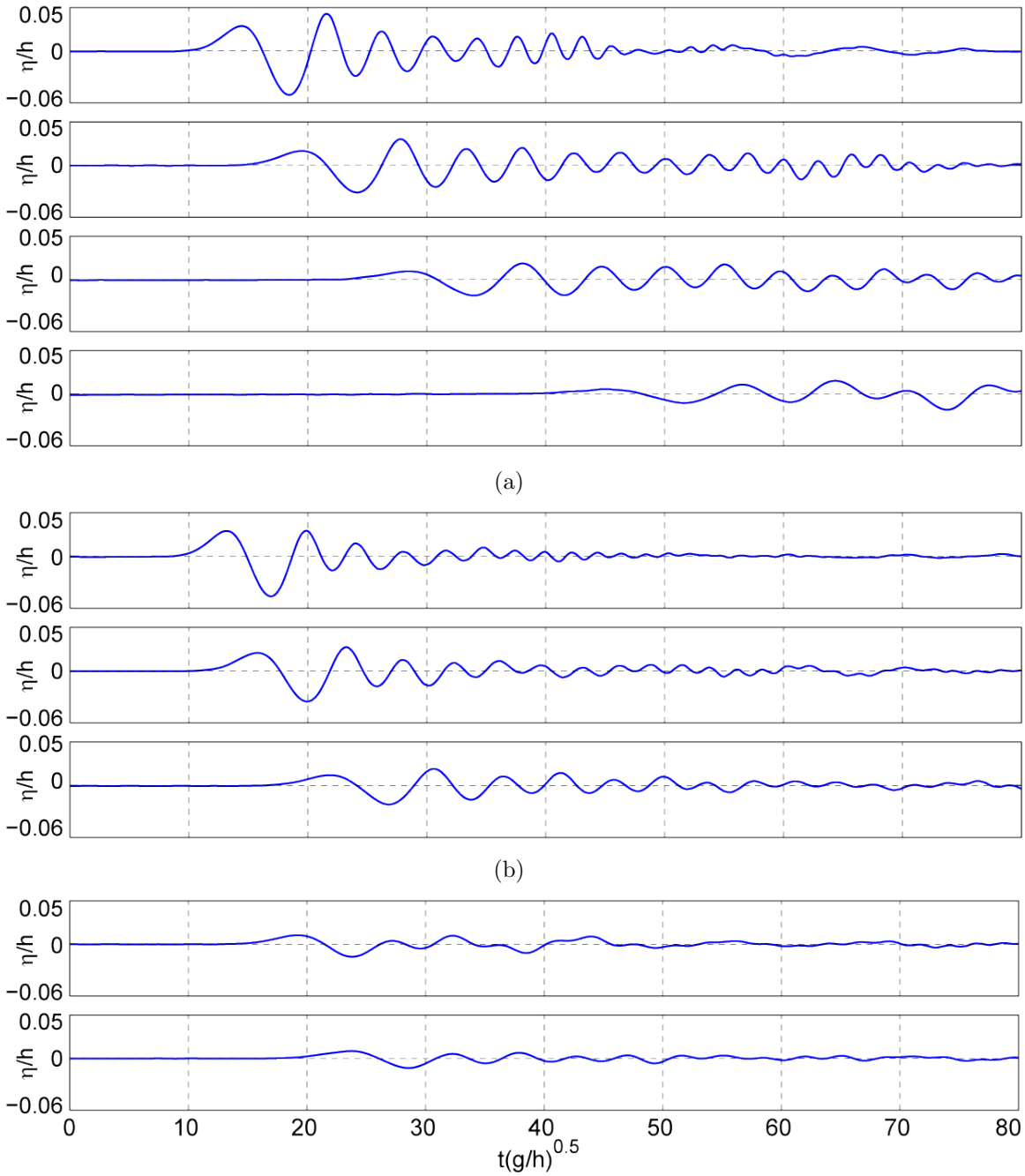

Figure 61: Non-linear oscillatory waves at $F = 1.87$, $S = 0.12$, $V = 1.75$, $h = 0.6$ m measured at (a) $\theta = 0°$, $r/h = 9.03, 14.17, 23.33, 40.17$, (b) $\theta = 30°$, $r/h = 7.66, 10.29, 16.36$ and 61(c) $\theta = 60°$, $r/h = 13.26, 17.32$.

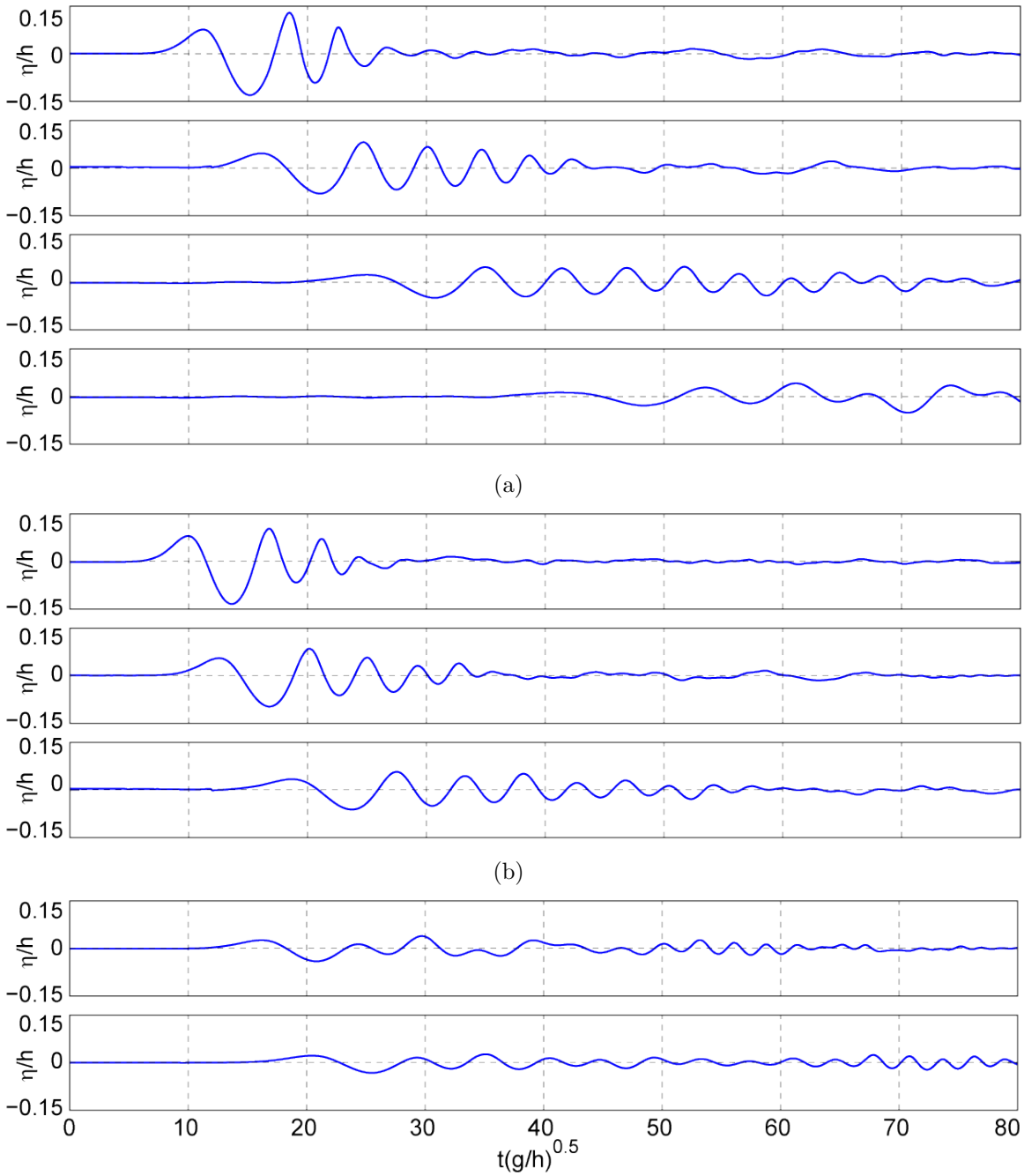

Figure 62: Non-linear transition waves at $F = 2.04$, $S = 0.46$, $V = 1.75$, $h = 0.6$ m measured at (a) $\theta = 0°$, $r/h = 9.03, 14.17, 23.33, 40.17$, (b) $\theta = 30°$, $r/h = 7.66, 10.29, 16.36$ and 62(c) $\theta = 60°$, $r/h = 13.26, 17.32$.

The wave amplitude decayed with the angular direction, but the wave front was found to maintain the radial wave shape. The wave train does not necessarily have the same properties for all the individual waves in the train. Dispersion effects lead to the existence of shallow water waves, intermediate water depth waves and deep water waves in the same wave train. The non-linear transition waves are characterized by a main leading wave crest and trough followed by a dispersive train. In non-linear waves, the main leading wave is followed by a dispersive trailing wave of oscillating wave types. The wave train stretches as the wave propagates away from the landslide source.

The wave type classification is based on the landslide Froude number F and relative landslide thickness S at impact. The wave type classification with landslide Froude number F and relative landslide thickness S at impact is shown in Fig. 63.

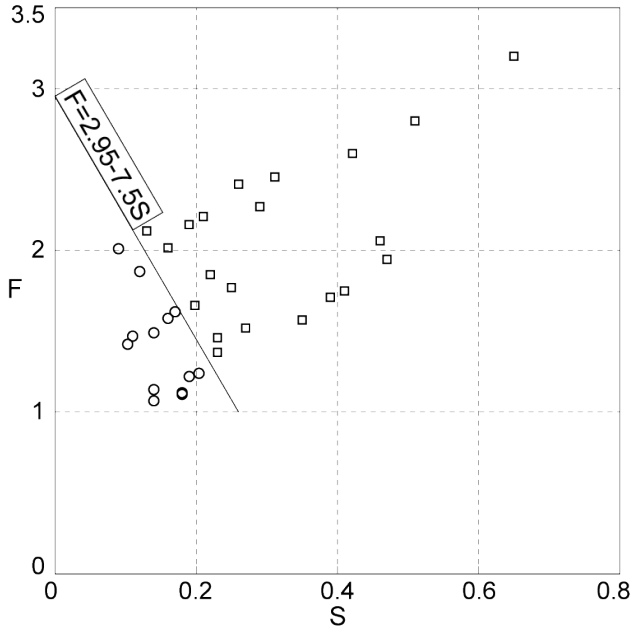

Figure 63: Wave type classification based on landslide Froude number $F = v_s/\sqrt{gh}$ and relative landslide thickens $S = s/h$ with ($\circ$) non-linear oscillatory waves, ($\square$) non-linear transition waves.

A similar classification was performed for waves generated by a vertical plunger and a falling block based on theoretical solutions of Noda (1970) and experimental

results of Wiegel *et al.* (1970) based on relative box thickness and slide Froude number. The tsunami wave types generated by unconfined 3D granular landslides may be classified as

$$F < 2.95 - 7.5S \qquad \text{non-linear oscillatory waves} \tag{32a}$$

$$F > 2.95 - 7.5S \qquad \text{non-linear transition waves} \tag{32b}$$

The non-linear oscillatory type of waves are observed for relatively slow and thin landslides at impact. The non-linear transition waves are observed for relatively faster and thicker landslides than those that generate non-linear oscillatory waves.

5.3 Tsunami Wave Propagation

5.3.1 Wave Amplitude Attenuation

The wave heights of the generated tsunami waves are an essential parameter in estimating the hazards associated with tsunamis. Specifically, the amplitude of the wave crests and troughs should be considered for hazard assessment and mitigation. For linear waves, the crest and trough amplitudes may be estimated as half of the wave height. Impulsively generated waves are often in the non-linear regime in the near field. Hence, the method of deriving the wave amplitudes from the wave heights may lead to an underestimation of the hazards associated with tsunami waves. Since the crests and troughs of the generated waves travel with different speeds, the crests and troughs have to be considered independently. In case of impulsively generated waves, the first wave crest may not necessarily be the highest wave crest, and this depends on the wave generation parameters. In some cases, the second crest amplitude is observed to be larger than the first crest amplitude. As the waves propagate away from the source, the leading wave amplitudes decay away from the source while the trailing wave amplitudes may amplify in magnitude as a result of dispersion effects. Hence, far away from the impulsive source, the leading wave due to amplitude decay may become only a precursor to a more destructive wave among the trailing waves

(Ward (2001b)). A wave amplitude envelope is defined as a surface which encloses the maximum positive crest amplitude a_C and negative trough amplitude a_T across the propagating distances independent of their location in the wave train.

The definitions of the crest and trough amplitudes are shown in Fig. 64(a). While the subscripts in a_c and a_t denote the amplitudes of the crest and trough respectively, the subscripts with the capital letter denotes the maximum crest and trough amplitudes. In three-dimensional cases, the 1D wave envelope is extended to define a 2D wave surface envelope that encloses the maximum crest and trough amplitudes across the radial and angular direction. The definition of the surface wave envelope for the wave crest amplitude is shown in Fig. 64(b).

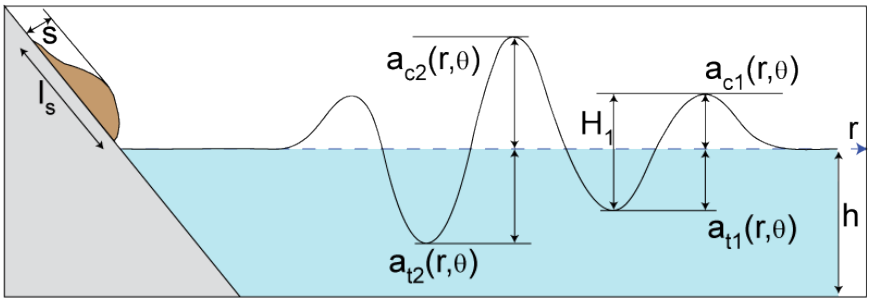

(a)

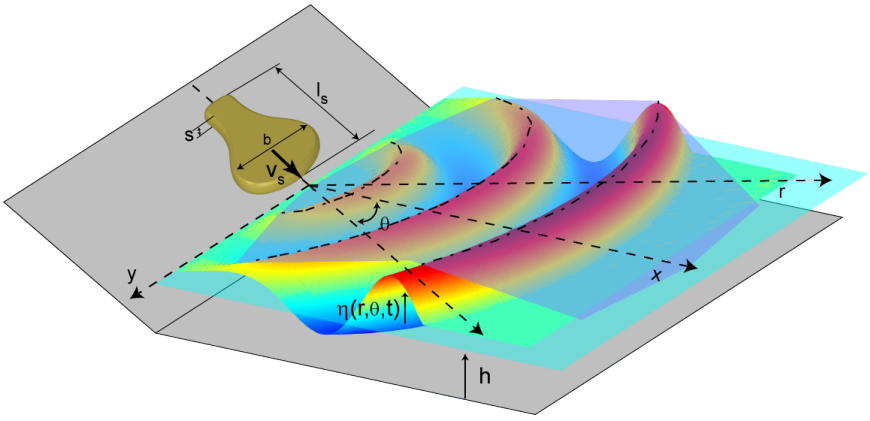

(b)

Figure 64: Wave parameter definitions: (a) amplitudes of wave crest and trough along with the wave height measured at the location (r, θ), (b) 2D wave envelope enclosing the maximum wave crests at (r, θ) for a 3D wave.

The measured surface envelope of the maximum crest amplitude is shown in Fig. 65 for four cases with varying relative landslide volume, landslide Froude number, relative landslide thickness and width at impact.

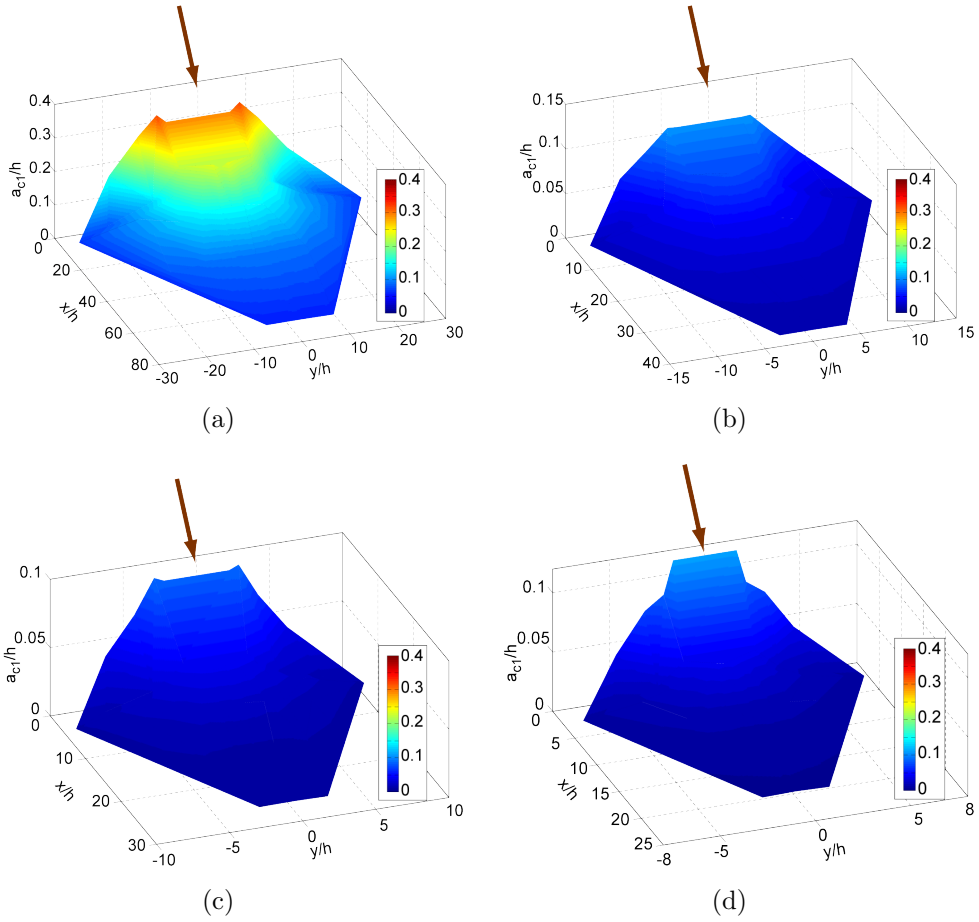

Figure 65: Wave surface envelope of maximum crest amplitude a_C/h shown for (a) $F = 3$, $V = 28$, $S = 0.75$, $B = 4.7$ at $h = 0.3$ m; (b) $F = 2.3$, $V = 3.5$, $S = 0.29$, $B = 3$ at $h = 0.6$ m; (c) $F = 1.8$, $V = 1$, $S = 0.25$, $B = 1.6$ at $h = 0.9$ m and (d) $F = 1.4$, $V = 0.4$, $S = 0.23$, $B = 1$ at $h = 1.2$ m.

Unlike 2D waves, the surface envelope demonstrates an angular decay of the wave amplitude with the radial decay. Within the experimental range, the relative maximum wave crests are generated at lower water depths. The relative wave amplitude increases as the slide thickness approaches the water depth. The amplitude attenuation of the generated wave crest and trough can be represented in general by the

function

$$\frac{a}{h} = k_a f\left(\frac{r}{h}\right) g\left(\theta\right) \tag{33}$$

where a is the amplitude of wave crest or trough, h is the water depth, r is the radial propagation distance and θ is the propagation direction relative to the landslide direction. The function shown in Eq. 33 decouples the wave generation process and the wave propagation. The function k_a, defined as the wave amplitude parameter, incorporates the wave generation mechanism by coupling the landslide parameters with the water body. The function $f(r/h)$ denotes the variation of the amplitude with radial propagation distance r/h and $g(\theta)$ denotes the amplitude dependency on the angular direction of propagation θ. A multi-variable regression analysis for the leading wave crest amplitude with respect to propagation distance and direction provided the functional form of the leading wave crest amplitude as

$$\frac{a_{c1}}{h} = k_{ac1}\left(\frac{r}{h}\right)^{n_{c1}} \cos\theta \tag{34}$$

with a correlation coefficient $r^2 = 0.99$, where r/h is the relative propagation distance, θ is the propagation direction with reference to the landslide direction, h is the water depth, k_{ac1} is the wave amplitude parameter for the leading wave crest and n_{c1} is the exponent of the propagation distance. The exponent n_{ac1} of the relative propagation distance is negative, thus demonstrating the decay of the leading wave crest amplitude with propagation distance. The parameter k_{ac1} and the exponent n_{c1} are functions of the landslide parameters and represent the wave generation mechanism by 3D granular landslides. Further information on these parameters can be found in Sec. 5.3.3. The decay of the leading wave crest amplitude with propagation distance is shown in Fig. 66(a). The wave amplitudes are normalized with the angular decay rate and the wave amplitude parameter for the leading wave crest.

The amplitude attenuation function for the leading wave trough amplitude is also found to behave similar to the leading wave crest amplitude shown in Eq. 34. The

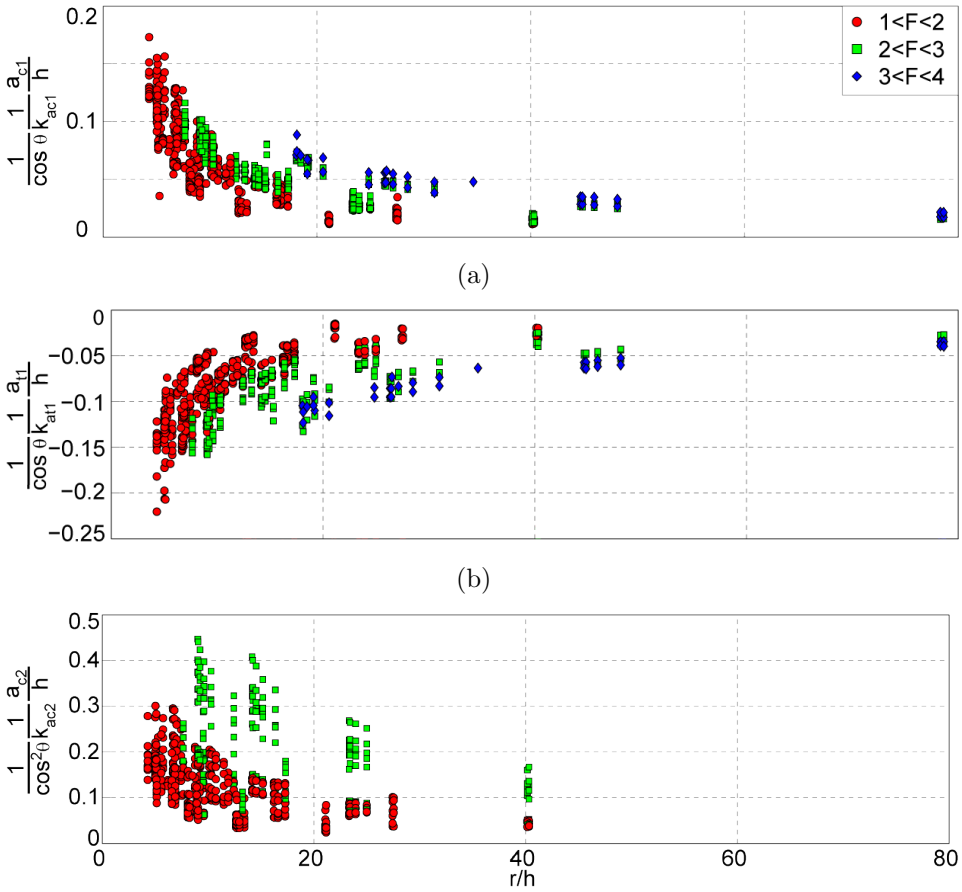

Figure 66: Wave amplitude decay with propagation distance from source: (a) 1^{st} wave crest amplitude, (b) 1^{st} wave trough amplitude and (c) 2^{nd} wave crest amplitude for the entire experimental range of water depths and landslide source parameters.

multi-variable regression analysis for the leading wave trough amplitude provided the leading wave trough amplitude function as

$$\frac{a_{t1}}{h} = k_{at1}\left(\frac{r}{h}\right)^{n_{t1}}\cos\theta \tag{35}$$

with correlation coefficient $r^2 = 0.99$, where a_{t1} is the leading wave trough amplitude, k_{at1} is the wave amplitude parameter for the leading wave trough and n_{t1} is the attenuation rate of the leading wave trough amplitude with propagation distance. The prediction of k_{at1} and n_{t1} with the landslide parameters is discussed in Sec. 5.3.3. The decay of the leading wave trough amplitude with propagation distance is shown in Fig. 66(b). The multi-variable regression analysis for the second wave crest

amplitude gave the amplitude function as

$$\frac{a_{c2}}{h} = k_{ac2}\left(\frac{r}{h}\right)^{n_{c2}} \cos^2\theta \tag{36}$$

with correlation coefficient $r^2 = 0.96$, where a_{c2} is the second wave crest amplitude, k_{ac2} is the wave amplitude parameter and n_{c2} is the rate of decay of the second wave crest amplitude with propagation distance. The trailing wave crest amplitude was found to decay faster in the angular direction θ when compared with the leading wave crest and trough amplitude. The decay is proportional to $\cos^2\theta$ in the angular direction. This variation in the decay rate of the second wave crest amplitude from the leading wave amplitudes is due to the difference in the wave generation mechanism between the leading wave front and the trailing wave front. While the direct impact of the bulk landslide motion with the water body generates the leading wave front in the wave train, the initial collapse of the impact crater generates the trailing wave front in the wave train with varying attenuation behavior when compared with the leading wave front characteristics. The attenuation of the trailing wave crest amplitude with propagation distance is shown in Fig. 66(c). Further regression analysis of the trailing wave trough amplitudes or the wave amplitudes of the subsequent trailing waves yielded no clear functional behavior. In some cases, the amplitudes were found to steadily decay for a part of the propagation distance and then increase again in the far field locations. The decay of the leading wave amplitudes and the distribution of wave energy from the front of the wave train towards the back of the wave train resulted in an increase in the trailing wave amplitudes of the generated wave train. Further, the trailing waves in the far field were prone to wave reflections from the wave basin walls.

The amplitude decay of the leading wave crest and trough follow a $\cos\theta$ dependency while the second wave crest amplitude follows $\cos^2\theta$ in the angular direction. The rate of decay with the propagation distance however varies depending on the depth of the water body and the landslide source parameters. In general, the rate of

decay was found to increase with an increase in water depth in the present experimental study. In 3D cases, the wave height attenuation was observed by Huber and Hager (1997) to behave as

$$\frac{H}{H_5} = 3\cos^2\left(\frac{2\theta}{3}\right)\left(\frac{r}{h}\right)^{-2/3} \tag{37}$$

where H_5 is the wave height at reference location $r/h = 5$. In comparison with Eq. 37, the decay rate of the wave amplitude away from the landslide source varied in the experimental study. The decay rate is dependent on the landslide water body coupling and the nature of the generated wave as shown in Secs. 5.3.1 and 5.3.3.

5.3.2 Wave Height Partition

The linear wave theory assumes equipartition between wave crest and trough.

$$\frac{a_c}{h} = \frac{a_t}{h} = \frac{1}{2}\frac{H}{h} \tag{38}$$

However, impulsively generated waves are often in the non-linear range and the equipartition assumption for the wave height no longer holds. The amplitudes of the leading wave crests and troughs are shown in Fig. 67(a). The wave height parti-

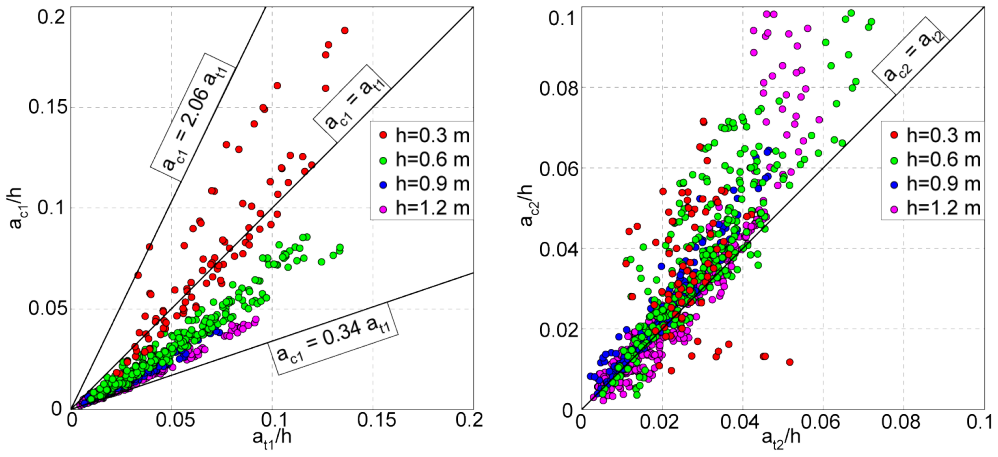

Figure 67: Wave height partition between crest and trough amplitudes for (a) leading wave and (b) trailing wave in the generated wave train.

tion in the present study varies between $a_{c1}/h = 0.34 a_{t1}/h$ and $a_{c1}/h = 2.06 a_{t1}/h$ for

the leading wave in the generated wave train. The relation between the crest amplitudes of the first and second wave is ill-defined. In deep water cases, the first wave crest is the dominant wave in the wave train, $a_{c1}/h \geq a_{c2}/h$. This is true in cases where the wave height is dominated by the wave trough. In shallow to intermediate water depth cases, the second wave crest amplitude is larger than the first wave crest amplitude.

5.3.3 Wave Amplitude Prediction

The empirical functions obtained for the wave crest and trough amplitudes in Sec. 5.3.1 decouples the wave generation mechanism and the wave propagation characteristics through the wave amplitude parameter k_a, radial propagation function $f(r/h)$ and the angular function $g(\theta)$ (Eq. 33). The wave amplitude parameter k_a couples the landslide parameters to the water body and enables predicting the amplitude of the near field waves of the generated tsunami. The wave amplitude parameter, in general, is dependent on the relative landslide parameters and the hill slope angle and can be written as

$$k_a = f\left(S, B, L, V, F, \alpha\right) \tag{39}$$

where $S = s/h$ is the relative landslide thickness at impact, $B = b/h$ is the relative landslide width at impact, $L_s = Vol_s/(sbh)$ is the relative landslide length at impact, $V = V_s/h^3$ is the relative landslide volume at impact, $F = v/\sqrt{gh}$ is the landslide Froude number at impact and α is the angle of the hill slope. Due to the unconfined deformable nature and long runouts of the granular landslide source, the entire landslide length may not be tsunamigenic and affect the regression analysis. A landslide length is defined as $l_s = V_s/(sb)$ and is used in the regression analysis to analyze the dependency on the landslide lengths. Herein, the governing parameters are identified resulting in a predictive equations for the wave amplitude parameters and the decay rate of the amplitude with propagation distance. The rate of decay

of the crest amplitude with propagation distance depends on the water depth regime and the characteristics of the generated wave. Since the wave characteristics are indirectly dependent on the landslide source parameters in the near field area, the decay rate is defined in terms of the landslide parameters.

A multi-variable regression analysis for the leading wave crest parameters gives

$$k_{ac1} = 0.54\left(\frac{s}{h}\right)^{0.85}\left(\frac{v_s}{\sqrt{gh}}\right)^{1.8} \tag{40}$$

$$n_{c1} = -1.24\left(\frac{b}{h}\right)^{-0.36}\left(\frac{s}{h}\right)^{-0.03}\left(\frac{v_s}{\sqrt{gh}}\right)^{0.25} \tag{41}$$

with a correlation coefficient $r^2 = 0.98$ for the wave amplitude parameter and $r^2 = 0.93$ for the decay rate. Thus the evolution of the leading wave crest amplitude can be predicted in terms of the landslide parameters as

$$\frac{a_{c1}}{h} = 0.54\left(\frac{s}{h}\right)^{0.85}\left(\frac{v_s}{\sqrt{gh}}\right)^{1.8}\left(\frac{r}{h}\right)^{-1.24\left(\frac{b}{h}\right)^{-0.36}\left(\frac{s}{h}\right)^{-0.03}\left(\frac{v_s}{\sqrt{gh}}\right)^{0.25}}\cos\theta \tag{42}$$

with a good correlation coefficient of $r^2 = 0.98$. The crest amplitude of the leading wave front is found to be strongly influenced by the landslide Froude number at impact, F and the relative landslide thickness, S. The landslide Froude number and relative landslide width define the landslide inflow rate per unit width into the water body and hence determine the impact characteristics. In accordance with the generation mechanism of the leading wave crest amplitude which results from the direct impact of the landslide with the water body, the dependence of the crest amplitude on these quantities is justified.

The rate of decay is found to strongly depend on the landslide Froude number at impact and the relative landslide width at impact. A weak dependence on the relative landslide thickness and volume is also observed during the regression analysis. The rate of decay is found to depend inversely on the landslide width at impact. The relative width of landslide at impact is indicative of the nature of the landslide source at impact and defines the mass and momentum flux of the landslide into the water

body. As the relative landslide width increases at impact, the nature of the tsunami source is analogous to the change in the source from a point source to a line source. For the same characteristics, the point source has a higher decay rate of the generated wave than a line source. Hence as the relative landslide width increases, the rate of decay of the leading wave crest amplitude decreases.

The comparison between the measured wave crest amplitude and predicted values is shown in Fig. 68. The dominant non-dimensional parameter in the amplitude

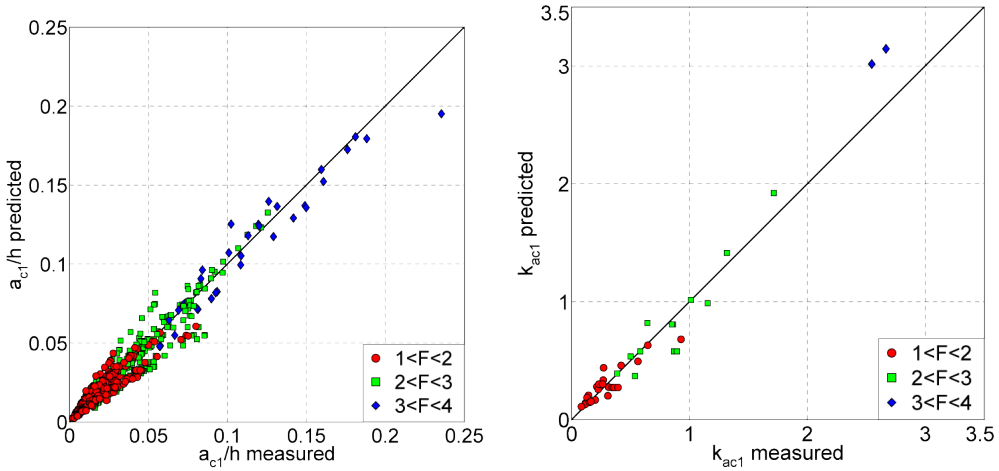

(a) (b)

Figure 68: Comparison between measured and computed values : (a) leading wave crest amplitude computed with Eq. 42; (b) wave amplitude parameter of the leading wave crest computed with Eq. 41.

prediction is the landslide Froude number at impact $F = v_s/\sqrt{gh}$. The relative slide thickness is significant in predicting the wave amplitudes. The rate of decay of the crest amplitude with radial distance however depends on the slide Froude number at impact and the relative landslide width $B = b/h$ at impact. The dependency of the wave amplitude parameter on the relative landslide volume is minor when compared to the effect of the slide thickness and Froude number.

The multiple regression analysis for the leading wave trough amplitude yields the predictive equations for the wave trough amplitude parameter k_{at1} and the trough

amplitude decay rate n_{at1} as

$$k_{at1} = 0.8\left(\frac{s}{h}\right)^{0.6}\left(\frac{V_s}{sbh}\right)^{-0.14}\left(\frac{v_s}{\sqrt{gh}}\right)^{1} \quad (43)$$

$$n_{t1} = -1.4\left(\frac{b}{h}\right)^{-0.14}\left(\frac{V_s}{sbh}\right)^{-0.1}\left(\frac{v_s}{\sqrt{gh}}\right)^{-0.16} \quad (44)$$

with correlation coefficient $r^2 = 0.88$ for the wave amplitude parameter k_{at1} and $r^2 = 0.97$ for the trough decay rate n_{t1}. The attenuation of the wave trough amplitude of the leading wave front can be written as

$$\frac{a_{t1}}{h} = 0.8\left(\frac{s}{h}\right)^{0.6}\left(\frac{V_s}{sbh}\right)^{-0.14}\left(\frac{v_s}{\sqrt{gh}}\right)^{1}\left(\frac{r}{h}\right)^{-1.4\left(\frac{b}{h}\right)^{-0.14}\left(\frac{V_s}{sbh}\right)^{-0.1}\left(\frac{v_s}{\sqrt{gh}}\right)^{-0.16}}\cos\theta \quad (45)$$

with correlation coefficient $r^2 = 0.93$. The dominant parameter in prediction of the trough amplitude is the landslide Froude number F. The other important parameters are the relative landslide thickness S and the relative landslide length L_s. The rate of the amplitude decay depends inversely on the landslide width B, length L_s and Froude number F at impact. The comparison between the measured and predicted values of the leading wave trough amplitudes is shown in Fig. 69.

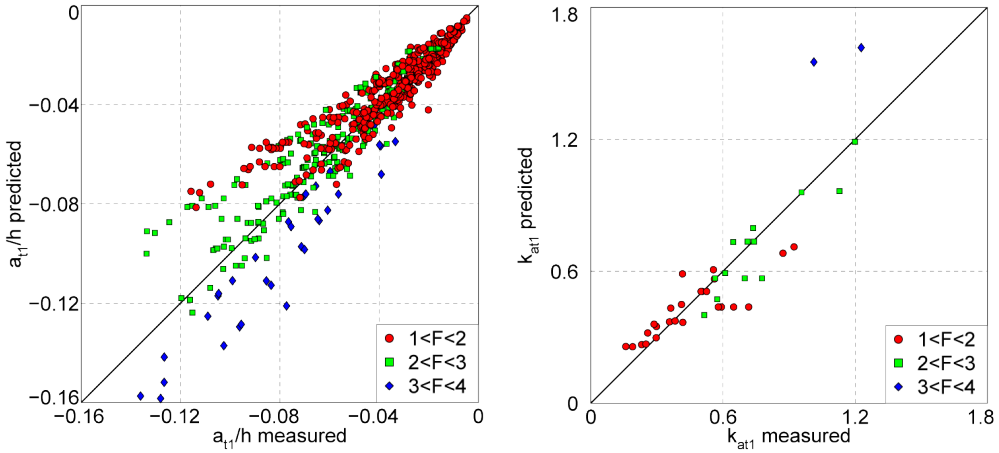

(a) (b)

Figure 69: Comparison between measured and computed values : (a) leading wave trough amplitude computed with Eq. 45; (b) wave amplitude parameter of the leading wave trough computed with Eq. 44.

The leading wave trough is generated through the depression following the water displacement or creation of an impact crater when the landslide impacts the water

surface. The size and depth of the cavity directly influence the magnitude of the leading wave trough amplitude. Since the displaced water volume flux is directly proportional to the landslide Froude number and landslide thickness at impact, these factors directly influence the amplitude of the leading wave trough.

The multiple regression analysis for the second wave crest amplitude results in

$$k_{ac2} = 1.0\left(\frac{s}{h}\right)^{0.8}\left(\frac{V_s}{sbh}\right)^{-0.5}\left(\frac{b}{h}\right)^{-0.4}\left(\frac{v_s}{\sqrt{gh}}\right)^{1} \quad (46)$$

$$n_{c2} = -1.5\left(\frac{b}{h}\right)^{-0.07}\left(\frac{V_s}{sbh}\right)^{-0.3}\left(\frac{v_s}{\sqrt{gh}}\right)^{-0.5} \quad (47)$$

with correlation coefficient $r^2 = 0.83$ for the wave amplitude parameter k_{ac2} and $r^2 = 0.93$ for the decay rate n_{c2}. The amplitude of the trailing wave crest can then be predicted by the equation

$$\frac{a_{c2}}{h} = 1.0\left(\frac{s}{h}\right)^{0.8}\left(\frac{V_s}{sbh}\right)^{-0.5}\left(\frac{b}{h}\right)^{-0.4}\left(\frac{v_s}{\sqrt{gh}}\right)^{1}\left(\frac{r}{h}\right)^{-1.5\left(\frac{b}{h}\right)^{-0.07}\left(\frac{V_s}{sbh}\right)^{-0.3}\left(\frac{v_s}{\sqrt{gh}}\right)^{-0.5}}\cos^2\theta \quad (48)$$

with correlation coefficient $r^2 = 0.91$. The experimental cases with water depths of $h = 0.3$ m are not included in the regression analysis for the trailing wave crest as the 2^{nd} wave crest is ill-defined at the low water depth ranges. The comparison between the measured and predicted values of the leading wave trough amplitudes is shown in Fig. 70.

The amplitude of the second wave crest amplitude is found to strongly depend on the landslide Froude number, landslide thickness at impact and the landslide volume, with a minor dependence on the landslide width. The decay rate is found to inversely depend on the landslide Froude number at impact, relative landslide length and weakly on the landslide width. The prediction equation of the trailing wave crest amplitude given by Eq. 48 can be explained through the generation mechanism. While the leading waves are generated by the direct impact of the landslide with the water body, the trailing waves are generated by the runup and subsequent rundown of waves on the hill slope as a consequent of the water surface restoration post landslide

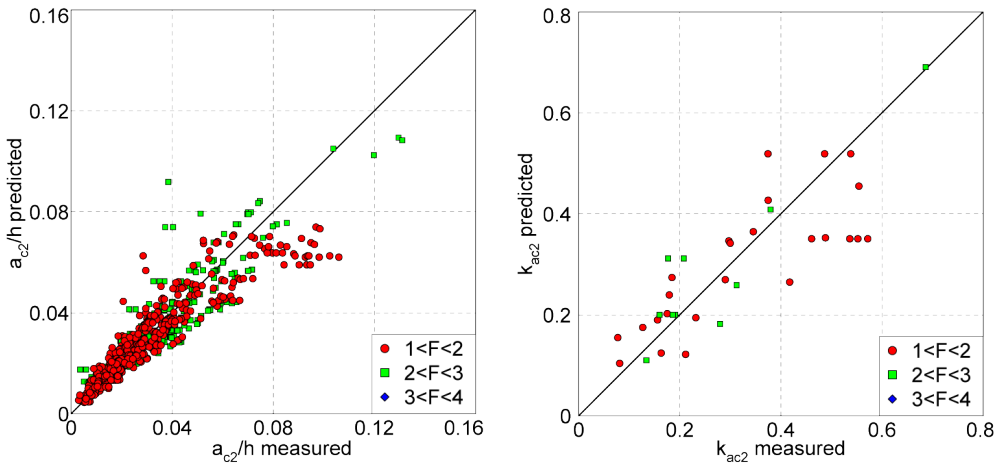

(a) (b)

Figure 70: Comparison between measured and computed values : (a) 2^{nd} wave crest amplitude based on Eq. 48; (b) wave amplitude parameter of the 2^{nd} wave crest amplitude given by Eq. 47.

impact. Since the impact cavity is generated as a result of the impact, the trailing wave amplitudes can be weakly related to the landslide parameters. The size of the impact cavity is directly related to the landslide Froude number and slide at impact and hence these directly influence the trailing wave crest amplitudes. The landslide volume is found to inversely influence the amplitude of the trailing wave crest. The collapse of an impact cavity is directly dependent on the air volume inside the cavity. The air volume relative to the landslide volume in the impact cavity was observed to be larger for short and thick slides than for thin and long slides Fritz (2002). Larger air volumes lead to higher and massive collapses of the crater which leads to higher wave runups on the hill slope and hence higher trailing wave amplitudes.

The accuracy of the wave amplitude predictions decreases from the front of the wave toward the back of the wave. The regression analysis for the amplitudes of the trailing waves yielded no clear empirical form of the predictive equations. The dependence of the trailing wave amplitudes on the radial propagation distance and the angular direction varied widely in the experimental trials.

5.3.4 Tsunami Wave Periods

The time periods of the generated tsunami waves are measured from the time series recordings of the water surface elevation at the wave gauge array. The individual waves in the generated wave train are identified by the zero upcrossing method. The upcrossing points are defined as the point in the wave train measurement, where the free surface of the water body departs the mean water level. The water surface variation between two successive upcrossing points constitute a wave. The initial upcrossing point is defined as the location when the water surface elevation reaches 5% of the first wave crest amplitude.

$$\eta = 0.05 a_{c1} \tag{49}$$

Since the wave profiles are measured in the time domain, the upcrossing points gives the time coordinate of the waves. The difference between successive upcrossing time of the waves gives the upcrossing wave periods of the individual waves in the generated wave train. In the present three-dimensional study, the landslide is observed to generate a wave train comprising of radial wave fronts. Hence, the wave periods that are measured at the individual wave gauges are the wave periods of the radial wave front at location (r, θ). The definition of the upcrossing and crest to crest wave periods that are measured for a radial wave front are shown in Fig. 71.

The wave periods corresponding to the first 3 waves, T_i, $i = 1, 2, 3$ are measured along with crest-to-crest and trough-to-trough wave periods for the first 3 waves, T_{ci}, T_{ti}, $i = 1, 2, 3$. The measurement of the third wave period was possible in some cases not disturbed by wave reflections or noise in the measurements. The wave periods are measured in the range $4 < r/h < 80$ and $0 < \theta < 90$ across all of the experimental trials. The measured wave periods for a particular wave front are found to be invariable in the angular direction, except close to the hill slope, $\theta = 90^o$. Thus the radial wave fronts in the present study have a nearly constant wave period

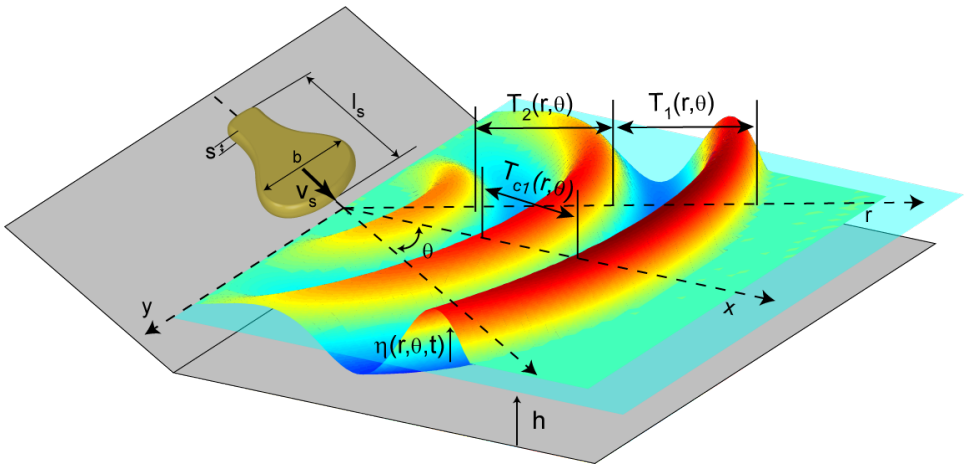

Figure 71: Definitions of the upcrossing and crest-to-crest wave periods of the radial wave fronts in a wave train generated by 3D granular landslides.

independent of the angular direction. The only variation in the wave periods arises due to wave propagation away from the landslide source in the radial direction. In general, the wave periods are found to increase with the radial propagation distance r/h. In the measured range $4 < r/h < 80$, the wave period of the first wave front is found to be $6 < T_1\sqrt{g/h} < 26$ and the first wave crest as $5 < T_{c1}\sqrt{g/h} < 18$. On average, the wave period of the first crest to second crest is found to be 18% shorter than the upcrossing wave periods of the first generated wave front. The wave periods of the second and third wave front is found in the range $3.5 < T_2\sqrt{g/h} < 10.5$ and $2 < T_3\sqrt{g/h} < 8$. The second crest to third crest wave period is in the range $3 < T_{c2}\sqrt{g/h} < 10$. There is almost no significant variation between the upcrossing period T_2 and the crest-to-crest period T_{c2} for the first trailing wave. The little to no variation indicates the presence of an oscillatory type of trailing wave with minor nonlinear effects either through the wave shape or wave partition. The wave periods further decreases from the front of the wave train towards the rear of the wave train.

The wave periods of the wave front are independent of the angular propagation direction θ. The general function that describes the evolution of the measured wave

periods with propagation distance r/h is given as

$$T\sqrt{\frac{g}{h}} = k_T f\left(\frac{r}{h}\right) \tag{50}$$

where k_T is the wave period parameter and $f(r/h)$ is a function that describes the variation with propagation distance r/h. The above function decouples the wave generation and propagation through the wave period parameter and the propagation function. Further details on the wave period parameter can be found in Sec. 5.3.5. The multiple regression analysis of the measured wave periods gives the evolution functions for the first three wave fronts of the generated wave train as

$$\begin{aligned} T_1\sqrt{\frac{g}{h}} &= k_{T1}\left(\frac{r}{h}\right)^{0.3} \\ T_2\sqrt{\frac{g}{h}} &= k_{T2}\left(\frac{r}{h}\right)^{0.25} \\ T_3\sqrt{\frac{g}{h}} &= k_{T3}\left(\frac{r}{h}\right)^{0.25} \end{aligned} \tag{51}$$

with correlation coefficient r^2 =0.98, 0.95 and 0.87 for the first three wave fronts respectively. k_{Ti} is the wave period parameter for the i^{th} wave front in the generated wave train. The evolution of the first three wave periods according to Eq. 52 is shown in Fig. 72. The evolution of the wave period along with the wave period parameter $1/k(T\sqrt{g/h})$ is shown versus the relative propagation distance r/h.

In an 2D experimental study with block landslides, Kamphuis and Bowering (1970) observed a linear increase of the wave period with propagation distance according to the equation

$$T_{Kamphuis}\sqrt{\frac{g}{h}} = 11 + 0.225\left(\frac{x}{h}\right) \tag{52}$$

Huber (1980) measured wave periods in the range $4 < T_{Huber}\sqrt{g/h} < 36$ over the propagation distance range $5 < r/h < 100$. The wave period increase with propagation distance in that study was defined as

$$T_{Huber}\sqrt{\frac{g}{h}} = 2.85\left(\frac{x}{h}\right)^{0.45} \tag{53}$$

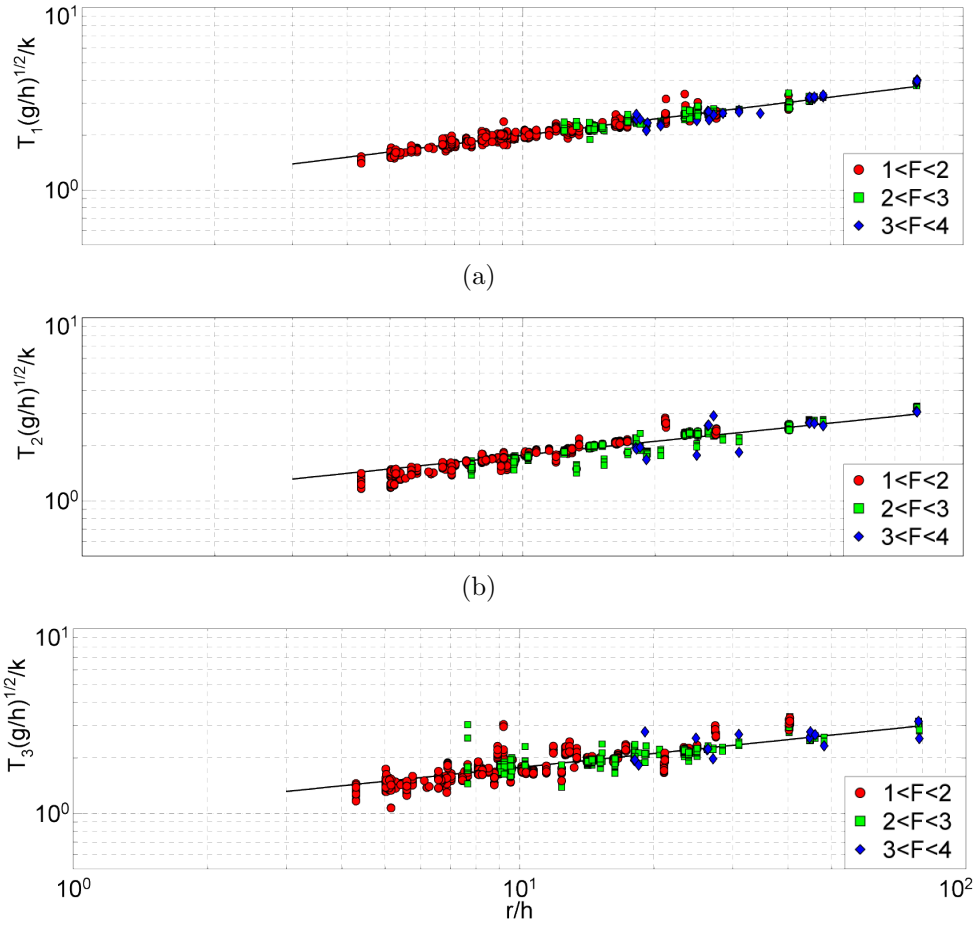

Figure 72: Time periods within the wave train as function of propagation distance (r/h) for (a) 1^{st} wave, (b) 2^{nd} wave and (c) 3^{rd} wave.

without reference to the wave generation mechanism or an anchor point. In the study by Fritz (2002), the wave periods were measured over the propagation distance $2 < x/h < 22$. The measured time periods of the first wave were found within the range $6 < T_{Fritz}\sqrt{g/h} < 22$. The evolution of the first wave period with propagation distance was given as

$$\frac{T_{fritz}}{T_{fritz}(x/h = 5)} = 0.6\left(\frac{x}{h}\right)^{1/3} \tag{54}$$

with the reference location at $X/h = 5$. In a further study, Heller (2008) found the evolution of wave period with propagation distance x/h as

$$T_{Heller}\sqrt{\frac{g}{h}} = 9P_{Heller}^{1/4}\left(\frac{x}{h}\right)^{5/16} \tag{55}$$

where P_{Heller} is defined as an impulse parameter that defines the landslide water body coupling analogous to the wave period parameter k_{T1} in the present study.

Since the wave period definitions vary with the different experimental studies, the wave periods are normalized at an anchor point for the ease of comparison. By fixing the reference location as $x/h = r/h = 5$, the measured time periods of the first wave can be written as

$$\frac{T_1}{T_1(r/h=5)} = 0.6\left(\frac{r}{h}\right)^{0.3} \text{ (Present Study)} \quad (56)$$

$$\frac{T_{Kamphuis}}{T_1(x/h=5)} = \frac{1}{12}\left(11 + 0.225\frac{x}{h}\right) \text{ (Kamphuis and Bowering (1970))} \quad (57)$$

$$\frac{T_{Heller}}{T_1(x/h=5)} = 0.6\left(\frac{x}{h}\right)^{5/16} \text{ (Heller (2008))} \quad (58)$$

The comparison of the present study with previously obtained functions of wave period propagation in Eq. 58 is shown in Fig. 73.

The differences between the above studies and the present study are mainly due to the variation in the wave generation between the 2D physical model and the fully 3D physical model. The generated wave characteristics are different in the 2D and 3D study between the 1D wave propagation and wave propagation as a radial front in 3D. Unlike the 2D case, in 3D the wave train is stretched in a radial fashion, which leads to a gradual increase in the length of the wave front as the propagation distance increases. The rate of wave period increase is slightly larger in the 2D case compared with 3D case (approximately 10%).

5.3.5 Wave Period Prediction

The wave period function obtained in Eq. 52 decouples the wave generation process through the wave period parameter k_T and the wave propagation function $f(r/h)$. The wave period parameter is found to depend on the landslide parameters and thus provides a coupling of the landslide parameters with the water body. The wave period in general depends on the duration of the landslide motion and wave generation at

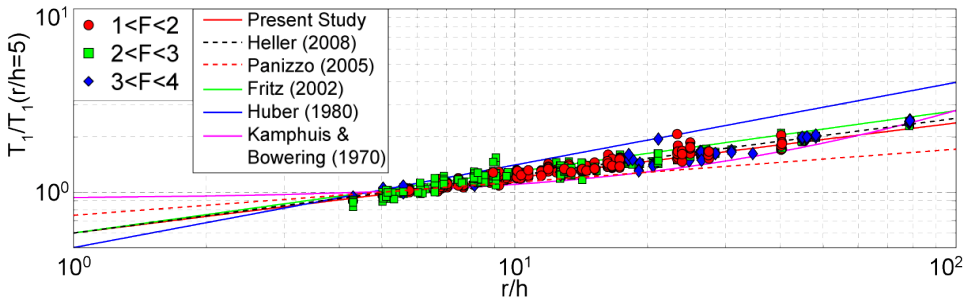

Figure 73: Evolution of wave period of the 1^{st} wave, T_1 with propagation distance r/h compared with the study of Kamphuis and Bowering (1970), Huber (1980), Fritz (2002), Heller (2008).

impact. The water displacement at impact and the collapse of the water surface at impact influence the time scales of wave generation and the wave periods. However, due to the unconfined spreading of the granular landslide and the fully 3D physical model, these times are difficult to measure. The time of granular motion is not clearly defined as different stages of the landslide motion have varying influence on the tsunami generation. The last part of the landslide motion constitutes a significant portion of the landslide motion, yet is inefficient for tsunami generation. It was observed that even when the landslide front comes to rest at the bottom of the TWB, the tail of the landslide is still in motion. The time of landslide motion and crater formation are invariably dependent on the landslide velocity and geometry. Hence, the wave periods can be predicted in terms of the measured landslide velocity and geometry at impact. A multi-variable regression analysis for the first wave period provided the prediction equation for the wave period parameter as

$$k_{T1} = 4.8 \left(\frac{s}{h}\right)^{0.05} \left(\frac{V}{sbh}\right)^{0.04} \left(\frac{v_s}{\sqrt{gh}}\right)^{0.15} \tag{59}$$

with a correlation coefficient of $r^2 = 0.94$. The landslide Froude number $F = v_s/\sqrt{gh}$ is identified as the primary parameter governing the time period of the leading wave, along with a minor dependency on the relative landslide length $L = V_s/(sbh)$ and relative thickness S. The dimensionless width B at impact had little to no influence on the wave period. By combining Eqs. 52 and 59, the prediction for the wave period

of the leading wave front can be obtained as

$$T_1\sqrt{\frac{g}{h}} = 4.8\left(\frac{s}{h}\right)^{0.05}\left(\frac{V}{sbh}\right)^{0.04}\left(\frac{v_s}{\sqrt{gh}}\right)^{0.15}\left(\frac{r}{h}\right)^{0.3} \tag{60}$$

with a good correlation coefficient of $r^2 = 0.97$. The comparison between the measured time period of the leading wave front and the predicted values is shown in Fig. 74(a).

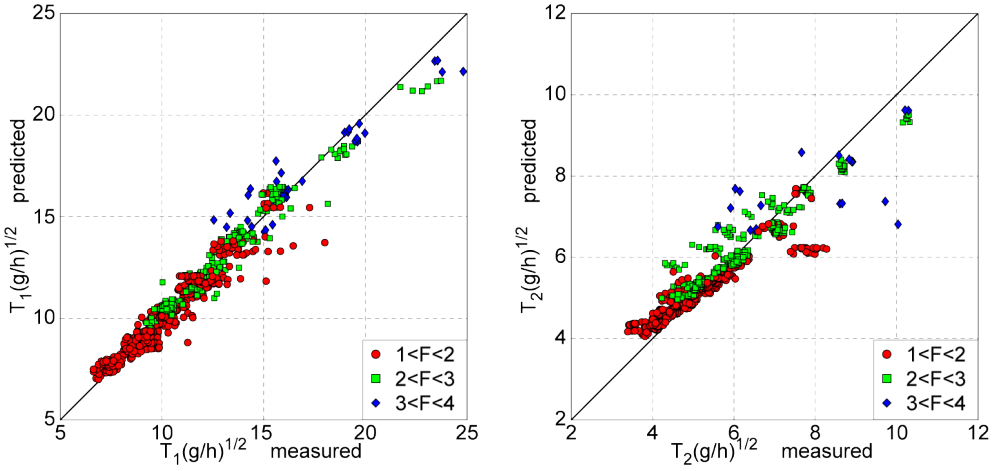

(a) (b)

Figure 74: Comparison between measured and predicted values of (a) 1^{st} wave period with Eq. 60 and (b) 2^{nd} wave period at all the wave gauges with Eq. 61.

The multiple regression analysis for the second wave period parameter resulted int he following prediciton equation,

$$T_2\sqrt{\frac{g}{h}} = 3\left(\frac{s}{h}\right)^{0.03}\left(\frac{V_s}{sbh}\right)^{0.01}\left(\frac{v_s}{\sqrt{gh}}\right)^{0.08}\left(\frac{r}{h}\right)^{0.25} \tag{61}$$

with a correlation coefficient for the wave period paramter k_{T2} as $r^2 = 0.86$ and the wave period T_2 as $r^2 = 0.93$. The dominant parameter in this case is also the slide Froude number at impact with some minor dependency on the relative landslide length and thickness at impact. The comparison between the measured and predicted values corresponding to the wave period of the trailing wave front is shown in Fig. 74(b). The regression analysis for the time period of the third wave front showed poor dependence on the landslide parameters and is inconclusive. While the first wave is

generated by the direct impact of the landslide with the water surface and the second wave is generated by the collapse of the impact cavity and subsequent runup and rundown on the hill slope, the third wave is generated by the oscillating wave uprush and draw down after the landslide impact with the water surface. Hence while the first two waves can be directly estimated in terms of the landslide parameters, the dependence of the third and the subsequent trailing waves on the landslide is poorly constrained.

5.3.6 Tsunami Wave Celerity

The determination of tsunami arrival times is critically important to issue (and cancel) tsunami warnings as well as evacuation efforts. The arrival times can be determined by ray paths and wave propagation velocity. In case of linear waves, the wave propagation velocity can be determined by the wave length L, or the wave period T and the water depth h from the linear dispersion relation. However the linear wave theory is valid for $a_c/h < 0.03$ (Dean and Dalrymple (1991)). In the present experiments, the generated waves are in the range $0.001 < a_c/h < 0.35$. While the near field waves are in the non-linear regime, some of the far field waves may fall in the linear wave regime. In the non-linear regime, the wave propagation velocity further depends on the relative wave amplitude a/h or the relative wave height H/h. While the increasing magnitudes of relative wave length L/h lead to an increase in the importance of the higher order effects on the wave train properties. The individual crests and troughs of the generated waves have independent wave lengths and they are found to propagate with different velocities. Hence, landslide generated tsunami waves are not steady in a reference frame moving at the wave propagation velocity, in contrast to the solitary or cnoidal wave. Hence each component of the generated waves are treated independently.

The tsunami wave propagation velocity is determined for individual wave crests

and troughs as the wave front propagates from wave gauge to wave gauge along a directional ray. The wave velocity was obtained by dividing the distance between the wave gauges along a particular ray by the travel time required for the individual wave crests and troughs to pass the location of the successive wave gauges. The wave gauges were placed in a radial and angular direction in the tsunami wave basin. The wave gauges were placed in the rays starting at 0^o from the direction of the landslide motion. The successive angles of the wave gauges were $5^o, 13^o, 25^o, 30^o, 45^o, 60^o$ and 90^o. The wave propagation velocity is measured by dividing the distance between successive wave gauges in a directional ray with the travel times of the successive wave crest and troughs. The propagation velocity measurements are estimated in the range $1.67 < r/h < 78.65$ across all the experimental trials and along all the directional rays. The velocity measurements are limited to the wave gauges where the measured wave profiles are independent of wave reflection. The measurements are made for the crests and troughs of the first three waves, which are the highest and the most important for hazard mitigation. Later trailing waves in most cases are disturbed by wave reflections off the tsunami wave basin walls and the hill slope. The propagation velocity of the leading wave front are found to be in the range $0.8 < c_{c1}/\sqrt{gh} < 1.2$, $0.7 < c_{t1}/\sqrt{gh} < 1.0$. The 1^{st} trailing wave propagation velocities are found to be in the range $0.65 < c_{c2}/\sqrt{gh} < 0.97$, $0.54 < c_{t2}/\sqrt{gh} < 0.94$ and the 2^{nd} trailing wave fronts in the range $0.5 < c_{c3}/\sqrt{gh} < 0.93$ and $0.5 < c_{t3}/\sqrt{gh} < 0.92$. The decrease in the propagation velocity from the leading wave to the trailing waves is due to the reduction of the wave lengths from the front of the wave to the back of the wave. The reduction of the wave length of the trough resulted in a decrease in the wave propagation velocity by up to 17%. The propagation velocity of the second wave was on average $18\% - 23\%$ lower than the leading wave velocity. The third wave was on average $22\% - 35\%$ slower than the leading wave. The propagation velocity of the leading wave crest also often exceeded the maximum possible linear propagation

velocity corresponding to the shallow water wave propagation velocity $c < \sqrt{gh}$ in some experimental trials at low water depths.

The wave propagation velocity of the leading wave front can be approximated by the theoretical approximation for a solitary wave. The speed of the solitary wave is given by

$$\frac{c_{c1}}{\sqrt{gh}} = 1 + \frac{a_{c1}}{2h} \tag{62}$$

wehre $a_{c1} = H$ for a solitary wave. Further this theoretical approximation is equal to

$$\frac{c_{c1}}{\sqrt{gh}} = \sqrt{1 + \frac{a_{c1}}{h}} \tag{63}$$

for small relative wave crest amplitudes, a_{c1}/h (Russell (1844)). While Eq. 62 corresponds to the first approximation of the Laitone theory (Laitone (1960)), Eq. 63 was also obtained as a first approximation to the theoretical studies of Boussinesq (1872), Rayleigh (1876) and McCowan (1891).

Equations. 62 and 63 also compare well with experimental observations of Dailey and Jr. (1953) and Naheer (1978). The breaking limit for solitary waves was given by McCowan (1894) as $H_b/h = 0.78$. Hence the theoretical relationships given by Eqs. 62 and 63 allow wave velocities up to 39% and 33% respectively, beyond the linear shallow water assumption of $c = \sqrt{gh}$ at breaking due to wave non-linearity. This may lead to potentially hazardous early arrivals of tsunami waves compared to estimates based on linear wave theory.

The measured propagation velocity of the first three waves of the landslide generated tsunamis are shown in Fig. 75. The wave velocities are normalized by the shallow water velocity. The velocity of the leading wave crest corresponds closely to the theoretical approximation of the solitary wave speed given by Eq. 62. The amplitude dispersion quantified by the relative wave amplitude plays an important role in the variation of wave velocity as seen by the dependence of the leading wave crest and trough velocities on the wave amplitudes.

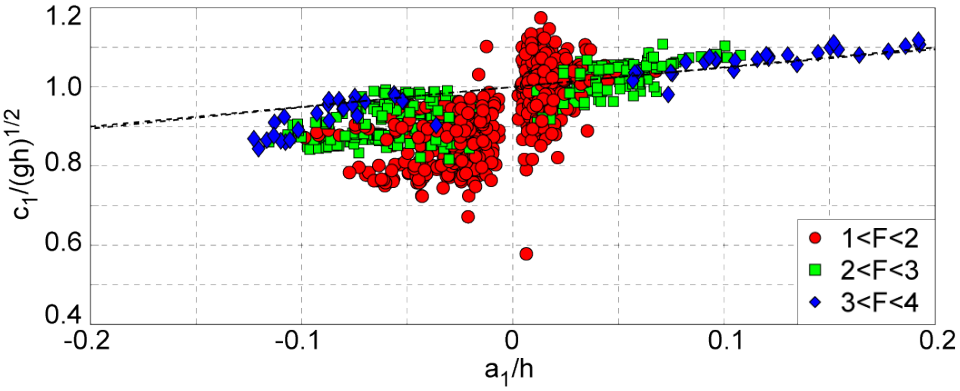

(a)

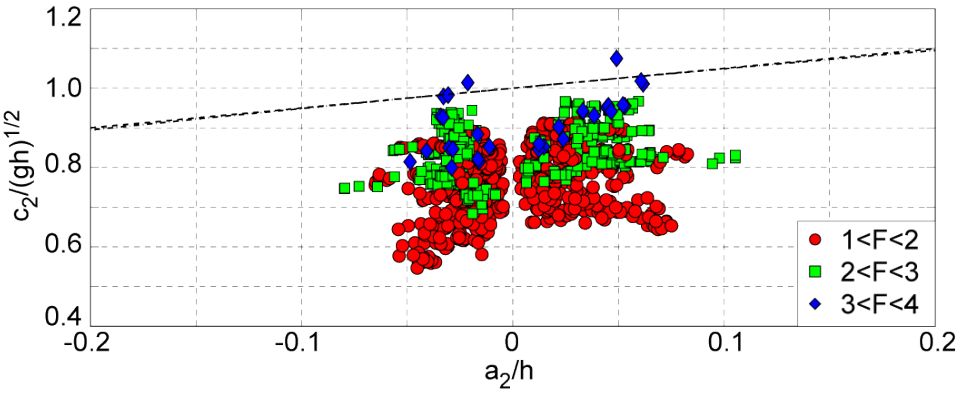

(b)

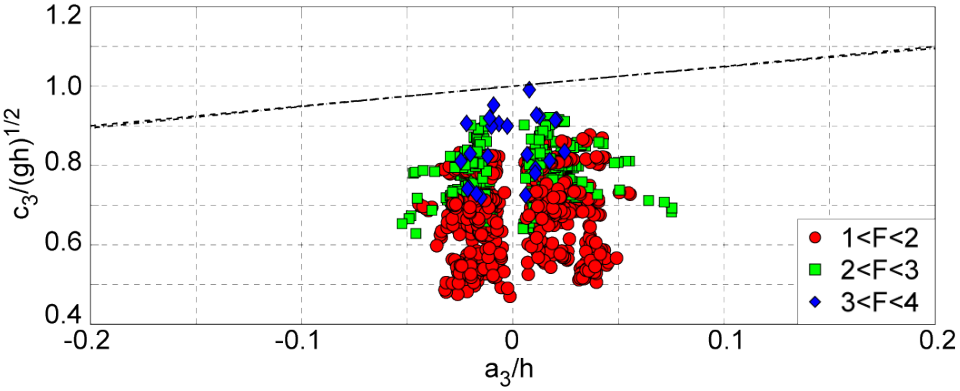

(c)

Figure 75: Wave propagation velocity: crest and trough celerities for (a) 1^{st} wave, (b) 2^{nd} wave and (c) 3^{rd} wave. Solitary wave speed approximation given by Eq. 62 is shown as dashed line in the figures.

The leading wave trough propagates with velocities close to the solitary wave speed. These are equal to or lower than the linear shallow water velocity. The crest and trough of the second wave propagate with much lower velocity compared to the leading wave. The velocity drop from the leading wave to the second wave is about 23% for the wave crest and 18% for the wave trough. The second waves propagate at speeds much lower than the linear shallow water velocity $\sqrt{gh}$. These waves are usually in the intermediate water depth regime and non-linear in nature. The propagation velocity of the third wave is lower than the leading wave and the second wave. Hence, neither linear wave theory nor solitary wave theory can be applied to study the trailing waves as these waves are usually in the intermediate to deep water regime for flat sea bed and often non-linear in nature. The reduction in the wave velocity can be explained by frequency dispersion which results in the shortening of the wave length of the trailing waves.

5.3.7 Tsunami Wave Lengths

The wavelengths are defined as the horizontal distance between the successive zero upcrossing points of the generated tsunami waves. The wavelength can be obtained from the measured wave periods by multiplying the wave period with the speed of the wave, assuming that the wave is steady in a reference frame moving with the speed of the wave. Hence, the wavelength measurement from the wave periods and wave speeds are accurate only in case of transient waves. In case of impulsively generated waves, different waves in the wave train move with different speeds. Hence, the measurement of the wavelength from the wave period and the wave speed results in a bias in the measured wavelengths. In the present study, the speed of wave is characterized as the speed of the individual wave crests and troughs. The wave celerity is approximated as the average speed of the crest and trough that was measured as the wave propagates between successive wave gauges along an angular ray. The zero

upcrossing and crest-to-crest wavelengths are measured as

$$\frac{L_i}{h} = T_i\sqrt{\frac{g}{h}}\frac{c_i}{\sqrt{gh}} \qquad (64)$$
$$\frac{L_{ci}}{h} = T_{ci}\sqrt{\frac{g}{h}}\frac{c_{ci}}{\sqrt{gh}}$$

where the subscript i denotes the number of the wave in the wave train and L_{ci} represents the wavelength measured between i^{th} crest and $(i+1)^{th}$ crest. The speed of a wave for the upcrossing wavelength is the mean of the measured wave crest and trough speed. In case of the crest-to-crest wavelength measurement, the wave speed is the mean of the two wave crests and the trough in between them. The definition of the zero upcrossing and crest to crest wavelength measurements are shown in Fig. 76.

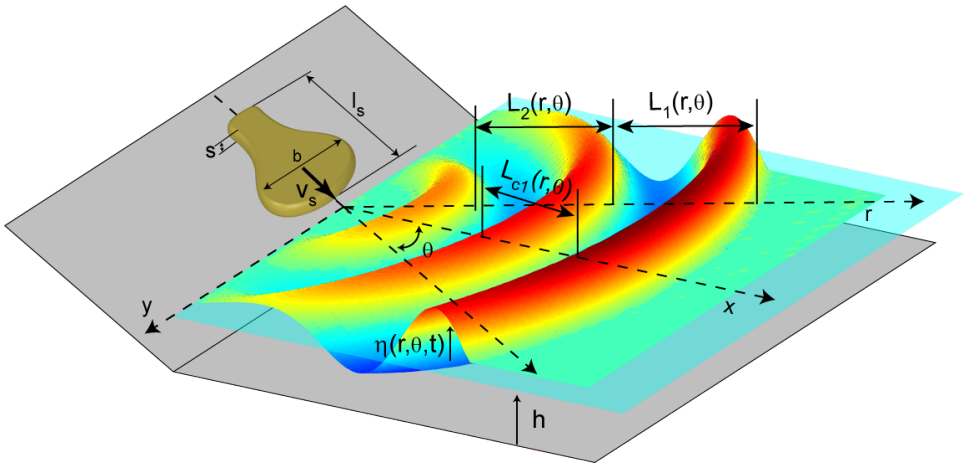

Figure 76: Definition of upcrossing and crest-to-crest wavelengths in a radial wave front.

The upcrossing wavelengths of the leading wave front L_1/h are determined in the propagation range $4 < r/h < 80$ and $0^o < \theta < 90^o$, across all the experimental trials. The measured upcrossing wavelengths are in the range $5 < L_1/h < 24$, while the crest-to-crest wavelength are in the range $3 < L_{c1}/h < 18$. The crest-to-crest wavelengths are considerably shorter than the upcrossing wavelength of the leading wave. The reduction on average was $25-33\%$. The wavelengths are found to increase

with the propagation distance from the landslide source. However, the variations in the wavelength with respect to the angular direction is found to be minimal. The landslide generated tsunami waves in three dimensional setup propagate as a wave front in the radial direction with nearly constant wave periods and wavelengths across a particular wave front with respect to the angular direction.

The uprossing wavelengths of the second waves are in the range $2 < L_2/h < 11$, while the crest to crest wavelengths follows $2.5 < L_{c2}/h < 12$. Unlike the leading wave, the crest-to-crest wavelength for the second wave is marginally higher than the upcrossing wavelengths. The minimal difference between the upcrossing and crest wavelengths lead to the presence of weakly non-linear oscillatory type of waves. Based on the measured wavelength ranges, the generated waves are mostly in the intermediate water depth regime $2 < L/h < 20$, except for a few cases where the waves reached the shallow water depth regime $L/h > 20$ for the first wavelength. The wavelength decreases in the wave train from the front of the wave train towards the back.

A multi-variable regression analysis for the wavelength data allows decoupling the wave generation mechanism and the wave propagation properties of the generated wave. The evolution of the wavelengths with the propagation distance can be described by the function

$$\frac{L_i}{h} = k_{Li} f\left(\frac{r}{h}\right) \tag{65}$$

where the subscript i refers to the number of the wave in the wave train, k_{Li} is the wavelength parameter for the i^{th} wave that defines the wave generation mechanism through the landslide parameters and $f(r/h)$ describes the evolution of the wavelength with propagation distance r/h. The wavelength function shown in Eq. 65 is independent of the angular direction with an assumption that the radial wave front has a constant wave period and wavelength. The multiple regression analysis for the

first three waves resulted in the following empirical functions for the wavelengths

$$\begin{aligned} \frac{L_1}{h} &= k_{L1}\left(\frac{r}{h}\right)^{0.3} \\ \frac{L_2}{h} &= k_{L2}\left(\frac{r}{h}\right)^{0.25} \\ \frac{L_3}{h} &= k_{L3}\left(\frac{r}{h}\right)^{0.25} \end{aligned} \tag{66}$$

with the correlation coefficients r_2 =0.98, 0.91 and 0.86 for the first, second and the third wave front respectively. The description of the wavelength parameter k_{Li} is described in Sec. 5.3.8. The wavelength evolution with the propagation distance for the first three wave fronts of the generated wave train is shown in Fig. 77. The relative wavelengths are normalized with the wavelength parameter k_L for comparison between the different waves of the wave train. The evolutions are shown as $(1/k_{Li})(L_i/h)$ versus the propagation distance r/h.

In an experimental study, Kamphuis and Bowering (1970) observed a linear variation of the measured wavelength with propagation distance given by

$$\frac{L_{Kamphuis}}{h} = 11 + 0.225\left(\frac{x}{h}\right) \tag{67}$$

The evolution of wavelengths with propagation distance was given by Huber (1980) as

$$\frac{L_{Huber}}{h} = 3\left(\frac{x}{h}\right)^{0.45} \tag{68}$$

In that study, Huber (1980) measured wave lengths in the range $4 < L_{Huber}/h < 40$ over the propagation distance range $5 < x/h < 100$. The experimental study of Fritz (2002) led to an empirical form for the wavelength of the leading wave as

$$\frac{L_{fritz}}{L_1(x/h=5)} = 0.6\left(\frac{x}{h}\right)^{1/3} \tag{69}$$

with the reference point taken at the location $x/h = 5$. Since the wavelength definitions vary in the different experimental studies, the empirical equations for the wavelengths are non dimensionalized with the wavelength at a reference location of

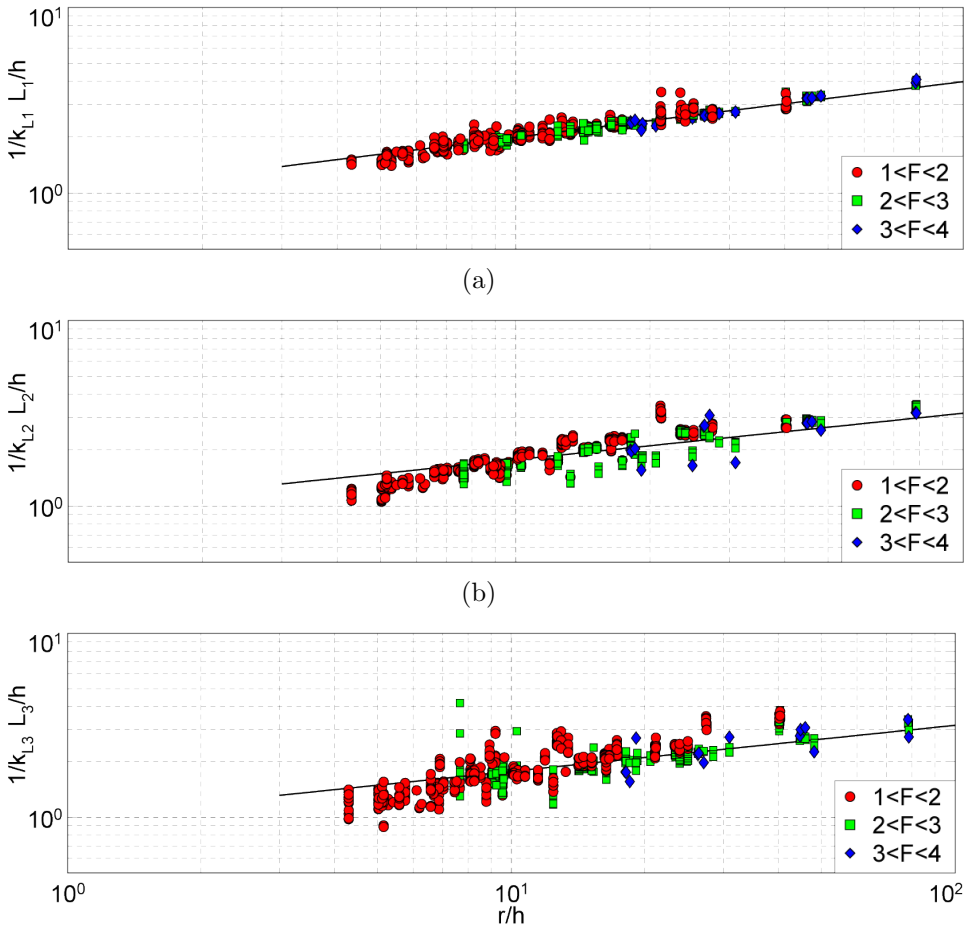

Figure 77: Measured wavelength as function of propagation distance r/h for (a) 1^{st} wave, (b) 2^{nd} wave and (c) 3^{rd} wave.

$x/h = r/h = 5$ to maintain a uniform definition of the wavelengths. The wavelengths in the various study can then be summarized as

$$\frac{L_1}{L_1(r/h=5)} = 0.6\left(\frac{r}{h}\right)^{0.3} \text{ (Present study)} \tag{70}$$

$$\frac{L_{Fritz}}{L_1(x/h=5)} = 0.6\left(\frac{x}{h}\right)^{1/3} \text{ (Fritz (2002))} \tag{71}$$

$$\frac{L_{Huber}}{L_1(x/h=5)} = 0.5\left(\frac{x}{h}\right)^{0.45} \text{ (Huber (1980))} \tag{72}$$

$$\frac{L_{Kamphuis}}{L_1(x/h=5)} = \frac{1}{12}\left(11 + 0.225\left(\frac{x}{h}\right)\right) \text{ (Kamphuis and Bowering (1970))} \tag{73}$$

The comparisons of the wavelength estimates normalized at $x/h = r/h = 5$ is

shown in Fig. 78.

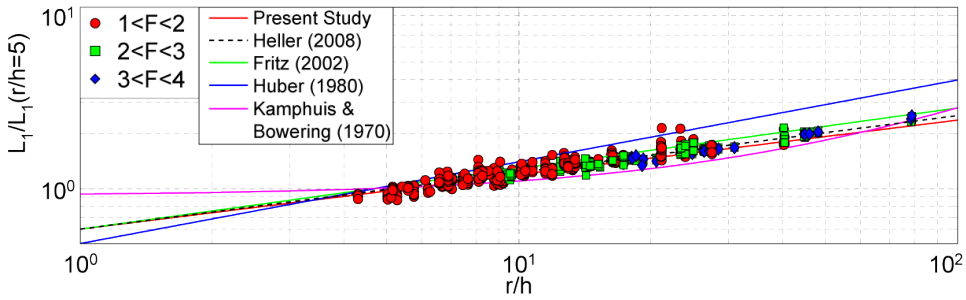

Figure 78: Evolution of wave length of the leading tsunami wave L_1 with propagation distance r/h compared with the study of Kamphuis and Bowering (1970), Huber (1980), Fritz (2002) and Heller (2008).

5.3.8 Wave Length Prediction

The multi-variable regression analysis for the wavelength parameter k_L for the leading wave front resulted in

$$k_{L1} = 4.5 \left(\frac{s}{h}\right)^{0.07} \left(\frac{V}{sbh}\right)^{0.06} \left(\frac{v_s}{\sqrt{gh}}\right)^{0.18} \tag{74}$$

with a correlation coefficient $r^2 = 0.93$. The dominant non-dimensional variables are the slide Froude number $F = v_s/\sqrt{gh}$ with minor dependence on relative slide length $L = V_s/(sbh)$ and relative thickens at impact $S = s/h$. Thus the empirical predictive equation for the wavelength of the leading wave front in the generated wave train is obtained as

$$\frac{L_1}{h} = 4.5 \left(\frac{s}{h}\right)^{0.07} \left(\frac{V}{sbh}\right)^{0.06} \left(\frac{v_s}{\sqrt{gh}}\right)^{0.18} \left(\frac{r}{h}\right)^{0.3} \tag{75}$$

with a correlation coefficient of $r^2 = 0.97$. The comparison between the measured and the predicted values of the first wavelength is shown in Fig. 79(a).

The multi-variable regression analysis for the wavelength parameter for the 1^{st} trailing wave resulted in a prediction equation for the wavelength as

$$\frac{L_2}{h} = 2.15 \left(\frac{s}{h}\right)^{0.07} \left(\frac{V}{sbh}\right)^{0.05} \left(\frac{v_s}{\sqrt{gh}}\right)^{0.23} \left(\frac{r}{h}\right)^{0.25} \tag{76}$$

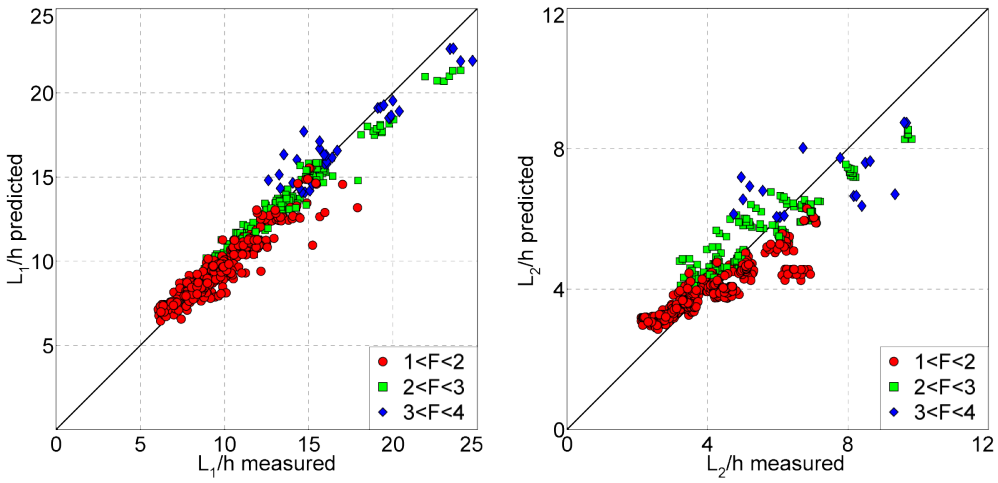

(a) (b)

Figure 79: Comparison between measured and predicted values of upcrossing wavelengths for (a) for the 1^{st} wave with Eq. 75 and (b) 2^{nd} wave with Eq. 76.

with a correlation coefficient for the wavelength parameter k_{L2} as $r^2 = 0.93$ and the wavelength L_2 as $r^2 = 0.9$. The dominant parameter in this case is also the slide Froude number at impact with some minor dependency on the relative slide length and thickness. The comparison between the measured and predicted values corresponding to the wavelength of the second wave is shown in Fig. 79(b). The regression analysis for the wavelength of the 3^{rd} wave remained inconclusive regarding the landslide parameters due to the weak dependence of the trailing waves on the landslide as a direct wave generation mechanism.

5.3.9 Tsunami Wave Non-Linearity

The wave non-linearity can be defined by three parameters:

- relative wave height H/h or amplitude a/h,
- wave steepness H/L, and
- Ursell number $U = (a_c L^2)/h^3$.

The importance of the above parameters depends on the water depth regime in which the wave is present. In the shallow water regime, the relative wave height or the

amplitude are important while in the deep water regime, the most relevant parameter is the wave steepness. In intermediate water depths, the most important parameter is the Ursell number, while the other two parameters may also be considered. As shown in the previous section, most of the landslide generated waves are in the intermediate water depth regime with $2 < L/h < 20$. The measured wave crest amplitudes in the present study are in the range $0.001 < a_c/h < 0.2$. Hence, while most generated waves are in the non-linear regime, some of the generated waves were in the weakly non-linear regime as well. It was also seen that the wave propagation velocity is governed by the amplitude dispersion effects. Hence, the higher order terms become important in the description of the wave unlike linear wave theory which includes only frequency dispersion but does not account for amplitude dispersion.

The evolution of the wave steepness for the leading wave H_1/L_1 with the propagation distance is shown in Fig. 80(a). The wave steepness is determined over the propagation distance $5 < r/h < 80$ across all the experimental trials. The wave steepness decreases with the propagation distance in accordance with a simultaneous wave amplitude decay and wave length increase with the propagation distance. The wave steepness for the leading wave is in the range $6 \times 10^{-4} \leq H_1/L_1 \leq 0.025$. While the condition for linear theory is $H/L < 0.006$, the generated waves within this range shown in Fig. 80(a) are not necessarily in the linear wave regime. These waves are often in the intermediate water depth regime and hence the Ursell number is analyzed for studying the wave non-linearity. The evolution of the Ursell number for the leading wave with propagation distance is shown in Fig. 80(b). The Ursell number for the 1^{st} wave increased with propagation distance and was found in the range $0.2 < U_1 < 55$. The condition for non-linearity with respect to the Ursell number is $U > 1$ (Lighthill (1978)). Hence, the generated waves are in the non-linear regime based on the Ursell number in the intermediate water depth regime. The majority of the leading tsunami waves have $U_1 < 26$, which is the limit for the applicability of cnoidal wave theory.

Most leading tsunami waves generated by 3D granular landslides may be described by Stokes theory in the intermediate water depth range. An increase in the landslide Froude number may lead to tsunami waves which may be described by cnoidal theory if the Ursell number satisfies $U_1 > 26$ in the intermediate water depth range.

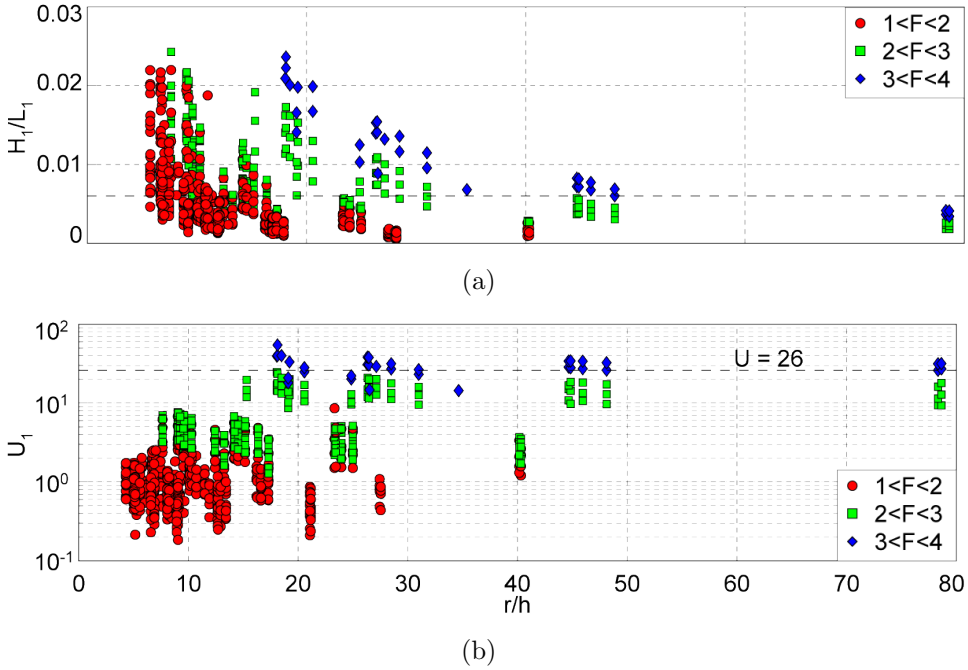

Figure 80: Leading wave non-linearity: (a) wave steepness H_1/L_1 versus propagation distance r/h with linear limit $H_1/L_1 = 0.006$; (b) Ursell number $U_1 = (a_{c1}L_1^2)/h^3$ versus propagation distance r/h with $U_1 = 26$.

The evolution of wave steepness and the Ursell number for the second wave of the generated wave train with propagation distance is shown in Fig. 81. The wave steepness in general decays with the propagation distance and is in the range $0.0015 < H_2/L_2 < 0.075$. The wave steepness of the second wave is larger than the first wave. When compared with the leading wave, the wave lengths of the second wave was smaller than the leading wave, which results in increased wave steepness of the second wave. The Ursell number for the second wave is in the range $0.02 < U_2 < 4$. While the wave steepness of some of the generated waves indicates linear waves, the Ursell parameter provides that the waves are linear if $U_2 < 1$ in the intermediate water

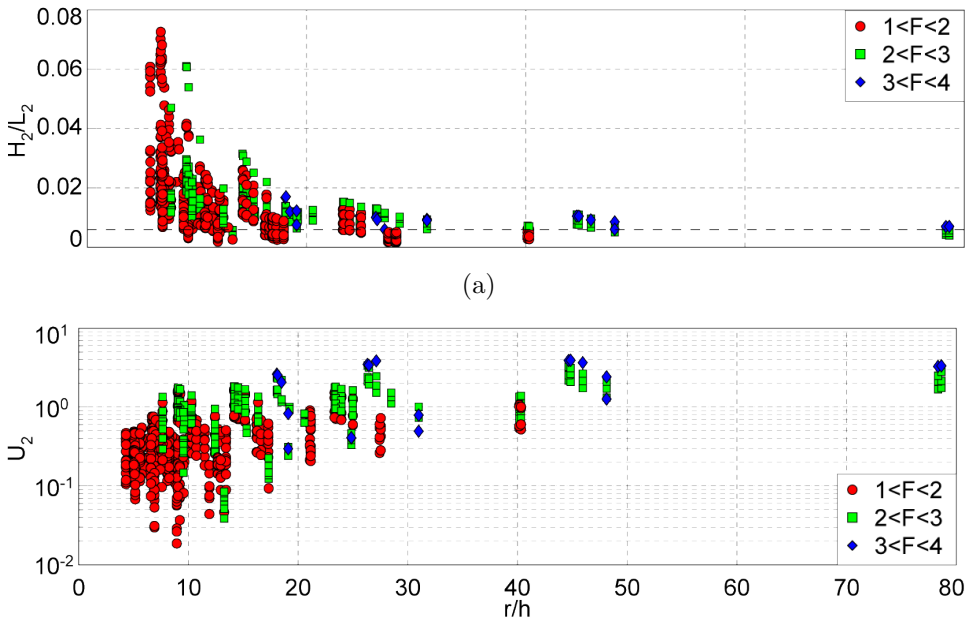

Figure 81: Second wave non-linearity: (a) wave steepness H_2/L_2 versus propagation distance r/h with linear limit $H_2/L_2 = 0.006$; (b) Ursell number $U_2 = (a_{c2}L_2^2)/h^3$ versus propagation distance r/h.

depth regime, $2 < leqL_2/h \leq 20$.

The wave steepness and Ursell number for the third wave is shown in Fig. 82. The wave steepness decays with propagation distance in the range $0.002 < H_2 < L_2 < 0.06$ while the Ursell parameter is in the range $0.007 < U_2 < 2$. Based on the Ursell parameter alone, most of the 3^{rd} tsunami waves may be described by linear Airy theory since almost all the waves satisfy $U_3 < 1$.

5.3.10 Energy Conversion

The wave generation process by the impact of landslides on a water body can be studied through the conversion rate of energy from the landslide into the water body. Herein, the kinetic energy of the landslide at impact is considered as source for the energy transfer. The non-dimensional kinetic energy of the landslide at impact may be given as

$$E_s = \frac{1}{2}DVF^2 \tag{77}$$

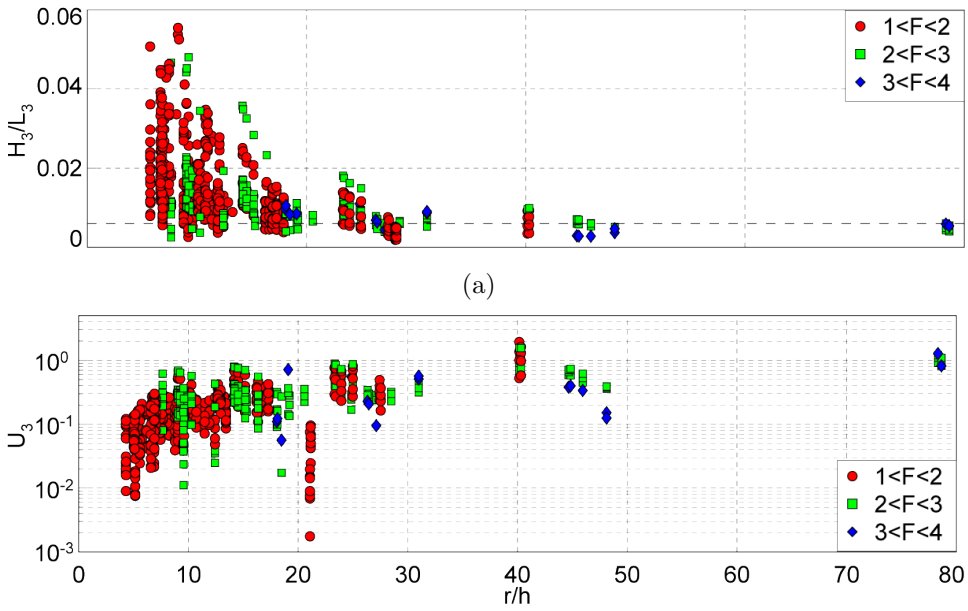

Figure 82: Third wave non-linearity: (a) wave steepness H_3/L_3 versus propagation distance r/h with linear limit $H_3/L_3 = 0.006$; (b) Ursell number $U_3 = (a_{c3}L_3^2)/h^3$ versus propagation distance r/h.

where $V = V_s/h^3$ is the relative landslide volume, D is the ratio of landslide density to water density and $F = v_s/\sqrt{gh}$ is the landslide Froude number at impact.

The wave energy comprises of two contributions: the wave kinetic energy which is composed of the water particle motion in the water body and potential energy due to the displacement of water particles from their mean position. The non-dimensional wave potential energy per unit width of the wave front from the wave profile measurements is determined as

$$dE_{pot} = \frac{1}{2}\frac{c}{\sqrt{gh}}\int_0^{T\sqrt{g/h}} \left(\frac{\eta}{h}\right)^2 dt\sqrt{g/h} \tag{78}$$

In a three-dimensional cylindrical coordinate system, the generated wave propagates as a radial front away from the landslide source. Hence the energy measured is a function of radial propagation distance and direction $dE_{pot}(r/h, \theta)$. The total potential energy of the wave front at propagation distance r/h is computed as

$$E_{pot} = \int_{-\frac{\pi}{2}}^{\frac{\pi}{2}} \left(\frac{1}{2}\frac{c}{\sqrt{gh}}\int_0^{T\sqrt{g/h}} \left(\frac{\eta}{h}\right)^2 dt\sqrt{g/h}\right)\frac{r}{h}d\theta \tag{79}$$

at a propagation distance r/h from the landslide source. Since the measured wave trains were transient and non-stationary in a moving reference frame, the individual wave crests and troughs propagated with varying velocities. This variation in the velocity was taken in account by measuring the potential energy of each individual crest and trough in the generated wave train. Since the wave profiles were measured at positions (r, θ) with respect to the origin at landslide impact location, the measurements are approximated as $dE_{pot} = f(r/h, \theta)$. This enables the interpolation of the energy measurements between the range $0 \leq r/h \leq R_{max}$ and $-\pi/2 \leq \theta \leq \pi/2$. The approximation for the leading wave crest was obtained as

$$dE_{pot}(r/h, \theta) = k_{Ec1} \left(\frac{r}{h}\right)^n \cos^2 \theta \tag{80}$$

where the rate of decay n varies for all the experimental trials analogous to the wave amplitude decay rate (see Sec. 5.3.1). The total potential energy of the wave front crest at propagation distance r/h away from the landslide source is measured as

$$E_{pot}(r/h) = \int_{-\frac{\pi}{2}}^{\frac{\pi}{2}} dE_{pot}(r/h, \theta) \left(\frac{r}{h}\right) d\theta \tag{81}$$

The kinetic energy of the generated waves is difficult to estimate directly due to lack of measurements regarding the water particle kinematics in the water column. The total wave energy may be estimated as $E_{tot} \approx 2E_{pot}$ by assuming equipartition of energy between potential and kinetic wave energy. The energy packet of the leading wave crest was found to decrease with the propagation distance attributed to dispersion and stretching of the wave energy packet of the impulse wave train. The decay of the wave energy of the leading wave crest with propagation distance r/h is shown in Fig. 83

The decay of the leading wave crest energy varies strongly with propagation distance r/h. In some cases, the energy decays rapidly as $E_{cr1}(r/h = 6)/E_{cr1}(r/h = 4) = 0.5$ for intermediate water depth regimes, while in some cases the decay is more gradual with $E_{cr1}(r/h = 32)/E_{cr1}(r/h = 4) = 0.5$ for shallow water depth waves.

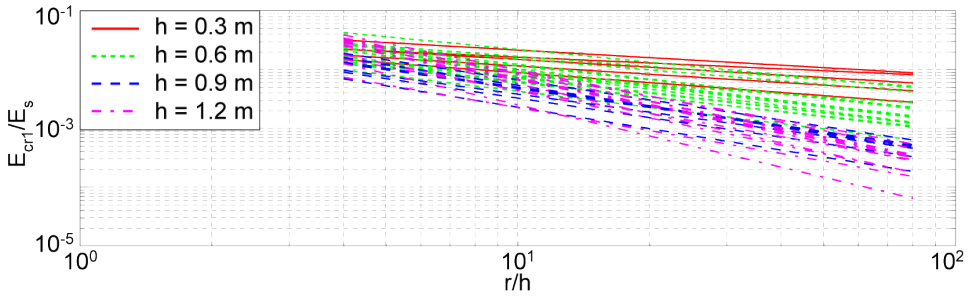

Figure 83: Decay of leading wave crest energy relative to landslide kinetic energy at impact with propagation distance r/h.

The decay rate strongly depends on the energy transfer from the landslide to the generated wave, the water depth regime and the non-linearity of the generated wave. The energy decay in the leading wave crest is due to the dispersion of the waves in the intermediate water depth regime. A part of the leading wave energy is transferred to the trailing waves in the wave train.

The multi-variable regression analysis for the leading wave crest energy $E_{c1}(r/h = 10)/E_s$ in terms of the landslide parameters yields

$$\frac{E_{cr1}(r/h=10)}{E_s} = 0.02\left(\frac{s}{h}\right)^{1}\left(\frac{V_s}{h^3}\right)^{-0.1}\left(\frac{v_s}{\sqrt{gh}}\right)^{0.8} \tag{82}$$

with correlation coefficient $r^2 = 0.86$. The comparison between the measured and predicted values computed with Eq. 82 is shown in Fig. 84(a). The dominant parameters are the slide Froude number and the relative thickness at impact. The dependency of the measured energy with slide thickness is shown in Fig. 84(b) where the regression has a correlation coefficient $r^2 = 0.86$. Between $0.5\% - 3\%$ of slide energy was transferred to the leading wave crest energy, which decays gradually away from the landslide source due to wave transfer into the trailing waves and wave dispersion effects.

The energy of the wave train is measured analogous to the energy measurement of the leading wave crest. Since the wave speed is different for different waves in the generated wave trains, the energy in the individual crests and troughs are measured

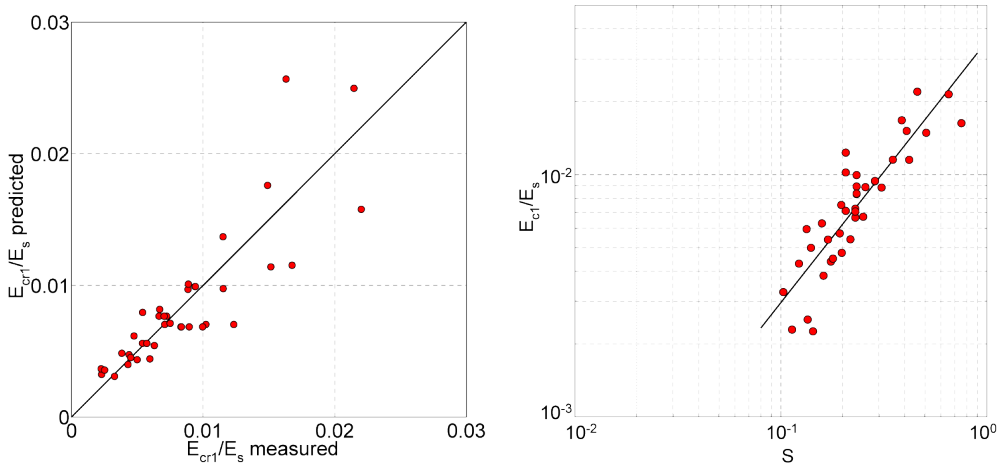

Figure 84: Energy of the leading wave crest: (a) $E_{c1}(r/h = 10)/E_s$ measured versus compared with Eq. 82; (b) $E_{c1}(r/h = 10)/E_s$ versus $S = s/h$ with regression $r^2 = 0.86$.

and added to get the energy of the wave train. The wave train measurement comprises of the energy packet in the first three waves. The wave profile recordings yielded the first three waves clearly and the wave profile beyond the first three waves were prone to reflection effects. Assuming equipartition the total non-dimensional energy of the wave train at the wave gauge per unit wave front is measured as

$$E_{wt} = \sum_{i=1}^{6} \frac{c_i}{\sqrt{gh}} \int_{T_i}^{T_{i+1}} \left(\frac{\eta}{h}\right)^2 dt \sqrt{\frac{g}{h}} \tag{83}$$

where the water surface between T_i and T_{i+1} represent a wave crest or trough depending on the index i. The decay of the wave train energy with propagation distance is shown in Fig. 85

The energy of the wave train is observed to decay with propagation distance away from the landslide source. But the decay rate, in general, is lower than the decay rate of the leading wave crest energy. Between $1\% - 15\%$ of the landslide energy was converted into the wave train energy. The multi-variable regression analysis for the wave train energy results in

$$\frac{E_{wt}}{E_s} = 0.15 \left(\frac{s}{h}\right)^{1.1} \left(\frac{V_s}{h^3}\right)^{-0.7} \left(\frac{v_s}{\sqrt{gh}}\right)^{1} \tag{84}$$

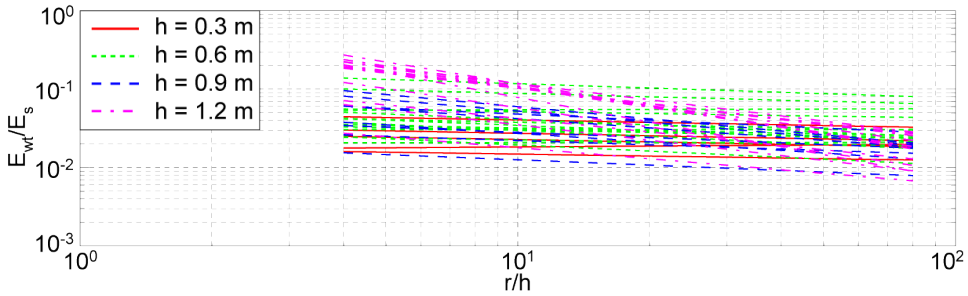

Figure 85: Decay of energy of the wave train relative to landslide kinetic energy at impact with propagation distance r/h.

with correlation coefficient $r^2 = 0.89$. The dominant parameters are the landslide Froude number and relative slide thickness at impact with dependencies on the relative slide volume. The comparison between the measured and predicted energy of the wave train is shown in Fig. 5.3.10. The wave generation efficiency increases with decreasing landslide volumes and increasing landslide thickness at impact. A similar behavior for wave conversion efficiency can be seen with explosions for increasing yield in the same water depth (LeMéhauté and Khangoankar (1992)).

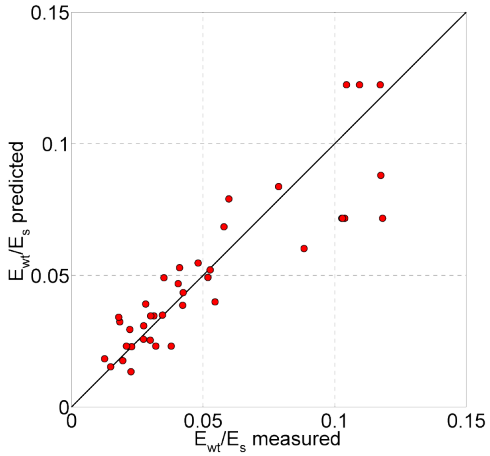

Figure 86: Energy of the wave train : $E_{wt}(r/h = 10)/E_s$ measured versus compared with Eq. 84.

The partition of the wave energy can be analyzed by normalizing the wave energy of the leading wave crest with the energy of the wave train. The multiple regression analysis for the ratio of the leading wave crest energy and wave train energy at

$r/h = 10$ results in

$$\frac{E_{c1}}{E_{wt}}(r/h = 10) = 0.125 \left(\frac{V_s}{h^3}\right)^{0.6} \left(\frac{v_s}{\sqrt{gh}}\right)^{0.3} \tag{85}$$

The comparison between the measured and predicted values of the energy partition between leading wave crest and wave train is shown in Fig. 87(a). The partition of energy between the leading wave crest and the wave train is observed to increase with an increase in the landslide volume or the landslide Froude number at impact. The measured energy in the leading wave crest at $r/h = 10$ versus the energy of the wave train at the same location is shown in Fig. 87(b). The theoretical maximum for the ratio E_{c1}/E_{wt} is 1 and none of the experimental trials exceeded this limit.

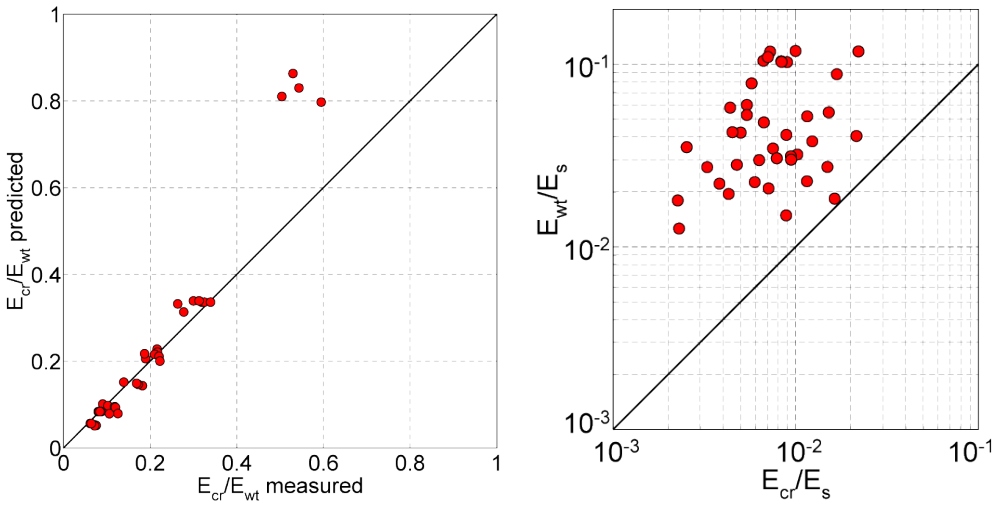

(a) (b)

Figure 87: Wave energy partition between leading wave crest and wave train: (a) comparison between measured and predicted at $r/h = 10$ with Eq. 85, (b) leading wave crest energy E_{cr}/E_s versus wave energy train E_{wt}/E_s at $r/h = 10$. Solid line represents $E_{cr} = E_{wt}$.

In a 2D experimental study conducted by Kamphuis and Bowering (1970), the landslide to wave energy conversion ranged from $10\% - 50\%$. The landslide was modeled as a weighted tray on a slope. The energy conversion was observed to decrease with increasing hill slope angle. Hill slope with $\alpha = 90^o$ resulted in the lowest conversion rates in the study. Huber (1980) measured the energy conversion rates

between granular landslides and wave between $1-40\%$. The accuracy of this estimate however is low since the energy was measured electronically by integrating the square of the analog signal and multiplying the sum by half. A similar measurement was made by Kamphuis and Bowering (1970). The granular landslide studies by Fritz (2002) led to measurement of energy conversion between landslide and leading wave crest in the range $2-30\%$ at a distance $x/h = 8$ from the impact. The conversion in case of the wave train was measured between $4-50\%$ at the same location. The flume experiments also provided a good comparison between the leading wave energy and the energy of a solitary wave with the same characteristics. In a different study, Watts (2000) determined the energy conversion rates between $2-13\%$ where the source is an underwater landslide block. Ataie-Ashtiani and Nik-Khah (2008) observed an energy conversion rate between $5-50\%$ with varying solid block landslides as the source of the wave generation. Heller (2008) measured energy conversion rates between $11.3-85.7\%$ for granular landslides.

An analogy to wave generation by landslide impacts can be made with wave generation by projectile impacts and underwater explosions. Gault and Sonett (1982) determine energy conversion rates for projectile impacts on water surfaces of 7% for a projectile impacting at $Ma = 7.5$. Jordaan (1969) estimated about 40% of underwater explosion energy is available to displace the water around the explosion. Underwater explosions in general were found to be inefficient wave generators. LeMéhauté and Khangoankar (1992) showed that in shallow waters when the explosion bubbles reaches the sea bed, at most 5% of the energy is transferred into the water body. The efficiency in shallow waters rapidly increased with increasing water depths and decreasing explosion yields. In water bodies of same depths, lower yield explosions are more efficient than higher yield explosions for wave generation. In deep water, LeMéhauté and Wang (1995) observed a maximum efficiency of 20% for the wave

generation. Most of the energy released in explosions is divided about equally between shock wave and thermal radiation effects, both of which are negligible regarding tsunami wave generation. A large portion of explosion energy that gets converted into potential energy during crater formation is lost to hydrodynamic dissipation during the crater collapse. The energy dissipated remained at about 40% (LeMéhauté and Khangoankar (1992)).

In comparison with 2D studies, the present 3D study yield lower energy conversion rates when compared with Kamphuis and Bowering (1970), Huber (1980), Fritz (2002), Heller (2008), Ataie-Ashtiani and Nik-Khah (2008). The 2D experiments result in efficient wave landslide tsunami wave generation since there is only one unconfined direction in the vertical where the water body can move. In comparison, there is no such confinement of the water body in 3D. During the landslide impact, the water body can flow through the side and around the landslide which decreases the efficiency of the wave generation. The landslide deformation is larger in 3D compared with 2D due to less constraint on the landslide motion. A bulk of the slide energy is lost into frictional effects during the sub aerial and sub aqueous motion. The unconfined granular landslide motion further loses energy as the landslide mass undergoes internal deformation during the motion. Additional energy is lost during the slide deflection from the hill slope onto the horizontal basin bottom. Energy dissipation also decreases the energy conversion during the collapse of the impact crater. Thus the resulting available energy is spread in the angular direction through the radial wave front propagation. The distribution of the wave energy packets in the generated wave train decays the energy of the wave with propagation direction.

5.4 Application of classical wave theories

5.4.1 Introduction

An understanding of the wave theory classification is essential in predicting the wave characteristics such as wave celerity, wave periods, wavelengths, dispersion effects, wave amplitude behavior through an analytical approach. The number of parameters that define a wave enable several types of wave classification. The waves can be primarily defined as an oscillatory or a translatory wave. The difference between the two arise from the mass transport by the wave. A purely oscillatory wave does not transport any mass, whereas a purely translatory wave transports mass. In reality, the ocean waves can be composed of both oscillatory and translatory waves, e.g wind waves. The next classification may be made in terms of the relative wave characteristics to the water depth as shallow, intermediate or deep water waves. A wave can undergo transformation from deep to shallow water during the course of its propagation. A formal classification of water wave theories was given by LeMéhauté (1976) based on the wave characteristics. A further classification and overview of wave theories was given by Lamb (1945), Wehausen and Laitone (1960), Ippen (1966), Dean (1970), Mei (1989), Dean and Dalrymple (2004). Historical reviews of wave theories was presented by Craik (2004), Sander and Hutter (1991) and Grimshaw (2007).

5.4.2 Classification of wave theories

The wave theories may be classified based on

- relative wave height H/h
- wave steepness H/L
- relative wave length L/h
- Ursell parameter $U = HL^2/h^3$

as linear or nonlinear waves. The limit value of the above parameters for wave classification was given by LeMéhauté (1976).Linear wave theories are valid for the range given by $H/h << 1$ and $U << 1$. Further linear waves can be classified into shallow water waves, intermediate water waves and deep water waves depending on the relative wave length as $L/h > 20$, $2 \leq L/h \leq 20$ and $L/h < 2$.

$$\begin{aligned} L/h &> 20 \text{ Linear Long Wave Theory (Airy)} \\ 2 \leq L/h &\leq 20 \text{ Small Amplitude Wave Theory } 1^{st} \text{ order (Airy)} \\ L/h &< 2 \text{ Small amplitude Wave Theory } 1^{st} \text{ order (Airy)} \end{aligned} \tag{86}$$

The linear long wave theory has assumptions of oscillatory wave type, irrotationality of the flow and hydrostatic pressure distributions. The small amplitude wave theory has the assumptions of oscillatory wave type, non-hydrostatic pressure distribution and irrotational flow in the water body.

The nonlinear wave theories can be classified as

- **Case:** $H/h << 1$ **&** $U < 10$

  There exist different wave theories to describe the wave characteristics in intermediate and shallow water depth regime. The shallow water wave $L/h > 20$ can be described by the Trochoidal wave theory (Gerstner) with the assumptions of oscillatory wave type, rotational flow fields in the water column and non-hydrostatic pressure distribution. The intermediate water wave can be described by either small amplitude wave theory by Stokes or Miche/Dubreil-Jacotin based on the assumptions of irrotationality or rotationality of the flow field. The oscillatory wave type and non hydrostatic pressure distribution assumptions are still made for both the theories.

- **Case:** $H/h < 1$ **&** $U \approx 1$

  The wave theories in this case are valid for intermediate to shallow water depth regimes given by $L/h > 10$. The presented water wave theories in this range are

the cnoidal wave theory given by Korteweg and de Vries, Solitary wave theory given by Scott-Russell and the solitary wave theory given by Boussinesq. While the cnoidal wave theory describes oscillatory type of wave form, the solitary wave theories in both the cases describe a translatory type of wave.

- **Case: All H/h & $U \gg 1$**

  The wave theories for this case are described for shallow water depths $L/h \gg 20$. In this regime, the wave theories have the assumptions of irrotational flow field and hydrostatic pressure distribution. The wave types described are translatory waves. The long wave theory by Airy, theory of tidal bore by Saint Venant and roll waves and flood wave and monoclinal wave theories by Thomas are valid in this regime.

5.4.3 Linear wave theory

The linear wave theory is so called because the terms of higher order in the derivation such as $(H/L)^2$ are neglected in the free surface boundary condition and water particle velocity components (Airy (1845)). The resulting equations defining the wave characteristics is known as Airy theory, linear wave theory, small amplitude wave theory and sinusoidal wave theory. The general range of validity of the linear wave theory is given by

$$H/h < 0.03H/L < 0.006 \tag{87}$$

which results in $U \to 0$. This theory has wide engineering applications and is used across shallow, intermediate and deep water depth regimes. The primary parameters that describe the wave are the wave length L, wave height H or wave amplitude a. The wave celerity c and the wave period T can be determined theoretically from these quantities. The wave propagation velocity or the wave celerity is theoretically defined as

$$c = \sqrt{\frac{g}{k}\tanh(kh)} = \frac{g}{\omega}\tanh(kh) \tag{88}$$

where k is the wave number and $\omega = 2\pi/T$ is the wave frequency. The wave length and wave period are related as $c = L/T = \omega/k$. In deep water $L/h < 2$, the wave speed is given as $c = gt/2\pi$ and in shallow water $L/h > 20$, $c = \sqrt{gh}$. Equation 88 can be rearranged to obtain the wave length in terms of the wave period as

$$L = \frac{gT^2}{2\pi} \tanh\left(\frac{2\pi h}{L}\right) \tag{89}$$

The wave celerity equation and its asymptotes are shown in Fig. 88. The experimental wavelength measurements for the first three waves are shown in the same figure. The frequency dispersion effects causes the wave group to stretch in the intermediate and deep water depth regime due to wave period dependent propagation velocity. In shallow water the wave celerity depends only on the water depth as given by the asymptote, while in intermediate water depths, the wave celerity depends on the water depth and the wave period.

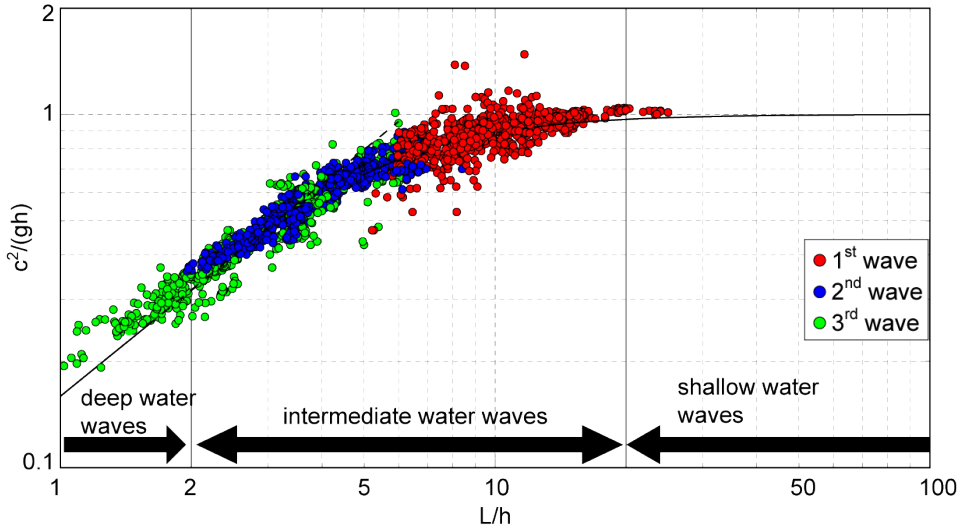

Figure 88: Nondimensional wave celerity versus non dimensional wave length shown for linear wave theory according to Eq. 89 (Dean and Dalrymple (2004)). The measured wave length of the first three waves is shown as point cloud.

The dispersion effects of the experimental data is shown in Fig. 88. The wave characteristics of the wave train vary from the leading wave towards the back of the train. Landslide generated waves span from shallow water depth to deep water depth

regime from the front of the wave train towards the rear.

5.4.4 Nonlinear wave theory

The nonlinear water wave theories are established by including the higher terms such as $(H/L)^2$ in the governing equation and boundary conditions. The nonlinear waves may still be periodic in nature but the wave profile is more peaked at the crest and flat at the trough when compared with the sinusoidal wave forms. The water particles under nonlinear waves describe open paths and hence the wave propagation includes mass transport. The set of nonlinear equations that govern the wave motion are governed by nonlinear partial differential equations which are usually difficult to solve analytically. In most cases, the governing equations may be solved numerically. As an effect of the inclusion of higher order terms in the equations, the resulting wave characteristics such as the wave periods, wavelengths and wave celerities depend on the wave amplitudes as well. Unlike linear wave theory, no nonlinear theory exists which covers the entire range from shallow water depths to deep water depths. The classical wave theories for nonlinear waves can be described based on the importance of key non dimensional wave parameters: relative wave length L/h, relative wave height H/h or amplitude a/h and the wave steepness H/L. These non dimensional parameters result in the Ursell parameter $U = HL^2/h^3$, which gives the ratio of nonlinear effects to dispersive effects. In deep water, the significant parameter was found to be the wave steepness, while the relative wave length and the wave height are the key parameters in the shallow water depth regime. In intermediate waters, the Ursell parameter is significant and is used to describe the various wave theory classifications.

The most widely used nonlinear wave theory was developed by Stokes (1847) by the perturbation method approach. The second order wave theory was developed for finite amplitude waves as a power series expansion of the wave steepness H/L based on

potential flow with a non hydrostatic pressure distribution. Stokes waves are steeper than sinusoidal waves and the accuracy of the results decreases with increasing wave steepness. For larger wave steepness up to the breaking limit, the fifth order theory is commonly used given by Skjelbreia and Hendrickson (1961) and Fenton (1985). The Stokes wave theory is applicable for deep water waves and partially in the intermediate water range. The range of Stokes theory is defined as $2 \leq L/h \leq 20$ according to LeMéhauté (1976). For the fifth order theory the limitation is reduced to $L/h < 10$ according to Keulegan (1950).

A finite amplitude wave theory was developed in shallow water by Korteweg and de Vries (1895) commonly known as the cnoidal wave theory based on the KdV equations in which h/L was assumed small. Cnoidal waves are periodic and have a constant form described by the Jacobi's elliptic cn-functions. This theory was developed based on the assumptions of hydrostatic pressure distribution for the first order and non hydrostatic pressure distributions of the second order. The cnoidal wave theory is applicable for $U > 26$ according to LeMéhauté (1976) and Sorensen (1993) and is valid in the range $L/h \geq 10$ according to Keulegan (1950). cnoidal wave theories were presented by Keulegan and Patterson (1940), Keller (1948), Laitone (1960), Chappelear (1962) and Fenton (1985). The first order cnoidal is most commonly used to describe waves of finite amplitudes in shallow waters. According to Wiegel (1960), Dean and Dalrymple (2004), the cnoidal wave theory is bound in a range limited by linear wave theory and solitary wave theory on the other end ($T \to \infty$).

A solitary wave theory was presented by Boussinesq (1871) and Boussinesq (1872). The solitary wave is defined by an infinitely long period and wavelength, and zero trough amplitude. the solitary wave consists of only the wave crest which is completely above the mean water level. The solitary wave theory by Boussinesq (1871) and Rayleigh (1876) has the assumption of non hydrostatic pressure distribution and rotation flow. The terms of $(H/h)^2$ in the derivation are neglected. The solitary wave

celerity c was found to be

$$c = \sqrt{g(h+a)} \tag{90}$$

with amplitude a and still water depth h. The solitary wave theories up to second order were presented by McCowan (1894) and Laitone (1960) where terms of order $(H/h)^3$ were neglected. This resulted in nonuniform distributions of the horizontal velocity when compared with Boussinesq (1871). The applications of solitary wave theory were given by Munk (1949) and Wiegel (1964). The theory of Boussinesq is recommend for wide practical engineering applications due to a good description of the main features of a solitary wave such as the wave celerity and surface profile. For numerical solutions of solitary wave theory, it is referred to Monaghan and Kos (2000), Shi *et al.* (1998), Teng (1997), Teng and Wu (1992), Teng and Wu (1994) among others. The validity of nonlinear wave theories is composed of mathematical validity on how well the theory is representative of the governing equations and the boundary conditions and physical validity, which associates theoretical wave components with observed or actual measurements. An analytical validity is given by Dean (1974).

5.4.5 Applicability of wave theories

The classical wave theories can be used to study and model the various water wave phenomenon in nature. While linear wave theory is applicable across all the water depth regimes, it is limited only for small amplitude water waves. Unlike linear theory, no non-linear water wave theory exists across shallow, intermediate and deep water depth regimes. Due to the wave generation mechanisms and frequency dispersion effects of waves generated by granular landslides, various sections of the wave train may exist in different water depth regimes (see Fig. 88). Additionally the tsunami waves generated by granular landslides in the present study are all found to be non-linear based on the wave steepness, relative wave height and Ursell parameter. The practical applications for the wave profiles may be made with cnoidal and solitary

wave theories for finite amplitude shallow water waves and Stokes theory for finite amplitude deep water waves. The above mentioned wave theories include mass transport due to irrotationality and nonlinearity. The radial and angular variability of the landslide generated tsunami waves must be kept in account when applying classical wave theories for analysis.

The range of applicability of classical wave theories is shown in Fig. 89 along with the present experimental data.

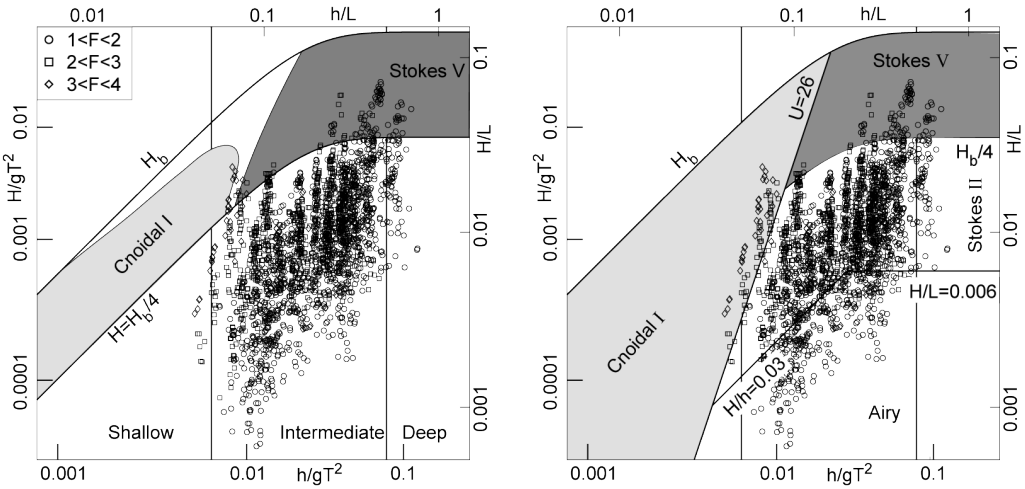

Figure 89: Applicability of analytical wave theories: (a) validities defined by the best fit dynamic free surface boundary condition (Dean (1970)); (b) recommended ranges by LeMéhauté (1976). Symbols correspond to ($\circ$) $1 < f < 2$; ($\square$) $2 < F < 3$; ($\diamond$) $3 < F < 3.5$. H_b is the breaking wave height and U is the Ursell parameter.

Stokes (1847) second order theory for finite amplitude waves was developed by the perturbation method expansion of H/L. The assumption of H/h small is applicable only in deep and intermediate water depths. The accuracy decreases with increasing wave steepness, which is remedied by the fifth order wave theory (Skjelbreia and Hendrickson (1961), Fenton (1985) up to the wave breaking limit. In the shallow water depth regime, cnoidal wave theory developed by Korteweg and de Vries (1895) describes waves of finite amplitudes. The transition between the applicable ranges for cnoidal wave theory and Stokes fifth order wave theory occurs in the intermediate

water depth range. The transition occurs at approximately $U = 26$ (LeMéhauté (1976)). The cnoidal wave theory is applicable for $U \geq 26$ and Stokes theory for $U < 26$. The leading wave crest in the present experimental study propagates with the solitary wave theory. The leading waves generated by landslides are observed to be in the range $U \geq 26$. Hence the cnoidal wave theory may be applicable to certain sections of the leading wave profiles in the generated wave train. The second wave in the wave train is observed to exist in the intermediate water depth regime with $2 < U < 400$. Some portions of the trailing waves with $U \geq 26$ may be described with cnoidal wave theory. All other waves with $U < 26$ may be described by Stokes wave theory. The trailing waves of the landslide generated wave train correspond to the Stokesian regime (Fig. 89). Some of the trailing waves in the far field fall in the linear water waves regime with $H/h < 0.03$ and $H/L < 0.006$ in Fig. 89(b) and may be described with Airy or small amplitude water wave theory. The landslide generated tsunami waves range approximately corresponds to those given by Kamphuis and Bowering (1970) and Huber (1980). This range further matches the range of explosion generated waves by LeMéhauté and Khangoankar (1992). While the leading waves can be explained by cnoidal wave theory, the trailing waves can be described by Stokes wave theory.

CHAPTER VI

TSUNAMI RUNUP AND RUNDOWN ON HILL SLOPE

6.1 Introduction

Tsunami generation by landslides is characterized by lateral wave propagation on the hill slope and the associated runup and rundown of the tsunami wave. The lateral tsunami waves are defined as the waves that propagate in a direction perpendicular to the landslide motion. In the wave reference coordinate system, the lateral tsunami waves travel along the directional ray of $\theta = 90°$. The definition of terms in the tsunami runup/rundown analysis is shown in Fig. 90.

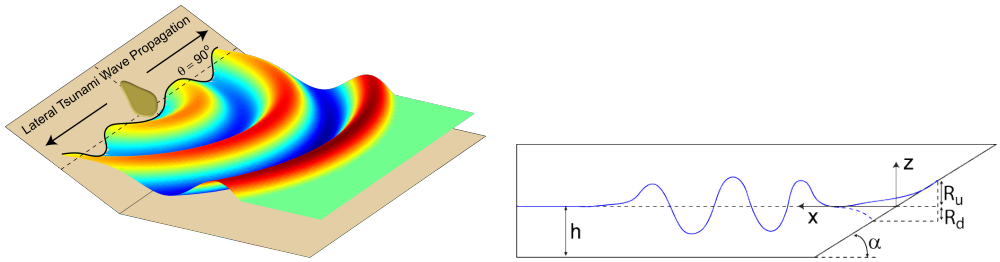

(a) (b)

Figure 90: Landslide generated tsunami runup wave definitions on the hill slope.

The tsunami runup and rundown in the near field area of landslide impact are important for tsunami hazard mitigation. The lateral waves are usually slower than the outwards propagating tsunami waves due to shallow water depths at the hill slope. But the arrival times can be earlier since the shoreline is closest to the landslide source. The coastal areas adjacent the landslide impacts are prone to hazards initially from the lateral tsunami waves.

The lateral waves in the present study are measured by an array of wave gauges on the hill slope and a camera array with viewing area on the hill slope. While the PIV camera covers the impact region, a second camera is placed laterally off axis

to cover the remainder area on the hill slope. The measurements are made relating to the lateral wave profile, shoreline variation during the lateral wave propagation, extents of maximum runup and rundown of the shoreline on the hill slope and lateral tsunami wave characteristics.

6.2 Shoreline Drawdown And Lateral Tsunami Waves

The image sequence recorded by the two overhead cameras is used to measure the shoreline displacement relative to time of landslide motion. The image sequences are calibrated and corrected for radial distortions. A checkered pattern of crosses is placed 0.3 m apart in the longitudinal and transverse directions on the hill slope to calibrate and correct the image sequence as shown in Fig. 91(b). Figure 91 shows the extent of the area on the hill slope that is available for shoreline measurements.

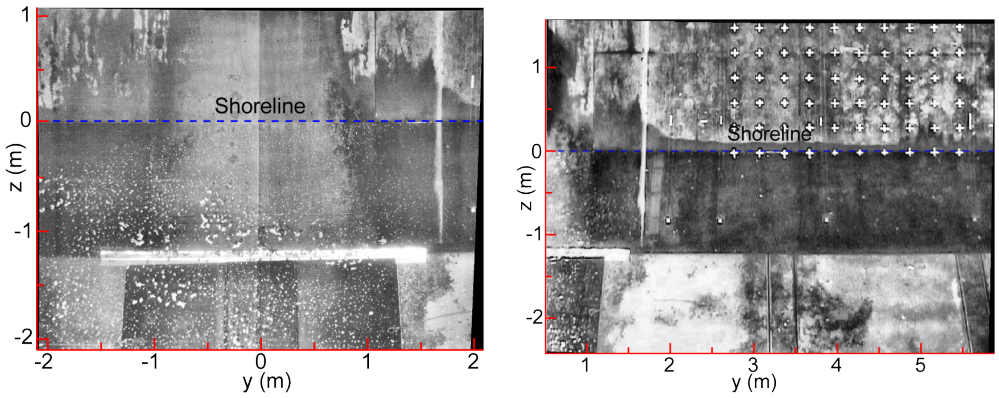

(a) (b)

Figure 91: Extent of the hill slope from (a) the impact area to (b) the edge of the measurement area. $y = 0$ corresponds to the impact location.

The wave generation mechanism for lateral tsunami wave by subaerial landslides is analogous to the wave generation process described in Sec. 5.2 . The subaerial landslides impact at the water surface induces a shoreline displacement on the hill slope during the impact process. The initial water displacement and the subsequent drawdown of the water surface generates the leading crest and trough of the lateral wave. The lateral wave is fully formed after a certain propagation distance away

from the impact. This distance varies in the experimental process depending on the landslide impact characteristics. The spatial extent of the shoreline is measured in the framed area. The time series of the shoreline is obtained from the shoreline measurements from the image sequence. The shoreline variations with time at the impact region during the wave generation process are shown in Fig. 92. Also shown is the maximum runup and drawdown of the water surface during the wave generation and lateral propagation along the hill slope.

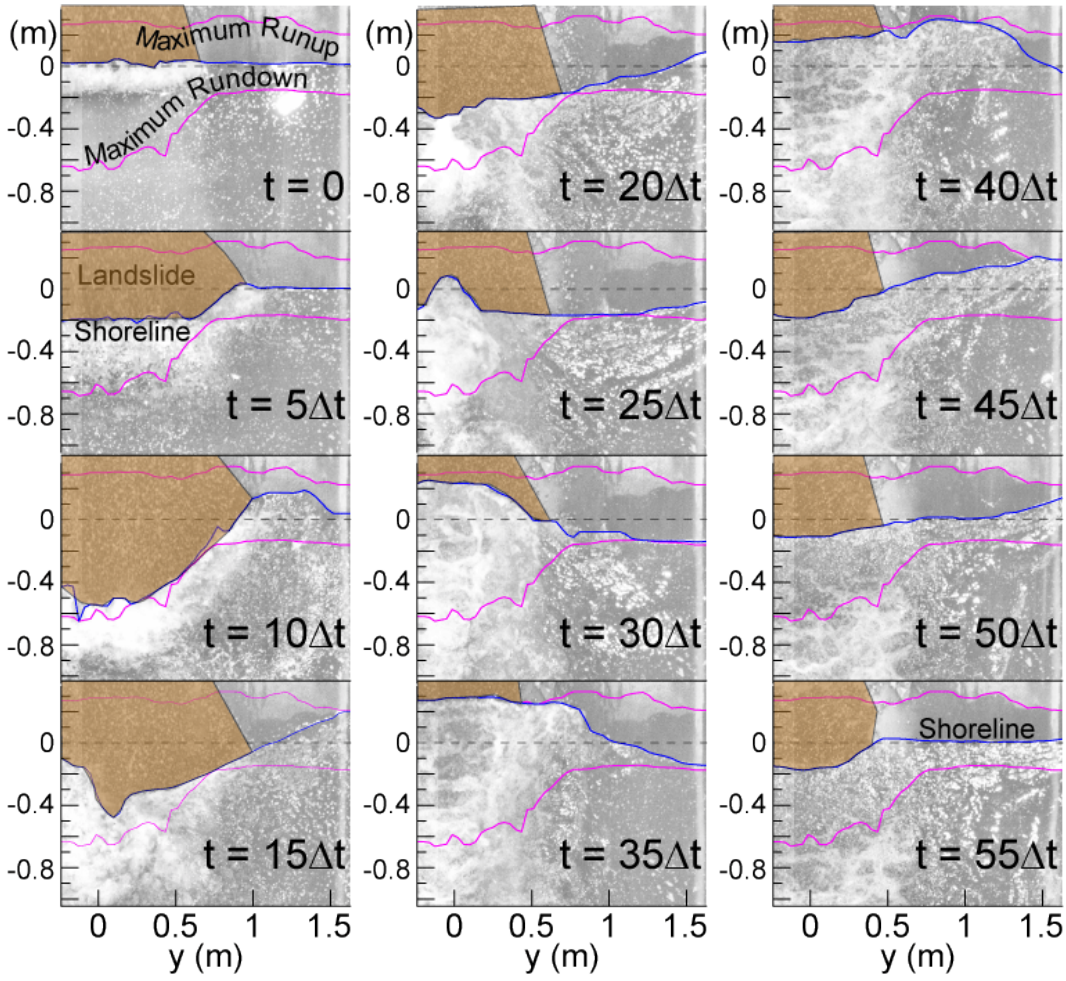

Figure 92: Shoreline variations shown in the landslide impact zone shown for $F = 1.8$, $S = 0.25$ and $V = 1.04$. Frame rate of the image sequence is $\Delta t = 1/15$ s. The total time of the image sequence is 3.7 s from the moment of landslide impact.

The time history of the tsunami runup and rundown at the impact region is obtained from the vertical component of the shoreline variations. The runup wave

propagates in the lateral direction on the hill slope post impact. The subaerial landslide impacts leads to an initial drawdown of the water surface followed by a runup after the collapse of the water surface displacement. The maximum tsunami runup and rundown on the hill slope, in the landslide impact zone occurs at the impact location along the landslide centerline, $y = 0$. The maximum runup and draw down at the landslide impact location is shown in Fig. 93.

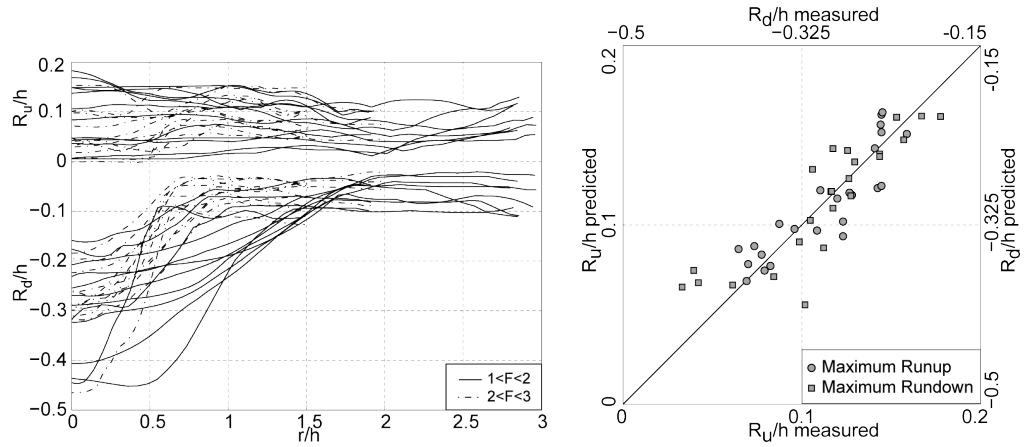

(a) (b)

Figure 93: Maximum runup and drawdown in the impact region: (a) amplitudes of maximum runup and drawdown of the shoreline in the landslide impact region $0 \leq r/h \leq 3$, (b) comparison between measured values and predicted with Eq. 92 at $r/h = 0$.

The drawdown is caused by the water displacement due to the granular landslide motion. As a result, the maximum tsunami runup and rundown may be directly related to the initial landslide impact at the water surface, which is primarily governed by the landslide Froude number F at impact and the landslide thickness S. The maximum runup and rundown is also influenced by the landslide volume and width at impact. A multi variable regression analysis yielded the predictive equations for the maximum tsunami runup and rundown as

$$\begin{aligned} \frac{R_u}{h} &= \frac{1}{4} F^{1.4} S^{0.7} B^{-0.5} V^{-0.1} \\ \frac{R_d}{h} &= \frac{2}{5} F^{1.8} S^{0.3} B^{-1.22} V^{0.18} \end{aligned} \tag{91}$$

with correlation coefficient of $r^2 = 0.89, 0.89$ for R_u and R_d respectively. The comparison between the measured values and predicted values of maximum tsunami runup and rundown at impact is shown in Fig. 93(b).

An increase in landslide Froude number increases the energy transfer from the landslide into the water body during the impact which causes a further increase in water displacement. An increase in the landslide thickness at impact produces an increased energy flux from the landslide to the water body at impact, which in turn increases the rate of water displacement away from the landslide source. The shoreline variation outward from the landslide impact region is shown in the range $2 < y < 5.5$ m in the TWB. The fully developed lateral wave propagation is seen in Fig. 94. The wave reflection from the end of the hill slope truncates the tsunami runup time series. The maximum tsunami runup and rundown on the hill slope is shown in Fig. 94.

The maximum tsunami runup and rundown at $y/h = 4$ is interpolated from the measured data. The multi variable regression analysis provides the predictive equation as

$$\begin{aligned} \frac{R_u(r/h=4)}{h} &= 0.2F^{0.5}S^{0.7}B^{-0.5}V^{0.5} \\ \frac{R_d(r/h=4)}{h} &= 0.2FS^{0.7}B^{-0.4}V^{-0.1} \end{aligned} \tag{92}$$

with correlation coefficient $r^2 = 0.9, 0.9$ for R_u and R_d respectively. The measured maximum tsunami runup and rundown with propagation distance along the hill slope is shown in Fig. 95(a). The comparison between the measured values at $r/h = 4$, $\theta = 90^\circ$ and computed values is shown in Fig. 95(b).

The maximum tsunami runup and drawdown along the hill slope at $r/h = 4$ depends directly on the landslide Froude number, relative landslide thickness and inversely on the relative landslide width at impact. The dependence on the relative landslide volume varies for the maximum tsunami runup and rundown.

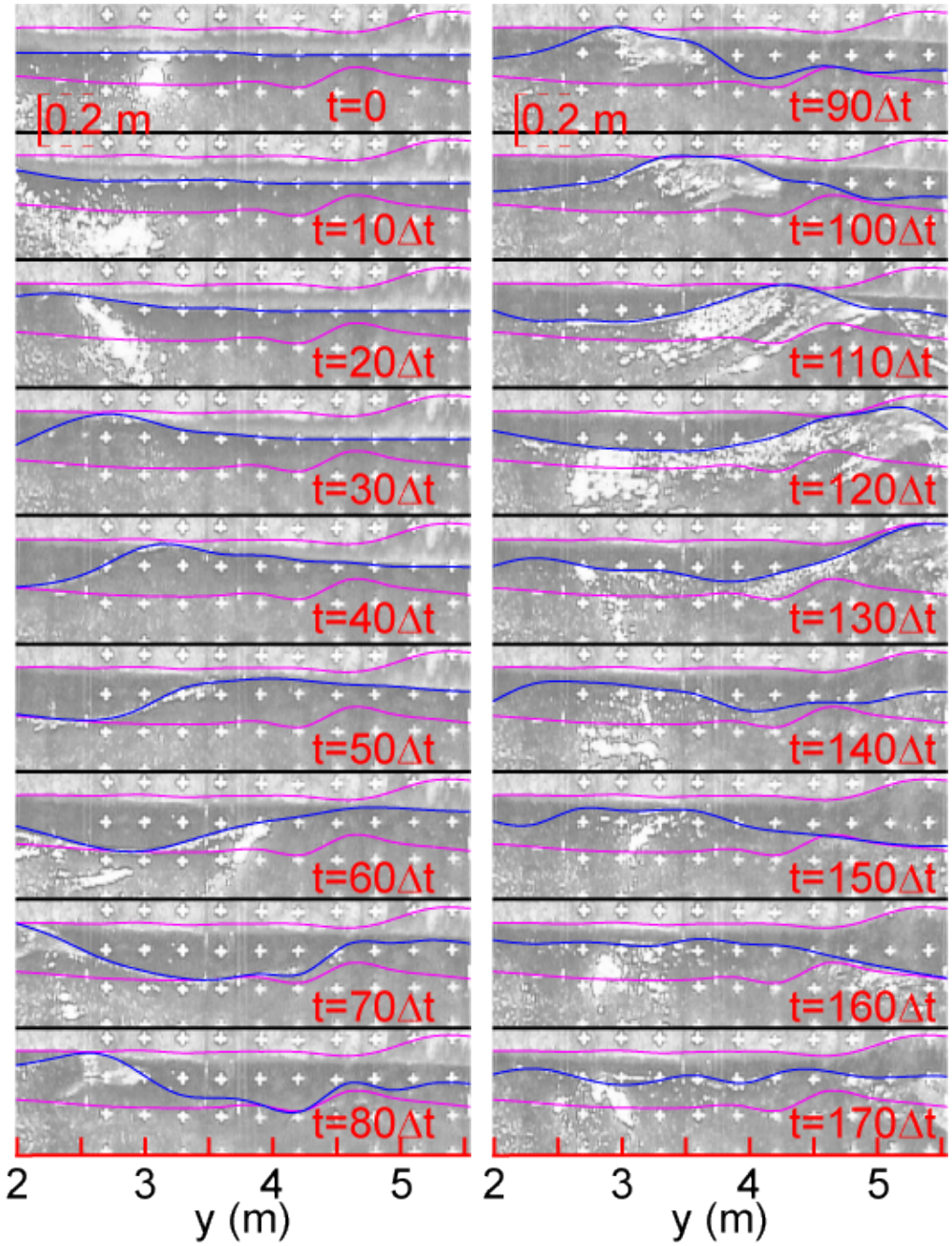

Figure 94: Shoreline variations shown away from the landslide impact zone, $2 < y < 5.5$ m for $F = 1.8$, $S = 0.25$ and $V = 1.04$. Frame rate of the image sequence is $\Delta t = 1/30$ s. The total time of the image sequence is 5.7 s from time of landslide impact. $y = 0$ corresponds to the impact location. The shoreline is represented by the blue line and the runup, rundown are represented by the pink line.

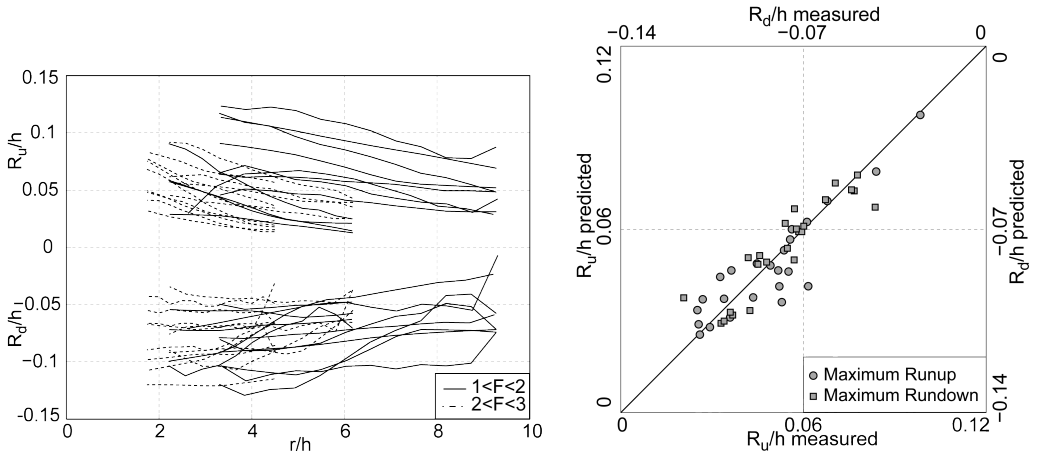

(a) (b)

Figure 95: Maximum runup and drawdown on the hill slope in $2 \leq r/h \leq 10$: (a) amplitudes of maximum runup and drawdown of the shoreline, (b) comparison between measured values and predicted with Eq. 93 at $r/h = 0$.

6.3 Lateral Tsunami Wave Period

The time period of the lateral tsunami waves are measured from the lateral wave time series from the image sequences and the tsunami runup time series from the wave gauges by the upcrossing method. Analogous to the offshore propagating tsunami wave, the runup period is defined from upcrossing to upcrossing point in the time series. The first upcrossing point is defined as the moment when the water surface is 5% of the first wave crest amplitude, $\eta = 0.05a_{c1}$. The measured wave period of the 1^{st} lateral wave is shown in Fig. 96 for all the experimental runs. The wave period of the 2^{nd} lateral wave could not be determined due to the time series truncation by wave reflection. Herein, the analysis for the leading lateral wave is presented.

The wave period of the leading lateral tsunami wave is measured in the propagation distance range $0 < r/h < 20$. The determined wave periods are within $10 < T\sqrt{g/h} < 20$. The lateral wave period compares with the offshore propagating wave which has the leading wave period as $4 < T_1\sqrt{g/h} < 20$ in the range $4 < r/h < 20$. This further exhibits the radial wave front nature of tsunami waves generated by 3D landslides on a constant bathymetry. The wave stretches out with

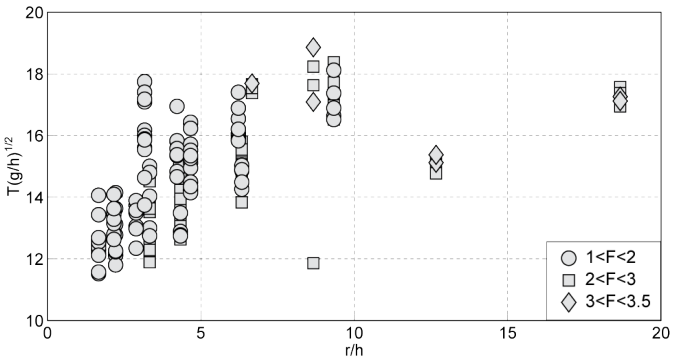

Figure 96: Time period of leading runup wave, $T\sqrt{g/h}$ along propagation distance r/h: ($\circ$) $1 < F < 2$, ($\square$) $2 < F < 3$

the propagation away from radial source. The evolution of the lateral wave period on the hill slope follows the evolution function of the wave period of the offshore propagating wave. The lateral wave period evolution follows

$$T\sqrt{\frac{g}{h}} = k_T \left(\frac{r}{h}\right)^{0.3} \tag{93}$$

with correlation coefficient $r^2 = 0.89$. The evolution of lateral wave period with propagation distance is shown in Fig. 97.

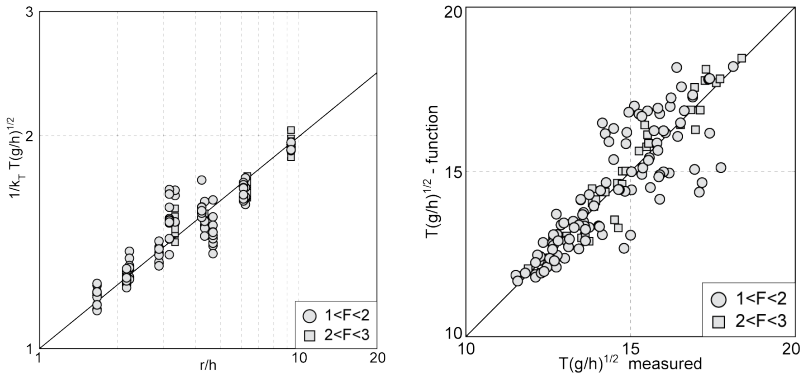

(a) (b)

Figure 97: Time period of the leading runup wave: (a) normalized with the time period coefficient $1/k_T T\sqrt{g/h}$ as a function of propagation distance r/h from landslide impact, (b) comparison of measured values with the predicted values with Eq. 93. ($\circ$) $1 < F < 2$, ($\square$) $2 < F < 3$, ($\diamond$) $3 < F < 3.5$

6.4 Lateral Tsunami Wave Celerity

The speed of the tsunami wave in the lateral direction is measured between runup gauges as the wave propagates on the hill slope. The wave speed is measured for the 1^{st} lateral wave in all the experimental runs and the 2^{nd} lateral wave in cases where the time series permits the crest and trough identification. The wave celerity is normalized with the shallow water speed $\sqrt{gh}$ where h is the still water depth. The lateral wave speed is measured in the range $0 < r/h < 20$. The propagation velocity of the leading lateral tsunami wave is in the range $0.35 < c_{cr1}/\sqrt{gh} < 1$ and $0.35 < c_{tr1}/\sqrt{gh} < 1$. The measured speed of the second wave is in the range $0.35 < c_{cr2}/\sqrt{gh} < 0.85$ and $0.3 < c_{tr2}/\sqrt{gh} < 0.85$. The reduction in wave speed from the 1^{st} to the 2^{nd} trailing wave may be due to dispersion effects similar to the offshore propagating wave speed. The celerity of the second wave is on an average 15% lower than that of the 1^{st} lateral wave. The propagation velocity of the lateral wave is bound by the shallow water speed in the basin at the upper limit. Unlike the offshore propagating wave, the lateral wave celerity is lower than the solitary wave speed in the wave basin. The measured speeds of the first and second lateral tsunami waves on the hill slope are shown in Fig. 98.

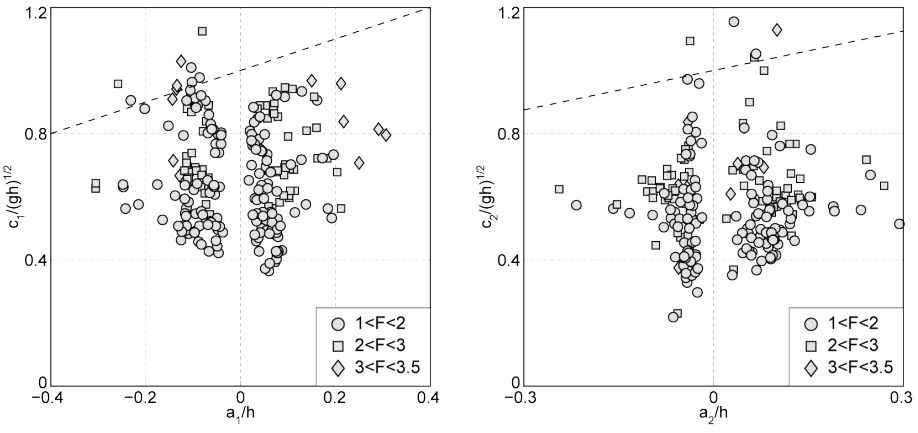

Figure 98: Wave speed of runup wave crest and trough: (a) first wave, (b) second wave. ($\circ$) $1 < F < 2$, ($\square$) $2 < F < 3$, ($\diamond$) $3 < F < 3.5$

The evolution of the lateral wave speed with propagation distance is shown in Fig. 99. The lateral wave crest and trough speeds are shown versus the propagation distance r/h at direction $\theta = 90°$ for the first two waves in the lateral tsunami wave train. The wave speed was found to increase with propagation distance similar to the increase in wave period for the outwards propagating wave and runup waves away from the landslide source. The dispersion effects due to the stretching of the wave away from the landslide source causes the wave speed to increase with propagation distance.

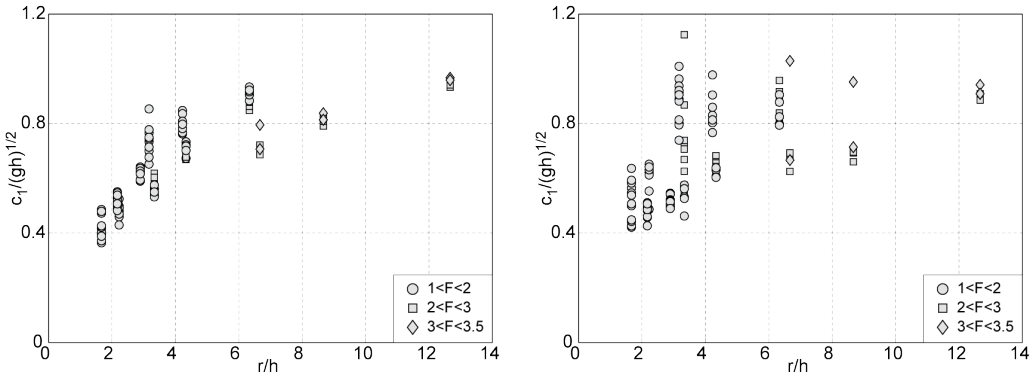

Figure 99: Evolution of runup wave speed with propagation distance shown for (a) first wave, (b) second wave. ($\circ$) $1 < F < 2$, ($\square$) $2 < F < 3$, ($\diamond$) $3 < F < 3.5$

6.5 Lateral Tsunami Wavelength

The lateral wave lengths are determined by multiplying the wave speed with the measured wave period,

$$\frac{L}{h} = \frac{c}{\sqrt{gh}} T \sqrt{\frac{g}{h}} \tag{94}$$

The wavelengths are based on the upcrossing wave periods of the 1^{st} lateral wave and the average lateral wave crest and trough speeds. The measured wavelengths are found in the range $2.5 < L/h < 12$ across the propagation distance $0 < r/h < 20$. In comparison, the wavelength of the offshore propagating wave is measured as $5 < L/h < 15$ in the propagation range $4 < r/h < 20$. The measured wavelengths

of the lateral waves are shorter than the offshore propagating wave. The generated lateral waves propagates in lower water depths than the offshore propagating wave. The lower water depths and the additional effects of the hill slope boundary causes the runup waves to have lower time periods, propagation speeds and wavelengths as they propagate away from impact area. The lateral wavelengths are found to increase with propagation distance according to the evolution function

$$\frac{L}{h} = k_L \left(\frac{r}{h}\right)^{0.3} \tag{95}$$

with correlation coefficient $r^2 = 0.9$, where k_L is the wavelength parameter. The rate of increase of the lateral wavelength is similar to the rate at which the wavelength of the offshore propagating waves are found to evolve with propagation distance. The evolution of the measured wavelength with propagation distance is shown in Fig. 100.

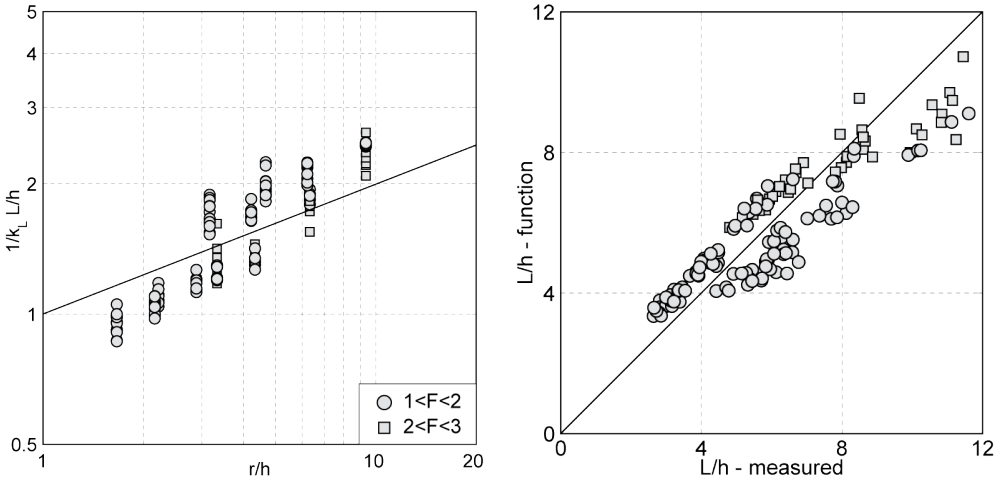

(a) (b)

Figure 100: Wavelength of the leading runup wave: (a) normalized with the time period coefficient $1/k_L L/h$ as a function of propagation distance r/h from landslide impact, (b) comparison of measured values with the predicted values with Eq. 95. (○) $1 < F < 2$, (□) $2 < F < 3$

CHAPTER VII

CONCLUSIONS

7.1 Summary

Tsunamis generated by 3D granular landslides are physically modeled in the 3D NEES tsunami wave basin at Oregon State University in Corvallis. The model is based on Froude's similarity. The study was initiated to understand tsunami generation by unconfined deformable granular landslides in three dimensions. This fills the gap between previous experimental studies with solid block landslides, numerical studies on landslide generated tsunamis and field observation of landslide generated tsunami events. Predictive equations for the tsunami wave characteristics are obtained which provides for initial rapid tsunami hazard estimation and mitigation. Further, the experimental data serves validation and advancement of numerical landslide generated tsunami models.

The key parameters that influence the tsunami wave generation by landslides are the still water depth h, landslide shape parameters such as thickness s, width b, volume V_s and landslide impact velocity v_s. The experimental study encompassed the range $1 < F < 3.4$, $0.09 < S < 0.8$, $1 < B < 4.7$ and $0.25 < V < 28$. The landslide Froude number is the most important parameter with respect to the tsunami wave characteristics, followed by the relative thickness S, width B and volume V. The landslide impact velocity varies with the landslide volume, location and velocity of landslide material release. The PIV based instantaneous landslide surface velocity field highlights uniform distribution of the streamwise velocity across the landslide width. The streamwise velocity decreases close to the landslide edges where the landslide thickness approaches zero. Faster landslides retain a compact shape and

reduced spread compared to slower landslides.

The 3D landslide generates a tsunami wave which propagates as a radial wave front away from the impact. Subaerial impacts always results in an initial water surface elevation followed by a trough. At impact, the maximum shoreline drawdown always exceeded the maximum runup. Lateral tsunami waves are sometimes more hazardous compared with outwards propagating wave due to the proximity of the landslide source. The observed waves in the present study are of non-linear oscillatory and non-linear transition wave types in the near field, while the far field waves decay in the linear regime. The leading wave crest amplitudes are directly dependent on the landslide Froude number and thickness at impact, while the landslide volume affects the leading wave trough and trailing waves. The radial decay rate depends additionally on the landslide width at impact. The angular decay rate of the leading wave is slower than the trailing waves. The tsunami wave periods and wavelengths are independent of the angular direction. The wave celerity of the first wave corresponds closely to the solitary wave speed. The dispersion effects in the wave train lead to a reduction in the celerity of the trailing waves.

The energy conversion between the landslide kinetic energy at impact and the generated wave is lower when compared with 2D cases owing to the spread of the unidirectional landslide energy through the radial wave front. Between 1%-15% of the landslide kinetic energy is converted into the wave train. The leading wave crest contains between 8%-60% of the wave train energy. The efficiency of wave generation increases with increasing landslide Froude number and relative landslide thickness at impact. On the other, hand the efficiency decreases with increasing landslide volumes. The 3D landslide generated waves are weakly non-linear in nature and span from shallow to deep water depth regime in the generated wave train.

7.2 Contributions to tsunami research

The present experimental study on 3D tsunamis generated by granular landslides is a systematic evolution of the earlier 2D physical models. This large scale study is the first of its kind where tsunami generation by deformable granular landslides are modeled in three dimensions. The ability to model the landslide with deformable granular material and variable control parameters expands the range of study of landslide tsunami generation. The limitations of modeling the landslide with a solid block is overcome in the present study by using deformable landslides which results in natural energy dissipation in the landslide tsunami system. An improvement is achieved in predicting the wave amplitude attenuation away from the landslide source, compared with earlier models. The reduced scale difference between model and prototype facilitates application to field cases. The empirical equations obtained in the present study may provide a rapid initial assessment of landslide generated tsunami hazards in field events. Of practical importance are mainly the prediction of wave amplitudes, the attenuation function of the wave amplitudes away from the landslide source and the wave propagation velocity which enables the prediction of tsunami arrival times. This study provides an improvement in understanding the 3D water surface behavior including shoreline displacements in the impact region which are essential for validating the numerical models. The experimental data provides high precision benchmarks for validating fully three dimensional numerical models simulating landslide tsunami generation.

7.3 Outlook

The outcome of the present study may be expanded upon several parameters that were constant, such as the granular material density and hill slope angle within the range offered by the pneumatic landslide tsunami generator. By varying the granular material, the effect of landslide mass on the wave generation may be investigated.

The application of the present study to field cases may not be extrapolated outside the present range of the experimental parameters. The experimental study may be expanded upon the limitations of the present non-dimensional parameters to enable a wider applications of the obtained results to field cases. In real world cases, landslide tsunami wave generation and propagation are often complicated due to the complex bathymetry, wave transformations and reflections. While the scenarios for studying tsunamis generated by landslides spanning from fjords to volcanic islands are numerous, experimental studies remain limited to select scenarios and parameters in large scale physical models. However, the physical model provides high precision data which serves as benchmark for validating numerical models. Field data from landslide generated tsunami are scarce and are nonexistent in the realm of the tsunami generation by landslides. The combination of field observation, physical models and numerical simulations will provide for a deeper understanding on the phenomenon. By ensuring accurate representation of the landslide water body coupling in the impact region, the wave generation may be studied in complex bathymetries and topographies. It should be noted that the various processes that occur such as the landslide motion, tsunami generation, propagation and runup overlap each other during the event and are individually complicated. Numerical models will allow capturing of the complex wave propagation patterns due to wave transformations in complex bathymetry. For accurate representation of the landslide generated tsunami events, the numerical model has to capture the complex interactions between the granulate, air and water phases in the impact region. The generated wave may then be simulated by wave propagation models. The field data combined with site specific physical models and numerical models can then be used to develop a further understanding of the complex landslide tsunami phenomenon in real world and expand upon the contributions to general tsunami research.

Bibliography

Abadie, A., Morichon, D., Grilli, S., and Glockner, S. (2008). VOF/Navier-Stokes numerical modeling of surface waves generated by subaerial landslides. *Houille Blanche-Revue International De L Eau*, *1*, 21–26.

Ahmadi, G. and Shahinpoor, M. (1983). Towards a turbulent modeling of rapid flow of granular materials. *Powder Tech.*, *35*, 241–248.

Airy, G. B. (1845). Tides and waves. *Encyclopaedia Metropolitana*, *5*, 241–392.

Amsden, A. A., Ruppel, H. M., and Hirt, C. W. (1980). SALE: a Simplified ALE computer program for fluid flows at all speeds. Report LA-8095, Los Alamos National Laboratories, Los Alamos, NM.

Ataie-Ashtiani, B. and Najafi-Jilani, A. (2008). Laboratory investigations on impulse waves caused by underwater landslides. *Coastal Engineering*, *55*, 989–10074.

Ataie-Ashtiani, B. and Nik-Khah, A. (2008). Impulsive waves caused by subaerial landslides. *Environ. Fluid Mech.*, *8*, 263–280.

Ball, J. W. (1970). Hydraulic model studies, wave action generated by slides into mica reservoir. Tech. rep., Western Canada Hydraulic Laboratories, Vancouver, Canada.

Birkhoff, G. (1950). *Hydrodynamics: a study in logic, fact and similitude*. New York: Dover Press.

Boussinesq, J. (1871). Théorie de l'intumescence liquide appelée onde solitaire ou de translation, se propageant dans un canal rentangulaire. *Comptes REndus de l'Académie des Science Paris*, *72*, 755–759.

Boussinesq, J. (1872). Théorie des ondes et des remous que se propagent le long d'un canal rectangulaire horizontal, en communiquant au liquide contenu dans ce canal des vitesses sensiblement pareilles de la surface au fond. *J. Math. Pures Appl.*, *17*, 55–108.

Briggs, M. J., Synolakis, C. E., Harkins, G. S., and Green, D. R. (1995). Laboratory experiments of tsunami runup on a circular island. *PAGEOPH*, *144*(3/4), 569–593.

Brugnot, G. (1979). Recent progress and new applications of the dynamics of avalanches. In *Proc. Snow in Motion Symp.*. International Glaciological Society.

Buckingham, E. (1914). On physically similar systems - Illustrations of the use of dimensional equations. *Physical Review*, *4*, 345–376.

Bukreev, V. I. and Guseev, A. V. (1996). Gravity waves generated by a body falling onto shallow water. *Journal of Applied Mechanics and TEchnical Physics*, *37*(2), 224–231.

Campbell, C. S. and Brennen, C. E. (1985). Computer simulation of granular shear flows. *J. Fluid Mech.*, *151*, 167–188.

Campbell, C. S. and Gong, A. (1986). The stress tensor in a two-dimensional granular shear flows. *J. Fluid Mech.*, *164*, 107–125.

Caratto, M., Semenza, E., and Turrini, M. C. (2002). Study of bank instability of the Pontesei hydraulic reservoir - Belluno Province - N.E. Italy. In J. RybáŘ, J. Stemberk, and P. Wagner (Eds.), *Proc. 1st European Conference on Landslides*. Tokyo: Balkema, 59–78.

Chappelear, J. E. (1962). Shallow water waves. *J. Geophys. Res.*, *67*, 4693–4704.

Chaudhry, H., Mercer, A. G., and Cass, D. (1983). Modeling of slide-generated waves in a reservoir. *J. Hydr. Engrg*, *109*(11), 1505–1520.

Chen, C. and Ling, C. (1996). Granular flow rheology: role of shear-rate number in transition regime. *Journal of Engineering Mechanic (ASCE)*, *122*, 469–480.

Chiang, W. L., d. Divorky, Pamicky, P., and Wier, W. (1981). Numerical model of landslide-generated waves. Tetra tech. report t-3472, U.S. Dept of Commerce, Pasadena, California.

Chwang, A. T. and Wu, T. Y. (1977). Cylindrical solitary waves. *Lecture note sin Physics, Waves on Water of Variable Depth*, *64*, 80–90.

Craik, A. D. D. (2004). The origins of water wave theory. *Annu. Rev. Fluid Mech.*, *36*(1-28).

Crawford, D. A., Boslough, M. B., Trucano, T. G., and Robinson, A. C. (1994). The impact of comet Shoemaker-Levy 9 on Jupiter. *Shock Waves*, *4*, 47–50.

Crawford, D. A. and Mader, C. L. (1998). Modeling asteroid impact and tsunami. *Science of Tsunami Hazards*, *16*(1), 21–30.

Cruden, D. M. (1991). A simple definition of a landslide. *Bulletin of the International Association of Engineering Geology*, (43), 27–29.

Cruden, D. M. and Varnes, D. J. (1996). *Landslides: Investigation and Mitigation. Special Report, 247*, Washington, D.C.: Transportation Research Board, National Academy Press, chap. Landslide types and processes. 36–75.

Dailey, J. W. and Jr., S. C. S. (1953). Characteristics of the solitary wave. *Trans. ASCE*, *118*, 575–587.

Dalrymple, R. A. (1985). *Physical modeling in coastal engineering*. Rotterdam: Balkema.

Das, M. M. and Wiegel, R. L. (1972). Waves generated by the horizontal motion of a wall. *J. Waterw. Harbors Coastal Engrg. Div., ASCE*, *98*(WW1), 49–65.

Davidson, D. D. and McCartney, B. L. (1975). Water waves generated by landslides in reservoirs. *J. Hydraulics Div., ASCE*, *101*(HY12), 1489–1501.

Davidson, D. D. and Whalin, R. W. (1974). Potential landslide-generated impulse water waves, libby dam and lake koocanusa, montana. Tech. Rep. H-74-15., Waterways Experiment Station, U.S. Army Corps of Engineers, Vicksburg, Miss.

Davies, T. R. H. (1982). Spreading of rock avalanche debris by mechanical fluidization. *Rock Mech.*, *64*, 111–122.

Dean, R. G. (1970). Relative validities of water wave theories. *Journal of the Waterways and Harbors Division ASCE*, *96*(WW1), 105–119.

Dean, R. G. (1974). Evaluation and development of water wave theories for engineering application. Special report 1, U.S. Army Coastal Engineering Research Center, Ft. Belvoir, VA.

Dean, R. G. and Dalrymple, R. A. (1991). *Water wave mechanics for engineers and scientists*, vol. 2 of *Advanced series on ocean engineering*. Singapore: World Scientific.

Dean, R. G. and Dalrymple, R. A. (2004). *Water wave mechanics for engineers and scientists*. Advanced series on ocean engineering 2. Singapore: World Scientific.

Demidovich, B. P. and Maron, I. A. (1987). *Computational Mathematics*. Moscow: Mir.

Denlinger, R. P. and Iverson, R. M. (2001). Flow of variably fluidized granular masses across three-dimensional terrain 2. Numerical predictions and experimental tests. *J. Geophys. Res.*, *106*(B1), 553–566.

Denlinger, R. P. and Iverson, R. M. (2004). Granular avalanches across irregular three-dimensional terrain. 1. Theory and Computation. *J. Geophys. Res*, *109*, F01014(doi:10.1029/2003JF000085).

Dent, J. D. and Lang, T. E. (1980). Modeling of snow flow. *J. Glaciol.*, *26*, 131–140.

Edgers, L. and Karlsrud, K. (1982). Soil flows generated by submarine slides - case studies and consequences. *Proc. 3rd Int. Conf. on the Behaviour of Offshore Structures.*, *2*, 425–437.

Enet, F. and Grilli, S. T. (2005). Tsunami landslide generation:modeling and experiments. In *Proc. 5th Int. Conf. on Ocean Wave Measurement*. Madrid, Spain: WAVES 2005.

Enet, F. and Grilli, S. T. (2007). Experimental study of tsunami generation by three-dimensional rigid underwater landslides. *J. Waterway, Port, Coastal and Ocean Engineering*, *133*(6), 442–454.

Erismann, T. (1986). Flowing, rolling, bouncing, sliding: Synopsis of basic mechanisms. *Acta Mech.*, *64*, 101–110.

Fedkiw, R. P., Aslam, T., Merriman, B., and Osher, S. (1999). A non-oscillatory eulerian approach to interfaces in multimaterial flows (the ghost fluid method). *Journal of Comp. Physics*, *152*(2), 457–492.

Fenton, J. D. (1985). A fifth-order stokes theory for steady waves. *J. Waterway Port Coastal and Ocean Engrg., ASCE*, *111*(2), 216–234.

Fincham, A. M. and Delerce, G. (2000). Advanced optimization of correlation imaging velocimetry algorithms. *Experiments in Fluids*, *29*, S13–S22.

Fritz, H. M. (2002). *Initial phase of landslide generated impulse waves*. Ph.D. thesis, Eidgenössischen Technischen Hochschule Zürich, Zürich.

Fritz, H. M., Hager, W. H., and Minor, H.-E. (2001). Lituya bay case: rockslide impact and wave run-up. *Science of Tsunami Hazards*, *19*(1), 3–22.

Fritz, H. M., Hager, W. H., and Minor, H.-E. (2003a). Landslide generated impulse waves. 1. instantaneous flow fields. *Experiments in Fluids*, *35*, 505–519.

Fritz, H. M., Hager, W. H., and Minor, H.-E. (2003b). Landslide generated impulse waves. 2. hydrodynamic impact craters. *Experiments in Fluids*, *35*, 520–532.

Fritz, H. M., Hager, W. H., and Minor, H.-E. (2004). Near field characteristics of landslide generated impulse waves. *Journal of Waterway, Port, Coastal and Ocean Engineering, ASCE*, *130*(6), 287–302.

Fritz, H. M., Kongko, W., Moore, A., McAdoo, B., Goff, J., Harbitz, C., Uslu, B., Kalligeris, N., Suteja, D., Kalsum, K., Titov, V., Gusman, A., Latief, H., Santoso, E., Sujoko, S., Djulkarnaen, D., Sunendar, H., and Synolakis, C. (2007). Extreme runup from the 17 July 2006 Java tsunami. *Geophys. Res. Lett.*, *34*, L12602.

Fritz, H. M., Mohammed, F., and Yoo, J. (2009). Lituya Bay Landslide Impact Generated Mega-Tsunami 50^th Anniversary. *Pure and Applied Geophysics*, *166*(1-2), 153–175.

Fritz, H. M. and Moser, P. (2003). Pneumatic landslide generator. *International Journal of Fluid Power*, *4*(1), 49–57.

Galvin, C. J. (1964). Wave-height prediction for wave generators in shallow water. Tech. Memo 4, U.S. Army, Coastal Engineering Research Center.

Gault, D. E. and Sonett, C. P. (1982). Laboratory simulation of pelagic asteroidal impact: Atmospheric injection, benthic topography and the surface wave radiation field. geological implications of impacts of large asteroids and comets on the earth. *Geological Society of America Special Paper*, *190*, 69–92.

Gharib, M., Rambod, R., and Shariff, K. (1998). A universal time scale for vortex ring formation. *J. Fluid Mech.*, *360*, 121–140.

Gillon, M. D. and Saul, G. J. (1996). *Landslides*, Rotterdam, chap. Stabilization of Cairnmuir landslide. 1693–1698.

Gisler, G., Weaver, R., Gittings, M., and Mader, C. (2003). Two-and three-dimensional asteroid ocean impact simulations. *International Journal of Impact Engineering*, *29*, 283–291.

Glimsdal, S., Pedersen, G. K., Langtangen, H. P., Shuvalov, V., and Dypvik, H. (2007). Tsunami generation and propagation from the Mjϕlnir asteroid impact. *Meteorites and Planetary Science*, *42*(9), 1473–1493.

Goguel, J. (1978). Scale dependent rockslide mechanisms. In B. Voight (Ed.), *Rockslides and Avalanches*. Elsevier, vol. 1, 167–180.

Gozali, S. and Hunt, B. (1989). Water waves generated by close landslides. *J. Hydr. Res.*, *27*(1), 49–60.

Gray, J. M. N. T., Wieland, M., and Hutter, K. (1999). Gravity driven free surface flow of granular avalanches over complex basal topography. *Proc. R. Soc. A*, *455*, 1841–1874.

Greve, R. and Hutter, K. (1993). The motion of granular avalanche in a convex and concave curved chute: experiments and theoretical predictions. *Phil. Tran. R. Soc. A*, *342*, 573–604.

Greve, R., Koch, T., and Hutter, K. (1994). Unconfined flow of granular avalanches along a partly curved surface. Part I. Theory. *Proc. R. Soc. A*, *445*, 399–413.

Grilli, S. T., Skourup, J., and Svendsen, I. A. (1989). An efficient boundary element method for nonlinear water waves. *Engng. Anal. Boundary Elements*, *6*(2), 97–107.

Grilli, S. T., Vogelmann, S., and Watts, P. (2002). Development of a 3d numerical wave tank for modeling tsunami generation by underwater landslides. *Engineering Analysis with Boundary Elements*, *26*, 301–313.

Grilli, S. T. and Watts, P. (1999). Modeling of waves generated by a moving submerged body. Applications to underwater landslides. *Engrg. Anal. Boundary Elem.*, *23*, 645–656.

Grilli, S. T. and Watts, P. (2005). Tsunami generation by submarine mass failure. i: modeling, experimental validation and sensitivity analysis. *J. Waterw. Port Coast. Ocean Eng.*, *131*(6), 283–297.

Grimshaw, R. H. J. (2007). *Solitary waves in fluids*. Southampton: WIT Press.

Grimstad, E. and Nesdal, S. (1991). The Loen rockslides - a historical review. Norwegian Geotechnical Institute Publication 182, Norwegian Geotechnical Institute.

Habib, P. (1975). Production of gaseous pore pressure during rockslides. *Rock Mechanics*, *7*(3), 193–197.

Haff, P. K. (1983). Grain flow as a fluid-mechanical phenomenon. *J. Fluid Mech.*, *134*, 401–430.

Hammack, J. L. (1973). A note on tsunamis: Their generation and propagation in an ocean of uniform depth. *J. Fluid Mech.*, *60*, 769–799.

Hampton, M. A., Lee, H. J., and Locat, J. (1996). Submarine landslides. *Reviews of Geophysics*, *34*(1), 33–59.

Harbitz, C. B., Pedersen, G., and Gjevik, B. (1992). Numerical simulations of large water waves due to landslides. *J. Hydr. Engrg., ASCE*, *118*(10), 1325–1342.

Hart, D. P. (1998). Super-resolution PIV by recursive local correlation. In *Proceedings of the International Conference on Optical technology and image processing in fluid, thermal and combustion flow, Yokohama, Japan*. VSJ-SPIE98, vol. AB149, 167–180.

Hartley, R. and Zissermann, A. (2000). *Multiple View Geometry in Computer Vision*. UK: Cambridge University Press.

Heim, A. (1932). *Landslides and human lives (Berdsturz und Menchenleben)*. Vancouver, B.C.: BiTech Publishers. Translated by N. Skermer.

Heinrich, P. (1992). Nonlinear water waves generated by submarine and aerial landslides. *J. Waterway, Port, Coastal and Ocean Engrg.*, *118*(3), 249–266.

Heller, V. (2008). *Landslide generated impulse waves: Prediction of near field characteristics*. Ph.D. thesis, Versuchsanstalt für Wasserbau Hydrologie und Glaziologie der Eidgenössischen Technischen Hochschule Zürich, Zürich.

Heller, V., Hager, W. H., and Minor, H.-E. (2008). Scale effects in subaerial landslide generated impulse waves. *Exp. Fluids*, *44*(5), 691–703.

Horrillo, J. J. (2006). *Numerical methods for tsunami calculation using full Navier-Stokes equations and the volume of fluid method*. Ph.D. thesis, University of Alaska, Fairbanks, Alaska.

Hsü, K. (1975). On sturzstorms - catastrophic debris streams generated by rockfalls. *Geol. Soc. Am. Bull.*, *86*, 129–140.

Huang, H. T., Dabiri, D., and Gharib, M. (1997). On errors of digital particle image velocimetry. *Meas. Sci. Technol.*, *8*, 1427–1440.

Huang, H. T., Fielder, H. F., and Wang, J. J. (1993a). Limitations and improvements of piv. part i: limitation of conventional techniques due to deformation of particle image patterns. *Experiments in Fluids*, *15*, 168–174.

Huang, H. T., Fielder, H. F., and Wang, J. J. (1993b). Limitations and improvements of piv. part ii: particle image distortion, a novel technique. *Experiments in Fluids*, *15*, 263–273.

Huber, A. (1980). Schwallwellen in Seen als Folge von Bergstürzen. VAW-Mitteilung 47, Versuchsanstalt für Wasserbau, Hydrologie und Glaziologie, ETH Zürich.

Huber, A. and Hager, W. H. (1997). Forecasting impulse waves in reservoirs. In *Dix-neuviéme Congrés des Grands Barrages*. Florence, Italy, C31, 993–1005.

Hudson, R. Y., Hermann, F. A., Sager, R. A., Whalin, R. W., Keulegan, G. H., Chatham, C. E., and Hales, L. Z. (1979). Coastal hydraulic models. Tech. rep., US Army Engineer Waterways Experiment Station, Vicksburg, Mississippi.

Hughes, S. (1993). *Physical models and laboratory techniques in coastal engineering*, vol. 7 of *Advanced series on ocean engineering*. Singapore: World Scientific.

Hunt, B. (1988). Water waves generated by distant landslides. *J. Hydr. Res.*, *26*(3), 307–322.

Hutter, K. (1991). Two- and three dimensional evolution of granular avalanche flow - theory and experiments revisited. *Acta Mechanica. Supplementum*, *1*, 167–181.

Hutter, K. (1996). Avalanche dynamics. In V. P. Singh (Ed.), *Hydrology of disasters*, Dordrecht, Boston, London: Kluwer Academic Publishers, chap. 11. 317–394.

Hutter, K. and Greve, R. (1993). Two-dimensional similarity solutions for finite-mass granular avalanches with Coulomb- and viscous-type frictional resistance. *J. Glaciol.*, *39*, 357–372.

Hutter, K. and Koch, T. (1991). Motion of a granular avalanche in an exponentially curved chute: experiments and theoretical predictions. *Phil. Tran. R. Soc. A*, *334*, 93–138.

Hutter, K., Koch, T., Plüss, C., and Savage, S. B. (1995). The dynamics of avalanches of granular materials form initiation to runout. *Acta Mech.*, *109*, 127–165.

Hutter, K. and Nohguchi, Y. (1990). Similarity solutions for a Voellmy model of snow avalanches with finite mass. *Acta Mech.*, *82*, 99–127.

Hutter, K. and Rajagopal, K. R. (1994). On flows of granular materials. *Continuum Mech. Thermodyn.*, *6*, 81–139.

Hutter, K., Siegel, M., Savage, S. B., and Nohguchi, Y. (1993). Two dimensional spreading of a granular avalanche down an inclined plane. Part I. Theory. *Acta Mech.*, *100*, 37–68.

Hutter, K., Wang, Y., and Pudasani, S. P. (2005). The Savage-Hutter avalanche model: how far can it be pushed? *Phil. Trans. R. Soc. A*, *363*, 1507–1528.

Imamura, F. and Gica, E. C. (1996). Numerical model for tsunami generation due to subaqueous landslide along a coast. *Science of Tsunami Hazards*, *14*(1), 13–28.

Ippen, A. T. (1966). *Estuary and coastline hydrodynamics*. New York: McGraw-hill.

Iverson, R. M. (1997). The physics of debris flows. *Rev. Geophys.*, *35*, 245–296.

Iverson, R. M., Logan, M., and Denlinger, R. P. (2004). Granular avalanches across irregular three-dimensional terrain. 2. Experimental tests. *J. Geophys. Res.*, *109*, F01015.

Jenkins, J. T. and Richman, M. W. (1985). Grad's 13-moment system for a dense gas of inelastic spheres. *Arch. Rat. Mech. Anal.*, *87*, 355–377.

Jenkins, J. T. and Savage, S. B. (1983). A theory for the rapid flow of identical, smooth, nearly elastic particles. *J. Fluid Mech.*, *130*, 186–202.

Jennings, D. N., Newton, C. J., Beetham, R. D., and Smith, G. (1991). *Landslides*, Rotterdam, chap. Stabilization of the nine mile creek schist landslide complex. 759–764.

Jiang, L. and LeBlond, P. H. (1992). The coupling of a submarine slide and the surface waves which it generates. *J. Geophys. Res.*, *97*(C8), 12731–12744.

Jiang, L. and LeBlond, P. H. (1993). Numerical modeling of an underwater Bingham plastic. *J. Geophys. Res.*, *98*(C6), 10303–10317.

Jiang, L. and LeBlond, P. H. (1994). Three-dimensional modeling of tsunami generation due to a submarine mudslide. *J. Phys. Ocean*, *24*, 559–573.

Johnson, C. and Mader, C. L. (1994). Modeling the 105ka Lanai tsunami. *Science of Tsunami Hazards*, *12*(1), 33–38.

Johnson, J. W. and Bermel, K. J. (1949). Impulsive waves in shallow water as generated by falling weights. *Trans. Am. Geophys. Union*, *30*(2), 223–230.

Jordaan, J. M. (1969). Simulation of waves by an underwater explosion. *J. Waterw. Harbors Coastal Engrg. Div., ASCE*, *95*(WW3), 355–377.

Jϕrstad, F. (1968). Waves generated by landslides in Norwegian fjords and lakes. *Norw. Geotech. Inst. Publ.*, *79*, 13–32.

Kajiura, K. (1963). The leading wave of a tsunami. *Bulletin Earthquake Research Institute, Tokyo University*, *41*(3), 398–571.

Kajiura, K. (1990). *Tsunamis*. New York: John Wiley.

Kamphuis, J. W. and Bowering, R. J. (1970). Impulse waves generated by landslides. In *Proc.* 12^{th} *Coastal Engineering Conf.*. ASCE, vol. 1, 575–588.

Keane, R. R. and Adrian, R. J. (1992). Theory of cross-correlation analysis of piv images. *Appl. Sci. Res.*, *49*, 191–215.

Keller, J. B. (1948). The solitary wave and periodic waves in shallow water. *Commun. pure Appl. Math.*, *1*, 323–339.

Kent, P. E. (1966). The transport mechanism in catastrophic rockfalls. *Journal of Geology*, *74*, 79–93.

Keulegan, G. H. (1950). *Engineering Hydraulics*, New York: Wiley, chap. Wave Motion.

Keulegan, G. H. and Patterson, G. W. (1940). Mathematical theory of irrotational translation waves. *J. Res., Nat. Bur. Stand.*, *24*, 47–101.

Koch, T. (1989). *Bewegung einer Granulatlawine entlang einer gekrümmten Bahn*. Diplomarbeit. Technische Hochschule Darmstadt. 122 pp.

Koch, T., Greve, R., and Hutter, K. (1994). Unconfined flow of granular avalanches along a partly curved surface. Part II. Experiments and numerical computations. *Proc. R. Soc. A*, *445*, 415–435.

Körner, H. J. (1976). Reichweite und Geschwindigkeit von Bergstürzen und Fliesschneelawinen. *Rock Mechanics*, *8*(3), 225–256. In German.

Korteweg, D. J. and de Vries, G. (1895). On the change of form of long waves advancing in a rectangular canal and on a new type of long stationary waves. *Philosophical Magazine Ser. 5*, *39*(422-443).

Korycansky, D. G. and Lynett, P. J. (2005). Offshore breaking of impact tsunami: The Van Dorn effect revisited. *Geophys. Res. Lett.*, *32*(L10608).

Korycansky, D. G. and Lynett, P. J. (2007). Run-up from impact tsunami. *Geophys. J. Int.*, *170*, 1076–1088.

Koschdon, K. and Schäfer, M. (2003). A Lagrangian-Eulerian finite-volume method for simulating free surface flows of granular avalanches. In K. Hutter and N. Kirchner (Eds.), *Lecture notes in applied and computational mechanics: Dynamic response of granular and porous materials under large and catastrophic deformation*, Berlin, Heidelberg, New York: Springer, vol. 11. 83–108.

Kranzer, H. C. and Keller, J. B. (1959). Water waves produced by explosions. *Journal of Applied Physics*, *30*(3), 398–407.

Kulikov, E. A., Rabinovich, A. B., Thomson, R. E., and Bornhold, B. D. (1996). The landslide tsunami of November 3, 1994, Skagway harbor, Alaska. *J. Geophys. Res.*, *101*, 6609–6615.

Laitone, E. V. (1960). The second approximation to cnoidal and solitary waves. *J. Fluid Mech.*, *9*, 430–444.

Lamb, H. (1945). *Hydrodynamics*. New York: Dover Publications.

Law, L. and Brebner, A. (1968). On water waves generated by landslides. In 3^{rd} *Australas. Conf. on Hydraulics and Fluid Mechanics*. Sydney, 155–169.

LeMéhauté, B. (1976). *An introduction to hydrodynamics and water waves*. New York: Springer.

LeMéhauté, B. and Khangoankar, T. (1992). Generation and propagation of explosion generated waves in shallow water. Tech. Rep. DNA-TR-92-40, Defense Nuclear Agency, Washington D.C.

LeMéhauté, B. and Wang, S. (1995). *Water waves generated by underwater explosion*. Advanced series on ocean engineering. Singapore: World Scientific.

Lighthill, J. A. (1978). *Waves in fluids*. Cambridge University Press.

Lindken, R. and Merzkirch, W. (2000). Velocity measurements of liquid and gaseous phase for a system of bubbles rising in water. *Experiments in fluids*, *29*, S194–S201.

Liu, P. L.-F., Lynett, P., Fernando, H., Bruce, E. J., Fritz, H., Highman, B., Morton, R., Goff, J., and Synolakis, C. (2005). Observations by the international tsunami survey team in sri lanka. *Science*, *308*, 1595.

Lun, C. K. K., Savage, S. B., Jeffrey, D. J., and Chepurniy, N. (1986). Kinetic theories for granular flows: inelastic particles in couette flow and slightly inelastic particles in a general flow field. *J. Fluid Mech.*, *140*, 223–256.

Lynett, P. and Liu, P. L.-F. (2002). A numerical study of submarine landslide generated waves and runup. *Proc.: Mathematical, Physical and Engineering Sciences*, *458*, 2885–2910.

MacFarlane, D. F. and Gillon, D. F. (1996). *Landslides*, Rotterdam, chap. The performance of landslide stabilization measures, Clyde power project, New Zealand. 1747–1757.

MacFarlane, D. F. and Jenks, D. G. (1996). *Landslides*, Rotterdam, chap. Stabilization and performance of No. 5 creek slide, Clyde power project, New Zealand. 1739–1746.

Mader, C. L. (1988). *Numerical modeling of water waves*. Berkeley.: University of California press.

Mader, C. L. (1999). Modeling of the 1958 Lituya Bay mega-tsunami. *Science of Tsunami Hazards*, *17*(2), 57–67.

Mader, C. L. and Gittings, M. L. (2006). Numerical model for the Krakatoa hydrovolcanic explosion and tsunami. *Science of Tsunami Hazards*, *24*(3), 174–182.

Madsen, C. L. and Gittings, M. L. (2002). Modeling the 1958 lituya bay mega-tsunami ii. *Science of Tsunami Hazards*, *20*(5), 241–250.

Madsen, O. S. (1971). On the generation of long waves. *J. Geophys. Res.*, *76*(36), 8672–8683.

Massoudi, M. and Boyle, E. J. (1991). A review of theories for flowing granular materials with applications to fluidized beds and solids transport. Report DOE/PETC/TR-91/8, U.S Department of energy.

McCowan, J. (1891). On the solitary wave. *Phil. Mag. J. Sci.*, *32*(5), 45–58.

McCowan, J. (1894). On the highest wave of permanent type. *Phil. Mag. J. Sci.*, *38*, 351.

McDougall, S. and Hungr, O. (2004). A model for the analysis of rapid landslide motion across three-dimensional terrain. *Can. Geotech. J.*, *41*, 1084–1097.

McEven, A. S. (1989). Mobility of large rock avalanches: Evidence from Valles Marineris, Mars. *Geology*, *17*(12), 1111–1114.

McGlaun, J. M., Thompson, S. L., and Elrick, M. G. (1990). CTH: a three-dimensional shock wave physics code. *Int. J. Impact Engrg.*, *10*, 351–360.

Mei, C. C. (1989). *The applied dynamics of ocean surface waves*. Advanced series on ocean engineering 1. Singapore: World Scientific.

Melosh, J. (1986). The physics of large landslides. *Acta Mech.*, *64*, 89–99.

Miller, D. J. (1960). Giant waves in lituya bay, alaska. *Geological Survey Professional Paper*, *354*, C. U.S. Government Printing Office, Washington, D.C.

Miller, R. L. (1970). Prediction curves for waves near the source of an impulse. In *Proc. 12th Coastal Engrg. Conf.*. Washington, D.C.: ASCE, 609–624.

Miller, R. L. and White, R. V. (1966). A single-impulse system for generating solitary, undulating surge, and gravity shock waves in the laboratory. Fluid Dynamics and Sediment Transport Laboratory Report 5, Dept. Geophys. Sci., Univ. Chicago, Ill.

Monaghan, J. J. (1992). Smoothed particle hydrodynamics. *Ann. Rev. Astron. Astrophys.*, *30*, 543–574.

Monaghan, J. J., Cas, R. A. F., Kos, A. M., and Hallworth, M. (1999). Gravity currents descending down a ramp. *J. Fluid Mech.*, *379*, 39–69.

Monaghan, J. J. and Kos, A. (1999). Solitary waves on a cretan beach. *Journal of Waterway, Port, Coastal and Ocean Engineering, ASCE*, *125*(3), 145–154.

Monaghan, J. J. and Kos, A. (2000). Scott russell's wave generator. *Physics of Fluids*, *12*(3), 622–630.

Müller, L. (1964). The rock slide in the vajont valley. *Rock Mech. Engrg. Geol.*, *2*(3-4), 148–212.

Munk, W. H. (1949). The solitary wave theory and its application to surf problems. *Annals of the New York Academy of Science*, *51*, 376–424.

Naheer, E. (1978). Laboratory experiments with solitary wave. *J. Waterw. Harbors Coastal Engrg. Div., ASCE*, *104*(WW4), 421–436.

Najafi-Jilani, A. and ATaie-Ashtiani, B. (2008). Estimation of near-field characteristics of tsunami generation by submarine landslide. *Ocean Engineering*, *35*, 545–557.

Noda, E. (1970). Water waves generated by landslides. *Journal of the Waterways, Harbors and Coastal Engineering Division, ASCE*, *96*(WW4), 835–855.

Noda, E. (1971). Fourier analysis of transient wave systems. *J. Waterway Harbors Coastal Engrg. Div.*, *97*(WW4), 835–855.

Normark, W. R., Moore, J. G., and Torresan, M. E. (1993). Giant volcano-related landslides and the development of the Hawaiian islands. In W. C. S. et al. (Ed.), *Submarine landslides: selected studies in the US exclusive economic zones.*, US Geol. Surv. Bull, vol. 2002. 184–196.

Novak, P. and Cabelka, J. (1981). *Models in hydraulic engineering*. Boston: Pitman.

Ogawa, T. (1924). Notes on the volcanic and seismic phenomena in the volcanic district of Shimabara, with a report on the earthquake of December 8, 1922. *Kyoto Imp. Univ., Ser. B*, *1*(2), 219–224.

Oppenheim, I. (1991). Statistical mechanical theory of inelastic granular systems. In *Joint NSF-DOE workshop on Flow of particulates and Fluids*. Worcester: Worcester Polytechnic Institute, 236–253.

Oppenheim, I. and McBride, J. (1990). Transport equations for suspensions of inelastic particles. *Physica A*, *165*, 279–302.

Panizzo, A., Bellotti, G., and Girolamo, P. D. (2002). Application of wavelet transform analysis to landslide generated waves. *Coastal Eng.*, *44*(4), 321–338.

Panizzo, A., Girolamo, P. D., and Petaccia, A. (2005). Forecasting impulse waves generated by subaerial landslides. *Journal of Geophysical Research*, *110*(C12).

Perl, I. P., Cheng, T. T., and McClung, D. M. (1980). A two-parameter model of snow avalanche motion. *Journal of Glaciology*, *26*, 197–207.

Pitman, E. B., Nichita, C. C., Patra, A., Bauer, A., Sheridan, M., and Bursik, M. (2003). Computing granular avalanches and landslides. *Physics of Fluids*, *15*(12), 3638–3646.

Plafker, G. and Eyzaguirre, V. R. (1979). *Rockslides and avalanches*, Amsterdam, Netherlands: Elsevier, vol. 2 of *Developments in Geotechnical Engineering, 14B*, chap. Rock avalanche and wave at Chungar, Peru. 269–279.

Pluss, C. (1987). *Experiments on granular avalanches*. Diplomarbeit. Abt X, Eidg. Techn. Hochshule, Zurich. 113pp.

Prins, J. E. (1958). Characteristics of waves generated by a local disturbance. *Trans. Am. Geophys. Union*, *39*(5), 865–874.

Pudasani, S. P., Eckart, W., and Hutter, K. (2003a). Gravity driver rapid shear flows of dry granular masses in helically curved and twisted channels. *Math. Models Meth. Appl. Sci.*, *13*, 1019–1052.

Pudasani, S. P. and Hutter, K. (2003). Rapid shear flows of dry granular masses down curved and twisted channels. *J. Fluid Mech.*, *495*, 193–208.

Pudasani, S. P., Hutter, K., and Eckart, W. (2003b). Gravity-driven rapid shear flows of dry granular masses in topographies with orthogonal and non-orthogonal metrics. In K. Hutter and N. Kirchner (Eds.), *Lecture notes in applied and computational mechanics: Dynamic response of granular and porous materials under large and catastrophic deformation*, Berlin, Heidelberg, New York: Springer, vol. 11. 43–82.

Pudasani, S. P., Wang, Y., Sheng, L.-T., Hsiau, S.-S., Hutter, K., and Katzenbach, R. (2008). Avalanching granular flows down curved and twisted channels: theoretical and experimental results. *Physics of Fluids*, *20*(7), 073302.

Quecedo, M., Pastor, M., and Herreros, M. I. (2004). Numerical modeling of impulse waves generated by fast landslides. *International Journal for Numerical Methods in Engrg.*, *59*, 1633–1656.

Radbruch-Hall, D. H. (1978). *Rockslides and Avalanches*, Amsterdam, Netherlands: Elsevier, vol. 1 of *Natural Phenomena*, chap. Gravitational creep of rock masses on slopes. 607–657.

Raffel, M., Willert, C. E., and Kompenhans, J. (1998). *Particle image velocimetry - a practical guide*. Berlin Heidelberg New York: Springer.

Raney, D. C. and Butler, H. L. (1975). A numerical model for predicting the effects of landslide generated water waves. Report, U.S. Army Corps of Engineers Waterways Experiment Station Report H-75-1, Springfield, Va.

Rayleigh, L. (1876). On waves. *London, Edinburgh, Dublin Phil Mag. J. Sci.*, *1*(4), 257–279.

Risio, M. D., Bellotti, G., Panizzo, A., and Girolamo, P. D. (2009a). Three-dimensional experiments on landslide generated waves at a sloping coast. *Coastal Engineering*, *56*, 659–671.

Risio, M. D., Girolamo, P. D., Bellotti, G., Aristodemo, F., Molfetta, M. G., and Petrillo, A. F. (2009b). Landslide-generated tsunamis runup at the coast of a conical island: New physical model experiments. *Journal of Geophys. Res.*, *114*(C01009).

Roth, G. I., Mascenik, D. T., and Katz, J. (1999). Measurements of the flow structure and turbulence within a ship bow wave. *Physics of Fluids*, *11*, 3512–3523.

Russell, J. S. (1837). Report on the committee of waves. *Report of the* 7^{th} *Meeting of the British Association for the Advancement of Science*, *7*, 417–496.

Russell, J. S. (1844). Report on waves. *Report of the* 14^{th} *Meeting of the British Association for the Advancement of Science*, *14*, 311–390.

Rzadkiewicz, S. A. and an P. Heinrich, C. M. (1997). Numerical simulation of submarine landslides and their hydraulic effects. *J. Port Coastal and Ocean Engrg.*, *123*(4), 149–157.

Saelevik, G., Jensen, A., and Pedersen, G. (2009). Experimental investigation of impact generated tsunami; related to a potential rock slide, Western Norway. *Coastal Engineering*, *56*, 897–906.

Salm, B. (1966). Contribution to avalanche dynamics. *IAHS AISH*, *69*, 199–214.

Sander, D. (1990). Weakly nonlinear unidirectional shallow water waves generated by a moving boundary. VAW-Mitteilung 105, Versuchsantalt fur Wasserbau, Hydrologie und Glaziologie, ETH Zurich.

Sander, J. and Hutter, K. (1991). On the development of the theory of solitary wave: A historical essay. *Acta Mechanica*, *86*, 111–152.

Savage, S. B. and Hutter, K. (1989). The motion of a finite mass of granular material down a rough incline. *Journal of Fluid Mechanics*, *199*, 177–215.

Savage, S. B. and Hutter, K. (1991). The dynamics of avalanches of granular materials from initiation to runout. Part I. Analysis. *Acta Mech.*, *86*, 201–223.

Scarano, F. and Riethmuller, M. L. (1999). Iterative multigrid approach in piv image processing with discrete window offset. *Experiments in Fluids*, *26*, 513–523.

Scarano, F. and Riethmuller, M. L. (2000). Advances in iterative multigrid piv image processing. *Experiments in Fluids*, *29*, S51–S60.

Scheidegger, A. E. (1973). On the prediciton of the reach and velocity of catastrophic landslides. *Rock Mechancis*, *5*(3), 231–236.

Scheidegger, A. E. (1975). *Physical Aspects of Natural Catastrophes*. Elsevier.

Schuster, R. L. and Wieczorek, G. F. (2002). Landslide triggers and types. In J. Rybář and J. Stemberk and P. Wagner (Ed.), *Proc.* 1^{st} *European Conference on Landslides*. Tokyo: Balkerma, 59–78.

Schwaiger, H. F. and Higman, B. (2007). Lagrangian hydrocode simulations of the 1958 Lituya Bay tsunamigenic rockslide. *Geochem. Geophys. Geosyst.*, *8*(Q07006).

Sedov, L. I. (1959). *Similarity and dimensional methods in mechanics*. New York: Academic Press.

Sethian, J. A. (1996). *Level set methods: evolving interfaces in geometry, fluid mechanics, computer vision and materials science*. Cambridge: Cambridge University Press.

Shi, A., Teng, M. H., and Wu, T. Y. (1998). Propagation of solitary waves through significantly curved shallow water channel. *J. Fluid Mech.*, *362*, 157–176.

Shreve, R. L. (1966). Sherman landslide, Alaska. *Science*, *154*, 1639–1643.

Shreve, R. L. (1968). The Blackhawk landslide. *The Geological Society of America*, *108*(47), 1–47.

Shusser, M. and Gharib, M. (2000). Energy and velocity of a forming vortex ring. *Physics of Fluids*, *12*(3), 618–621.

Shuvalov, V., Dypvik, H., and Tsikalas, F. (1999). 3-D hydrodynamic code SOVA for multimaterial flows, application to Shoemaker Levy 9 comet impact problem. *International Journal of Impact Engineering*, *23*, 847–858.

Simkin, T. and Fiske, R. S. (1983). *Krakatau 1883 - the volcanic eruption and its effects*. Washington D.C: Smithsonian Institution Press.

Skjelbreia, L. and Hendrickson, J. A. (1961). Fifth order gravity wave theory. In *Proc. 7^{th} Conf. on Coastal Engineering*. University of California, Berkley: Engineering foundation council on wave research, 184–196.

Slingerland, R. L. and Voight, B. (1979). Occurences, properties and predictive models of landslide-generated impulse waves. In B. Voight (Ed.), *Rockslides and avalanches*, Elsevier, Amsterdam.

Slingerland, R. L. and Voight, B. (1982). Evaluating hazard of landslide-induced water waves. *J. Waterw. Port Coastal and Ocean Div., ASCE*, *108*(WW4), 504–512.

Sorensen, R. M. (1993). *Basic wave mechanics for coastal and ocean engineers*. New York: Wiley.

Stokes, G. G. (1847). On the theory of oscillatory waves. *Transactions of the Cambridge Philosophical Society*, *8*, 441–455.

Storr, G. J. and Behnia, M. (1999). Experiments with large diameter gravity driven impacting liquid jets. *Experiments in Fluids*, *27*, 60–69.

Synolakis, C. E. (1991). Generation of long waves in laboratory. *J. Waterway, Port, Coastal, and Ocean Engrg., ASCE*, *116*(2), 252–266.

Synolakis, C. E., Bardet, J., Borrero, J. C., Davies, H. L., Okal, E. A., Silver, E. A., Sweet, S., and Tappin, D. R. (2002). Slump origin of the 1998 Papua New Guinea tsunami. *Proceedings of the Royal Society of London, Ser. A*, *458*, 763–789.

Synolakis, C. E., Borrero, J. C., Plafker, G., Yalciner, A., Greene, G., and Watts, P. (2000). Modeling the 1994 Skagway, Alaska tsunami. *EOS, Trans. Am. Geophys. Union*, *81*(F748). Abstract.

Tai, C. Y., Wang, Y., Gray, J. M. N. T., and Hutter, K. (1999). Methods of similitude in granular avalanche flows. In K. Hutter, Y. Wang, and H. Beer (Eds.), *Advances in cold-regions thermal engineering and sciences, Lecture notes in physics*, Berlin, Heidelberg, New York: Springer, vol. 533. 415–428.

Tai, Y. C. (2000). *Dynamics of granular avalanches and their simulations with shock-capturing and front-tracking numerical schemes*. Ph.D. thesis, Darmstadt University of Technology, Darmstadt.

Tai, Y. C., Gray, J. M. N. T., and Hutter, K. (2001). Dense granular avalanches: mathematical description and experimental validation. In N. L. Balmforth and A. Provenzale (Eds.), *Geomorphological fluid mechanics, Lecture notes in physics*, Berlin, Heidelberg, New York: Springer, vol. 582. 339–366.

Tai, Y. C., Noelle, S., Gray, J. M. N. T., and Hutter, K. (2002). Shock-capturing and front-tracking methods for grnaular avalanches. *J. Comput. Phys.*, *175*, 269–301.

Teng, H. M. and Wu, T. Y. (1992). Nonlinear water waves in channels of arbitrary shape. *J. Fluid Mech.*, *242*, 211–233.

Teng, H. M. and Wu, T. Y. (1994). Evolution of long waves in variable channels. *J. Fluid Mech.*, *266*, 303–317.

Teng, M. H. (1997). Solitary wave solution to boussinesq equations. *J. Waterway Port Coastal and Ocean Engrg., ASCE*, *123*(3), 138–141.

Tinti, S. and Bortolucci, E. (2000). Energy of water waves induced by submarine landslides. *Pure Appl. Geophys.*, *157*, 281–318.

Titov, V. V. and Synolakis, C. E. (1995). Modeling of breaking and nonbreaking long-wave evolution and runup using VTCS-2. *J. Waterways Ports and Ocean Engrg.*, *121*, 308–316.

Titov, V. V. and Synolakis, C. E. (1998). Numerical modeling of tidal wave runup. *J. Waterways Ports and Ocean Engrg.*, *124*, 157–171.

Tocher, D. and Miller, D. J. (1959). Field observations on effects of Alaskan earthquake of 10 july, 1958. *Science*, *129*, 394–395.

Townson, J. M. and Kaya, Y. (1988). Simulations of the waves in lake Botnen created by the Rissa landslide. *Proc. Inst. Civ. Engrg.*, *85*(2), 145–160.

Unoki, S. and Nakano, M. (1953). On the cauchy-poisson waves caused by the eruption of a submarine volcano. *Oceanogr. Mag.*, *4*, 99–141.

Ursell, F., Dean, R. G., and Yu, Y. S. (1960). Forced small-amplitude water waves: a comparison of theory and experiment. *J. Fluid Mech.*, *7*, 3–52.

VanKampen, N. G. and Oppenheim, I. (1986). Brownian motion as a problem of eliminating fast variables. *Physica A*, *138*, 231–248.

Varnes, D. J. (1978). *Slope movements type and processes*, TRB, National Research Council, Washington, D.C., vol. 176 of *Landslides analysis and control*. 11–33.

Villeneuve, M. and Savage, S. B. (1993). Nonlinear, dispersive, shallow-water waves developed by a moving bed. *J. Hydraulic Res.*, *31*(2), 249–266.

Vischer, D. L. and Hager, W. H. (1998). *Dam Hydraulics*. Chichester: John Wiley.

Voellmy, A. (1955). Über die Zerstörungskraft von Lawinen. *Schweizerische Bauzeitung*, *73*, 159–162,212–217,246–249,280–285.

Voight, B., Glicken, H., Janda, R. J., and Douglass, P. M. (1981). *Catastrophic rockslide-avalanche of May 18. The 1980 eruptions of Mount St. Helens, Washington*, vol. 1250, chap. U.S. Geological Survey Professional Paper. 347–377.

Voight, B., Janda, R. J., Glicken, H., and Douglass, P. M. (1983). Nature and mechanics of the Mount St. Helens rockslide-avalanche of 18 May 1980. *Géotechnique*, *33*, 243–273.

Vollmöller, P. (2004). A shock-capturing wave propagation method for dry and saturated granular flows. *J. Comput. Phys.*, *175*, 269–301.

Walder, J. S., Watts, P., Sorensen, O. E., and Janssen, K. (2003). Tsunamis generated by subaerial mass flows. *J. Geophys. Res.*, *108*(B5), 2236.

Walton, O. R. and Braun, R. L. (1986). Stress calculations for assemblies of inelastic spheres in uniform shear. *Acta Mech.*, *63*, 73–86.

Wang, Y., Hutter, K., and Pudasani, S. P. (2004). The Savage-Hutter theory: a system of partial differential equations for avalanche flows of snow, debris and mud. *J. Appl. Math. Mech.*, *84*, 507–527.

Ward, S. N. (2001a). Landslide tsunami. *Journal of Geophys. Res.*, *106*(6), 11201–11215.

Ward, S. N. (2001b). Landslide tsunami. *J. Geophys. Res.*, *106*(B6), 11201–11215.

Ward, S. N. and Day, S. (2001). Cumbre Vieja Volcano - potential collapse and tsunami at La Palma, Canary Island. *Geophys. Res. Letters*, *28*(17), 3397–3400.

Ward, S. N. and Day, S. (2003). Ritter island volcano - lateral collapse and the tsunami of 1888. *Geophysical Journal International*, *154*, 891–902.

Ward, S. N. and Day, S. (2008). Tsunami Balls: A granular approach to tsunami runup and inundation. *Commun. Comput. Phys.*, *3*(1), 222–249.

Watts, P. (1997). *Water waves generated by underwater landslides*. Ph.D. thesis, California Institute of Technology, Pasadena, CA, USA.

Watts, P. (1998). Wavemaker curves for tsunamis generated by underwater landslides. *Journal of Waterway, Port, Coastal and Ocean Engineering, ASCE*, *124*(3), 127–137.

Watts, P. (2000). Tsunami features of solid block underwater landslides. *Journal of Waterway, Port, Coastal and Ocean Engineering, ASCE*, *126*(3), 144–152.

Watts, P., Grilli, S. T., Kirby, J. T., Fryer, G. J., and Tappin, D. R. (2003). Landslide tsunami case studies using a Boussinesq model and a fully nonlinear tsunami generation model. *Nat. Hazards Earth Syst. Sci.*, *3*, 391–402.

WCHL (1970). Hydraulic model studies - wave action generated by slides into mica reservoir - british columbia. Report, Western Canada Hydraulics Laboratory, Vancouver.

Wehausen, J. V. and Laitone, V. E. (1960). *Surface Waves*, vol. IX of *Encyclopedia of Physics*. Berlin: Springer Verlag.

Weidman, P. B. and Zakhem, R. (1988). Cylindrical solitary waves. *J. Fluid Mech.*, *191*, 557–573.

Weiss, R., Fritz, H. M., and Wünnemann, K. (2009). Hybrid modeling of the mega-tsunami runup in Lituya Bay after half a century. *Geophysical Research Letters*, *36*(L09602).

Weiss, R. and Wuennemann, K. (2007). Understanding tsunami by landslides as the next challenge for hazard, risk and mitigation: Insight from multi-material hydrocode modeling. *Eos Trans. AGU*, *88*(52), Abstract S51C–06.

Weiss, R., Wünnemann, K., and Bahlburg, H. (2006). Numerical modelling of generation, propagation and run-up of tsunamis caused by oceanic impacts: model strategy and technical solutions. *Geophys. J. Int.*, *167*, 77–88.

Westerweel, J. (2000). Theoretical analysis of the measurement precision in particle image velocimetry. *Experiment in Fluids*, *29*, S3–S12.

Westerweel, J., Dabiri, D., and Gharib, M. (1997). The effect of a discrete window offset on the accuracy of cross-correlation analysis of digital piv recordings. *Experiments in fluids*, *231*, 20–28.

Wiegel, R. L. (1955). Laboratory studies of gravity waves generated by the movement of a submerged body. *Trans. Am. Geophys. Union*, *36*(5), 759–774.

Wiegel, R. L. (1960). A presentation of cnoidal wave theory for practical application. *J. Fluid Mech.*, *7*(273-286).

Wiegel, R. L. (1964). *Oceanographical engineering*. London: Prentice-Hall.

Wiegel, R. L., Noda, E. K., Kuba, E. M., Gee, D. M., and Tornberg, G. F. (1970). Water waves generated by landslides in reservoirs. *J. Waterways and Harbors Div.*, *96*(2), 307–333.

Wieland, M., Gray, J. M. N. T., and Hutter, K. (1999). Channelized free surface flow of cohesionless granular avalanche in a chute with shallow lateral curvature. *J. Fluid Mech.*, *293*, 73–100.

Willert, C. E. and Gharib, M. (1991). Digital particle image velocimetry. *Experiments in fluids*, *10*, 181–193.

Wu, T. Y. (1981). Long waves in ocean and coastal waters. *J. Engrg. Div., ASCE*, *107*, 401–522.

Wünnemann, K., Collins, G. S., and Melosh, H. J. (2006). A strain-based porosity model for use in hydrocode simulations of impacts and implications for the transient-crater growth in porous targets. *Icarus*, *180*, 514–527.

Yalin, M. S. (1971). *Theory of hydraulic models*. London: Macmillan.

Zweifel, A. (2004). *Impulswellen: Effeckte der Rutschdichte und der Wassertiefe*. Ph.D. thesis, ETH, Zürich, Switzerland.

Zweifel, A. and Hager, W. H. (2006). Plane impulse waves in reservoirs. *J. Waterw. Port Coastal and Ocean Engrg., ASCE*, *132*(5), 358.

VITA

Fahad Mohammed was born on March 4, 1980 in Guntur, India. He received his Master of Science in Civil Engineering from University of Texas at Austin in 2006. He received his Bachelor of Technology in Naval Architecture and Ocean Engineering from Indian Institute of Technology, Madras, India in 2004.